

SYNTHESIS OF CELLULOSE NANOFIBER COMPOSITES FOR MECHANICAL
REINFORCEMENT AND OTHER ADVANCED APPLICATIONS

A Dissertation
Submitted to the Graduate Faculty
of the
North Dakota State University
of Agriculture and Applied Science

By

Xuezhu Xu

In Partial Fulfillment of the Requirements
for the Degree of
DOCTOR OF PHILOSOPHY

Major Program:
Materials and Nanotechnology

June 2015

Fargo, North Dakota

North Dakota State University
Graduate School

Title

Synthesis of Cellulose Nanofiber Composites for Mechanical Reinforcement and
Other Advanced Applications

By

Xuezhu Xu

The Supervisory Committee certifies that this *disquisition* complies with North Dakota State
University's regulations and meets the accepted standards for the degree of

DOCTOR OF PHILOSOPHY

SUPERVISORY COMMITTEE:

Dr. Long Jiang

Chair

Dr. Erik K. Hobbie

Dr. Xiangfa Wu

Dr. Chad Ulven

Dr. Dilpreet Bajwa

Approved:

July 8, 2015

Date

Dr. Erik Hobbie

Department Chair

ABSTRACT

Cellulose nanofibers from bioresources have attracted intensive research interest in recent years due to their unique combination of properties including high strength and modulus, low density, biocompatibility/biodegradability and rich surface chemistry for functionalization. The nanofibers have been widely studied as nanoreinforcements in polymer nanocomposites; while the nanocomposite research is still very active, new research directions of using the nanofibers for hydrogels/aerogels, template for nanoparticle synthesis, scaffold, carbon materials, nanopaper, etc. have emerged. In this Ph.D. thesis, fundamental studies and application developments are performed on three types of cellulose nanofibers, i.e. cellulose nanocrystals (CNCs), cellulose nanofibrils (CNFs) and bacterial cellulose (BC). First CNCs and CNFs are systematically compared in terms of their effects on the mechanical properties, crystallization and failure behavior of the nanocomposites, which provides a guideline for the design of cellulose nanofiber reinforced composites. Second, CNFs and BC are used to develop core-shell carbon fibers and flexible carbon aerogels for energy storage applications. This part is focused on developing nanocarbon materials with multi-scale features. Lastly, hybrid CNC/CNF nanopaper with superior optical, mechanical, and electrical properties is developed and its application is demonstrated on a LED device.

ACKNOWLEDGEMENTS

First, I would like to express my sincere gratitude to my graduate research committee, Professors Long Jiang, Erik Hobbie, Xiangfa Wu, Chad Ulven, and Dilpreet Bajwa for their guidance and generous supports.

Also, I am very grateful to the financial supports from ND EPSCoR, NASA EPSCoR and KAUST Baseline.

Moreover, I am indebted to Professors Xiang-fa Wu, Chad Ulven, Yechun Wang, Robert Pieri, Erik Hobbie, Val R. Marinov and Xinnan Wang for their experimental supports. Special thanks go to Scott A. Payne and Moore Jayma at Electron Microscopy Center for acquiring wonderful SEM and TEM micrographs throughout the years. I would also like to thank the administrative and technical staff in the Mechanical Engineering department including Mrs. Tanya Erickson, Mrs. Laura McElmurray, Mrs. Tiffany Neuharth, and Mr. Shannon Viestenz.

Former and current graduate/undergraduate students from ME and other departments, Dr. Shanshan Huo, Jessica L. Lattimer and Tingting Zhou, Chenguang Long, Xingyu Chen, Myungken Oh and Xiaoyi Zhou are appreciated for their helps. Group members David Gutschmidt, Myungken Oh, Fei Liu, Qian Ma, Yong Wang are thanked for their generous supports in all kinds of forms, inside and outside the labs.

Outside NDSU, collaborators Dr. QianQian Wang and Dr. Junyong Zhu from USDA Forest Service Laboratory, Dr. Jian Zhou, Prof. Gilles Lubineau, Dr. D. H. Nagaraju, Prof. Husam N. Alshareef, Dr. Chao Shen and Prof. Boon Ooi from King Abdullah University of Science and Technology (Saudi Arabia) are greatly appreciated.

Last but not least, I thank my dear husband Dr. Jian Zhou for his great patience, love and endless supports. I would also dedicate my deepest thanks to my academic advisor Prof. Long

Jiang for his teaching/mentoring in study, research and life, which I will cherish throughout my life.

TABLE OF CONTENTS

ABSTRACT.....	iii
ACKNOWLEDGEMENTS.....	iv
LIST OF TABLES.....	xi
LIST OF FIGURES.....	xii
INTRODUCTION.....	1
Background.....	1
Objectives of this research.....	2
Overview of this research.....	3
CHAPTER 1. LITERATURE REVIEW.....	4
1.1. Introduction.....	4
1.2. Fundamentals of cellulose nanofibers.....	4
1.2.1. Origin and structure of cellulose nanofibers.....	4
1.2.2. Production of cellulose nanofibers.....	7
1.2.3. Energy consumption in producing cellulose nanofibrils (CNFs) and cellulose nanocrystals (CNCs).....	9
1.2.4. Properties of various cellulose nanofibers.....	10
1.3. Applications of cellulose nanofibers.....	12
1.3.1. Cellulose nanofibers as nanoreinforcement in polymer composites.....	12
1.3.2. Applying cellulose nanofibers in a variety of polymers.....	13
1.3.3. Nanofiber/polymer interactions.....	18
1.3.4. Mechanical performance of cellulose nanofiber reinforced nanocomposites.....	20
1.3.5. Modeling of mechanical properties.....	22
1.3.6. Colloidal materials.....	25
1.3.7. Hydrogel materials.....	27

1.3.8. Light-weight porous materials	29
1.3.9. Absorbing foam materials	30
1.3.10. Templating scaffold materials	32
1.3.11. Film materials	35
1.3.12. Conductive electrode materials	37
1.3.13. Flexible device materials	40
1.3.14. Stimulating materials	42
1.3.15. Liquid crystal materials	44
1.3.16. Biocompatible materials	46
1.4. Summary and research needs	48
1.5. References	49
CHAPTER 2. CELLULOSE NANOCRYSTALS VS. CELLULOSE NANOFIBRILS: A COMPARATIVE STUDY ON THEIR MICROSTRUCTURES AND EFFECTS AS POLYMER REINFORCING AGENTS.....	63
2.1. Abstract	63
2.2. Introduction	64
2.3. Materials and methods	66
2.4. Results and discussion.....	68
2.4.1. Morphology and crystalline structure of CNCs and CNFs.....	68
2.4.2. Dispersion and percolation of CNCs and CNFs in PEO	71
2.4.3. FT-IR	74
2.4.4. DSC	77
2.4.5. DMA	77
2.4.6. Mechanical reinforcing effects of CNCs and CNFs	79
2.4.7. Study of fracture surfaces	83
2.4.8. Mechanical property modeling.....	87

2.5. Conclusions	91
2.6. References	92
CHAPTER 3. COMPARISON BETWEEN CELLULOSE NANOCRYSTAL AND CELLULOSE NANOFIBRIL REINFORCED POLYETHYLENE OXIDE NANOFIBERS AND THEIR NOVEL SHISH-KEBAB-LIKE CRYSTALLINE STRUCTURES.....	98
3.1. Abstract	98
3.2. Introduction	98
3.3. Experimental section	100
3.4. Results and discussion.....	102
3.4.1. Rheology of the PEO/CNC and PEO/CNF dispersions	102
3.4.2. Morphology of electrospun nanofibers.....	105
3.4.3. PEO crystallization in the electrospun nanofibers.....	106
3.4.4. Thermal properties of PEO/CNC and PEO/CNF nanofibers	109
3.4.5. Mechanical properties of nanofiber mats	113
3.5. Conclusions	120
3.6. References	120
CHAPTER 4. POROUS CORE-SHELL CARBON FIBERS DERIVED FROM LIGNIN AND CELLULOSE NANOFIBRILS.....	124
4.1. Abstract	124
4.2. Introduction	124
4.3. Materials, preparations and characterizations	125
4.3.1. Materials	125
4.3.2. Preparation of acetylated CNFs/silicone oil suspension.....	126
4.3.3. Electrospinning and fiber carbonization.....	126
4.3.4. Characterizations	127
4.4. Results and discussion.....	128

4.5. Conclusions	132
4.6. References	132
CHAPTER 5. FLEXIBLE, HIGHLY GRAPHITIZED CARBON AEROGEL BASED ON BACTERIAL CELLULOSE/LIGNIN: CATALYST-FREE SYNTHESIS AND ITS APPLICATION IN ENERGY STORAGE DEVICES.....	134
5.1. Abstract	134
5.2. Introduction	135
5.3. Experimental section	137
5.4.1. Materials and BC-LRF hydrogel preparation.....	137
5.4.2. Preparation of BC-LRF carbon aerogel.....	138
5.4.3. Characterizations	138
5.5. Results and discussion.....	140
5.5.1. Formation of lignin-resorcinol-formaldehyde (LRF) hydrogels	140
5.5.2. Formation and microstructure of BC-LRF carbon aerogels	141
5.5.3. Mechanical properties of hydrogels and carbon aerogels	145
5.5.4. Surface area and porosity of BC-LRF carbon aerogels	147
5.5.5. Functionalization and dispersion of BC-LRF carbon aerogels	149
5.5.6. Electrochemical properties of BC-LRF carbon aerogels.....	150
5.5.7. High areal capacitance of BC-LRF carbon aerogels	152
5.6. Conclusion.....	156
5.7. References	156
CHAPTER 6. TRANSPARENT, LOW-HAZE, FLEXIBLE HYBRID CELLULOSE NANOPAPER AS ELECTRODES FOR APPLICATION IN LIGHT EMITTING DIODE DEVICES.....	161
6.1. Abstract	161
6.2. Introduction	162
6.3. Materials and methods	163

6.3.1. Materials	163
6.3.2. Fabrication of cellulose nanopaper (CNP)	164
6.3.3. Synthesis of silver nanowires	164
6.3.4. Fabrication of nanopaper electrode	165
6.3.5. Preparing LED device on nanopaper electrode	165
6.3.6. Characterizations	165
6.4. Results and discussion.....	166
6.4.1. Preparation of CNP and AgNWs/CNP electrodes.....	166
6.4.2. Optical properties of CNP	168
6.4.3. Mechanism for high optical transparency	171
6.4.4. Mechanical properties of the hybrid CNP	174
6.4.5. Sheet resistance and transmittance of AgNWs/CNP electrodes.....	176
6.4.6. Damage-tolerant electrical conductivity of AgNWs/CNP electrodes	178
6.4.7. AgNWs/CNP electrodes in LED devices	180
6.5. Conclusion.....	182
6.6. References	183
CHAPTER 7. CONCLUSIONS AND FUTURE WORK.....	189
7.1. Conclusions	189
7.2. Future work	192
APPENDIX. LIST OF PUBLICATIONS	194
A.1. Publications in Thesis (5)	194
A.2. Other related publications (15).....	194
A.2.1. Book Chapters (1).....	194
A.2.2. Journal Publications (4)	194
A.2.3. Conference Posters/Proceedings (10).....	195

LIST OF TABLES

<u>Table</u>	<u>Page</u>
1.1. Acid hydrolysis conditions and characteristics of the produced CNCs.....	9
1.2. Properties of commonly used nanoreinforcement materias.....	11
1.3. Mechanical reinforcement of cellulose nanofibers in polymer composites.....	16
2.1. XRD results of pure CNCs and CNFs.	70
2.2. Melting characteristics of neat PEO, PEO/CNCs and PEO/CNFs.	77
2.3. Mechanical properties of PEO/CNC and PEO/CNF nanocomposite films.....	81
3.1. XRD results of pure PEO, PEO/CNC (7 wt%), and PEO/CNF (7 wt%) nanofibers.....	109
3.2. DSC results for the electrospun nanofibers.	112
3.3. Mechanical properties of PEO/CNC and PEO/CNF nanofiber mats.....	116
5.1. Sizes of the nanofibers or nano-aggregates in BC, LRF, and BC-LRF aerogels and carbon aerogels.....	144
5.2. Surface area and pore size for BC-LRF carbon aerogels.....	149
5.3. Areal capacitance of the BC-LRF aerogels	155
6.1. Electrical and optical properties of AgNWs/CNP electrodes.....	177

LIST OF FIGURES

<u>Figure</u>	<u>Page</u>
1.1. (A) Hierarchical structure of fibrous cellulose, adapted from the artwork of Lavoine; (B) CNFs and (C) CNCs	6
1.2. (A) SEM of a bacterial cellulose network including the bacterial cells; (B) a bacterial cellulose pellicle; (C) SEM of supercritical carbon dioxide (CO ₂) dried bacterial cellulose aerogel	7
1.3. Different surface modification methods for CNCs and CNFs.	12
1.4. TEM images of stained 100 nm thick CMC hydrogels: (A) pure polymeric CMC hydrogel with no CNCs, (B, D) CNC-reinforced hydrogel with 0.25 % loading, (C) aldehyded–CNC (-C=O)-reinforced hydrogel with 0.375 % loading; a few individual CNCs or CHO–CNCs are highlighted with red boxes. (E) TEM images of CNCs, (F) TEM images of aldehyded–CNCs	19
1.5. (A) Schematic illustration and network microscopic structure of CNC–PAM hydrogels; (B) A schematic illustration of the crosslinking mechanism of PVA, MWCNT and CNFs	19
1.6. (A) Effect of the ACN content on strain at break (σ_b), stress at break (ϵ_b), and Young’s modulus E for PLA/acetylated CNC nanocomposites as well as the neat PLA-F sheet; (B) Mechanical properties of CNC/PAM gels with different CNC contents	22
1.7. Evolution of the nanocomposite shear storage modulus at $T/T\alpha = 1.15$ with the filler content. Comparison with the one predicted by the mechanical percolation approach (heavy line) and the one predicted by the mean field approach (light line)	25
1.8. (A) Schematic illustration of the organization of the isotropic and chiral nematic phases of a biphasic CNC suspension at equilibrium; (B-C) SEM images of polymerized styrene-water emulsions stabilized by (A) bacterial cellulose nanofibers and (B) cotton cellulose nanocrystals (CNCs); (D) SEM micrographs of CNCs film; (E) Solid CNC film in diffuse light, showing its iridescence when viewed normal to the surface (left) and at an oblique angle	27
1.9. (A) TEMPO-CNF wet gel obtained after vacuum filtration of TEMPO-CNF aqueous dispersion (water content in the cake is 70–90%); (B) Freestanding acidic-pH induced hydrogels of cellulose nanofibrils; (C) CNFs in aqueous dispersion (1.27 wt%) and CNF/Ag ⁺ hydrogel; (D) Illustration depicting the attachment of Ag ⁺ ions to CNFs, and the subsequent reduction of Ag ⁺ to Ag nanoparticles by using NaBH ₄	29
1.10. (A) CNFs/starch foam with (B) 10 wt% CNFs, scale bars is 300 mm; (B) photos and SEM images of CNF aerogels	30

1.11. (A) Aerogel with a water absorbency of 155 g/g, water can then be released from the sample by compression; (B) Time-dependent absorption spectra of the dye solution containing CNFs.....	32
1.12. (A-B) HRTEM images of BC, Au-BC nanocomposites. Inset shows the related electron diffraction pattern; (C-D) SEM images of flexible magnetic aerogels and stiff magnetic nanopaper using BC as templates	34
1.13. (A) photo of BC sheet, BC/epoxy sheet and epoxy resin; (B) Light scattering effect of the ribbons; (C) “focus” and “blurry” transmitted light spots of the nonstretched and stretched ribbons of CNF/PEG films	37
1.14. (A) Transparent, conductive, and printable composites consisting of TEMPO-oxidized CNFs and carbon nanotube; (B) Photos of CNF and RGO-CNF papers with increasing graphene contents	40
1.15. All-solid-state supercapacitor and its electrochemical performances; (B) Device structure of solar cells on CNC substrates, Chemical structure of PBDTTT-C and PCBM as an effective solar layer; (C) $J-V$ characteristics of the solar cell on CNC substrate in the dark (thin black line) and under 95 mW/cm ² of AM1.5 illumination (thick red line); the $J-V$ characteristics on a semi-logarithmic scale in the dark (thin black line) and under illumination (thick red line)	42
1.16. (A) functionalization of the surface of cellulose nanocrystals (CNCs) with either carboxylic acid (CNC-CO ₂ H) or amine (CNC-NH ₂) moieties renders the CNCs pH-responsive; (B) Light-healable supramolecular nanocomposites based on modified CNCs, the crack in polymer disappears under 20 s UV exposure	44
1.17. (A) illustration showing screw symmetry and helical pitch resulting from twisted close packing of the nanorods; (B) Proposed correspondence between CNC rigid rod assembly orientation in one domain of the chiral nematic phase solid film; (C) Photoic patterns printed in chiral nematic resins	46
1.18. (A) The wound-covering of the full-skin injury model in a mouse; (B) Laser scanning confocal images of cells cultured on the porous side of BC	48
2.1. High resolution TEM images of CNCs (a) and CNFs (b)	69
2.2. Wide angle X-ray diffraction patterns of CNCs and CNFs	70
2.3. PEO/CNF and PEO/CNC nanocomposite films at room temperature. CNF and CNC concentration: 7%	72
2.4. TEM images of PEO/CNC (7%) nanocomposite film (a) and CNC crystallites (b)	73
2.5. TEM images of PEO/7 wt% CNFs (a-c) and PEO/10 wt% CNFs (d)	74

2.6. FT-IR spectra in the region of hydroxyl stretching for PEO/CNC (a) and PEO/CNF (b) composites with various nanofiber contents	75
2.7. FT-IR spectra for PEO/CNC (a) and PEO/CNF (b) composites with various nanofiber contents	76
2.8. $Tan \delta$ of PEO/CNC nanocomposite films. The arrows point to the glass transition temperature (T_g) of pure PEO and the composites	79
2.9. $Tan \delta$ of PEO/CNF nanocomposite films. The arrows point to the glass transition temperature (T_g) of pure PEO and the composites	79
2.10. Tensile stress-strain curves for pure PEO and PEO/CNC films with 1%, 4%, 7%, and 10% CNCs	81
2.11. Tensile stress-strain curves for pure PEO and PEO/CNF films with 1%, 4%, 7%, and 10% CNFs	81
2.12. Side (a) and fracture (b) surfaces of pure PEO film	84
2.13. Fracture surfaces of PEO/CNC nanocomposite film with 7 wt% CNCs. The long arrow indicates the tensile load direction; the short arrows point to the crazes generated on the film surfaces after tensile tests	84
2.14. Fracture surfaces of PEO/CNF nanocomposite film with 7 wt% CNFs. Details circled by the ellipse indicate the interlocking between fibrils at the fracture surface	85
2.15. Illustrations of fracture mechanisms of PEO/CNC and PEO/CNF nanocomposites	86
2.16. Young's modulus as a function of cellulose nanofiber content: experimental values vs. model predictions. $\zeta=2L/w$ and $\zeta=0.5L/w$ are used for PEO/CNCs and PEO/CNFs, respectively, in the Halpin-Kardos model	90
3.1. TEM images of needle-like CNCs (a) and network of CNFs (a'); (b) viscosity vs. shear rate of the PEO/CNC dispersions; (c) viscosity vs. shear rate of the PEO/CNF dispersions. (d) comparison of zero-shear viscosity between PEO/CNC and PEO/CNF dispersions. Inset: zero-shear viscosity of pure aqueous CNF dispersions	104
3.2. Photo (a) and FE-SEM micrograph (b) of PEO/CNC 1% nanofiber mat; (c – d) FE-SEM images of PEO/CNF 1% nanofiber mat; (e) diameter distribution of the PEO/CNC nanofibers; (f) diameter distribution of PEO/CNF nanofibers	106
3.3. (a) TEM images of pure PEO nanofibers; (b) PEO/CNF 4% nanofibers; (c) PEO/CNF 4% nanofiber after mild water etching; (d) SAED pattern taken from Figure b; (e) PEO/CNC 4% and (f) PEO/CNF 4% nanofibers after PEO removal; (g) illustration of the shish-kebab-like structure; (h) WAXD patterns of PEO/CNC and PEO/CNF 7% nanofibers	108

3.4. DSC thermograms for the melting and non-isothermal crystallization of PEO/CNC and PEO/CNF nanofibers. (a) PEO/CNC melting; (b) PEO/CNF melting; (c) PEO/CNC crystallization; (d) PEO/CNF crystallization	111
3.5. Stress-strain curves of PEO/CNC (a) and PEO/CNF (b) nanofiber mats with various filler contents; (c) FE-SEM images of pure PEO nanofiber membrane after testing; (d) 1 wt% PEO/CNC nanofiber membrane after testing; (e) fibrillation in the neck region of the PEO/CNF 4% fiber	115
4.1. (a) Reaction scheme of CNF acetylation; (b) Acetylated CNFs dispersed in a silicone oil/chloroform mixture (~0.5 wt%) and (c) FT-IR spectra of pure CNFs and surface modified CNFs	128
4.2. SEM images of electrospun lignin/PAN hollow fibers (a) and CNFs-lignin/PAN core-shell fibers (b, c, d)	130
4.3. SEM images of carbonized lignin/PAN hollow fiber (a) and CNFs-lignin/PAN core-shell fiber (b)	131
5.1. (A) Schematic macromolecular structure of a LRF hydrogel and a LRF16 hydrogel sample; (B) FTIR spectra of dried LRF gel powder; (C) Ternary plot of the gel property of various LRF hydrogels (refer to Table S1 for the formulation of each sample); (D) Process to produce BC-LRF hydrogel	141
5.2. SEM images of (A) BC aerogel; (B) LRF16 aerogel; (C) BC-LRF16 aerogel; (D) BC carbon aerogel; (E - F) LRF16 carbon aerogel; (G - I) BC-LRF16 carbon aerogel; (J) Microstructure evolution of the BC-LRF carbon aerogel	143
5.3. (A) TEM image of BC carbon aerogel; (B) TEM image of BC-LRF16 carbon aerogel; (C) high magnification of TEM image of BC carbon aerogel; (D-E) SAED of BC carbon aerogel and BC-LRF16 carbon aerogel; (F) intensity profile taken by the box in C	145
5.4. (A) Shape recovery of pristine BC hydrogels; (B) Thickness recovery versus time for the hydrogel after being immersed in water; (C) Comparison of BC hydrogels and BC-LRF carbon aerogels; (D) Comparison between BC carbon aerogel and BC-LRF carbon aerogel; (E) Representative compression test curve of BC-LRF16 carbon aerogels; the inset shows the stain and stress profiles; (F) Reversible deformation of the BC-LRF carbon aerogel under 20% strain	146
5.5. (A) Representative N ₂ adsorption-desorption isotherms; (B) pore size distributions of the BC-LRF carbon aerogels; (C) the same pore size distributions within a smaller size range.....	148
5.6. (A) FTIR spectra of the pristine and HNO ₃ -NaOH treated BC-LRF16 carbon aerogels; (B) XPS spectra of the two carbon aerogels. The insets show a stable dispersion of the treated BC-LRF16/acetylene black/PTFE (85:10:5) in ethanol (left) and the spin-coated film of the dispersion on a glass slide (right)	150

5.7. Electrochemical characteristics of BC-LRF16 carbon aerogel based electrodes. (A) Cyclic voltammetry plots between 2 and 50 mV/s. (B) Galvanostatic charge-discharge curves at various current densities. (C) Specific capacitance as a function of current density. The inset shows capacitance retention under repeated charge-discharge. (D) Nyquist plots (inset is the expanded view at high frequencies).	152
5.8. Specific capacitance as a function of mesopore surface area for the BC-LRF carbon aerogels.....	153
6.1. (A) From left to right, aqueous CNFs/CNCs aqueous suspension with increasing CNC content from 0 % to 100 % based on CNFs+CNCs total weight, all suspensions have the same fiber content of 4 wt.%; the first suspension shows a micron-sized pulp fiber suspension as a comparison; (B) Schematic of the process to prepare CNP and AgNWs/CNP electrodes	168
6.2. (A) Demonstration of a piece of plastic-like nanopaper (CNF:CNCs 6:10); (B) Direct transmittance of nanopaper; (C) Direct transmittance of various nanopaper with different CNFs:CNCs weight ratio	169
6.3. (A) Haze values of the hybrid nanopapers compared to commercial transparent substrates; (B) Total transmittance and diffuse reflection as a function of CNC content; (C) Comparison of visual appearance of all-CNF nanopaper and hybrid nanopaper (CNC content: 83 wt.%), samples were located 0 and 1 cm from the background; (D) A piece of nanopaper pasted on a PET bottle. “NDSU” is printed on the nanopaper by a commercial ink-printer	170
6.4. SEM images of (A) regular paper made of micron-sized pulp paper; (B) traditional CNP; (C) our novel CNP (CNFs:CNCs=2:10)	171
6.5. (D) SEM image of traditional nanopaper (CNFs: 100 %) and (E) SEM image of our novel nanopaper (CNFs/CNCs 83 %). (A) AFM phase image (dimension $2 \times 2 \mu\text{m}^2$) of a hybrid CNP (CNC content: 83 wt.%); (B) R_{RMS} vs. CNC content; (C) Porosity and bulk (apparent) density vs. CNC content; (D) TEM image of CNF/CNC network in CNP; (E) Illustration of CNF/CNC network: CNFs form a percolating network while CNCs fill the “voids” within the network. (E) Relationship of calculated scattering factor γ pores and the direct transmittance	172
6.6. Mechanical properties of various CNP films, (A) Young’s modulus E vs. CNC content; (B) stress at break σ vs. CNC content; (C) strain at break ϵ and (C); (D) tensile modulus E vs. ultimate tensile strength σ of our nanopaper compared to various plastics	176

6.7. (A) SEM images of nanopaper electrodes and their sheet resistance dependent on AgNW density; (B) Representative SEM image of nanopaper electrode cross-section area; Scale bars in pictures are 20 μm ; (C) Sheet resistance as a function of AgNW areal density. (D) Total transmittance of various samples vs. wavelength; (E) total transmittance as a function of AgNW areal density; (F) Demonstration presents a series circuit composed of a battery, a $2\times 3\text{ cm}^2$ transparent AgNWs/CNP paper (CNC: 83 wt.%) and a LED lamp	178
6.8. (A) in-situ electrical resistance measurement setup, conductive paper electrode: CNP (CNC content: 83 %) with 174 mg/m^2 AgNWs under bending, the resistance is measured for a middle area of the sample (Length: 0.8 cm; Width: 0.2 cm); (B) initial 12 cycles for electrical resistivity measurement and in-situ cyclic bending of various paper electrodes; (C) 1000 cycles electrical resistivity measurements under cyclic compression for various samples; (D) In-situ electrical resistivity of a representative electrode (348 mg/m^2 AgNW density) under tensile mode	180
6.9. (A) Photo of nanopaper electrode with AgNWs grids for sandwiching LED devices; inset is an optical microscopy image of surface morphology of the AgNWs grids (two micron-sized probes were inset into nanopaper electrode to measure the conductivity); (B-C) current density vs. voltage (I-V) characteristic and light output power vs. current (L-I) characteristics, and (inset) external quantum efficiency vs. current (EQE-I) characteristics of freestanding LED device and embedded red LED device; (D) Sandwiched paper electrode/LED device/paper electrode emitting red light	182

INTRODUCTION

Background

Developing novel materials from renewable resources has been one of the most active research areas in the past decade; it has attracted researchers from materials science, chemical engineering and chemistry alike and has received funding from many government agencies and private investors. Biomass, renewable organic materials such as wood, grass and agricultural crops or wastes, represent an important category of renewable resources and have been under intensive research with the aim of developing novel industrial materials and applications. Polylactic acid (PLA) based on starch, carbon fibers derived from lignin and polyurethane (PU) from soybean oil are among the examples of important biobased products.

Cellulose and lignin are the two major components of plants and represent the two most abundant natural polymers in the world. The cellulose exists in the plants as a fibrous structural component, which is bonded together by the lignin and hemicellulose “adhesive” of the plants, literally forming natural composites, i.e. plants. The fibrous cellulose exhibits a hierarchical structure, whose destruction allows the isolation of nanoscale cellulose nanofibers; the isolated nanofibers can be in the form of long, flexible cellulose nanofibrils (CNFs) comprising both crystalline and amorphous cellulose, or in the form of short, needle-like cellulose nanocrystals (CNCs) comprising mostly crystalline cellulose. A third type of cellulose nanofibers is produced by a bacterium and the fibers are conventionally called bacterial cellulose (BC). BC contains high-purity, long and entangled cellulose nanofibers with a uniform diameter.

All the three types of cellulose nanofibers show exceptional mechanical properties, high aspect ratio (especially for CNFs and BC), large surface area, and rich surface chemistry, which have brought them tremendous research interest. They have first been widely studied as

nanoreinforcements for polymers to produce more environmentally friendly polymer nanocomposites. The reinforced nanocomposites show enhanced mechanical properties at low nanofiber loadings, increased gas barrier properties while retaining clarity, improved thermal stability, etc. Other more recent application developments of the cellulose nanofibers include hydrogels and foams/aerogels, templates for nanoparticle synthesis, scaffold materials, transparent and conductive nanopaper, and flexible electronic devices. These developments are focused on biomedical, optical, electronic, sensing, and energy storage sectors, which create high added-values and depend traditionally on non-renewable materials.

Objectives of this research

Although cellulose nanofibers as nanoreinforcements in polymer nanocomposites have been widely studied, there are questions remained unanswered. For example, what are the differences between CNFs and CNCs in terms of their reinforcing effect? Which one to use when designing a cellulose nanofiber composite? What are their impacts to the properties of electrospun polymer nanofibers if the cellulose nanofibers are incorporated into the polymer nanofibers? Do they alter the crystalline structure of the polymer and change its failure behavior?

For other advanced applications, can we turn cellulose nanofibers into carbon nanofibers and use them for energy storage? Can we make flexible carbon aerogel using cellulose nanofibers and lignin? Can we combine the different types of cellulose nanofibers to create nanopaper with tunable optical and mechanical properties? With superior direct transmittance and low haze that outperform the state-of-art products? On top of that, can we use this nanopaper as a substrate to make flexible, transparent electrodes that show high electrical conductivity and damage tolerance?

This Ph.D research project is designed to answer the above questions. It spans from nanocomposites, hierarchical carbonaceous materials, to transparent electrodes, all of which are actively researched areas in both academia and industry. Through this project, fundamental understanding, processing technology, and proof-of-concept applications will be developed and the knowledge base about cellulose nanofibers will be augmented.

Overview of this research

This research starts out to seek fundamental differences between CNFs and CNCs, especially when they are used as nanoreinforcements in polymer composites (Chapter 3). The understanding can assist the intelligent design of cellulose nanofiber reinforced nanocomposites. Electrospun polymer nanofibers are different from bulk polymer in many aspects. The cellulose nanofibers can be incorporated into the electrospun nanofiber through the electrospinning process to create a “nanofiber-in-nanofiber” structure. The impacts of CNFs and CNCs to the electrospinning process and the size/crystalline structure/mechanical properties/failure mechanisms of the electrospun fibers are systematically studied and compared (Chapter 4). Developing core-shell carbon fiber and carbon tubes using lignin and CNFs via electrospinning is reported in Chapter 5; flexible, fully-biobased carbon aerogels based on BC and lignin and their applications in supercapacitors are presented in Chapter 6. Finally in Chapter 7, hybrid CNC/CNF nanopaper is produced to have tunable optical and mechanical properties by simply adjusting the CNC/CNF ratio. The product with the optimized ratio outperforms most reported nanopaper. By depositing silver nanowires (AgNWs) on the nanopaper, a transparent electrode with high, damage-tolerant conductivity is produced, and its application in a LED device is demonstrated.

CHAPTER 1. LITERATURE REVIEW*

1.1. Introduction

A huge knowledge base about cellulose nanofibers has been established after over a decade of intensive research. In this chapter, the origins, structures and production methods of cellulose nanofibers will first be discussed. Their properties and surface functionalization to tailor their surface chemistry for different applications will then be given. Finally the applications of the cellulose nanofibers, from early nanocomposites to the most recent flexible electronics, will be summarized.

1.2. Fundamentals of cellulose nanofibers

1.2.1. Origin and structure of cellulose nanofibers

Cellulose, synthesized by plants, algae, and bacteria, is the most abundant natural polymer on the earth. Cellulose nanofibers derived from various species of plants are the longest and most widely studied cellulose nanofibers. Current industrially important cellulose nanofibers are primarily developed from woody biomass. Wood is typically composed of three major components: cellulose (~45%), hemicellulose (~25%) and lignin (~20%); the structure of wood can be considered as a fiber reinforced composite – the fibrous cellulose bonded by surrounding hemicellulose and lignin adhesive.

The fibrous cellulose exhibits a hierarchical structure with the cellulose elementary fibrils as its nanoscale building blocks (**Figure 1.1A**).¹ These elementary fibrils can be isolated from

* The content in this chapter was co-authored by Xuezhu Xu and Long Jiang. Xuezhu Xu had primary responsibility for collecting references and manuscript drafting. Long Jiang was the primary developer of the abstract and conclusions. Long Jiang gave comments and Xuezhu Xu revised all versions of this chapter. Long Jiang served as proofreader for this chapter.

different plants through direct mechanical fibrillation,² mechanical fibrillation after enzymatic hydrolysis³ or mechanical fibrillation after chemicals such as 2,2,6,6-tetramethylpiperidine-1-oxyl radical (TEMPO)-mediated oxidation⁴. While wood pulp is the most commonly used feedstock for the nanofibril production, many different types of natural fibers have also been attempted.

The isolated fibrils often entangle/bundle with each other and form a network structure (**Figure 1.1B**).⁵ Along the fibrils there exist segments of amorphous and crystalline cellulose; the amorphous segments can be removed by acid hydrolysis so that only the needle-shaped cellulose nanocrystals are retained (**Figure 1.1C**). A recent paper has reviewed various available methods to produce the long, flexible fibrils and the short, rigid crystals.⁶ Different terms have been used to describe these two types of nanoscale cellulosic materials in literature. Herein the former is denoted by cellulose nanofibrils (CNFs) and the latter by cellulose nanocrystals (CNCs). CNFs and CNCs contain abundant hydroxyl groups (-OH) on their surfaces because of the structure of cellulose molecules. Other chemical groups such as carboxyl groups (from TEMPO oxidation) and sulfate groups (from sulfuric acid hydrolysis) are also present due to these chemical treatments. Diameters between 2 and 100 nm have been reported for CNCs and CNFs and their length can vary between tens of nanometers to micrometers.⁷ CNCs and CNFs show high tensile strength (> 1 GPa) and high modulus (about 40 GPa).^{8,9} Research on cellulose nanofibers has experienced explosive growth in recent years due to their high potential in a wide variety of advanced applications, which are derived from the nanofibers' high strength, high modulus, large aspect ratio/surface area, rich surface chemistry, optical properties, low density and biobased nature.^{10,11,12,13,14}

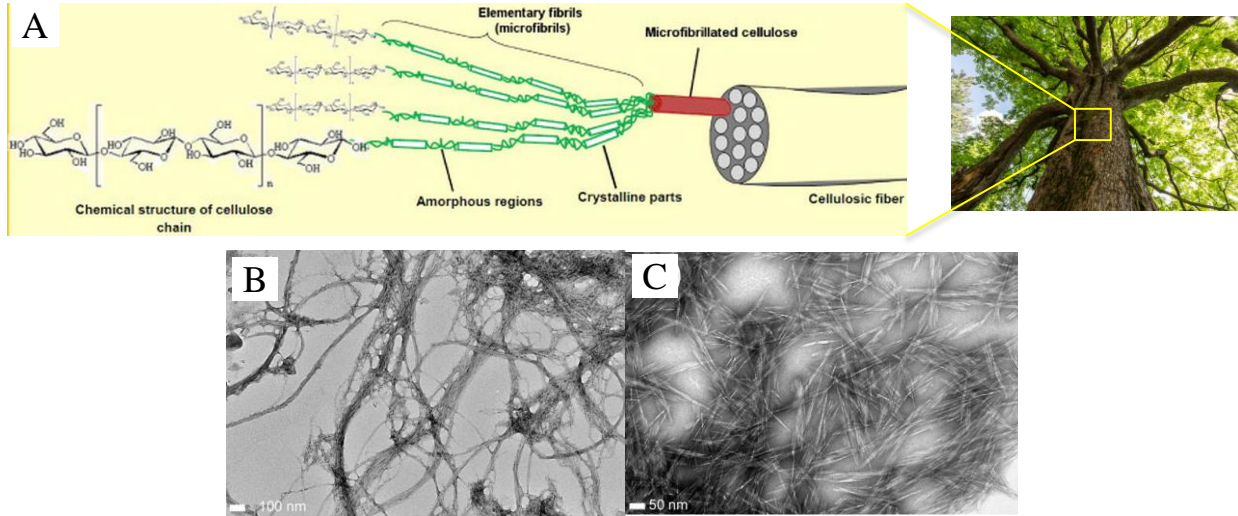


Figure 1.1. (A) Hierarchical structure of fibrous cellulose, adapted from the artwork of Lavoine²⁰; (B) CNFs²³ and (C) CNCs²³.

Besides the plant-based cellulose nanofibers, bacterial cellulose (BC) represents another important category of cellulose nanofibers. BC is produced naturally by bacterium *gluconacetobacter xylinum* through a fermentation process (**Figure 1.2A**). The product, bacterial cellulose pellicle, is formed at the air/liquid interface of the culture medium and is essentially a cellulose hydrogel containing networked BC nanofibers (**Figure 1.2B**). High purity/crystallinity nanofibers can be readily obtained by removing the bacterial cells and other impurities through cleaning the gel with sodium hydroxide (NaOH) solution and water (**Figure 1.2C**). Moduli of BC have been measured to be 78-114 GPa.^{15,16}

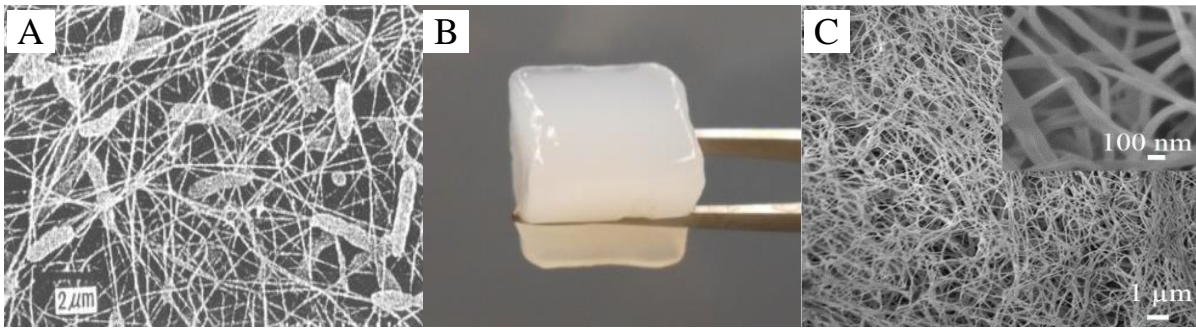


Figure 1.2. (A) SEM of a bacterial cellulose network including the bacterial cells;¹⁷ (B) a bacterial cellulose pellicle; (C) SEM of supercritical carbon dioxide (CO₂) dried bacterial cellulose aerogel.¹⁴

1.2.2. Production of cellulose nanofibers

CNFs and CNCs are mostly extracted from plants and agricultural residues including soft wood,² bamboo,^{18,19} jute fibers,²⁰ coconut husk fibers,²¹ pineapple leaf,²² rice straw,²³ and potato peel²⁴. The production of CNFs generally includes the following steps: 1) lignin, semicellulose and other impurities are removed from the raw lignocellulosic materials through a typical pulping process, where chemicals such as NaOH and sodium chlorite (NaClO₂)¹⁸ are often used; 2) the obtained pulp is destructured to produce CNFs through a nanofibrillation process such as multiple passes of mechanical grinding,^{2,23} intensive ultrasonication¹⁸ or microfluidization.²⁵ CNFs with a wide range of diameter (10 – 1000 nm) and crystallinity (> 40 % cellulose I) are typically obtained.¹⁸ Pretreatments before the nanofibrillation by using various chemicals may change the crystalline structure in the obtained CNFs. The pretreatment (or further refinement) by TEMPO mediated oxidation can result in highly uniform, extremely fine (2.09 nm)²³ CNFs with high aspect ratio. The TEMPO treatment leads to surface carboxylation to the CNFs, which causes ionic repulsion among the nanofibers and stabilizes CNF colloidal suspension. In general, the smaller the fiber diameter, the higher degree of surface carboxylation is present.

CNCs are typically made from micro-sized cellulosic materials (e.g., wood pulp, microcrystalline cellulose, cotton and other natural fibers) through an acid hydrolysis process that removes amorphous cellulose and other non-cellulose components. The hydrolysis conditions, including acid/fiber ratio, temperature, hydrolysis time, acid concentration, and sonication time, show strong effects on the yield, sulfur content (in the case sulfuric acid), anionic sites, Zeta potential, width, length and aspect ratio of the produced CNCs (**Table 1.1**).¹⁹ Depending on their origin and the hydrolysis conditions, CNCs with a diameter ranging from two to over one hundred nanometer and a length up to hundreds of nanometer have been produced. For example, Santos et al (2013)²² used pineapple leaves to produce CNCs. Acid hydrolysis using sulfuric acid (H_2SO_4) at 45 °C for 30 min generates needle-like (4 nm wide, 250 nm long), crystalline (73 %) CNCs with a high thermal stability (225 °C). Hydrochloric acid (HCl),²⁶ phosphoric acid (H_2PO_4),²⁷ hydrobromic acid (HBr)²⁸ have also been used for the hydrolysis reaction, which generates differently surface-functionalized CNCs with varying thermal stability.²⁹ Recent studies have focused on using new raw materials³⁰ and facile manufacturing techniques,³¹ obtaining controlled aspect ratios,³² high CNC yield (94 %),²⁶ and high maximum degradation temperature (364 °C),²⁶ desulfation,^{33,34} as well as comparative studies on CNCs and CNFs.^{5,7,35}

Table 1.1. Acid hydrolysis conditions and characteristics of the produced CNCs.¹⁹

Source material	Bamboo	Eucalyptus	Sisal	Curauá
Hydrolysis conditions				
Acid-fiber ratio (mL/g)	1:10	1:9	15:1	15:1
Temperature (°C)	60	50	50	50
Hydrolysis time (min)	12	50–65	30	45
H ₂ SO ₄ concentration (wt%)	65	65	65	65
Sonication time (min)	4	1	7	7
Characteristics of the CNCs				
Yield (%)	30	17	9	–
Sulfur content (% S)	1.04	0.96	0.53	0.95
Total anionic sites (mmol kg ⁻¹)	324	275	166	297
Zeta potential (mV)	-59 ± 2	-48 ± 7	-49 ± 2	-52 ± 1
Length (nm)	100 ± 28	100 ± 33	119 ± 45	129 ± 32
Width (nm)	8 ± 3	7 ± 1	6 ± 1	5 ± 1
Height (nm)	4.5 ± 0.9	4.5 ± 1.0	3.3 ± 1.0	4.7 ± 1.0
Aspect ratio	22	22	36	27

1.2.3. Energy consumption in producing cellulose nanofibrils (CNFs) and cellulose nanocrystals (CNCs)

Production of CNFs is an energy intensive process. Kelley et al studied energy consumption in three CNF production methods (i.e. homogenization,³⁶ microfluidization³⁷ and micro-grinding) using untreated wood pulp as the feedstock. The energy consumption was found to be very high: 22 kWh/kg, 2.8 kWh/kg and 3.4 kWh/kg for the three methods, respectively.³⁸ The energy was calculated based on electrical energy consumption ($E_e = V \cdot I \cdot t$, where V , I , t are the voltage, current and time, respectively) based on the dry raw material mass.³⁹ Reducing the energy consumption by pretreating the raw materials (e.g. environmentally-friendly enzymatic treatment⁴⁰ and TEMPO-oxidation⁴¹) has been successfully attempted. Ankerfors found that the energy consumption could be reduced to 0.5 – 2.3 kWh/kg after pretreating the feedstock with chemicals or enzymes.³⁷ It should be emphasized that the calculated energy consumptions for CNFs do not include the energy spent during the pulping process, which

involves intensive heating and chemical reactions. As for the CNCs, the energy cost involved in their production is rarely studied. They may have a lower energy cost than CNFs because the hydrolysis reaction under mild conditions constitutes their main production process.

1.2.4. Properties of various cellulose nanofibers

In the literature, the properties of CNFs and CNCs, isolated from different sources (bacteria, tunicate, plants, etc.) using different methods (e.g. acid, enzymatic, mechanical, and oxidative methods) vary significantly.⁷ The variations are derived from the fact that different source materials, processing methods/conditions, and testing methods are used in the literature.

Cellulose nanofibers (i.e. CNFs, CNCs and BC) in general compare favorably to other important nanoparticles/fibers such as nanoclay, carbon nanotubes/vapor growth carbon fibers (VGCF), boron (BN) nanotubes, graphene (xGnP-Graphite NanoPlatelets) (**Table 1.2**). Young's modulus of the cellulose nanofibers are mostly measured by nano-indentation. In one report, the modulus of CNCs is measured to range between 18-50 GPa;⁴² in another report, the modulus of BC was shown to be 78 GPa.⁴³ Other studies have reported the Young's modulus up to 130 GPa and the tensile strength of 10 GPa.^{8,9} CNCs also show very low coefficient of thermal expansion (CTE) and thermal conductivity.⁴⁴ These exceptional mechanical and thermal properties, combining with their large surface area/aspect ratio and low density, have made CNCs and CNFs ideally suited to the development of environmentally friendly polymer nanocomposites.

Table 1.2. Properties of commonly used nanoreinforcing materials.

	Exfoliated Nanoclay	Carbon Nanotube VGCF Cylinder	BN Nanotubes	Graphene (xGnP-Graphite)	Cellulose Nanofibers
Physical structure	Platelet -1nm x 100nm	NT -1nm × 100nm VGCF -20nm × 100um	Cylinder	Platelet -1nm × 100nm	Fiber-like
Chemical structure	hydrous aluminium phyllosilicates	Hexagonal carbon	Boron Nitride	Hexagonal carbon	Cellulose
Interactions	Hydrogen bond Dipole-Dipole	π - π	Hydrogen bond	π - π	Hydrogen Bond
Tensile modulus	0.17 TPa	NT 1.0-1.7 TPa VGCF 0.25-0.5 TPa	1 TPa	1.0 TPa	0.13 TPa
Tensile strength	1 GPa	(NT 180 GPa) VGCF 3-7 GPa	-	-(10-20 GPa)	10 GPa
Electrical resistivity	10 ¹⁰ - 10 ¹⁶ cm	NT 50 × 10 ⁻⁶ Ωcm VGCF 5-100 × 10 ⁻³ Ωcm	insulator	50×10 ⁻⁶ Ωcm 1 Ωcm ⊥	10 ¹⁰ -10 ¹⁶ Ωcm
Thermal conductivity	6.7 × 10 ⁻¹ W/mK	3000 W/mK (NT) 20-2000 W/mK (VGCF)	- 3000W/mK	3000 W/Mk 6 W/mK ⊥	insulator
CTE	8 - 16 × 10 ⁻⁶	-1 × 10 ⁻⁶	1 × 10 ⁻⁶	-1 × 10 ⁻⁶ 29 × 10 ⁻⁶ ⊥	8 - 16×10⁻⁶
Density	2.8 - 3.0 g/cm ³	NT 1.2-1.4 g/cm ³ VGCF 1.8-2.1 g/cm ³	2.0 g/cm ³	2.0 g/cm ³	1.5 g/cm³

CNCs and CNFs have abundant –OH groups on their surfaces, which have been intensively explored to functionalize the nanofibers for different applications through esterification, silylation, polymer grafting, acetylation, etc.⁴⁵ These surface functionalization methods can improve their dispersability in different solvents/polymer matrixes and expand their utilization in nanotechnology-related applications, including nanocomposites, drug delivery, protein immobilization, and inorganic reaction template. **Figure 1.3** shows the surface modification methods that have been explored in literature.⁴⁶

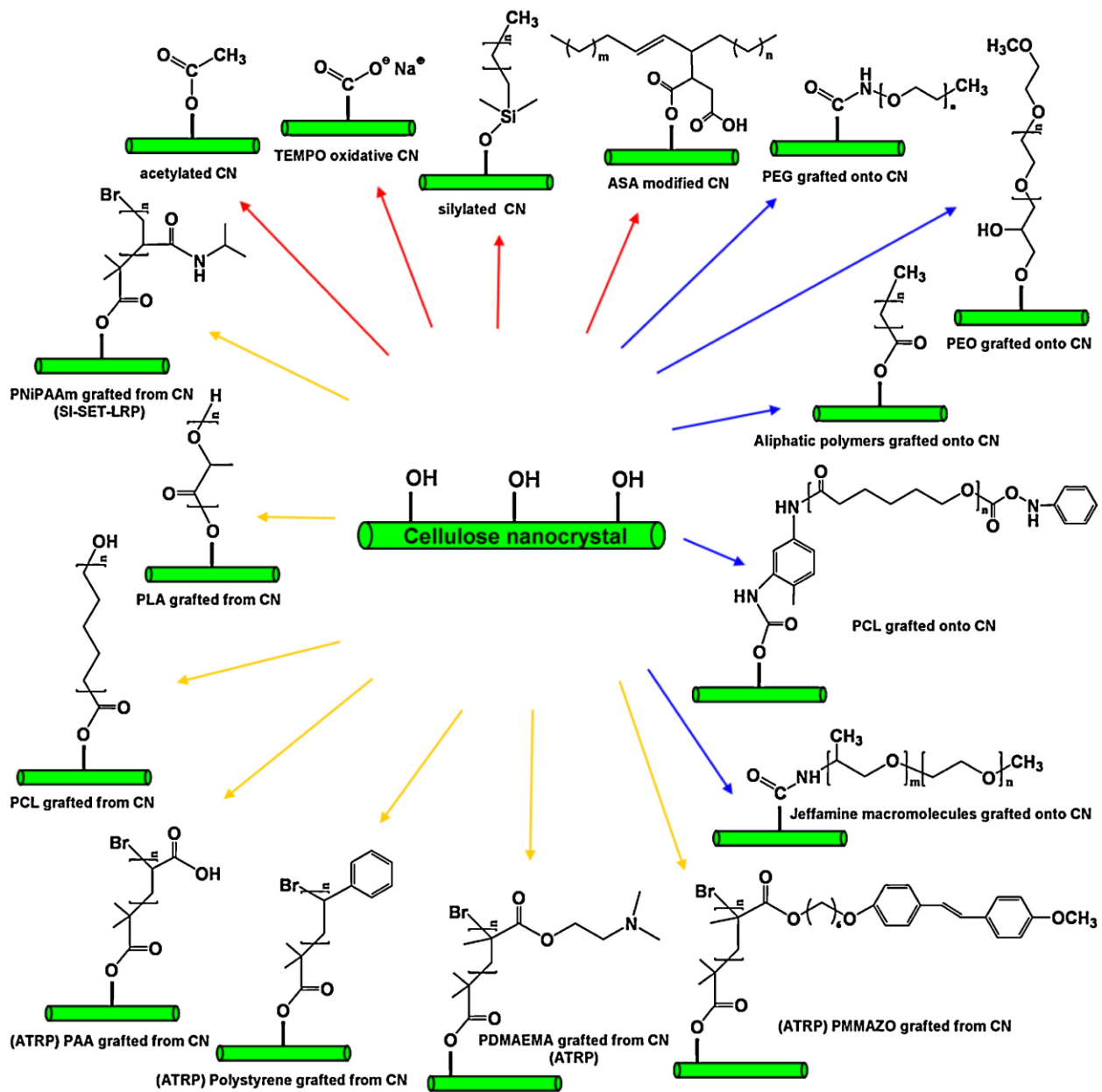


Figure 1.3. Different surface modification methods for CNCs and CNFs.⁴⁶

1.3. Applications of cellulose nanofibers

1.3.1. Cellulose nanofibers as nanoreinforcement in polymer composites

Based on the composite mechanics theories, for a given polymer matrix and fiber volume ratio, the mechanical properties of the polymer/fiber composite is determined by the aspect ratio and the intrinsic properties of the reinforcement fiber. However, due to the facts that

polymer/fiber interfacial bonding is not ideal and the existence of “interphase”, fiber diameter (or surface area) is also an important factor. Assuming equal fiber volume ratio in a composite, smaller fiber diameter leads to larger interfacial surface area and consequently, larger interfacial stress transfer and stronger reinforcing effect. For the cellulose nanofibers, their exceptional strength and modulus, large aspect ratio (especially for CNFs and BC), and nanoscale diameter make them ideal nanoreinforcement materials to be used in polymer nanocomposites.^{10,11,12,13,14} Moreover, their low density (1.5–1.6 g/cm³; 2.6 g/cm³ for glass fiber, as a comparison) imparts them much higher specific strength and modulus than glass fiber and metallic materials. Their biobased nature also gives them environmental advantage over carbon fibers, carbon nanotubes (CNTs), etc.

1.3.2. Applying cellulose nanofibers in a variety of polymers

In the literature, cellulose nanofibers have been used to reinforce petroleum- and biobased polymers including poly(vinyl alcohol) (PVA),^{47,48,10,49–53} poly(acrylamide) (PAM),⁵⁴ poly(ethylene glycol) (PEG),⁵⁵ poly(ethylene oxide) (PEO),⁵⁶ poly(lactic acid) (PLA),⁵⁷ poly(vinylidene fluoride) (PVDF)/poly(methyl methacrylate) (PMMA) blend,⁵⁸ polystyrene (PS),⁵⁹ sodium carboxymethyl cellulose (CMC),⁶⁰ alginate,⁶¹ xylan,⁶² and lignin.⁶³ (**Table 1.3**). These studies can be categorized into three groups: 1) cellulose nanofiber reinforced petroleum-based polymers;^{10,47–53,56} 2). fully biobased nanocomposites using natural polymers such as collagen, lignin, CMC, xylan and alginate;^{60–63} 3). nanocomposites for biomedical applications using FDA-approved PEG, PEO, PVA and PLA as matrixes.^{10,47–53,55–57} In most studies, the nanocomposites are produced by solution casting after mixing a polymer solution with a CNC or CNF suspension. CNCs are much more widely used in the literature probably due to its higher

availability (by simple acid hydrolysis) than CNFs, especially during the early time of cellulose nanofiber research.

Attempting large scale production, Lin et al⁵⁹ used an extruder to blend PEG-surface modified CNCs and PS to prepare PEG-CNCs/PS nanocomposites. The CNCs became dark and opaque after extrusion due to a thermal degradation at 200 °C. The authors highlighted that the PEG coating on the surface improved the dispersion of CNCs and also protected the CNCs from thermal degradation as well. More studies are needed to solve the difficulties of processing cellulose nanofibers using standard melt processing techniques such as extrusion and injection molding.

Developing fully biobased nanocomposites based on collagen, lignin, CMC, xylan and alginate⁶⁰⁻⁶³ is important because the composites can provide nature-mimic properties, lower the demand for petroleum-based polymers and decrease environmental footprints. For example, alginate, which is an anionic polysaccharide distributed widely in the cell walls of brown algae, readily binds with water and forms gel. It is capable of absorbing 200–300 g/g water per its own weight within a short period of time, and can be used to replace commercial superabsorbent polymers such as poly(acrylic acid) sodium salt, which is widely used in many personal hygiene products. However, alginate gel is fragile and shows poor shape recovery and the gelation process is relatively slow. Hence, Huq et al (2012)⁶¹ attempted to use the rigid CNCs to speed up the gelation because alginate and CNCs form physical crosslinks, and to improve the mechanical properties. The maximum tensile strength of the gel was achieved at only 5 wt.% CNC content, the Young's modulus was improved by up to 2-fold. This report demonstrates successful reinforcement of cellulose nanofibers on soft gels, which would help to expand the application areas of the nanofibers.

Polymers such as PEG, PEO and PVA are biocompatible and their hydrogels are widely used in medical products. Cellulose nanofibers have been incorporated into these gels to tune their mechanical and viscoelastic properties.^{10,47-53,55-57} The addition of the nanofibers generally results in dramatically improved strength, strain at break and Young's modulus. For instance, Zheng et al (2013),⁵¹ Yang et al (2013)⁵⁵ and Zhang et al (2015)⁵⁸ used CNFs or CNCs to reinforce PVA, PEG and PAM, respectively. The increases in strength, strain at break and Young's modulus range from 2.5 to 29-fold. Transparency, biocompatibility and bio-origin are the clear advantages of the cellulose nanofibers over other nanoreinforcements (e.g. nanoclay, CNTs, graphene, etc.) in these medical hydrogel (and other) applications.

Table 1.3. Mechanical reinforcement of cellulose nanofibers in polymer composites

Matrix polymer	Additive	Surface modification	Additive content (%)	Manufacturing method	Morphology	Evaluation methods	Mechanical Performance	Other significant functionalities	Ref	Year
Latex	CNFs	SWNT-OH was added	6 vol.%	Casting	Composite film	DMA	Rigid nanofibril network facilitated stress transfer from matrix to fibrils, high mechanical properties were maintained at high temperature	-	Dalmas et al. ⁶⁴	2007
collagen	CNCs	Sulfate (-OSO ₃ ⁻) groups introduced by sulfuric acid hydrolysis	-	Dip glass slide in collagen and CNC solution repeatedly	Layer-by-layer assembly film on glass	UV-vis	Adsorbing between collagen amide groups and hydroxyl groups on CNCs	-	Mesquita et al. ⁶⁵	2011
PEO	CNCs	Sulfate (-OSO ₃ ⁻) groups introduced by sulfuric acid hydrolysis	≤ 20 wt.%	Electrospinning	Composite nanofibrous mat	Tensile test	Tensile strength increased 2.8-fold; E increased to 2-fold; strain decreased to 1/2.	-	Zhou et al. ⁶⁶	2011
PLA	CNCs	Acetylated (CO ₂ -CH ₃)	≤ 10 wt.%	Casting	Composite film	Tensile test, DMA	Maximum tensile strength at 6 wt.%; E of 10 wt.% composite was 1.5-fold; strain decreased upon addition of CNCs	-	Lin et al. ⁶⁷	2011
Lignin	CNCs	Sulfate (-OSO ₃ ⁻) groups introduced by sulfuric acid hydrolysis	≤ 75 wt.%	Electrospinning	Composite nanofibrous mat	Rheometer	Increased viscosity by two-magnitude; shear-thinning behavior upon mechanical shearing	-	Ago et al. ⁶⁸	2012
Xylan	CNCs	Sulfate (-OSO ₃ ⁻) groups introduced by sulfuric acid hydrolysis	20 wt.%	Freeze-drying	Composite foam	Compression	Stress at 50% strain: ~ 300% increment; E: 400% increment	-	Kohnke et al. ⁶²	2012
Alginate	CNCs	Sulfate (-OSO ₃ ⁻) groups introduced by sulfuric acid hydrolysis	≤ 8 wt.%	Casting	Composite film	Tensile test	Maximum tensile strength at 5 wt.%; E of 5 wt.% was 2-fold; strain decreased upon addition of CNCs	-	Huq et al. ⁶¹	2012
CMC	CNCs	Aldehyded (H-C=O)	≤ 50 wt.%	Injected into mold by syringe	Composite hydrogel	Rheometer	Young's modulus increased up to 140 % at 16 wt.% modified CNCs	CNC improved structural integrity upon swelling	Yang et al. ⁶⁰	2013
PVA	CNFs	TEMPO oxidized (COONa); SWNT-OH was added	17 wt.%	Freeze-drying	Composite aerogel	Compression	Yield stress increased to 12-fold; Young's modulus increased up to 29-fold	Surface area increased 2.2-fold	Zheng et al. ⁵¹	2013
PS	CNCs	PEG-grafted	≤ 20 wt.%	Extrusion at 200 °C	Composite film	DMA	Storage modulus increased up to 9-fold	Water vapor permeability	Lin et al. ⁵⁹	2013
PLA	CNCs	PLA was maleic anhydride (C ₂ H ₂ (CO) ₂ O) grafted to be compatible with CNCs	≤ 5 wt.%	Electrospinning	Composite nanofibrous mat	Tensile test	Stress at break increased to ~7-fold; Young's modulus increased up to ~17-fold; strain down to 85% at 5 wt.% CNCs.	Biocompatibility	Zhou et al. ⁵⁷	2013
PEG	CNCs	Sulfate (-OSO ₃ ⁻) groups introduced by sulfuric acid hydrolysis	≤ 1.4 vol.%	UV-crosslinking	Composite hydrogel	Tensile test	Stress at break increased by ~5-fold; modulus by ~3-fold; strain by ~3-fold	Extensibility	Yang et al. ⁵⁵	2013

Table 1.3. Mechanical reinforcement of cellulose nanofibers in polymer composites (continued).

Matrix polymer	Additive	Surface modification	Additive content (%)	Manufacturing method	Morphology	Evaluation methods	Mechanical Performance	Other significant functionalities	Ref	Year
PAM	CNCs	TEMPO oxidized (-COONa)	≤ 0.6 vol.%	Polymerization of monomer AM into PAM	Composite hydrogel	Tensile, compression	Tensile stress increased by 10-fold; modulus increased by 6-fold at 0.6 % CNCs; strain increased ~2.5-fold	-	Yang et al. ⁵⁴	2014
PVA	CNCs	Methacrylate polymer grafted	-	Mixing	Composite hydrogel	Rheometer	Gel-sol transition upon applications of strains	Rapid self-healing	McKee et al. ⁴⁸	2014
PVDF/PMMA	CNCs	Sulfate (-OSO ₃ ⁻) groups introduced by sulfuric acid hydrolysis	≤ 6 wt.%	Casting	Composite film	Tensile test	Slight change in stress at break; Young's modulus increased up to 200 % at 6 wt.% CNCs; strain decreased down to ~28%	-	Zhang et al. ⁵⁸	2015

1.3.3. Nanofiber/polymer interactions

Mechanical properties of a composite depend to a great extent on fiber/polymer interfacial bonding. Polymers such as PVA, PAM, PEG and PEO have hydrogen-bond-forming groups that can interact with the hydroxyl (-OH), sulfate (-OSO₃⁻) and carboxyl (-COO⁻) groups on the pristine or treated cellulose nanofibers. For example, the hydroxyl groups on the side chains of PVA interact strongly with the polar sulfate or ionic (-COONa) groups introduced by sulfuric acid hydrolysis or TEMPO-oxidation during the synthesis of CNCs.⁵⁸ The favorable surface chemistry facilitates a homogenous dispersion of CNCs throughout the matrix (**Figure 1.4A**). Yang et al (2014)⁵⁴ reinforced the PAM by using TEMPO-oxidized CNCs at a very low content (≤ 0.6 vol.%) to obtain strengthened nanocomposite hydrogels (**Figure 1.4A**). The strong hydrogen bonding between the functional group (-C=O) and the abundant hydroxyl (-OH) groups facilitates the formation of a high-density physical crosslink, which results in increased mechanical properties. Moreover, individual CNCs connect with each other through hydrogen bonding to form a fiber network. These strong multiple-level crosslinks enable the nanocomposite hydrogel to maintain its structural integrity upon swelling.

Cellulose nanofibers can be surface modified to chemically crosslink with the matrix polymer. Yang et al⁶⁰ used CNCs and aldehyde-modified CNCs to reinforce CMC hydrogels.. Both CNCs can be dispersed well in CMC and lead to reinforced hydrogel. However, the aldehyde-modified CNCs, acting as both a filler and a chemical cross-linker, results in the reinforced hydrogels with higher elasticity, dimensionally stability, and higher allowable nanoparticle loadings compared to hydrogels with unmodified CNCs. (**Figure 1.4E-F**).

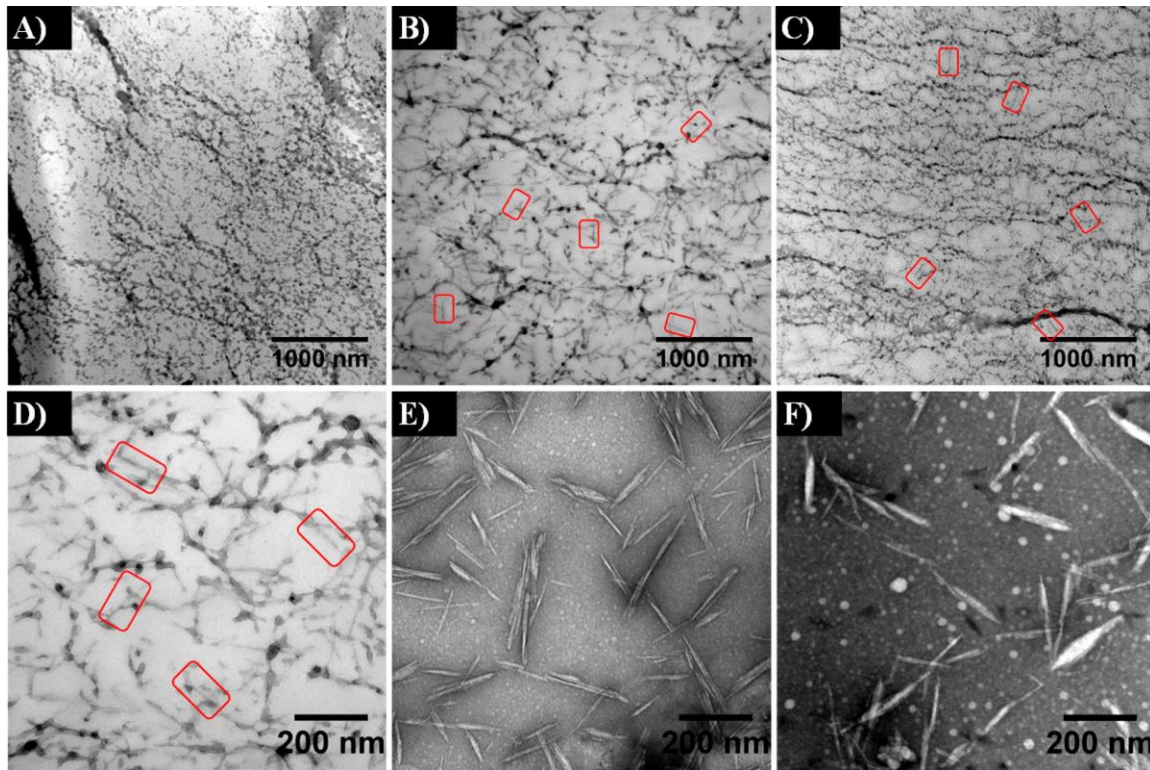


Figure 1.4. TEM images of stained 100 nm thick CMC hydrogels: (A) pure polymeric CMC hydrogel with no CNCs, (B, D) CNC-reinforced hydrogel with 0.25 % loading, (C) aldehyde-CNC (-C=O)-reinforced hydrogel with 0.375 % loading; a few individual CNCs or CHO-CNCs are highlighted with red boxes. (E) TEM images of CNCs, (F) TEM images of aldehyde-CNCs.⁶⁰

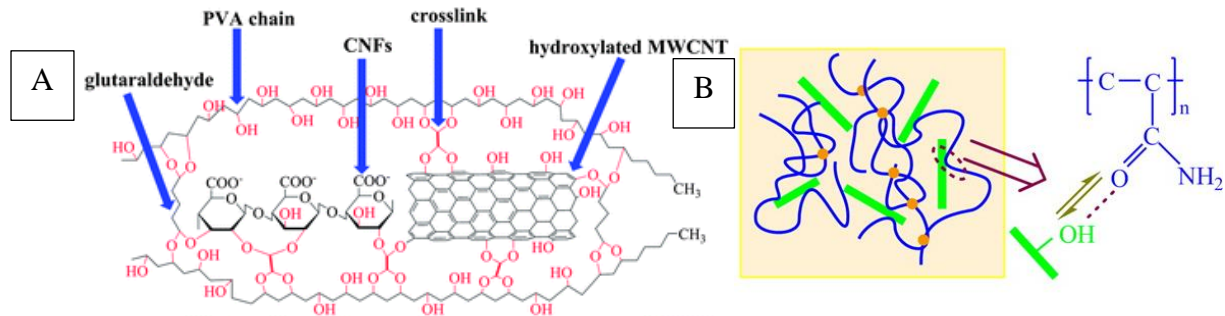


Figure 1.5. (A) Schematic illustration and network microscopic structure of CNC-PAM hydrogels;⁵⁴ (B) A schematic illustration of the crosslinking mechanism of PVA, MWCNT and CNFs.⁵¹

To reinforce hydrophobic polymers such as PLA, PS and PVDF, surface modification by grafting “short polymer chains” onto the cellulose nanofibers has to be performed to increase the fiber-polymer compatibility. For example, to reinforce PLA using CNCs, Lin et al (2011)⁶⁷ first

acetylated the CNCs to change the hydroxyl groups into ester (COO-CH₃) groups. The CNCs can be easily suspended in apolar solvents such as dichloromethane (CH₂Cl₂), which is also a good solvent for PLA. PLA/CNCs nanocomposites were prepared by mixing the two components in the solvent followed by solution casting. CNCs are uniformly dispersed in the matrix and the composites show superior mechanical performance and thermal stability.

1.3.4. Mechanical performance of cellulose nanofiber reinforced nanocomposites

The mechanical properties of the nanocomposites are the most important and most studied properties. Numerous studies have been devoted to them on the composites prepared by solution casting (most often used), electrospinning, freeze-drying, extrusion, and other methods.^{10,47-63} A percolated cellulose nanofiber network is often reported to form in the composites above threshold nanofiber content, and substantial increase in mechanical properties is commonly observed after the formation of the network.

The mechanical properties are often evaluated using dynamic mechanical analysis, tensile/compression tests or rheometric characterization. For instance, the tensile strength of xylan foam is increased by up to 300 % after the addition of CNCs while the Young's modulus is increased by up to 400 %. Lee et al (2012) compared the reinforcement effect of CNFs and BC in epoxy composites. The composites were produced by impregnating CNF and BC paper with epoxy resin using vacuum assisted resin infusion technique. The reinforced epoxy nanocomposites show a modulus and a strength of ~8 GPa and ~100 MPa (at 60 vol.% fiber content), respectively, which are much larger than those of unreinforced epoxy (3 GPa and 71 MPa, respectively). No significant difference in the modulus is observed between the CNF and BC reinforced nanocomposites. However, the BC reinforced composite shows higher tensile

strength and higher strain at break than the CNF reinforced one. This can be due to the higher strength and strain of the BC nanopaper.

Generally, the tensile strength of the cellulose nanofiber reinforced composites increases with the nanofiber content initially, and then peaks at an optimal content; Young's modulus often increases linearly with the content. However, often times, the strain at break is decreased because of the formation of interfacial layer between the filler and matrix that facilitates early crack propagation.^{58,61,66,67} In some hydrogels the strain at break is increased due to the existence of solvent that prevents cracking.^{54,55,62} For example, as shown in **Figure 1.6**, the mechanical properties of CNC/PAM gels with different CNC contents are reported by Yang et al (2014).⁵⁴ The pure PAM gel has a strain at break, stress at break and Young's modulus of 30 kPa, 260 % and 5.5 kPa, respectively. All of these parameters are improved upon addition of CNCs. The Young's modulus of CNC/PAM nanocomposite hydrogel with 0.6% v/v of CNC is increased by 6.1-fold from 5.5 to 33.8 kPa. The strain at break also increases with increasing CNC content.

In summary, abundant research has been devoted to the study of mechanical properties of cellulose nanofiber reinforced polymer nanocomposites, as demonstrated by a large number of research papers, reviews and patents.^{69,70} In most cases the reinforcement is attributed to the formation of a three-dimensional nanofiber network within the polymeric matrix. The properties of the nanofiber composites can be controlled through the formation and fine-tuning of the network. Various mechanical modeling methods have been used to predict the properties of the composites, as will be discussed below.

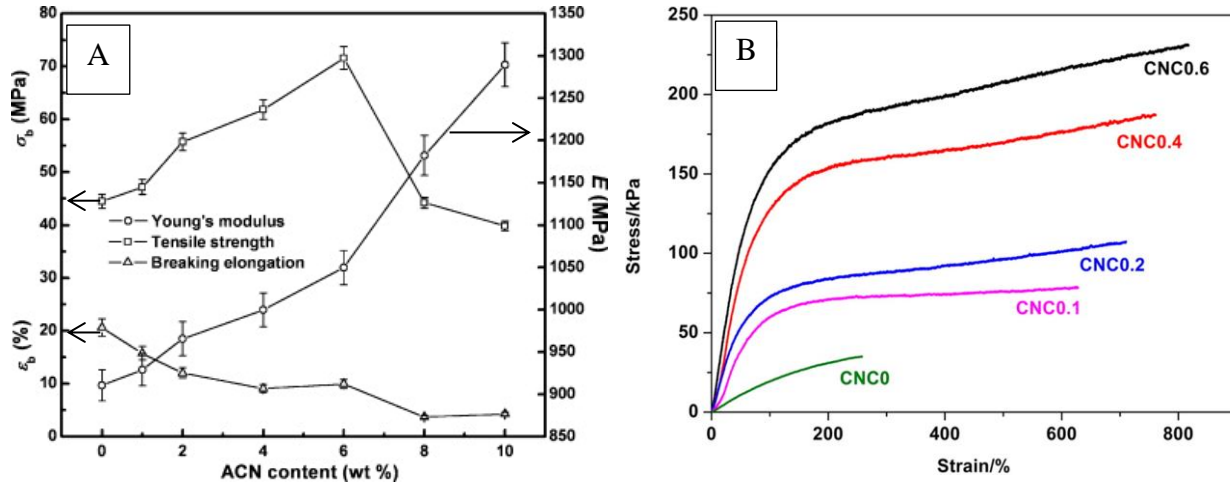


Figure 1.6. (A) Effect of the ACN content on strain at break (σ_b), stress at break (ϵ_b), and Young's modulus E for PLA/acetylated CNC nanocomposites as well as the neat PLA-F sheet;⁶⁷ (B) Mechanical properties of CNC/PAM gels with different CNC contents.⁵⁴

1.3.5. Modeling of mechanical properties

The often used models include the Halpin–Kardos model based on mean field approach,⁷¹ and the Ouali model based on the percolation theory and extension of the phenomenological series-parallel model proposed by Takayanagi.^{72,73,74} The percolation theory indicates that above the percolation threshold, the cellulosic nanoparticles can connect and form a three-dimensional continuous pathway through the nanocomposites. The formation of this cellulose network was supposed to result from strong interactions between nanoparticles, like hydrogen bonds. This mechanical percolation effect explained both the high reinforcing effect and the thermal stabilization of the composite modulus up to 500 K for cellulose nanocrystal reinforced latex films, as reported by Dalmas et al (2007).⁶⁴

The formation of this rigid network was assumed to be governed by a percolation mechanism and the most important parameters are the aspect ratio of the rod-like nanoparticles, which is the ruler of the percolation threshold, and the modulus of the percolating nanoparticle network, which is obviously different from the one of individual nanocrystals. This modulus can

be assumed similar, in principle, to the one of a paper sheet for which the hydrogen bonding forces provide the basis of its stiffness. However, because of the nanoscale effect stronger interactions are expected. This modulus can be experimentally determined from tensile tests performed on films prepared by water evaporation of a suspension of nanocrystals. Values ranging from about 1 to 15 GPa have been reported. Therefore, any parameter that affects the formation of the percolating nanocrystal network or interferes with it is a critical issue that changes dramatically the mechanical performances of the composite.⁵ Three main parameters were identified to affect the mechanical properties of such materials, viz. the morphology and dimensions of the nanoparticles, the processing method, and the microstructure of the matrix and matrix/filler interactions.

Various models exist for the mechanical properties of heterogeneous materials. The Halpin–Tsai semi-empirical equation⁷¹ describes the modulus of an aligned short-fiber composite:⁷¹

$$E_{\parallel} = E_m \frac{1 + \eta_{\parallel} \zeta \varphi_f}{1 - \eta_{\parallel} \varphi_f} \quad (1.1.)$$

$$E_{\perp} = E_m \frac{1 + 2\eta_{\perp} \varphi_f}{1 - \eta_{\perp} \varphi_f} \quad (1.2.)$$

where,

$$\eta_{\parallel} = \frac{\frac{E_f}{E_m} - 1}{\frac{E_f}{E_m} + \zeta} \quad (1.3.)$$

$$\eta_{\perp} = \frac{\frac{E_f}{E_m} - 1}{\frac{E_f}{E_m} + 2} \quad (1.4.)$$

where E_{\parallel} and E_{\perp} are the longitudinal and transverse Young's modulus of the unidirectional composite, φ_f is the fiber volume fraction, E_m is the Young's modulus of the matrix, and E_f is the modulus of the fiber. ζ is a shape factor dependent on fiber geometry and orientation. Different equations have been proposed to calculate ζ . Equation $\zeta = 2L/w$ is used for relatively short fibers such as CNCs.^{64,75} Equation $\zeta = (0.5L/w)^{1.8}$ is proposed by Van Es for high aspect ratio fibers.⁷⁶ L and w is the fiber length and fiber diameter, respectively. The modulus of a 3D randomly oriented composite (E_C) can be calculated based on the laminate theory:⁷⁶

$$E_C = 0.184E_{\parallel} + 0.816E_{\perp} \quad (1.5.)$$

The Ouali model is based on the percolation theory and is an extension of the phenomenological series-parallel model proposed by Takayanagi.^{72,73,74} The Ouali model simulates polymer composites using three phases: matrix, percolating filler network, and non-percolating filler phase. The model is given by the following equation:

$$E_C = \frac{(1 - 2\psi + \psi\varphi_f)E_mE_f + (1 - \varphi_f)\psi E_f^2}{(1 - \varphi_f)E_f + (\varphi_f - \psi)E_m} \quad (1.6.)$$

where the subscripts f and m refer to the filler and matrix phases, φ_f is the volume fraction of the filler, and E is the modulus. ψ denotes the volume fraction of the percolating filler network and is obtained from:

$$\psi = 0 \quad (1.7.)$$

$$\varphi_f \leq \varphi_c \quad (1.8.)$$

$$\psi = \varphi_f \left(\frac{\varphi_f - \varphi_c}{1 - \varphi_c} \right)^b \quad (1.9.)$$

$$\varphi_f > \varphi_c \quad (1.10.)$$

where b is the critical percolation exponent and a value of 0.4 is used for a three-dimensional network.^{72,73} φ_c is the critical percolation threshold (volume fraction):⁷⁷

$$\varphi_c = 0.7/(L/w) \quad (1.11.)$$

where L and w are the length and diameter of the filler, respectively.

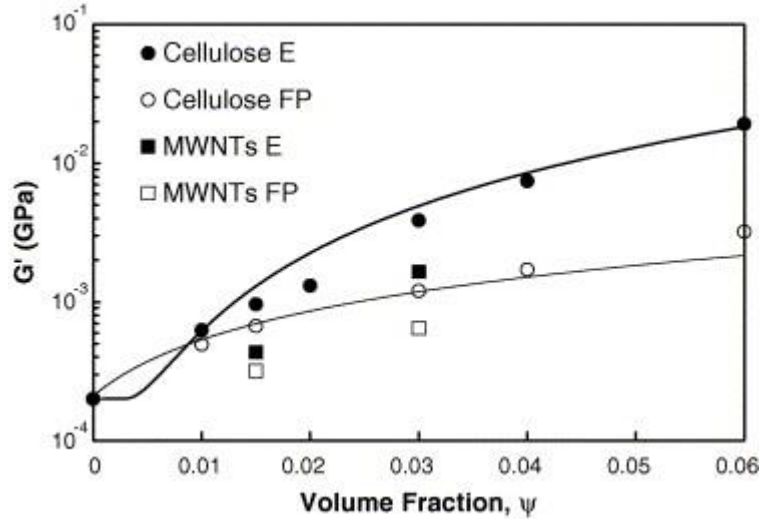


Figure 1.7. Evolution of the nanocomposite shear storage modulus at $T/T_g = 1.15$ with the filler content. Comparison with the one predicted by the mechanical percolation approach (heavy line) and the one predicted by the mean field approach (light line).⁶⁴

By using above-mentioned modelling theories, in Dalmas et al (2007)'s study,⁶⁴ two different types of high aspect ratio flexible nanofibers, CNFs and CNTs, were dispersed in an amorphous thermoplastic polymer matrix. In the case of CNF-reinforced nanocomposites a large mechanical reinforcement effect was observed. This effect was explained by the formation of a rigid nanofibril network linked by strong hydrogen bonds. The formation of this network was assumed to be governed by a percolation mechanism. By using this theory, the experimental result for shear modulus fits well with the model prediction (**Figure 1.7**).

1.3.6. Colloidal materials

Due to their nanoscale sizes and surface charges, CNCs and CNFs form stable colloidal dispersions when dispersed in water and some polar solvents. These colloidal dispersions have

been widely studied for their rheological behavior,⁷⁸ colloidal stability^{79,80} and self-assembly.^{81–83} For example, CNCs can self-assemble into a liquid crystal phase in colloids (**Figure 1.8A**).⁸⁴ The liquid crystalline forms chiral nematic domains that is sensitive to salts due to electrostatic interaction (2009).⁸⁰ Fall et al shows that the origin of colloidal stability for a CNF dispersion is the electrostatic repulsion arising from deprotonated carboxyl groups at the fiber surface; decreasing pH or increasing salt concentration results in a decrease in surface charge, thus causing CNF aggregation.⁷⁹ Kalashnikova et al indicates that CNCs exhibit amphiphilic characteristic which can be used to stabilize oil/water interfaces in an oil–water emulsion.^{32,85} Their results show that electrostatic interaction plays a major role in controlling the interfaces and the surface charge density of CNCs is a key factor determining if a stable oil-water emulsion can be achieved. A surface charge density higher than 0.03 e/nm^2 is not able to efficiently stabilize the interfaces. CNC colloidal dispersions are also able to disperse single walled carbon nanotubes (SWNTs).⁸⁶ In this case, SWNTs and CNCs form a self-assembled hybrid structure, where several CNCs align along the SWNT axis. This structure is formed due to short-range hydrophobic interactions between the SWNTs and specific crystalline faces of the CNCs. The stability of the CNC/SWNT dispersion is also attributed to long-range electrostatic repulsion between the CNCs. In another study, Varjonen et al demonstrates using amphiphilic protein to modulate the self-assembly of CNFs, which forms a stable interfacial layer in an oil/water emulsion.⁸² CNCs formed patterned solid film after evaporation of solvents, as shown in **Figure 1.8D**. Control of the iridescent color in solid films of CNCs was achieved through heating CNC colloid suspension (**Figure 1.8E**).⁸⁷

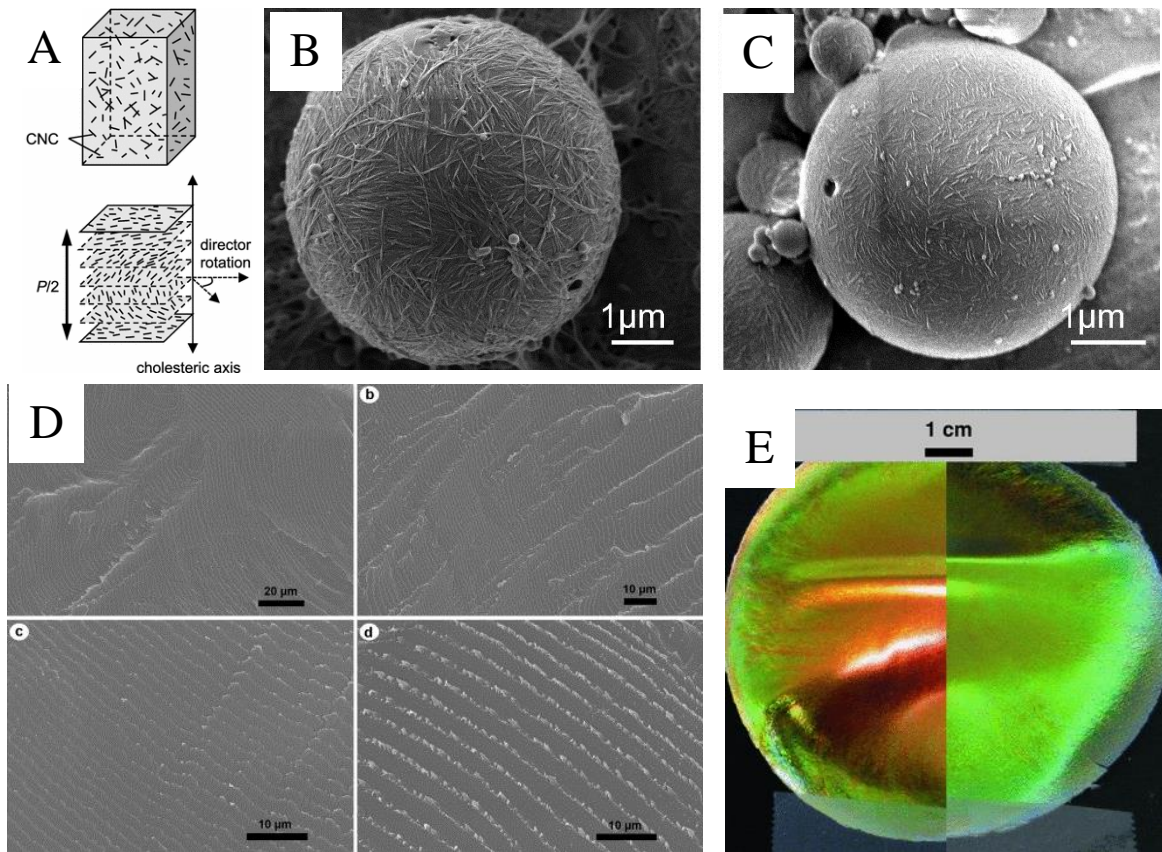


Figure 1.8. (A) Schematic illustration of the organization of the isotropic and chiral nematic phases of a biphasic CNC suspension at equilibrium; (B-C) SEM images of polymerized styrene-water emulsions stabilized by (A) bacterial cellulose nanofibers and (B) cotton cellulose nanocrystals (CNCs);³²⁻⁸⁵ (D) SEM micrographs of CNCs film;⁸⁴ (E) Solid CNC film in diffuse light, showing its iridescence when viewed normal to the surface (left) and at an oblique angle.⁸⁷

1.3.7. Hydrogel materials

Hydrogel Gel is a solid, jelly-like material that can have properties ranging from soft and weak to hard and tough. Gels are defined as a substantially dilute cross-linked system, which exhibits no flow when in the steady-state. Filtrating-induced free standing wet gel-like TEMPO-oxidized CNFs “cake” was presented by Sehaqui et al (2012).⁸ (Figure 1.9A) Gel materials made of CNFs were also obtained at pH = 2 (Figure 1.9B). CNFs switch from dispersion state stabilized by ionization of the surface carboxyl groups to hierarchically assembled physical

hydrogels due to protonation. reported.⁸¹ These gels with high water content (99.9 %) are suitable to be converted into ultralow-density, tough aerogels with large surface areas, transparent films, robust frameworks of polymer nanocomposites or high-capacity supports and the other functional materials. Except by adjusting the pH value, TEMPO-CNFs based hydrogels can also be obtained by metal ion loading due to a strong binding force (**Figure1.9C-D**).⁸⁸ In this case, the TEMPO catalyst induces negatively charges surface (COOR) that provide high binding capability to transition metal species such as silver ion: Ag(+) (2013).⁸⁸ Simultaneously formation of CNF-Ag(+) hydrogels reduced to Ag nanoparticles. The functionalized stiff hydrogel has a storage modulus of 6.8 KPa will be important for as building blocks for porous aerogels and flat thin films.

Except the CNFs, CNCs were also adapted in polymer-based hydrogels such as superabsorbent polyacrylamide (PAM) as a reinforcing material.⁸⁹ Natural bacterial cellulose (BC) that occurs in a form of water-rich hydrogel thick films/cubes/pellets is used as gel material as well. Nakayama et al used BC hydrogels as framework to infuse gelatin within its fibrous network.⁹⁰ Gelatin is intrinsically fragile and weak, however, with the tough supporting originated from flexible fibril-fibril network in BC, the composite hydrogel presents a high mechanical strength. CNCs was used as a stuffing filler for polymer hydrogel as reported by Zhou et al (2011). They used in situ free-radical polymerization to polymerize polyacrylamide (PAM) with assistance of CNCs into hydrogels.⁸⁹ They ascribed the accelerated formation and increased crosslink density of hydrogels to the CNCs. They believed that CNCs were not only a reinforcing agent for hydrogel, but also acted as a multifunctional cross-linker for gelation. Results show that a CNC loading of 6.7 wt% led to the maximum mechanical properties for hydrogels.

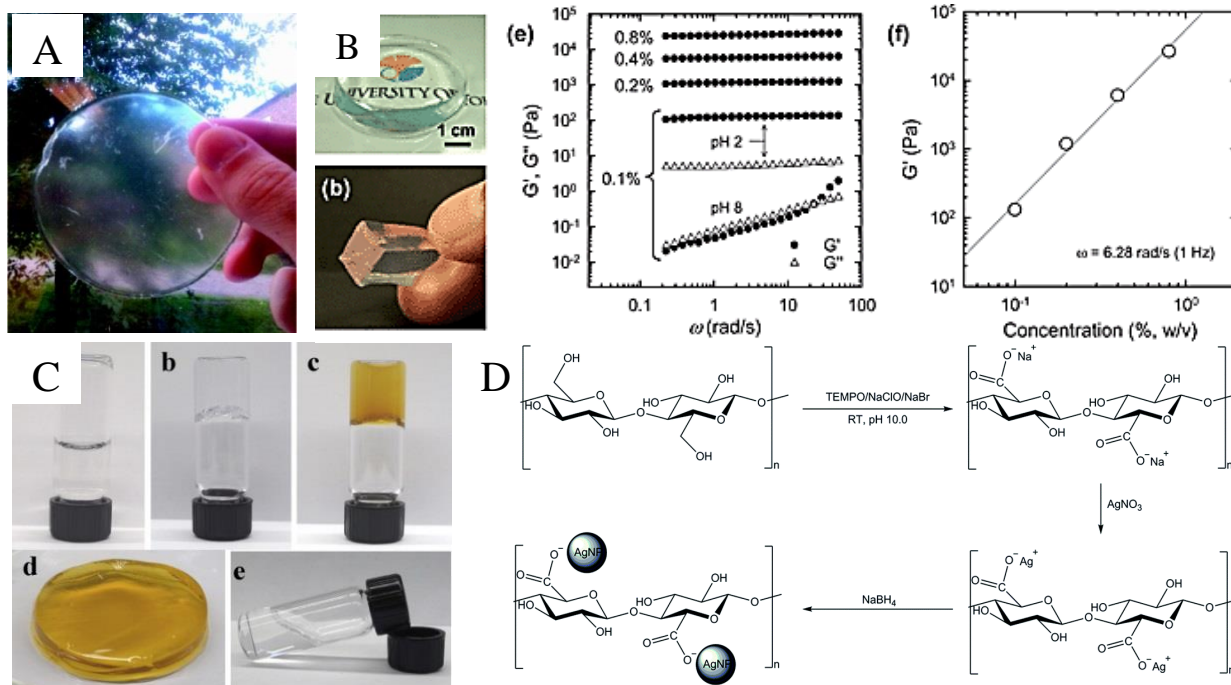


Figure 1.9. (A) TEMPO-CNF wet gel obtained after vacuum filtration of TEMPO-CNF aqueous dispersion (water content in the cake is 70–90%);⁸ (B) Freestanding acidic-pH induced hydrogels of cellulose nanofibrils;⁸¹ (C) CNFs in aqueous dispersion (1.27 wt%) and CNF/Ag⁺ hydrogel;⁸⁸ (D) Illustration depicting the attachment of Ag⁺ ions to CNFs, and the subsequent reduction of Ag⁺ to Ag nanoparticles by using NaBH₄.¹³

1.3.8. Light-weight porous materials

Light-weight porous CNF foams/sponges/aerogels/superabsorbent were attempted for utilization of its low density, high surface area, flexibility and biodegradability characteristics. Initially, pure BC hydrogels were easily converted into light-weight aerogels via supercritical carbon dioxide (CO₂) drying technique.⁹¹ Supercritical CO₂ is substituting liquid solvent within hydrogel network by CO₂ at liquid/vapor/gas critical point and elimination of CO₂ forming porous solid network. This drying technique effectively lowers the surface tension at the solid network and prevents network collapse. This technique in addition of freeze-drying technique⁹² is often used to prepare porous materials. For CNFs in nanocomposite foams, Svagan et al (2008) prepared biomimetic foams with up to 40 wt % CNF in starch, which resembled the

biological cell's dimension ranged 20–70 μm (**Figure 1.10A**).⁹³ The manufacturing was through freeze-drying the nanocomposites, which results a significant improvement in modulus and yield strength. Liu et al used CNFs to support poly(vinyl alcohol) foams prepared through freeze-drying technique.⁹⁴ Another example of CNF aerogel was shown in **Figure 1.10B**. This type of CNF went through defibrillated from rice straw cellulose and surface modification and drying, formed aerogel that is light ($< 8.1 \text{ mg/cm}^3$) and ultra-porous (99.5 %).⁹⁵ Except the film-like or cubic shapes of various porous materials, fabricating CNF aerogel spheres were tried by Cai et al (2014).⁹⁶ The CNF aqueous gel droplets were produced by spraying through a steel nozzle, were collected into liquid nitrogen for instant freezing followed by freeze-drying. Above mentioned fabrication of free-standing CNF foams/aerogel blocks and spheres featured ultralight and high porous structure ensured high liquid uptake capacity and will find applications for selective oil removal and recovery.

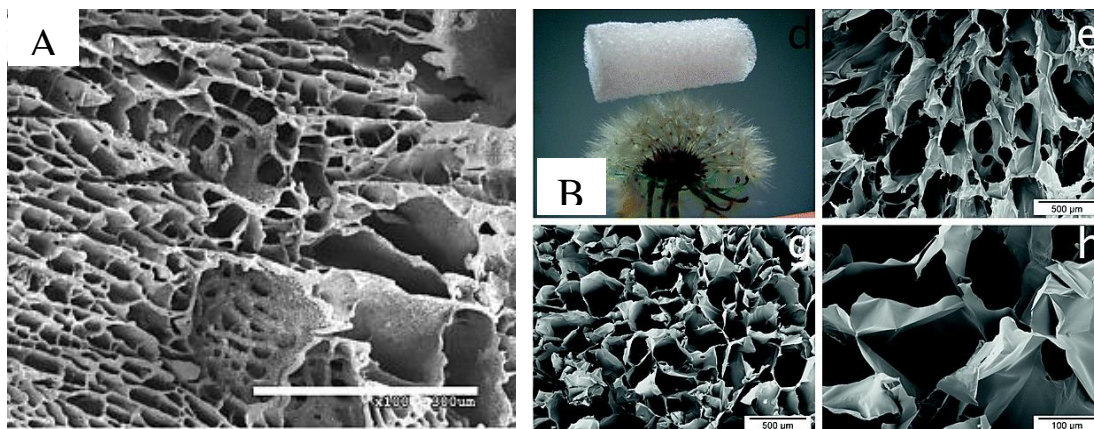


Figure 1.10. (A) CNFs/starch foam with (B) 10 wt% CNFs, scale bars is 300 μm ,⁹³ (B) photos and SEM images of CNF aerogels.⁹⁵

1.3.9. Absorbing foam materials

For water absorbing, pristine CNF foam was manufactured through freeze-drying of CNF suspension, as reported by Aulin et al (2010), and Chen et al (2011), respectively.^{97,98} In Chen's

study, the native CNF foam without any surface chemical modification presents a water absorbency of 155 g/g (**Figure 1.11A**). Furthermore, surface-modified CNF aerogel was used as absorbents that absorbed higher values of 210 and 375 g/g water and chloroform, respectively.⁹⁵ Chloroform represents a standard oil-type chemical. Later, dye-absorbing capability interests the researchers as well. Through surface quaternized CNFs were found with high water absorbency and adsorption capacity for anionic dyes (Pei et al, 2013) (**Figure 1.11B**).⁹⁹ Surface quaternization of CNFs were pretreated through a reaction with trimethylammonium chloride (ammonium salt) was reported with a high water absorbency (750 g/g) and high surface cationic charge density. A comparison of water absorbency of 155 g/g, 210 g/g and 750 g/g in the references suggests that different modifying agents result in different degree of absorbencies due to the nature of the modifier. Nevertheless, the CNFs perform excellently as an absorbing foaming material.

Except the modifiers such as organic chemicals, inorganic modifiers such as titanium dioxide (TiO₂) with multiple functions were reported as well. TiO₂ coating was found able to turn the hydrophilic CNF foams/aerogels into hydrophobic and oleophilic (Korhonen et al 2011).¹⁰⁰ For example, it absorbs paraffin oil, instead of water and glycerol. This characteristic makes an excellent oil-removal material in environmental applications. Chemical vapor deposition of the TiO₂ on CNF aerogel was found having photoswitchable absorbency (Kettunen et al 2011).¹⁰¹ As mentioned by Korhonen et al, the TiO₂ coating disables the CNFs uptaking water anymore, however, an interesting phenomenon was discovered by Kettunen et al: it uptake water upon UV illumination with a 16 g/g absorbency, which can be dried and recovered in the dark. They ascribed this to the hydrophilic oxygen vacancies of TiO₂ generated by photons. To summarize, comparing to CNCs and BC, CNFs were found having a high preference to be used

as a multi-functional tunable absorbing foam material for water, oil and dyes. This property makes the CNFs as a successful light-weight, sustainable, reusable and recyclable candidate for various applications.

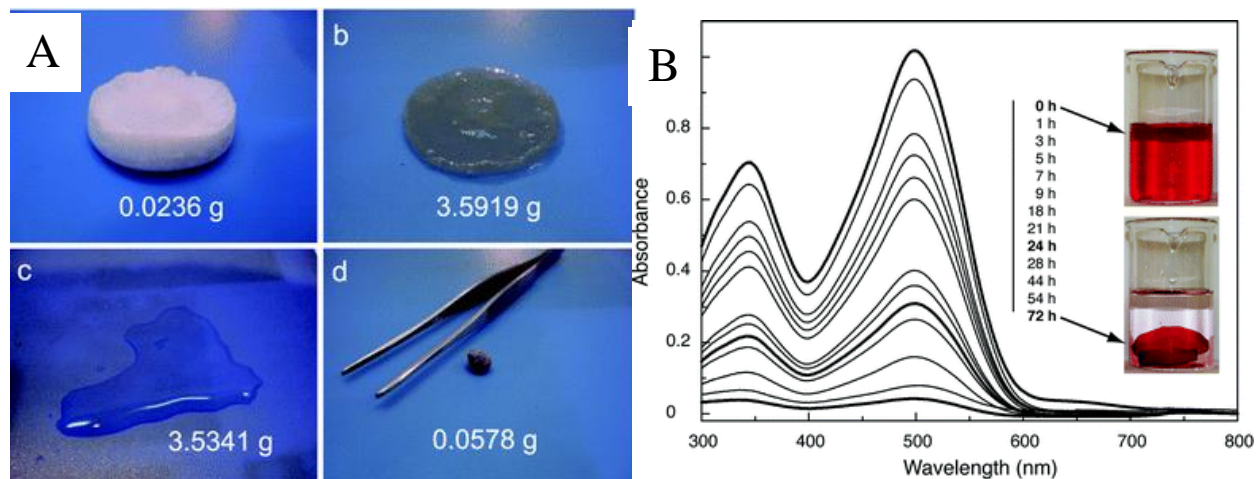


Figure 1.11. (A) Aerogel with a water absorbency of 155 g/g, water can then be released from the sample by compression;⁹⁷ (B) Time-dependent absorption spectra of the dye solution containing CNFs.⁹⁹

1.3.10. Templating scaffold materials

CNFs, CNCs, and bacterial cellulose, were especially favored to be used as a scaffold/templating material with nanoparticle decoration. Organic (such as ionic liquid salt: imidazolium)¹⁰² and inorganic particles (Fe,¹⁰³ SiO₂,¹⁰⁴ Ag,¹⁰⁵ Au,¹⁰⁶ (**Figure1.12B**) Pd,¹⁰⁷ Se,¹⁰⁸ CaCO₃¹⁰⁹ CoFe₂O₄,¹¹⁰ (**Figure1.12C-D**) carbon dots¹¹¹ and etc) were successfully grafted onto CNFs or BC (**Figure1.12A**). In these studies, CNCs' inherent colorless and high transparency, liquid crystalline formed nematic phase, functional groups (-OH, or -COO⁻) acting as reducing agent, mobility were intensively emphasized. In details, for example, Dujardin et al synthesized SiO₂ aerogel by sol-gel mineralization within CNC nematic suspension. Formed SiO₂ particular aggregates network featured a hierarchical mesoporous structure with certain alignment.¹⁰⁴ The SiO₂/CNCs composites were calcinated, remaining SiO₂ framework for specific applications. Besides the CNCs, scientists also attempted to generate inorganic hollow nanotube aerogels by

atomic layer deposition onto native nanocellulose templates.¹¹² Titanium dioxide (TiO₂), zinc oxide (ZnO₂), aluminum oxide (Al₂O₃) nanotube aerogels were fabricated through freeze-drying and calcination as well. These metal oxide materials with high porosity have lots of important applications such as humidity sensor and etc. From these protocols, we conclude there is high facility to use either CNCs or CNFs are playing important roles as sacrificing material for interesting nanoscale microstructures.

Finally, other important templating examples for nanoparticles are detailed here. To synthesize nanoparticles on CNCs, metal-compounds such as silver nitrate (AgNO₃), sodium selenite (Na₂SeO₃),¹⁰⁸ palladium chloride (PdCl) and etc were reduced with/without reducing agents in CNFs or CNCs colloidal suspensions. With reducing agent such as dopamine (C₈H₁₁NO₂), the Ag nanoparticles were synthesized onto BC framework.¹¹³ Without addition of reducing agent, the carboxyl groups (-COONa⁺) with Na⁺ as cation, function as a source to exchange with Ag⁺ for the Ag nanoparticle.¹¹⁴ Separation by centrifugation and air-drying processes are able to obtain the particle-decorating CNFs, CNCs or BC. Without addition of reducing agent to produce Ag nanoparticles, was also successfully attempted via hydrothermal synthesis of BC with Ag decoration.¹¹⁵ Yang et al (2012) blended AgNO₃ with BC hydrogels, then hydrothermalized it in a sealed container at 80 °C for 4 h, by which, the Ag⁺ was reduced to Ag nanoparticles easily as well.

Biosensing¹⁰⁶ and electromagnetic¹¹⁰ functions were applied to bacterial cellulose aerogels. For the biosensing, gold (Au) nanoparticles was synthesized by using hydrochloroauric acid (HAuCl₄ · 3H₂O) as the precursor, which was reduced to Au by poly(ethyleneimine) (C₂H₅N)_n.¹⁰⁶ Bacteria cellulose nanofibers function as robust biotemplates for the facile fabrication (**Figure1.12A-B**) Obtained Au-BC was used to detect H₂O₂ with a high

sensitivity. The flexibility of BC was further emphasized by loading magnetic (CoFe_2O_4) nanoparticles using BC cellulose nanofibrils as templates.¹¹⁰ In this study, they used BC as templates for making lightweight magnetic aerogels, which can be further compacted into a stiff magnetic nanopaper. The 20–70 nm thick cellulose nanofibrils act as templates for the non-agglomerated growth of ferromagnetic cobalt ferrite nanoparticles (diameter, 40–120 nm) (**Figure 1.12C-D**). Unlike solvent-swollen gels and ferrogels, their magnetic aerogel presents to be dry, lightweight, porous, flexible, and can be actuated by a small household magnet. It can absorb water and release it upon compression for microfluidics devices and as electronic actuators. Ferroelectromagnet (CoFe_2O_4) in wet-spun micron-sized CNF fibers was also reported by Walther et al.¹¹⁶ To sum, CNFs, CNCs and BC play an important role as a scaffold/templating material for synthesizing various nanoparticles, surface charges are very important to the synthesis process as it reduces metal-compounds into nanoparticles, these characteristics are unique and existing in the CNFs, CNCs and BC.

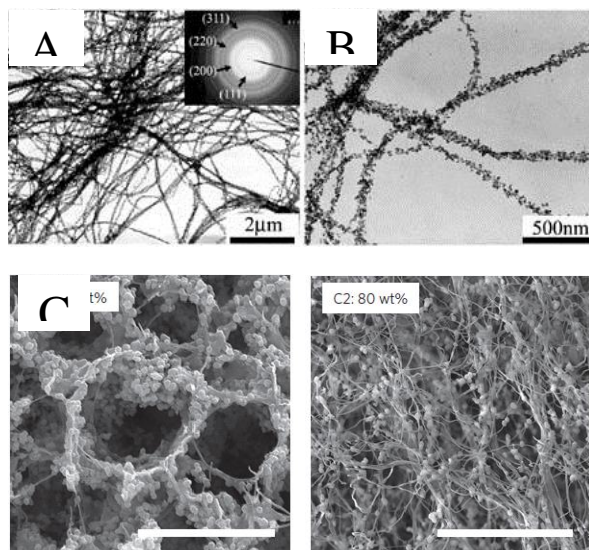


Figure 1.12. (A-B) HRTEM images of BC, Au-BC nanocomposites. Inset shows the related electron diffraction pattern;¹⁰⁶ (C-D) SEM images of flexible magnetic aerogels and stiff magnetic nanopaper using BC as templates.¹¹⁰

1.3.11. Film materials

Very recently, cellulose nanofiber reinforced polymers and transparent cellulose nanopapers have been attempted as the substrates for transparent, flexible electrodes.^{8,12,116–123} CNFs were initially used as nanoreinforcements in polymers to make transparent composite substrate.^{124,125,126} All-CNF nanopapers were subsequently developed using a filtration and pressing process,^{3,117,119,127} and the products show high toughness/strength/modulus and high transparency. However, even with high transparency, the nanopapers show high haze because of its high percentage of diffusive transmittance caused by strong light scattering by large fiber bundles and/or pores in the nanopaper.^{128,129,130,131} The transparency T of a medium is defined as the ratio of transmitted radiant power to incident radiant power, where the transmitted radiant power is the sum of direct transmittance T_{direct} (Regular T) and diffuse transmittance $T_{diffuse}$, i.e., $T = T_{direct} + T_{diffuse}$. Therefore nanopaper can have high transparency and high haze at the same time if its $T_{diffuse}$ is larger than its T_{direct} . While high haze of the nanopapers is a useful feature for applications such as skylight and indoor lighting, which often prefers diffuse light, such nanopapers are not suitable for applications that require high optical transparency, e.g., flexible displays and touch screens.

The most unique of bacterial cellulose (BC) hydrogel is its intrinsic interconnecting network. Surface acetylation of bacterial cellulose nanofibers to reinforce acrylic resin for optically transparent composites was demonstrated by Ifuku et al (2007).¹³² Because the acetylation decreased the refractive index of cellulose, a high regular transmittance of composites comprised of 63 % BC nanofiber was obtained. Similar study was found in another study by Yano et al (2005), as shown in **Figure 1.13A**. Transmittance increases from BC sheet, BC/epoxy sheet and epoxy resin. The optically transparent BC/epoxy is made of resin reinforced

with networks of bacterial nanofibers (70 %).¹²⁴ Low thermal expansion coefficients ($6 \times 10^{-6}/^{\circ}\text{C}$), excellent Young's moduli (20 GPa) and tensile strengths (325 MPa) were achieved in this flexible plastic composite film reinforced with this renewable resource. Artificial Nacre composed of polyvinyl alcohol/clay/CNFs (clay+CNFs: 70 %) was reported by Wang et al (2014).¹³³ Nacre from mother of pearl is an organic-inorganic composite film material features strong, resilient and iridescent characteristics. The artificial nacre is highly transparent, with an excellent balance of strength and toughness and a fatigue-resistant property (Clay/CNFs: 1:2), superior to natural nacre and other conventional layered clay/polymer binary composites. Another recent report by Tang et al (2015) demonstrates a key characteristic of CNF-reinforced poly(ethylene glycol) with high haze (translucent).¹²³ This type of hazy film materials has a high total transmittance because fiber size is smaller than the wavelength of visible light enables a high total transmittance, however, internal pores induces large light scattering in the forward direction, that is the reason making it appears hazy. This feature scatters transmitted lights into different direction, the spot enlarged as shown in **Figure 1.13C**. However, from a life-cycle perspective, these petroleum-based substrates are expensive and environmentally less attractive than easily recyclable or biodegradable substrates. Substrate film materials which could be synthesized from renewable feedstocks, such as CNFs, CNCs and BC, at a low cost, are particularly attractive for the realization of a sustainable solar cell technology.

All CNF-based nanopaper (**Figure 1.13B**) was made as well, as reported by Hu et al (2013).¹³⁴ The CNF-nanopaper was intelligently functionalized by ITO glass coating as a substrate. This type of Nanopaper has a high total transmittance and haze (translucent) The nanofibril size is less than the wavelength of visible light enables a high total transmittance, however, internal pores induces large light scattering in the forward direction, that is the reason

making it appears hazy. Comparing these two main types of engineered materials including CNFs/CNCs/BC in polymer composite films, all-cellulose nanofiber-based nanopaper has the ability of acting as flexible/toughening agents under the scenarios of being with/without polymer additives.

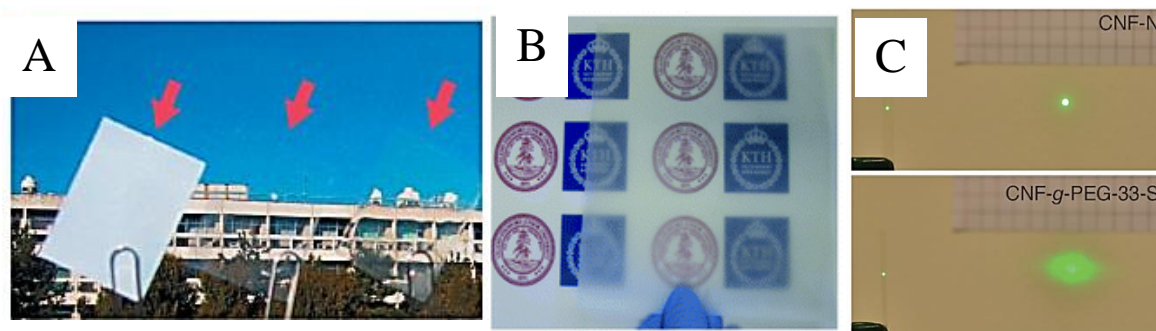


Figure 1.13. (A) photo of BC sheet, BC/epoxy sheet and epoxy resin;¹²⁴ (B) Light scattering effect of the ribbons;¹²³ (C) “focus” and “blurry” transmitted light spots of the nonstretched and stretched ribbons of CNF/PEG films.

1.3.12. Conductive electrode materials

Mechanically flexible/robust, highly transparent/conductive electrodes are required in next generation large-area displays, touch screens,¹³⁵ light-emitting diode (LED) light sources¹³⁶ and solar energy devices.¹³⁷ Indium tin oxide (ITO) has long been used to make glass based transparent electrodes. The drawbacks with these traditional electrodes are obvious: brittleness, high cost, limited/unrenewable raw materials, and environmentally damaging manufacturing processes. To overcome these challenges, poly(3,4-ethylenedioxythiophene)/polystyrene sulfonate (PEDOT/PSS),^{138,139} carbon nanotubes (CNTs), graphene and silver nanowires (AgNWs)^{140–143} have been coated on flexible polymer substrates with the aim of replacing ITO/glass electrodes. The performance of these new flexible electrodes is comparable with the ones on stationary substrates such as glass; it features light-weight because the polymers have a weight density (1.0-1.5 g/cm³) that is much lower than that of glass (2.2 g/cm³). It also has

rollability and stretchability, high electrical conductivity,¹³¹ high processibility (rollable, heatable and printable) for further-step device assembly. Disadvantages of these new flexible electrodes may include that it has high processing difficulties and no long time heat-stainability at over melting temperatures (>200 °C).

Nanopaper, which is made of cellulose nanofibers without additional petroleum-based polymers, is attracting sustainable attention due to its rich natural raw source, abundant tunable surface chemistry and high optical/mechanical properties.^{119,144} Usually, thin layer of conductive activators such as PEDOT/PSS were doped onto or into the nanopaper to provide a high electrical conductivity, which is called nanopaper electrode. With a low-cost, environmental-friendly, high performance, the intellectual merit will be the discovery and development a fully biobased transparent electrode with mechanical and optical properties not attainable by current state-of-the-art. Successful completion of this research is expected to provide the industry a novel, superior electrode suitable for a wide variety of applications, and therefore its impact is significant.

For conductor inside the film, composite film consisting of TEMPO-oxidized CNFs and carbon nanotubes (CNTs) was fabricated by Koga et al (2013)¹⁴⁵ (**Figure 1.14A**). TEMPO-oxidization introduces abundant anionic sodium carboxyl groups (-COONa) on the CNFs surfaces that facilitate a well dispersion of CNTs. The supporting function of CNFs makes it to be used as an alternative to conventional polymers for various electrical materials, which provides a promising route to realize green and flexible electronics. Besides the CNTs, another conductor, reduced graphene oxide sheets (RGO) was also attempted to incorporate with amine (-NH₂)-modified CNFs (**Figure 1.14B**).¹⁴⁶ They possess a combination of high electrical and mechanical performances. For example, the RGO/CNFs exhibits an electrical percolation

threshold of 0.3 wt% with an electrical conductivity of 4.79×10^{-4} S/m. Furthermore, with 10 wt% of graphene, a conductivity of 71.8 S/m was obtained.

The incorporation of conductors (CNTs, RGO) within cellulose nanofibers reminds us to question whether the cellulose itself can be converted into an electrical conductive material. Herein, some research groups have been reporting on emphasis of converting the carbon-rich cellulose (plant-based CNF, CNCs, bacterial cellulose) into carbon nanofibers.¹⁴⁷⁻¹⁵⁴ For example, Liang et al (2012) reported to fabricate conductive (0.20-0.41 S/cm), and stretchable conductors from pyrolyzed bacterial cellulose (600 to 1400 °C) and polydimethylsiloxane (PDMS).¹⁴⁷ The conductivity was higher than conventional carbon nanotubes and graphene-based composites. Moreover, as reported by Wu et al (2013), an ultralight, flexible, and fire-resistant carbon nanofiber aerogels from bacterial cellulose was synthesized.¹⁵⁵ freeze-dried BC aerogel was turned into carbon aerogel by pyrolysis at 1300 °C. The reason they used the BC aerogel as the starting material for pyrolysis is that it is able to maintain a “fluffy” status before and after carbonization with large surface area and lots of pores between the individual carbon nanofibers. Moderate electrical conductivity and a superior mechanical property with a compressive strain at high as 90 % of the carbon aerogel were obtained.

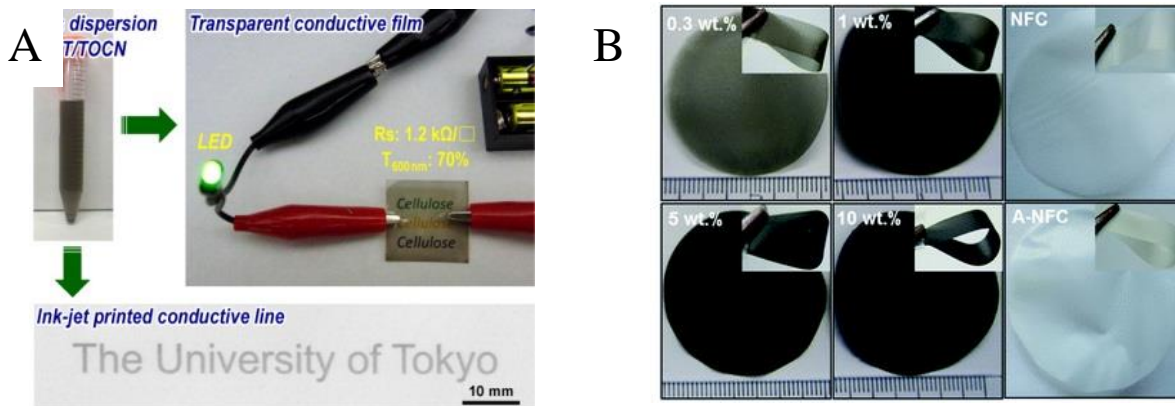


Figure 1.14. (A) Transparent, conductive, and printable composites consisting of TEMPO-oxidized CNFs and carbon nanotube;¹⁴⁵ (B) Photos of CNF and RGO-CNF papers with increasing graphene contents.¹⁴⁶

1.3.13. Flexible device materials

Flexible electronic devices such as supercapacitors, batteries, light emitting diodes (LED) using cellulose nanofibers as a supporting material is very interesting. In the development of high performance energy storage supercapacitors, unique free-standing, light-weight, flexible and higher electrochemical characteristics are the current state-of-the-arts.^{14,156-159} Researchers are searching for higher flexibility (in a form of foldable solid-state thin film or deformable aerogel), higher energy/power densities, higher/adaptable surface area or pore sizes for higher electrochemical energy storage, reliability and etc.

As well known, CNCs are a unique chiral nematic liquid crystals, which forms long-range ordering in solution. It maintains this ordering even in dry solid state. Researchers such as Shopsowitz et al (2011) borrowed this ordering from the CNCs and used it as a templating in silica (SiO₂) film. After pyrolyzing in an inert atmosphere at 900 °C, carbon-silica composite films were obtained. Pure needle-like carbon with ordering alignment was formed by eliminating the SiO₂ through alkali (NaOH) etching. They used the mesoporous film (surface area as high as 1465 m²/g) in supercapacitors, which had a specific capacitance of 170 F/g at 0.23 A/g current

load. This value was comparable to the ones reported for hard-templated mesoporous carbons measured under similar conditions.

The bacterial cellulose exhibits inherent interconnecting network, which forms unique flexibility and high/adaptable surface area or pore sizes. These characteristics are similar to lab-synthesized carbon (graphene) aerogels.¹⁶⁰ As reported by Chen et al (2013),^{161,162} BC was used as a starting material to fabricate flexible carbon electrode, based on which, foreign atom or metal oxides such as nitrogen/manganese dioxide (MnO₂) were doped into/onto carbon to form an electrochemical active components. The synthesis method is through a low-cost, eco-friendly, low-temperature, and scalable hydrothermal method or high temperature vacuum-pyrolysis (Chen et al 2013)(**Figure 1.15A**).¹⁶¹ The flexible all-solid-state supercapacitor device can reversibly deliver a maximum power density of 390.53 kW/kg and exhibits a good cycling durability with 95.9% specific capacitance retained after 5000 cycles. The electrochemical performance of cellulose nanofiber-based carbons is comparable or higher than most of other conventional capacitors such as silicon-carbide-derived carbon, graphene and etc.^{14,160,163} This next-generation inexpensive, flexible, lightweight, and sustainable supercapacitor system with large power densities, long cycle life, and good operational safety makes it suitable to meet the pressing demands for portable and flexible equipment.

Substrating/covering function for flexible light-emitting diode displays (LED)¹⁶⁴ and organic solar cells^{128,165} of cellulose nanofiber-based film materials was demonstrated. For example, Zhou et al (2013) report on the first demonstration of polymer solar cells fabricated on CNCs (**Figure1.15B**). Remarkably, some performance parameters of the solar cells on substrate are not that different to the ones obtained on a glass/ITO substrate. The solar cells on the CNC substrates reach a power conversion efficiency of 2.7% (**Figure 1.15C**). Interestingly, these

solar cells can be easily separated and recycled into their major components using low-energy processes at room temperature, opening the door for a truly recyclable solar cell technology. Efficient and easily recyclable organic solar cells on CNC substrates are expected to be an attractive technology for sustainable, scalable, and environmentally-friendly energy production.

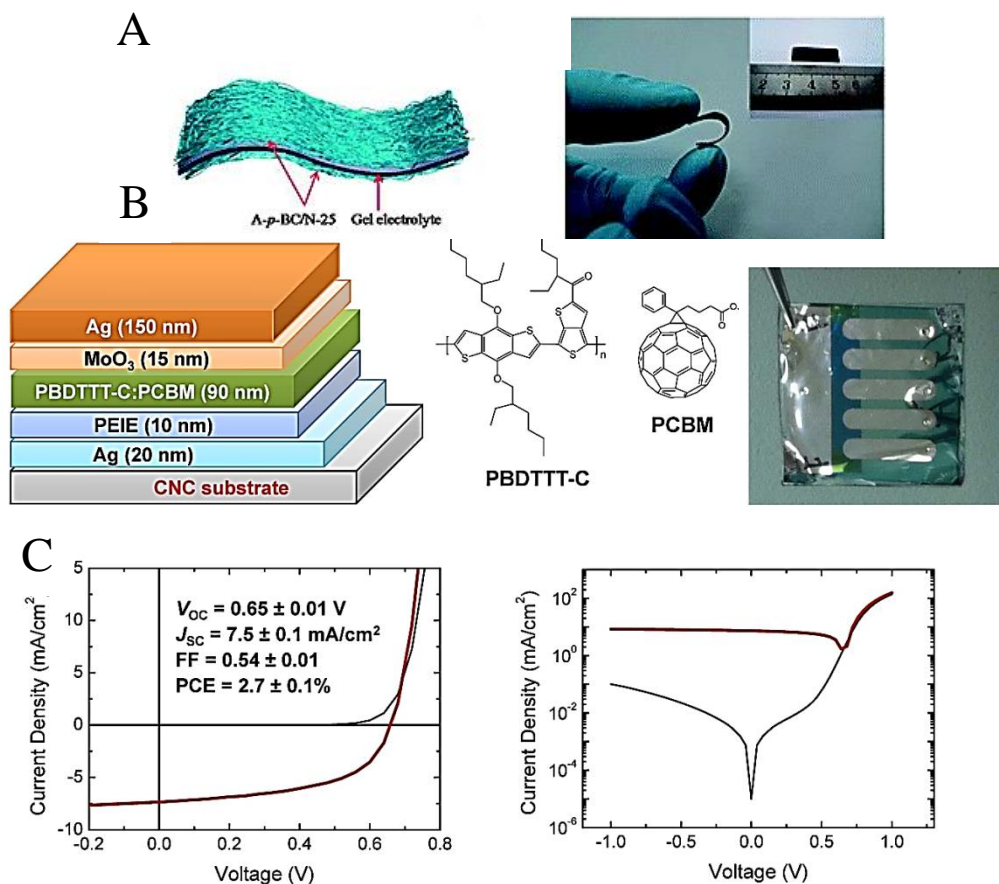


Figure 1.15. All-solid-state supercapacitor and its electrochemical performances;¹⁶¹ (B) Device structure of solar cells on CNC substrates, Chemical structure of PBDTTT-C and PCBM as an effective solar layer; (C) J - V characteristics of the solar cell on CNC substrate in the dark (thin black line) and under 95 mW/cm² of AM1.5 illumination (thick red line); the J - V characteristics on a semi-logarithmic scale in the dark (thin black line) and under illumination (thick red line).¹⁶⁵

1.3.14. Stimulating materials

Colloid, gel, porous foam, film materials and functional electrode and device materials based on various cellulose nanofibers have been extensively discussed. It is noted that the BC and plant-based CNFs assemble each other with similar fibrous-like fiber dimension; hence

many of their properties and performances are similar. However, the needle-like CNCs feature an array of novel applications, which have not been found in the BC and CNFs. These interesting stimulating performances especially found on CNCs include pH-responsive, light-healable and electro-mechanical material are discussed as following.^{89,166,167}

As earlier discussed in the gel material, CNFs switch from dispersion state stabilized by ionization of the surface carboxyl (CO_2H) groups to hierarchically assembled physical hydrogels due to protonation, which is the process of getting H^+ by addition of acids.⁸¹ Way et al. (2012)¹⁶⁶ functionalized CNC surface with either carboxylic acid ($\text{CNC}-\text{CO}_2\text{H}$) or amine ($\text{CNC}-\text{NH}_2$) to render the pH-responsibility. For example, CO_2H functionalized CNCs were dispersible at high pH and form gels in an acidic environment (**Figure 1.16A**). Inversely, amine groups ($-\text{NH}_2$) functionalized CNCs are protonated at low pH, forming aqueous dispersions in water due to electrostatic repulsions of the ammonium inhibiting aggregation. However, a transition to hydrogels is observed at higher pH where the $\text{CNC}-\text{NH}_2$ are neutralized by $-\text{OH}$ groups when hydrogen bonding dominated.

In another study, Biyani et al (2013) demonstrate a light-healable supramolecular nanocomposites based on modified CNCs (**Figure 1.16B**).¹⁶⁷ This system contains polymers that can be repaired after being damaged. This characteristic can improve the reliability, functionality, and lifetime of engineering composite materials. Telechelic poly(ethylene-co-butylene) was functionalized with hydrogen-bonding ureidopyrimidone (UPy) and cellulose nanocrystals (CNCs) decorated with UPy. When these materials are exposed to ultraviolet radiation, the UPy are excited and the absorbed energy is converted into heat. As a result, deliberately introduced defects can be healed quickly and efficiently, even at a filler content of 20 wt% the material exhibits a high strength and stiffness.

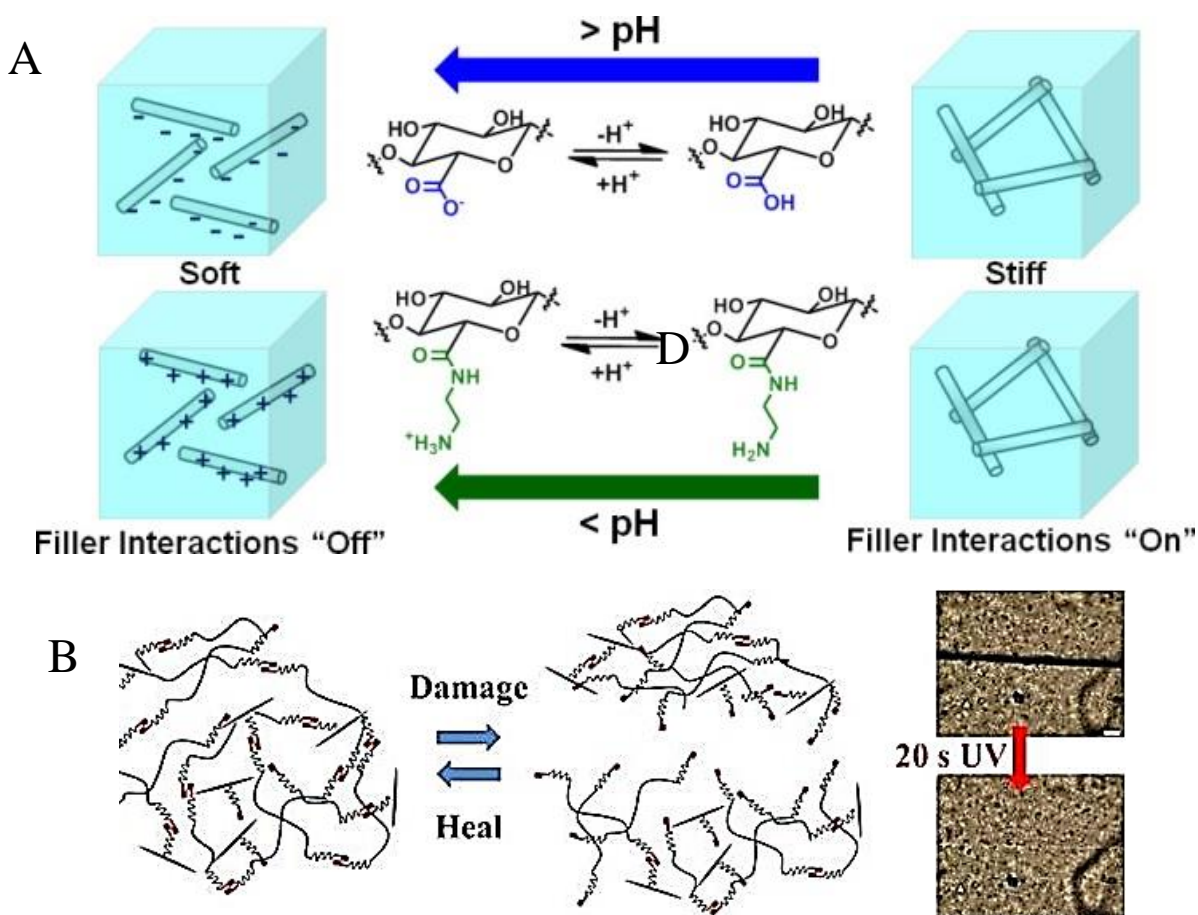


Figure 1.16. (A) functionalization of the surface of cellulose nanocrystals (CNCs) with either carboxylic acid (CNC-CO₂H) or amine (CNC-NH₂) moieties renders the CNCs pH-responsive;¹⁶⁶ (B) Light-healable supramolecular nanocomposites based on modified CNCs, the crack in polymer disappears under 20 s UV exposure;¹⁶⁷

1.3.15. Liquid crystal materials

CNCs are chiral nematic liquid crystals, which consist of mesogens organized into a long-range helical assembly (**Figure 1.17A**), exhibit unique properties such as selective reflection of circularly polarized light. The incorporation of chiral nematic organization into solid-state materials could give rise to novel mesoporous/optical properties. This unique behavior does not present in other fibrous-like nanoscale cellulose such as the BC and plant-based CNFs. Dujardin et al (2003) mixed silica precursor with CNC aqueous solution to prepare mesoporous silica by sol-gel method.¹⁰⁴ Removal of the CNC template produced a birefringent silica replica that

exhibited helically ordered patterns and mesoporosity due to the presence of co-aligned cylindrical pores. This method offers a cost-effective, environmentally route to the template-directed synthesis of mesoporous materials.

Structured color humidity indicator can also be made from self-assembled CNC films, as reported by Zhang et al (2013).¹⁶⁸ The helical pitch (distance of one cycle of nanorod layers) in CNC film responds to water, which results iridescence changes (**Figure 1.17B-C**). On exposure to liquid water, and high relative humidity, a reversible shift in the film iridescence from dry state blue-green to wet state red-orange is observed. The color transition is attributed to sorption of water that causes the pitch of the Bragg reflector to enlarge, and this leads to a red shift in the iridescence. The color shift for a 40 μm thick CNC film is relatively slow, occurring on timescale of 1–3 min. Thinner films change color in less than 2 s. One latest report based on the nematic liquid crystal behavior was reported by Khan et al (2015),¹⁶⁹ in which, they borrowed the “Bragg reflector” concept and expended it to resin (phenol-formaldehyde) composites. Chiral nematic mesoporous resins were prepared using CNCs as a template, which underwent swelling and changed their reflected color as well. By treating the films in chemical inks, the density of functional groups in the resin changes, subsequently affecting their degree of swelling. As a result, the iridescent color changes. Writing on the films gives latent images that are revealed only upon swelling of the films. Using inkjet printing makes higher resolution photonic patterns both as text and images that can be visualized by swelling and erased by drying. This approach to printing photonic patterns in resin films is suitable for anti-counterfeit tags, signage, and decorative applications. Humidity color indicator of either pure CNCs or CNC-templating composites with periodic patterning interacts with an electromagnetic field is useful for optical filters, photonic crystals and other materials.

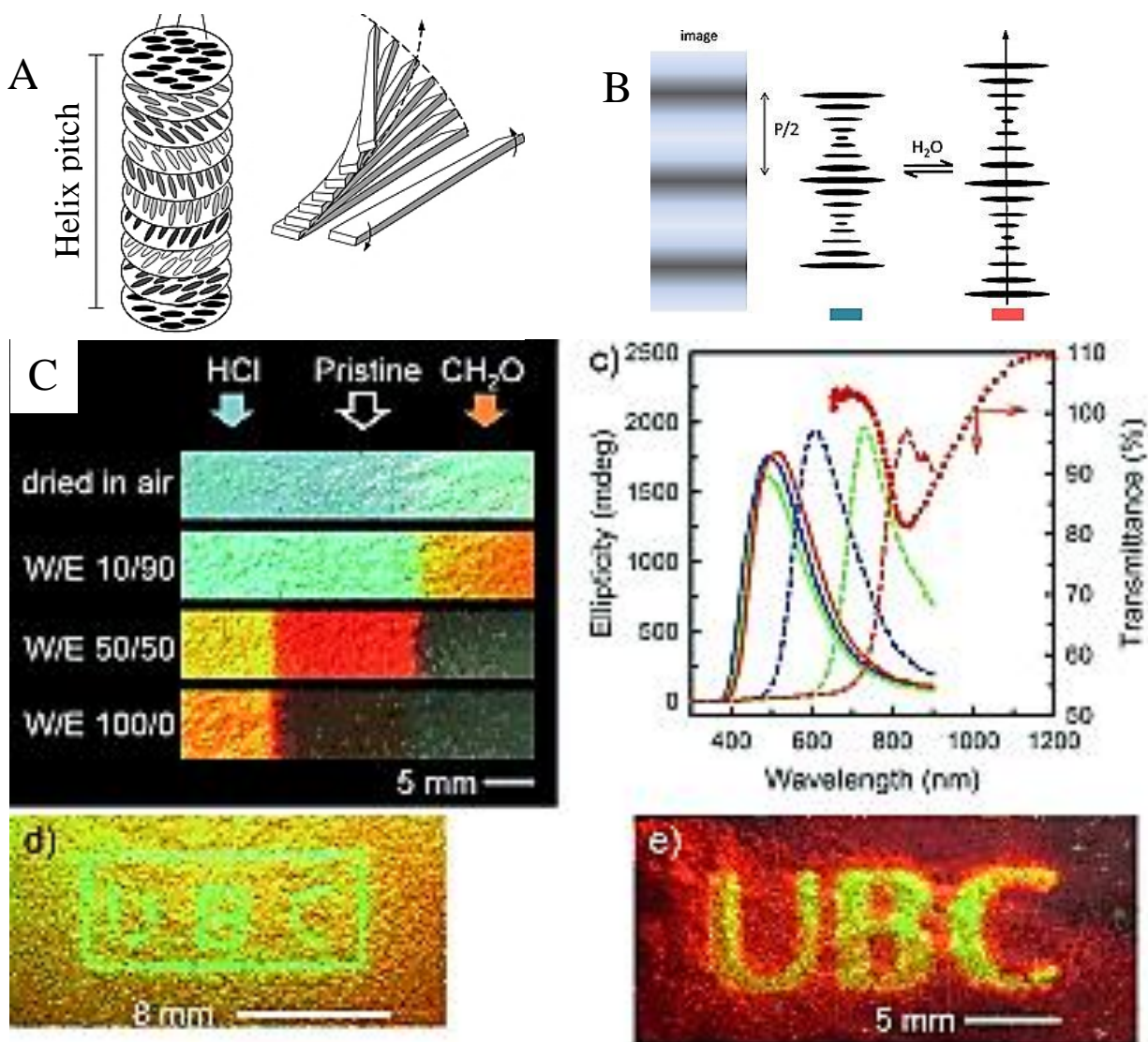


Figure 1.17. (A) illustration showing screw symmetry and helical pitch resulting from twisted close packing of the nanorods;¹⁰⁴ (B) Proposed correspondence between CNC rigid rod assembly orientation in one domain of the chiral nematic phase solid film;¹⁶⁸ (C) Photoic patterns printed in chiral nematic resins.¹⁶⁹

1.3.16. Biocompatible materials

Cellulose nanofibers have been applied in a wide array of biomedical applications such as bacterial-killing, enzyme immobility, drug delivery, tissue implants and wound healing. Wang et al (2014)¹³ synthesized silver (Ag)-CNF hydrogels and evaluated the role of CNFs in stabilizing Ag nanoparticles in bacterial growth medium, antibacterial properties of CNF–AgNPs was

reported. Antimicrobial obtained by surface functionalization with aminoalkyl groups (-NH₂)¹⁷⁰ was also reported, which simultaneously against *S. aureus* and *E. coli* and nontoxic to human adipose-derived mesenchymal stem cells and thus was useful for biomedical applications.

Preparation of gold/magnetite nanoparticles embedded on cellulose nanocrystals for immobilization of papain enzyme was reported by mahmoud et al (2013).¹⁷¹ Magnetite nanoparticles (Fe₃O₄NPs) and Au nanoparticles (AuNPs) embedded on CNCs was used as a magnetic support for the covalent conjugation of papain and facilitated recovery of immobilized enzyme. Fe₃O₄NPs (10–20 nm in diameter) and AuNPs (3–7 nm in diameter) were stable and well-dispersed on the CNC surface. The nanocomposite was successfully used for the immobilization and separation of papain from the reaction mixture.

Skin tissue repairing/cell scaffolding functions of BC were reported due to the unique intrinsic naturally-occurring architected network and hydrogel nature.^{172–174} As reported by Fu et al (2012), the toxicity of BC to biological cells was evaluated *in vitro* with respect to proliferation, adhesion property and morphology (**Figure1.18A**). They prove that BC films as wound-covering material was reproducible and more efficient and low toxicity of the BC film and good proliferation of cells on the BC film were observed. A faster and better healing effect and less inflammatory response in the BC was observed, indicating high clinical potential of the BC. Except the pure BC film, BC is also capable to support other biocompatible macromolecules such as collagen for use in bone tissue regeneration.¹⁷³ Both BC and BC-COL was considered to be an alternative biomaterial for bone tissue engineering (**Figure1.18B**). In another study, artificial blood vessel was generated from BC.¹⁷⁴ The BC pellicle had an asymmetric structure composed of a fine network of nanofibrils similar to a collagen network. The shape of the stress-strain response of BC was reminiscent of the stress-strain response of the carotid artery, most

probably due to the similarity in architecture of the nanofibrill networks. Cell adhered to and proliferated on the BC pellicle (**FigureB**). BC as demonstrated in these studies exhibits attractive properties for use as future biomedical engineering materials.

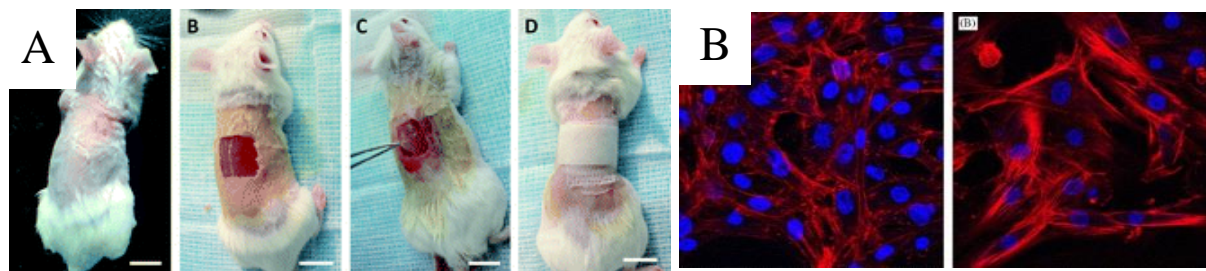


Figure 1.18. (A) The wound-covering of the full-skin injury model in a mouse;¹⁷² (B) Laser scanning confocal images of cells cultured on the porous side of BC.¹⁷⁴

1.4. Summary and research needs

This review summarizes the fundamentals about the three types of cellulose nanofibers and their applications in nanocomposites, gels, templates, scaffold, and optical, electrical/electronic and biomedical devices. Despite more than a decade of research on the cellulose nanofiber reinforced composites, there is still not a single research designed to perform a comparative study between CNCs and CNFs about their different contributions to multiple properties of the composites, based on which a design guideline can be formulated to make intelligent use of the different nanofibers. The development of the cellulose nanofibers for applications in the electrical/electronic devices is still at its early stage. There is much work to be done to gain knowledge and develop processing techniques to advance the research in this field. This Ph.D. project is therefore designed with the aim of pushing the boundaries of research on cellulose nanocomposites and electrical/electronic devices.

1.5. References

1. Lavoine, N., Desloges, I., Dufresne, A. & Bras, J. Microfibrillated cellulose - its barrier properties and applications in cellulosic materials: a review. *Carbohydrate polymers* **90**, 735–64 (2012).
2. Wang, Q. Q. *et al.* Morphological development of cellulose fibrils of a bleached eucalyptus pulp by mechanical fibrillation. *Cellulose* **19**, 1631–1643 (2012).
3. Henriksson, M., Berglund, L. A., Isaksson, P., Lindström, T. & Nishino, T. Cellulose nanopaper structures of high toughness. *Biomacromolecules* **9**, 1579–1585 (2008).
4. Fukuzumi, H., Saito, T., Iwata, T., Kumamoto, Y. & Isogai, A. Transparent and high gas barrier films of cellulose nanofibers prepared by TEMPO-mediated oxidation. *Biomacromolecules* **10**, 162–5 (2009).
5. Xu, X., Liu, F., Jiang, L. & Zhu, J. Cellulose Nanocrystals vs. Cellulose Nanofibrils: A Comparative Study on Their Microstructures and Effects as Polymer Reinforcing Agents. *ACS Applied Materials & Interfaces* **5**, 2999–3009 (2013).
6. Abdul Khalil, H. P. S. *et al.* Production and modification of nanofibrillated cellulose using various mechanical processes: a review. *Carbohydrate polymers* **99**, 649–65 (2014).
7. Sacui, I. A. *et al.* Comparison of the Properties of Cellulose Nanocrystals and Cellulose Nanofibrils Isolated from Bacteria, Tunicate, and Wood Processed Using Acid, Enzymatic, Mechanical, and Oxidative Methods. *ACS Applied Materials & Interfaces* **6**, 6127–6138 (2014).
8. Sehaqui, H. *et al.* Cellulose Nanofiber Orientation in Nanopaper and Nanocomposites by Cold Drawing. *ACS Applied Materials & Interfaces* **4**, 1043–1049 (2012).
9. Tanpichai, S. *et al.* Effective Young's Modulus of Bacterial and Microfibrillated Cellulose Fibrils in Fibrous Networks. *Biomacromolecules* **13**, 1340–1349 (2012).
10. Peresin, M. S., Habibi, Y., Zoppe, J. O., Pawlak, J. J. & Rojas, O. J. Nanofiber composites of polyvinyl alcohol and cellulose nanocrystals: manufacture and characterization. *Biomacromolecules* **11**, 674–681 (2010).
11. Nakagaito, A. N. & Yano, H. The effect of fiber content on the mechanical and thermal expansion properties of biocomposites based on microfibrillated cellulose. *Cellulose* **15**, 555–559 (2008).
12. Huang, J. *et al.* Highly transparent and flexible nanopaper transistors. *ACS nano* **7**, 2106–13 (2013).

13. Wang, M. S., Jiang, F., Hsieh, Y.-L. & Nitin, N. Cellulose nanofibrils improve dispersibility and stability of silver nanoparticles and induce production of bacterial extracellular polysaccharides. *Journal of Materials Chemistry B* **2**, 6226 (2014).
14. Xu, X. *et al.* Flexible, Highly Graphitized Carbon Aerogels Based on Bacterial Cellulose/Lignin: Catalyst-Free Synthesis and its Application in Energy Storage Devices. *Advanced Functional Materials* (2015).doi:10.1002/adfm.201500538
15. Guhados, G., Wan, W. & Hutter, J. L. Measurement of the elastic modulus of single bacterial cellulose fibers using atomic force microscopy. *Langmuir* **21**, 6642–6646 (2005).
16. Hsieh, Y.-C., Yano, H., Nogi, M. & Eichhorn, S. J. An estimation of the Young's modulus of bacterial cellulose filaments. *Cellulose* **15**, 507–513 (2008).
17. Klemm, D., Schumann, D., Udhardt, U. & Marsch, S. Bacterial synthesized cellulose-artificial blood vessels for microsurgery. *Prog. Polym. Sci.* **26**, 1561–1603 (2001).
18. Chen, W., Yu, H. & Liu, Y. Preparation of millimeter-long cellulose I nanofibers with diameters of 30–80nm from bamboo fibers. *Carbohydrate Polymers* **86**, 453–461 (2011).
19. Brito, B. S. L., Pereira, F. V., Putaux, J.-L. & Jean, B. Preparation, morphology and structure of cellulose nanocrystals from bamboo fibers. *Cellulose* **19**, 1527–1536 (2012).
20. Yu, L. *et al.* Cellulose nanofibrils generated from jute fibers with tunable polymorphs and crystallinity. *Journal of Materials Chemistry A* **2**, 6402 (2014).
21. Rosa, M. F. *et al.* Cellulose nanowhiskers from coconut husk fibers: Effect of preparation conditions on their thermal and morphological behavior. *Carbohydrate Polymers* **81**, 83–92 (2010).
22. Santos, R. M. Dos *et al.* Cellulose nanocrystals from pineapple leaf, a new approach for the reuse of this agro-waste. *Industrial Crops and Products* **50**, 707–714 (2013).
23. Jiang, F., Han, S. & Hsieh, Y.-L. Controlled defibrillation of rice straw cellulose and self-assembly of cellulose nanofibrils into highly crystalline fibrous materials. *RSC Advances* **3**, 12366 (2013).
24. Chen, D., Lawton, D., Thompson, M. R. & Liu, Q. Biocomposites reinforced with cellulose nanocrystals derived from potato peel waste. *Carbohydrate polymers* **90**, 709–16 (2012).
25. Qing, Y. *et al.* A comparative study of cellulose nanofibrils disintegrated via multiple processing approaches. *Carbohydrate polymers* **97**, 226–34 (2013).

26. Yu, H. *et al.* Facile extraction of thermally stable cellulose nanocrystals with a high yield of 93% through hydrochloric acid hydrolysis under hydrothermal conditions. *Journal of Materials Chemistry A* **1**, 3938 (2013).
27. Espinosa, S. C., Kuhnt, T., Foster, E. J. & Weder, C. Isolation of Thermally Stable Cellulose Nanocrystals by Phosphoric Acid Hydrolysis. *Biomacromolecules* **14**, 1223–1230 (2013).
28. Sadeghifar, H., Filpponen, I., Clarke, S. P., Brougham, D. F. & Argyropoulos, D. S. Production of cellulose nanocrystals using hydrobromic acid and click reactions on their surface. *Journal of Materials Science* **46**, 7344–7355 (2011).
29. Lu, Q. *et al.* A mechanochemical approach to manufacturing bamboo cellulose nanocrystals. *Journal of Materials Science* **50**, 611–619 (2015).
30. Flauzino Neto, W. P., Silvério, H. A., Dantas, N. O. & Pasquini, D. Extraction and characterization of cellulose nanocrystals from agro-industrial residue – Soy hulls. *Industrial Crops and Products* **42**, 480–488 (2013).
31. Leung, A. C. W. *et al.* Characteristics and properties of carboxylated cellulose nanocrystals prepared from a novel one-step procedure. *Small* **7**, 302–5 (2011).
32. Kalashnikova, I., Bizot, H., Bertoncini, P., Cathala, B. & Capron, I. Cellulosic nanorods of various aspect ratios for oil in water Pickering emulsions. *Soft Matter* **9**, 952 (2013).
33. Jiang, F., Esker, A. R. & Roman, M. Acid-catalyzed and solvolytic desulfation of H₂SO₄-hydrolyzed cellulose nanocrystals. *Langmuir* **26**, 17919–25 (2010).
34. Lin, N. & Dufresne, A. Surface chemistry, morphological analysis and properties of cellulose nanocrystals with gradiented sulfation degrees. *Nanoscale* **6**, 5384–93 (2014).
35. Siqueira, G., Bras, J. & Dufresne, A. Cellulose whiskers versus microfibrils: influence of the nature of the nanoparticle and its surface functionalization on the thermal and mechanical properties of nanocomposites. *Biomacromolecules* **10**, 425–432 (2009).
36. Quiévy, N. *et al.* Influence of homogenization and drying on the thermal stability of microfibrillated cellulose. *Polymer Degradation and Stability* **95**, 306–314 (2010).
37. Ankerfors, M. Microfibrillated cellulose : Energy-efficient preparation techniques and key properties. 1–49 (2012).
38. Spence, K. L., Venditti, R. a., Rojas, O. J., Habibi, Y. & Pawlak, J. J. A comparative study of energy consumption and physical properties of microfibrillated cellulose produced by different processing methods. *Cellulose* **18**, 1097–1111 (2011).

39. Tejado, A., Alam, M. N., Antal, M., Yang, H. & Van de Ven, T. G. M. Energy requirements for the disintegration of cellulose fibers into cellulose nanofibers. *Cellulose* **19**, 831–842 (2012).
40. Henriksson, M., Henriksson, G., Berglund, L. a. & Lindström, T. An environmentally friendly method for enzyme-assisted preparation of microfibrillated cellulose (MFC) nanofibers. *European Polymer Journal* **43**, 3434–3441 (2007).
41. Isogai, A., Saito, T. & Fukuzumi, H. TEMPO-oxidized cellulose nanofibers. *Nanoscale* **3**, 71–85 (2011).
42. Lahiji, R. R. *et al.* Atomic force microscopy characterization of cellulose nanocrystals. *Langmuir* **26**, 4480–8 (2010).
43. Guhados, G., Wan, W. & Hutter, J. L. Measurement of the elastic modulus of single bacterial cellulose fibers using atomic force microscopy. *Langmuir* **21**, 6642–6646 (2005).
44. Diaz, J. A. *et al.* Thermal Conductivity in Nanostructured Films: From Single Cellulose Nanocrystals to Bulk Films. *Biomacromolecules* **15**, 4096–4101 (2014).
45. Peng, B. L., Dhar, N., Liu, H. L. & Tam, K. C. Chemistry and applications of nanocrystalline cellulose and its derivatives: A nanotechnology perspective. *Can.J. Chem. Eng.* **89**, 1191–1206 (2011).
46. Dufresne, A. Nanocellulose: a new ageless bionanomaterial. *Materials Today* **16**, 220–227 (2013).
47. Zhang, W. *et al.* High performance poly (vinyl alcohol)/cellulose nanocrystals nanocomposites manufactured by injection molding. *Cellulose* **21**, 485–494 (2013).
48. McKee, J. R. *et al.* Healable, Stable and Stiff Hydrogels: Combining Conflicting Properties Using Dynamic and Selective Three-Component Recognition with Reinforcing Cellulose Nanorods. *Advanced Functional Materials* **24**, 2706–2713 (2014).
49. Qiu, K. & Netravali, A. N. Bacterial cellulose-based membrane-like biodegradable composites using cross-linked and noncross-linked polyvinyl alcohol. *Journal of Materials Science* **47**, 6066–6075 (2012).
50. Peng, J., Ellingham, T., Sabo, R., Turng, L.-S. & Clemons, C. M. Short cellulose nanofibrils as reinforcement in polyvinyl alcohol fiber. *Cellulose* (2014).doi:10.1007/s10570-014-0411-3
51. Zheng, Q., Javadi, A., Sabo, R., Cai, Z. & Gong, S. Polyvinyl alcohol (PVA)–cellulose nanofibril (CNF)–multiwalled carbon nanotube (MWCNT) hybrid organic aerogels with superior mechanical properties. *RSC Advances* **3**, 20816 (2013).

52. Bondeson, D. & Oksman, K. Polylactic acid/cellulose whisker nanocomposites modified by polyvinyl alcohol. *Composites Part A: Applied Science and Manufacturing* **38**, 2486–2492 (2007).
53. Javadi, A. *et al.* Polyvinyl Alcohol-Cellulose Nanofibrils-Graphene Oxide Hybrid Organic Aerogels. *ACS Applied Materials & Interfaces* **5**, 5969–5975 (2013).
54. Yang, J., Han, C., Zhang, X., Xu, F. & Sun, R. Cellulose Nanocrystals Mechanical Reinforcement in Composite Hydrogels with Multiple Cross-Links : Correlations between Dissipation Properties and Deformation Mechanisms. *macromolecules* **47**, 4077–4086 (2014).
55. Yang, J., Han, C., Duan, J., Xu, F. & Sun, R. Mechanical and Viscoelastic Properties of Cellulose Nanocrystals Reinforced Poly(ethylene glycol) Nanocomposite Hydrogels. *ACS Appl. Mater. Interfaces* **5**, 3199–3207 (2013).
56. Zhou, C., Chu, R., Wu, R. & Wu, Q. Electrospun polyethylene oxide/cellulose nanocrystal composite nanofibrous mats with homogeneous and heterogeneous microstructures. *Biomacromolecules* **12**, 2617–25 (2011).
57. Zhou, C. *et al.* Electrospun Bio-Nanocomposite Scaffolds for Bone Tissue Engineering by Cellulose Nanocrystals Reinforcing Maleic Anhydride Grafted PLA. *ACS Applied Materials & Interfaces* **5**, 3847–3854 (2013).
58. Zhang, Z. *et al.* Using Cellulose Nanocrystals as a Sustainable Additive to Enhance Hydrophilicity, Mechanical and Thermal Properties of Poly(vinylidene fluoride)/Poly(methyl methacrylate) Blend. *ACS Sustainable Chemistry & Engineering* **3**, 574–582 (2015).
59. Lin, N. & Dufresne, A. Physical and/or Chemical Compatibilization of Extruded Cellulose Nanocrystal Reinforced Polystyrene Nanocomposites. *macromolecules* **46**, 5570–5583 (2013).
60. Morphology, N., Yang, X., Bakaic, E., Hoare, T. & Cranston, E. D. Injectable Polysaccharide Hydrogels Reinforced with Cellulose Nanocrystals: Morphology, Rheology, Degradation, and Cytotoxicity. *Biomacromolecules* **14**, 4447–4455 (2013).
61. Huq, T. *et al.* Nanocrystalline cellulose (NCC) reinforced alginate based biodegradable nanocomposite film. *Carbohydrate polymers* **90**, 1757–63 (2012).
62. Köhnke, T., Lin, A., Elder, T., Theliander, H. & Ragauskas, A. J. Nanoreinforced xylan–cellulose composite foams by freeze-casting. *Green Chemistry* **14**, 1864 (2012).
63. Ago, M., Okajima, K., Jakes, J. E., Park, S. & Rojas, O. J. Lignin-based electrospun nanofibers reinforced with cellulose nanocrystals. *Biomacromolecules* **13**, 918–26 (2012).

64. Dalmas, F., Cavaillé, J.-Y., Gauthier, C., Chazeau, L. & Dendievel, R. Viscoelastic behavior and electrical properties of flexible nanofiber filled polymer nanocomposites. Influence of processing conditions. *Compos. Sci. Technol.* **67**, 829–839 (2007).
65. De Mesquita, J. P. *et al.* Hybrid layer-by-layer assembly based on animal and vegetable structural materials: multilayered films of collagen and cellulose nanowhiskers. *Soft Matter* **7**, 4405 (2011).
66. Zhou, C., Chu, R., Wu, R. & Wu, Q. Electrospun Polyethylene Oxide / Cellulose Nanocrystal Composite Nanofibrous Mats with Homogeneous and Heterogeneous Microstructures. *Biomacromolecules* **12**, 2617–2625 (2011).
67. Lin, N., Huang, J., Chang, P. R., Feng, J. & Yu, J. Surface acetylation of cellulose nanocrystal and its reinforcing function in poly(lactic acid). *Carbohydrate Polymers* **83**, 1834–1842 (2011).
68. Ago, M., Okajima, K., Jakes, J. E., Park, S. & Rojas, O. J. Lignin-Based Electrospun Nanofibers Reinforced with Cellulose Nanocrystals. *ACS Applied Materials & Interfaces* **13**, 918–926 (2012).
69. Mariano, M., El Kissi, N. & Dufresne, A. Cellulose nanocrystals and related nanocomposites: Review of some properties and challenges. *Journal of Polymer Science Part B: Polymer Physics* **52**, 791–806 (2014).
70. Durán, N., Lemes, A. P. & Seabra, A. B. Review of Cellulose Nanocrystals Patents : Preparation , Composites and General Applications. *Recent Patent on Nanotechnology* **6**, 1–12 (2012).
71. Halpin, J.C.; Kardos, J. L. Moduli of Crystalline Polymers Employing Composite Theory. *J. Appl. Phys.* **43**, 2235–2241 (1972).
72. Ouali, N.; Cavaillé, J. Y.; Perez, J. Elastic, viscoelastic, and plastic behavior of multiphase polymer blends. *Plast. Rubber Compos. Pro. Apps.* **16**, 55–60 (1991).
73. Takayanagi, M.; Uemura, S.; Minami, S. Takayanagi.pdf. *J. Polym. Sci., Part C: Polym. Symp.* **5**, 113 (1964).
74. Favier, V., Chanzy, H. & Cavaillé, J. Y. Polymer nanocomposites reinforced by cellulose whiskers. *Macromolecules* **28**, 6365–6367 (1996).
75. Capadona, J. R., Shanmuganathan, K., Tyler, D. J., Rowan, S. J. & Weder, C. Stimuli-responsive polymer nanocomposites inspired by the sea cucumber dermis. *Science* **319**, 1370–1374 (2008).

76. Van Es, M. A.; Xiqiao, F.; van Turnhout, J.; van der Giessen, E. Van Es, M. A.; Xiqiao, F.; van Turnhout, J.; van der Giessen, E. *Specialty polymer additives: principles and applications* 391–414 (2001).
77. Fourier, J.; Canova, G. R.; Shrivastava, S. C.; Cavaille, J. Y. Mechanical Percolation in Cellulose Whisker. *Polym. Eng. Sci.* **37**, 1732–1739 (1997).
78. Shafiei-sabet, S., Hamad, W. Y. & Hatzikiriakos, S. G. Rheology of Nanocrystalline Cellulose Aqueous Suspensions. *Langmuir* **28**, 17124–17133 (2012).
79. Fall, A. B., Lindstr, S. B., Sundman, O., Odberg, L. & Lars, W. Colloidal Stability of Aqueous Nanofibrillated Cellulose Dispersions. *Langmuir* **27**, 11332–11338 (2011).
80. Hirai, A., Inui, O., Horii, F. & Tsuji, M. Phase Separation Behavior in Aqueous Suspensions of Bacterial Cellulose Nanocrystals Prepared by Sulfuric Acid Treatment. *Langmuir* 497–502 (2009).
81. Saito, T., Uematsu, T., Kimura, S., Enomae, T. & Isogai, A. Self-aligned integration of native cellulose nanofibrils towards producing diverse bulk materials. *Soft Matter* **7**, 8804 (2011).
82. Varjonen, S. *et al.* Self-assembly of cellulose nanofibrils by genetically engineered fusion proteins. *Soft Matter* **7**, 2402 (2011).
83. Håkansson, K. M. O. *et al.* Hydrodynamic alignment and assembly of nanofibrils resulting in strong cellulose filaments. *Nature communications* **5**, 4018 (2014).
84. Liu, D., Chen, X., Yue, Y., Chen, M. & Wu, Q. Structure and rheology of nanocrystalline cellulose. *Carbohyd. Polym.* **84**, 316–322 (2011).
85. Kalashnikova, I., Bizot, H., Cathala, B. & Capron, I. Modulation of Cellulose Nanocrystals Amphiphilic Properties to Stabilize Oil / Water Interface. *Biomacromolecules* **13**, 267–275 (2012).
86. Olivier, C. *et al.* Cellulose Nanocrystal-Assisted Dispersion of Luminescent Single-Walled Carbon Nanotubes for Layer-by-Layer Assembled Hybrid Thin Films. *Langmuir* **28**, 12463–12471 (2012).
87. Beck, S., Bouchard, J., Chauve, G. & Berry, R. Controlled production of patterns in iridescent solid films of cellulose nanocrystals. *Cellulose* **20**, 1401–1411 (2013).
88. Dong, H., Snyder, J. F., Tran, D. T. & Leadore, J. L. Hydrogel, aerogel and film of cellulose nanofibrils functionalized with silver nanoparticles. *Carbohydrate polymers* **95**, 760–7 (2013).

89. Zhou, C., Wu, Q., Yue, Y. & Zhang, Q. Application of rod-shaped cellulose nanocrystals in polyacrylamide hydrogels. *Journal of colloid and interface science* **353**, 116–23 (2011).
90. Nakayama, a. *et al.* High Mechanical Strength Double-Network Hydrogel with Bacterial Cellulose. *Advanced Functional Materials* **14**, 1124–1128 (2004).
91. Liebner, F. *et al.* Aerogels from unaltered bacterial cellulose: application of scCO₂ drying for the preparation of shaped, ultra-lightweight cellulosic aerogels. *Macromolecular bioscience* **10**, 349–52 (2010).
92. Online, V. A., Jiang, F. & Hsieh, Y. Super water absorbing and shape memory nanocellulose aerogels from TEMPO-oxidized cellulose nanofibrils via cyclic freezing – thawing. *Journal of Materials Chemistry A* **2**, 350–359 (2014).
93. Svagan, A. J., Samir, M. a. S. A. & Berglund, L. a. Biomimetic Foams of High Mechanical Performance Based on Nanostructured Cell Walls Reinforced by Native Cellulose Nanofibrils. *Advanced Materials* **20**, 1263–1269 (2008).
94. Liu, D., Ma, Z., Wang, Z., Tian, H. & Gu, M. Biodegradable Poly (vinyl alcohol) Foams Supported by Cellulose Nanofibrils : Processing , Structure , and Properties. *Langmuir* **30**, 9544–9550 (2014).
95. Jiang, F. & Hsieh, Y.-L. Amphiphilic superabsorbent cellulose nanofibril aerogels. *Journal of Materials Chemistry A* **2**, 6337 (2014).
96. Cai, H. *et al.* Aerogel Microspheres from Natural Cellulose Nanofibrils and Their Application as Cell Culture Scaffold. *Biomacromolecules* **15**, 2540–2547 (2014).
97. Chen, W., Yu, H., Li, Q., Liu, Y. & Li, J. Ultralight and highly flexible aerogels with long cellulose I nanofibers. *Soft Matter* **7**, 10360 (2011).
98. Aulin, C., Netrval, J., Wågberg, L. & Lindström, T. Aerogels from nanofibrillated cellulose with tunable oleophobicity. *Soft Matter* **6**, 3298 (2010).
99. Pei, A., Butchosa, N., Berglund, L. a. & Zhou, Q. Surface quaternized cellulose nanofibrils with high water absorbency and adsorption capacity for anionic dyes. *Soft Matter* **9**, 2047 (2013).
100. Korhonen, J. T., Kettunen, M., Ras, R. H. A. & Ikkala, O. Hydrophobic Nanocellulose Aerogels as Floating, Sustainable, Reusable, and Recyclable Oil Absorbents. *ACS Applied Materials & Interfaces* 1813–1816 (2011).
101. Kettunen, M. *et al.* Photoswitchable Superabsorbency Based on Nanocellulose Aerogels. *Advanced Functional Materials* **21**, 510–517 (2011).

102. Eyley, S. & Thielemans, W. Imidazolium grafted cellulose nanocrystals for ion exchange applications. *Chemical communications (Cambridge, England)* **47**, 4177–9 (2011).
103. Eyley, S. *et al.* Ferrocene-Decorated Nanocrystalline Cellulose with Charge Carrier Mobility. *Langmuir* **28**, 6514–6519 (2012).
104. Dujardin, E., Blaseby, M. & Mann, S. Synthesis of mesoporous silica by sol–gel mineralisation of cellulose nanorod nematic suspensions. *Journal of Materials Chemistry* **13**, 696–699 (2003).
105. Liu, H., Wang, D., Song, Z. & Shang, S. Preparation of silver nanoparticles on cellulose nanocrystals and the application in electrochemical detection of DNA hybridization. *Cellulose* **18**, 67–74 (2010).
106. Zhang, T. *et al.* Biotemplated Synthesis of Gold Nanoparticle-Bacteria Cellulose Nanofiber Nanocomposites and Their Application in Biosensing. *Advanced Functional Materials* **20**, 1152–1160 (2010).
107. Cirtiu, C. M., Dunlop-bri, A. F. & Moores, A. Cellulose nanocrystallites as an efficient support for nanoparticles of palladium : application for catalytic hydrogenation and Heck coupling under mild conditions †. *Green Chemistry* **13**, 288–291 (2011).
108. Shin, Y., Blackwood, J. M., Bae, I.-T., Arey, B. W. & Exarhos, G. J. Synthesis and stabilization of selenium nanoparticles on cellulose nanocrystal. *Materials Letters* **61**, 4297–4300 (2007).
109. Gebauer, D. *et al.* A transparent hybrid of nanocrystalline cellulose and amorphous calcium carbonate nanoparticles. *Nanoscale* **3**, 3563–6 (2011).
110. Olsson, R. T. *et al.* Making flexible magnetic aerogels and stiff magnetic nanopaper using cellulose nanofibrils as templates. *Nature nanotechnology* **5**, 584–588 (2010).
111. Junka, K., Guo, J., Filpponen, I., Laine, J. & Rojas, O. J. Modification of Cellulose Nanofibrils with Luminescent Carbon Dots. *Biomacromolecules* **15**, 876–881 (2014).
112. Korhonen, J. T. *et al.* Inorganic Hollow Nanotube Aerogels by Atomic Layer Deposition onto Native Nanocellulose Templates. *ACS Nano* 1967–1974 (2011).
113. Sureshkumar, M., Siswanto, D. Y. & Lee, C.-K. Magnetic antimicrobial nanocomposite based on bacterial cellulose and silver nanoparticles. *Journal of Materials Chemistry* **20**, 6948 (2010).
114. Ifuku, S., Tsuji, M., Morimoto, M., Saimoto, H. & Yano, H. Synthesis of Silver Nanoparticles Templated by TEMPO-Mediated Oxidized Bacterial Cellulose Nanofiber. *Biomacromolecules* **10**, 2714–7 (2009).

115. Yang, G., Xie, J., Deng, Y., Bian, Y. & Hong, F. Hydrothermal synthesis of bacterial cellulose/AgNPs composite: A “green” route for antibacterial application. *Carbohydrate Polymers* **87**, 2482–2487 (2012).
116. Walther, A., Timonen, J. V. I., Díez, I., Laukkanen, A. & Ikkala, O. Multifunctional high-performance biofibers based on wet-extrusion of renewable native cellulose nanofibrils. *Advanced materials* **23**, 2924–8 (2011).
117. Sehaqui, H., Liu, A., Zhou, Q. & Berglund, L. a Fast preparation procedure for large, flat cellulose and cellulose/inorganic nanopaper structures. *Biomacromolecules* **11**, 2195–8 (2010).
118. Huang, J. *et al.* Highly transparent and flexible nanopaper transistors. *ACS nano* **7**, 2106–13 (2013).
119. Zhu, H. *et al.* Transparent nanopaper with tailored optical properties. *Nanoscale* **5**, 3787–92 (2013).
120. Fang, Z. *et al.* Novel nanostructured paper with ultrahigh transparency and ultrahigh haze for solar cells. *Nano letters* **14**, 765–73 (2014).
121. Eichhorn, S. J. *et al.* Review: current international research into cellulose nanofibres and nanocomposites. *Journal of Materials Science* **45**, 1–33 (2009).
122. Fang, Z. *et al.* Highly transparent and writable wood all-cellulose hybrid nanostructured paper. *Journal of Materials Chemistry C* **1**, 6191 (2013).
123. Tang, H., Butchosa, N. & Zhou, Q. A Transparent, Hazy, and Strong Macroscopic Ribbon of Oriented Cellulose Nanofibrils Bearing Poly(ethylene glycol). *Advanced materials* **27**, 2070–6 (2015).
124. Yano, H. *et al.* Optically Transparent Composites Reinforced with Networks of Bacterial Nanofibers. *Advanced Materials* **17**, 153–155 (2005).
125. Fernandes, S. C. M. *et al.* Novel transparent nanocomposite films based on chitosan and bacterial cellulose. *Green Chemistry* **11**, 2023 (2009).
126. Iwamoto, S., Nakagaito, a. N., Yano, H. & Nogi, M. Optically transparent composites reinforced with plant fiber-based nanofibers. *Applied Physics A* **81**, 1109–1112 (2005).
127. Sun, X., Wu, Q., Ren, S. & Lei, T. Comparison of highly transparent all-cellulose nanopaper prepared using sulfuric acid and TEMPO-mediated oxidation methods. *Cellulose* **22**, 1123–1133 (2015).
128. Fang, Z. *et al.* Novel nanostructured paper with ultrahigh transparency and ultrahigh haze for solar cells. *Nano letters* **14**, 765–73 (2014).

129. Hsieh, M.-C., Kim, C., Nogi, M. & Suganuma, K. Electrically conductive lines on cellulose nanopaper for flexible electrical devices. *Nanoscale* **5**, 9289–95 (2013).
130. Fang, Z. *et al.* Highly transparent paper with tunable haze for green electronics. *Energy Environ. Sci.* **7**, 3313–3319 (2014).
131. Hu, L. *et al.* Transparent and conductive paper from nanocellulose fibers. *Energy & Environmental Science* **6**, 513 (2013).
132. Ifuku, S. *et al.* Surface modification of bacterial cellulose nanofibers for property enhancement of optically transparent composites: dependence on acetyl-group DS. *Biomacromolecules* **8**, 1973–8 (2007).
133. Wang, J., Cheng, Q., Lin, L. & Jiang, L. Synergistic Toughening of Bioinspired Poly (vinyl alcohol)-Clay-Nanofibrillar Cellulose Artificial Nacre. *ACS Nano* 2739–2745 (2014).
134. Hu, L. *et al.* Transparent and conductive paper from nanocellulose fiber. *Energy & Environmental Science* **6**, 513–518 (2013).
135. Madaria, A. R., Kumar, A. & Zhou, C. Large scale, highly conductive and patterned transparent films of silver nanowires on arbitrary substrates and their application in touch screens. *Nanotechnology* **22**, 245201 (2011).
136. Reineke, S. *et al.* White organic light-emitting diodes with fluorescent tube efficiency. *Nature* **459**, 234–8 (2009).
137. Leem, D.-S. *et al.* Efficient organic solar cells with solution-processed silver nanowire electrodes. *Advanced materials (Deerfield Beach, Fla.)* **23**, 4371–5 (2011).
138. Zhou, J. & Lubineau, G. Improving electrical conductivity in polycarbonate nanocomposites using highly conductive PEDOT/PSS coated MWCNTs. *ACS Applied Materials & Interfaces* **5**, 6189–200 (2013).
139. Zhou, J., Fukawa, T., Shirai, H. & Kimura, M. Anisotropic Motion of Electroactive Papers Coated with PEDOT/PSS. *Macromolecular Materials and Engineering* **295**, 671–675 (2010).
140. Hu, L., Kim, H. S., Lee, J., Peumans, P. & Cui, Y. Scalable Coating and Properties of Transparent, Flexible, Silver Nanowire Electrodes. *ACS Nano* **4**, 2955–2963 (2010).
141. De, S. *et al.* Silver nanowire networks as flexible, transparent, conductive films: extremely high DC to optical conductivity ratios. *ACS Nano* **3**, 1767–1774 (2009).

142. Zeng, X.-Y., Zhang, Q.-K., Yu, R.-M. & Lu, C.-Z. A new transparent conductor: silver nanowire film buried at the surface of a transparent polymer. *Advanced materials (Deerfield Beach, Fla.)* **22**, 4484–8 (2010).
143. Liang, J. *et al.* Silver nanowire percolation network soldered with graphene oxide at room temperature and its application for fully stretchable polymer light-emitting diodes. *ACS nano* **8**, 1590–600 (2014).
144. Henriksson, M., Berglund, L. A., Isaksson, P. & Lindstro, T. Cellulose Nanopaper Structures of High Toughness. *Biomacromolecules* **9**, 1579–1585 (2008).
145. Koga, H. *et al.* Transparent, Conductive, and Printable Composites Consisting of TEMPO-Oxidized Nanocellulose and Carbon Nanotube. *Biomacromolecules* **14**, 1160–1165 (2013).
146. Luong, N. D. *et al.* Graphene/cellulose nanocomposite paper with high electrical and mechanical performances. *Journal of Materials Chemistry* **21**, 13991 (2011).
147. Liang, H.-W. *et al.* Highly conductive and stretchable conductors fabricated from bacterial cellulose. *NPG Asia Materials* **4**, e19 (2012).
148. Falco, C., Baccile, N. & Titirici, M.-M. Morphological and structural differences between glucose, cellulose and lignocellulosic biomass derived hydrothermal carbons. *Green Chemistry* **13**, 3273 (2011).
149. Shopsowitz, K. E., Hamad, W. Y. & MacLachlan, M. J. Chiral nematic mesoporous carbon derived from nanocrystalline cellulose. *Angewandte Chemie* **50**, 10991–5 (2011).
150. Vuorema, A. *et al.* Ultrathin Carbon Film Electrodes from Vacuum-Carbonised Cellulose Nanofibril Composite. *Electroanalysis* **22**, 619–624 (2010).
151. Sukanuma, S. *et al.* Synthesis and acid catalysis of cellulose-derived carbon-based solid acid. *Solid State Sciences* **12**, 1029–1034 (2010).
152. Fukuhara, K. *et al.* Structure and catalysis of cellulose-derived amorphous carbon bearing SO₃H groups. *ChemSusChem* **4**, 778–84 (2011).
153. Wang, B. *et al.* Pyrolyzed bacterial cellulose: a versatile support for lithium ion battery anode materials. *Small (Weinheim an der Bergstrasse, Germany)* **9**, 2399–404 (2013).
154. Chen, L.-F., Huang, Z.-H., Liang, H.-W., Gao, H.-L. & Yu, S.-H. Three-Dimensional Heteroatom-Doped Carbon Nanofiber Networks Derived from Bacterial Cellulose for Supercapacitors. *Advanced Functional Materials* **24**, 5104–5111 (2014).

155. Wu, Z.-Y., Li, C., Liang, H.-W., Chen, J.-F. & Yu, S.-H. Ultralight, Flexible, and Fire-Resistant Carbon Nanofiber Aerogels from Bacterial Cellulose. *Angewandte Chemie* **125**, 2997–3001 (2013).
156. Futaba, D. N. *et al.* Shape-engineerable and highly densely packed single-walled carbon nanotubes and their application as super-capacitor electrodes. *Nature materials* **5**, 987–94 (2006).
157. El-Kady, M. F., Strong, V., Dubin, S. & Kaner, R. B. Laser scribing of high-performance and flexible graphene-based electrochemical capacitors. *Science (New York, N.Y.)* **335**, 1326–30 (2012).
158. Zhang, L. L. *et al.* Highly conductive and porous activated reduced graphene oxide films for high-power supercapacitors. *Nano Letters* **12**, 1806–12 (2012).
159. Simon, P. & Gogotsi, Y. Materials for electrochemical capacitors. *Nature materials* **7**, 845–54 (2008).
160. Process, S., Cong, H., Ren, X., Wang, P. & Yu, S. Macroscopic Multifunctional Graphene-Based Hydrogels and Aerogels by a Metal Ion Induced. *ACS Nano* **6**, 2693–2703 (2012).
161. Chen, L.-F. *et al.* Flexible all-solid-state high-power supercapacitor fabricated with nitrogen-doped carbon nanofiber electrode material derived from bacterial cellulose. *Energy & Environmental Science* **6**, 3331 (2013).
162. Chen, L.-F., Huang, Z.-H., Liang, H.-W., Guan, Q.-F. & Yu, S.-H. Bacterial-cellulose-derived carbon nanofiber@MnO₂ and nitrogen-doped carbon nanofiber electrode materials: an asymmetric supercapacitor with high energy and power density. *Advanced materials* **25**, 4746–52 (2013).
163. Carbon, C. *et al.* High-Rate Electrochemical Capacitors Based on Ordered Mesoporous Silicon Carbide-Derived Carbon. *ACS Nano* **4**, 1337–1344 (2010).
164. Okahisa, Y., Yoshida, A., Miyaguchi, S. & Yano, H. Optically transparent wood–cellulose nanocomposite as a base substrate for flexible organic light-emitting diode displays. *Composites Science and Technology* **69**, 1958–1961 (2009).
165. Zhou, Y. *et al.* Recyclable organic solar cells on cellulose nanocrystal substrates. *Scientific reports* **3**, 1536 (2013).
166. Way, A. E., Hsu, L., Shanmuganathan, K., Weder, C. & Rowan, S. J. pH-Responsive Cellulose Nanocrystal Gels and Nanocomposites. *ACS Macro Letters* **1**, 1001–1006 (2012).

167. Biyani, M. V, Foster, E. J. & Weder, C. Light-Healable Supramolecular Nanocomposites Based on Modified Cellulose Nanocrystals. *ACS Macro Letters* **2**, 236–240 (2013).
168. Zhang, Y. P., Chodavarapu, V. P., Kirk, A. G. & Andrews, M. P. Structured color humidity indicator from reversible pitch tuning in self-assembled nanocrystalline cellulose films. *Sensors and Actuators B: Chemical* **176**, 692–697 (2013).
169. Khan, M. K., Bsoul, A., Walus, K., Hamad, W. Y. & MacLachlan, M. J. Photonic Patterns Printed in Chiral Nematic Mesoporous Resins. *Angewandte Chemie* **127**, 4378–4382 (2015).
170. Fernandes, S. C. M. *et al.* Bioinspired Antimicrobial and Biocompatible Bacterial Cellulose Membranes Obtained by Surface Functionalization with Aminoalkyl Groups. *ACS Applied Materials & Interfaces* **5**, 3290–3297 (2013).
171. Mahmoud, K. A., Lam, E., Hrapovic, S. & Luong, J. H. T. Preparation of Well-Dispersed Gold/Magnetite Nanoparticles Embedded on Cellulose Nanocrystals for Efficient Immobilization of Papain Enzyme. *ACS Applied Materials & Interfaces* **5**, 4978–4985 (2013).
172. Fu, L. *et al.* Skin tissue repair materials from bacterial cellulose by a multilayer fermentation method. *Journal of Materials Chemistry* **22**, 12349 (2012).
173. Saska, S. *et al.* Bacterial cellulose-collagen nanocomposite for bone tissue engineering. *Journal of Materials Chemistry* **22**, 22102 (2012).
174. Bäckdahl, H. *et al.* Mechanical properties of bacterial cellulose and interactions with smooth muscle cells. *Biomaterials* **27**, 2141–9 (2006).

CHAPTER 2. CELLULOSE NANOCRYSTALS VS. CELLULOSE NANOFIBRILS: A COMPARATIVE STUDY ON THEIR MICROSTRUCTURES AND EFFECTS AS POLYMER REINFORCING AGENTS*

2.1. Abstract

Both cellulose nanocrystals (CNCs) and cellulose nanofibrils (CNFs) are nanoscale cellulose fibers that have shown reinforcing effects in polymer nanocomposites. CNCs and CNFs are different in shape, size and composition. This study systematically compared their morphologies, crystalline structure, dispersion properties in polyethylene oxide (PEO) matrix, interactions with matrix, and the resulting reinforcing effects on the matrix polymer. Transparent PEO/CNC and PEO/CNF nanocomposites comprising up to 10 wt% nanofibers were obtained via solution casting. Scanning electron microscopy (SEM), wide-angle X-ray diffraction (WXR), transmission electron microscopy (TEM), Fourier transform infrared spectroscopy (FTIR), dynamic mechanical analyzer (DMA) and tensile testing were used to examine the above-mentioned properties of nanocellulose fibers and composites. At the same nanocellulose concentration, CNFs led to higher strength and modulus than did CNCs due to CNFs' larger aspect ratio and fiber entanglement, but lower strain-at-failure due to their relatively large fiber

* The content in this chapter was co-authored by Xuezhu Xu, Fei Liu, Long Jiang, JY Zhu, Darrin Haagenon and Dennis P Wiesenborn. Content in this chapter was published in ACS Applied Materials & Interfaces 03/2013; 5(8): 2999-3009. Xuezhu Xu had primary responsibility for performing the sample preparation and all of the tests. Assurances from Fei Liu and Darrin Haagenon on tensile test and FT-IR experimental evaluations were much acknowledged. Xuezhu Xu drafted and revised the manuscript. Long Jiang generated the idea and supervised the project.

agglomerates. The Halpin-Kardos and Ouali models were used to simulate the modulus of the composites and good agreements were found between the predicted and experimental values. This type of systematic comparative study can help to develop the criteria for selecting proper nanocellulose as a biobased nano-reinforcement material in polymer nanocomposites.

2.2. Introduction

Biobased materials have attracted immense research interest in recent years because of their great potential for producing a variety of high value products with low impact on the environment. Both cellulose nanocrystals (CNCs) and cellulose nanofibrils (CNFs) can be isolated from plant cell walls. The abundant availability of plant biomass and the superior mechanical properties of cellulose made nanocellulose including CNCs and CNFs a desirable reinforcing material for polymer nanocomposites.¹ Cellulose is a linear chain polysaccharide consisting of repeated β -(1 \rightarrow 4)-D-glucopyranose units. Hydroxyl groups are abundant on CNC and CNF surfaces, allowing potential hydrogen bonding and surface modifications.

CNCs (also called cellulose nanowhiskers) are needle-like cellulose crystals of 10 - 20 nm in width and several hundred nanometers in length. They are produced from various biological sources (e.g., bleached wood pulp, cotton, manila, tunicin, bacteria, etc.) often by strong acid hydrolysis.^{2,3} Acid treatments remove non-cellulose components and most amorphous cellulose from the source materials and produce high purity cellulose crystals. Therefore, CNCs are highly crystalline. CNCs have been incorporated as reinforcing agents into a wide range of polymer matrices such as poly(oxyethylene), poly(vinyl alcohol), natural rubber, starch and polyurethane.⁴⁻¹² CNFs form long flexible fiber networks with a fibril diameter similar to or larger than CNCs. CNFs can be produced by TEMPO-mediated oxidation (2,2,6,6-tetramethylpiperidine-1-oxyl radical), multi-pass high-pressure homogenization, enzymatic

hydrolysis^{13,14} or direct mechanical fibrillation.¹⁵ The morphologies and dimensions of CNFs can vary substantially, depending on the degrees of fibrillation and any pretreatment involved. CNFs contain amorphous cellulose and are not as highly crystalline as CNCs. Numerous studies have been carried out using various cellulosic fibers or fibrils for polymer reinforcement.^{16–26} These studies indicate that fibrils with smaller diameters and longer lengths exhibit stronger reinforcing effect. For example, Siqueira et al. compared the effects of CNCs and microfibrillated cellulose (MFC, average diameter ca. 50 nm) on the crystallization and mechanical properties of polycaprolactone (PCL) matrix. The authors find that CNCs act as a better nucleation agent for PCL than MFC due to the latter's entanglement and confinement effect which restricts the growth of PCL crystallites.²³ MFC imparts higher modulus to the composites than do CNCs for the same reason. However, MFC and CNCs were both shown to decrease the strength and strain-at-failure of PCL, with higher fiber contents leading to larger decrease.

Both MFC and CNFs have large aspect ratios and are expected to have some similarities as reinforcing materials; however, extended mechanical fibrillation imparts CNFs complex fibril networks and much thinner fibrils compared with MFC. It is of great interest to compare the performance of CNFs and CNCs as reinforcing materials for nanocomposites. In this study, we compared the effect of CNCs and CNFs on the mechanical and thermal dynamic properties of PEO to understand the contributions of their morphologies and dispersions to the properties of PEO nanocomposites. Experimentally measured mechanical properties were compared with theoretical predictions based on two mechanical models and correlated with the microstructures of the nanocomposites. Remarkable differences in the reinforcing effects between CNCs and CNFs were demonstrated and a microstructural explanation was provided. Different forms of cellulose nanofibers as reinforcement agents in polymer nanocomposites have

been intensively studied and great potential has been shown for their industrial applications. In spite of all previous studies, a greater clarity is needed on the reinforcing effects of different cellulose nanofibers. The results from this study show clear distinctions between short rigid CNCs and long relatively tough CNFs in terms of their reinforcing effects and mechanisms, thus providing a practical guidance for the development of polymer nanocomposites containing cellulose nanofibers. Novel applications of PEO/cellulose nanocomposites as water absorption and retention materials²⁷ and as solid-solid phase change materials for energy storage²⁸ can also benefit from this study.

2.3. Materials and methods

CNCs and CNFs derived from bleached dry lap eucalyptus pulp were kindly provided by the USDA Forest Service Lab. Their methods of production have been detailed elsewhere.^{15, 29} Briefly, CNCs were produced by sulfuric acid hydrolysis followed by repeated centrifugation²⁹ whereas CNFs were produced through a multi-pass high pressure grinding process using a SuperMassColloider (MKZA6-2, Masuko Sangyo Co., Ltd, Japan).¹⁵ The as-received CNCs and CNFs were in the forms of 5.7 wt% suspension and 1.8 wt% gel (both in water), respectively. PEO with a viscosity average molecular weight (M_v) of 1,000,000 was purchased from Sigma-Aldrich. PEO/CNC and PEO/CNF nanocomposite films were prepared by solution casting. PEO was first dissolved in deionized water to make a 4 wt% solution. Various amounts of CNC suspension or CNF gel were added to the solution to make mixtures comprising 0, 1, 4, 7 and 10 wt% of CNCs or CNFs (based on PEO solid weight). The mixtures were first homogenized using a homogenizer (IKA T25 digital Ultra-Turrax) at 1,000 rpm for 5 minutes at room temperature and then stirred using a magnetic stirrer at approximately 100 rpm at 60 °C for 12

hours. Nanocomposite films were obtained by casting the mixtures in glass Petri dishes and drying the casts in a vacuum oven at 80 °C for approximately 5 hours.

TEM was used to study the morphology of CNC and CNF fibers and their dispersion states in PEO matrix. TEM imaging was conducted on a JEOL JEM-2100 Lab6 operating at 200 kV. To prepare the CNC and CNF samples for TEM study, the CNC suspension and CNF gel were both diluted with distilled water. Specifically, 0.5 ml of the 5.7% CNC suspension was diluted 100 times in distilled water. A drop (accurate measurements were not allowed due to the high viscosity of the gel) of the 1.8% CNF gel was added to 0.5 mL of distilled water and manually stirred. A drop of each diluted sample was placed onto 300 mesh Formvar coated copper grids. Extra liquid was wicked off with filter paper. Samples were allowed to dry at room temperature and finally stained with 1% phosphotungstic acid (PTA) or iodine vapor to produce additional contrast. To study dispersion of CNCs and CNFs in the PEO matrix, drops of mixture solutions were deposited onto carbon-coated copper grids and allowed to dry at room temperature. The specimens were also stained with iodine vapor to enhance image contrast.

Wide angle X-ray diffraction (WAXD) measurements were performed using an X-Ray powder diffractometer (Philips X'Pert MPD) operating at 45 kV and 40 mA with a Cu K α X-ray source. Pure dry CNC and CNF films (prepared by vacuum drying of the as-received dispersion and gel) were scanned from 2.5~60° at a scanning speed of 0.05°/s.

Dynamic mechanical analysis (DMA) of composite films was conducted using a DMA Q800-0790 (TA Instruments) equipped with a film tension clamp. Test samples (12.74 × 6.29 mm²) were prepared using a die cutter. Tests were run from -100 to 20 °C (T_g of PEO: -48 °C) at a rate of 3°C/min. Oscillation amplitude of 20 μm (within linear range) and a preload force of 0.01 N were applied on all samples. At least three repeats were tested for each sample.

Differential scanning calorimetry (DSC) tests were conducted using a Q1000 from TA Instruments. Samples (2~6 mg each) were sealed in aluminum pans, tested under continuous nitrogen flow (50.0 ml/min), and scanned from 25 to 100 °C at a ramp rate of 10 °C/min.

A Fourier transform infrared (FTIR) spectrometer (Nicolet 6700) from Thermo Scientific was used to examine interactions between the nanofibers and the PEO matrix. Thirty-two repetitive scans with a resolution of 0.482 cm⁻¹ were performed on each sample.

Tensile tests were conducted using an Instron 5545 Tensile tester equipped with a 100 N load cell. Tensile specimens were cut using a dumbbell die with a width and length of 2 and 20 mm (narrow section of the die), respectively. The speed of testing was 20 cm/min. Ten specimens were measured for each sample to get an average value.

2.4. Results and discussion

2.4.1. Morphology and crystalline structure of CNCs and CNFs

CNCs and CNFs show substantially different shapes and sizes in TEM micrographs (**Figure 2.1**). CNCs present a simple needle-like structure with an average length (L) of 151 ± 39 nm, a width (w) of 19 ± 5 nm, and a resultant aspect ratio of L/w of 8 (based on 100 measurements from 5 micrographs). CNFs exhibit a complex, highly-entangled, web-like structure. Twisted/untwisted, curled/straight, and entangled/separate nanofibrils and their bundles with diameters ranging from 6 to 100 nm in diameter can be identified from the micrograph. The highly entangled structure of CNFs significantly increases resistance to flow and results in gel-like behavior of the as-received CNF sample. By contrast, the as-received CNC suspension shows much lower viscosity than the CNF sample even at higher fiber concentration (5.7 vs. 1.8 wt%) due to the former's low aspect ratio and lack of entanglement. Given CNFs' complex network morphology, it was difficult to measure the length and diameter of individual

CNF with high accuracy. Based on the individual CNF and bundles which could be clearly identified from the micrographs, CNFs show an average width and length of 20 ± 14 nm and 1030 ± 334 nm (based on 50 measurements from 4 micrographs), resulting in an aspect ratio of $L/w \geq 52$. Admittedly, the actual aspect ratio of CNFs in the composites might vary due to the existence of CNF bundles.

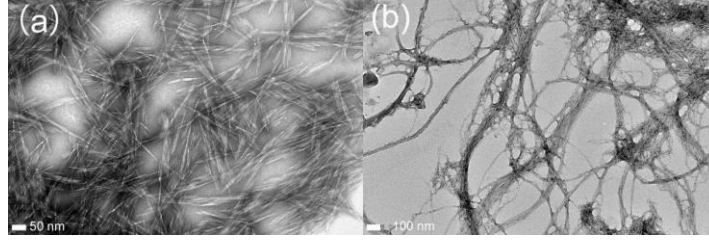


Figure 2.1. High resolution TEM images of CNCs (a) and CNFs (b).

X-ray diffraction patterns of CNCs and CNFs are compared in **Figure 2.2**. The XRD results including peak angle (2θ), d -spacing, full width at half maximum (FWHM), average crystal size (thickness) in the direction normal to the reflecting plane (L) and crystallinity index (CI) are summarized in **Table 2.1**. The crystal size was determined by the Scherrer Equation:³⁰

$$FWHM(2\theta) = \frac{K\lambda}{L \cos \theta} \quad (2.1.)$$

Where K is the Scherrer constant (0.89) and λ is the X-ray wavelength. CI of CNCs and CNFs can be determined based on XRD results using several different methods.³¹ Segal method allows rapid comparison of cellulose crystallinity and is commonly used in paper industry.³²

$$CI = \frac{I_{002} - I_{amorphous}}{I_{002}} \quad (2.2.)$$

Where I_{002} is the maximum intensity of the (002) diffraction and $I_{amorphous}$ is the intensity of amorphous diffraction, which is taken at 2θ angle between (002) and (101) peaks where the intensity is at a minimum. The second method separates amorphous and crystalline

diffractions and calculates the ratio of the crystalline diffraction to the overall diffraction as *CI* using MDI Jade 6.5 software (Materials Data, Inc.).³³

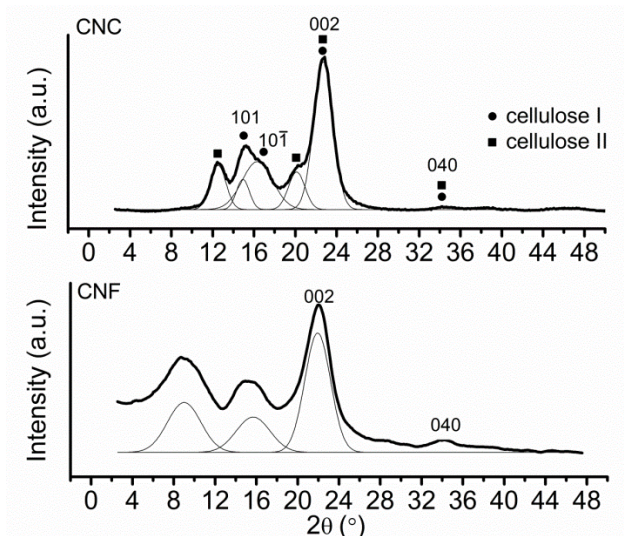


Figure 2.2. Wide angle X-ray diffraction patterns of CNCs and CNFs.

Table 2.1. XRD results of pure CNCs and CNFs.

	2θ	d (Å)	FWHM	L (Å)	CI (%)	(<i>Segal</i>)	CI (%) (<i>Jade</i>)
CNCs	12.5	7.1	0.996	35	81.0		95
	15.1	5.8	1.033	27			
	17.5	5.2	1.029	78			
	20.1	4.4	1.488	54			
	22.7	3.9	1.102	38			
	34.3	2.6	8.146	10			
CNFs	9.2	9.6	0.964	13	64.4		39
	14.9	6.0	1.370	15			
	22.4	4.0	1.135	29			
	33.9	2.6	1.984	42			

CNCs show diffraction peaks at 15.1° , 17.5° , 22.7° and 34.3° , representing cellulose I crystal planes (101), $(10\bar{1})$, (002) and (040), respectively.²⁵ Diffractions from cellulose II are also present in the CNC pattern at angles of 12.5° , 20.1° , 22.7° , and 34.3° .³⁴ The coexistence of cellulose I and cellulose II in CNCs is attributed to the alkali pulping and acid hydrolysis processes that CNCs experience during production. Alkali and acid treatments to natural fibers

transform cellulose I to cellulose II.^{34,35} XRD results of CNFs are surprisingly scarce in the literature. This study found that CNFs showed broadened and merged peaks, which also shifted to lower angles. Millett et al. found that the diffraction peaks of ball milled natural fibers were also shifted to lower angles with increasing milling time because of the superposition of the broadened crystalline diffraction peaks upon increasingly strong amorphous diffractions.³⁵ This is also the case in this study. The high pressure mechanical grinding used in CNF manufacturing could deform or even completely destruct cellulose crystals, leading to broadened and shifted diffraction peaks.²⁵

Crystallinity index (*CI*) values determined by both the Segal method and Jade software show that CNCs have higher crystallinity than CNFs, which is in agreement with the microstructures of the two nanofibers. However, the two methods show large differences in *CI* values, with the Jade software producing a larger value for CNCs and a lower value for CNFs. The differences are attributed to Segal method's over-simplicity and the resultant inaccurate results.³¹

2.4.2. Dispersion and percolation of CNCs and CNFs in PEO

The degree of transparency of the nanocomposite films indicates the status of dispersion of CNCs and CNFs. As shown in **Figure 2.3**, the PEO/CNC film was nearly optically transparent while the PEO/CNF film was translucent, indicating CNCs' smaller nanoparticle sizes and better dispersion. A closer observation showed that PEO/CNCs exhibits higher transparency than does PEO/CNFs, most likely due to CNCs' smaller sizes and lack of agglomeration and entanglement. This property is advantageous to optical applications where several common nanocomposites (e.g. carbon and clay naocomposites) can't be used because of their lack of transparency.



Figure 2.3. PEO/CNF and PEO/CNC nanocomposite films at room temperature. CNF and CNC concentration: 7%.

CNCs are seen homogeneously dispersed in the PEO matrix without signs of fiber aggregation (**Figure 2.4a**). No obvious CNC percolation network is found in the composites. At a higher magnification (**Figure 2.4b**), elementary cellulose crystallites with multi-layer structures are clearly identified. The structures showed an overall average thickness of approximately 3.6 nm, an average dark layer thickness of 0.386 nm and an average light layer thickness of 0.173 nm. The thickness of one dark layer and one light layer comprised a d-spacing of 0.559 nm. Very recently, Liu et al showed a similar structure and indicated that the structure represents cellulose crystal lattice fringes.²⁶ The cellulose elementary crystallites were reported to have a cross-sectional size of 3~5 nm,³⁶ which matches the measured overall thickness of the multi-layer structure in this study. The larger average width of CNCs than the multilayer structure thickness (19 nm compared to 3.6 nm) indicates that most CNCs contain more than one laterally-aggregated elementary cellulose crystallite.³⁷

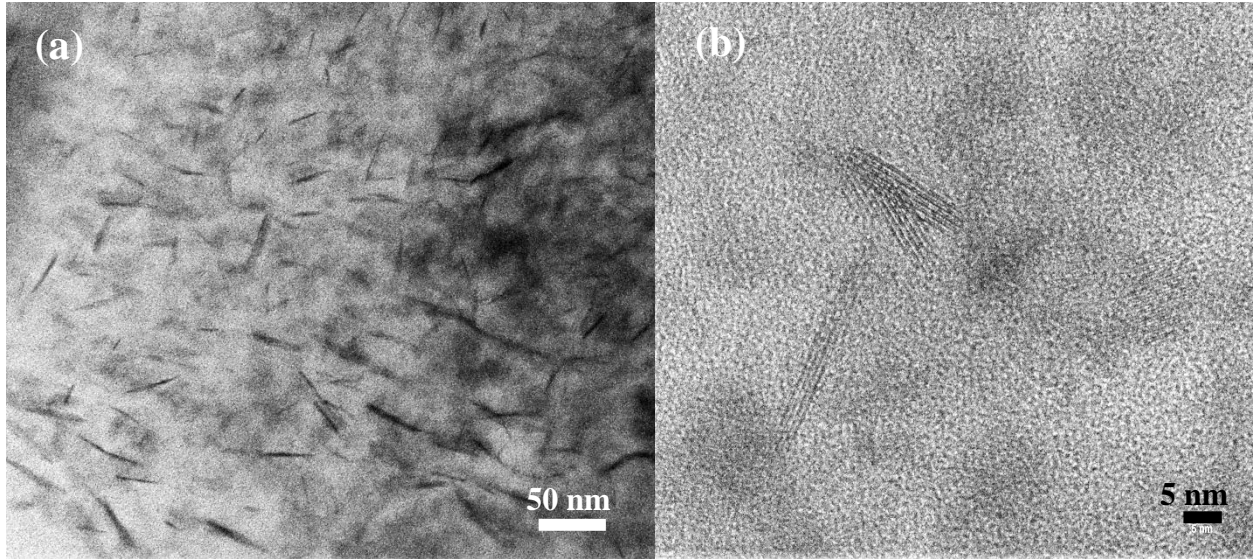


Figure 2.4. TEM images of PEO/CNC (7%) nanocomposite film (a) and CNC crystallites (b).

CNFs maintained their entangled fibril structure in the PEO matrix (**Figure 2.5**). An average fibril width of 20 nm was estimated based on the micrographs. The grinding process produced CNFs with a wide width distribution, ranging from a single elemental fibril (~6 nm) to nanofibrils (~100 nm) as shown in **Figure 2.5b**. CNF fibril length also varied substantially, with both long (**Figure 2.5a and 5d**) and short (**Figure 2.5b and 5c**) fibrils clearly seen. Additionally, CNF entanglements and network structure throughout the matrix are evident in the Figures. These entanglements play an important role in the force transferring from matrix to fibrils and from fibrils to fibrils. CNF aggregates can also be seen in **Figure 2.5a and 5d**.

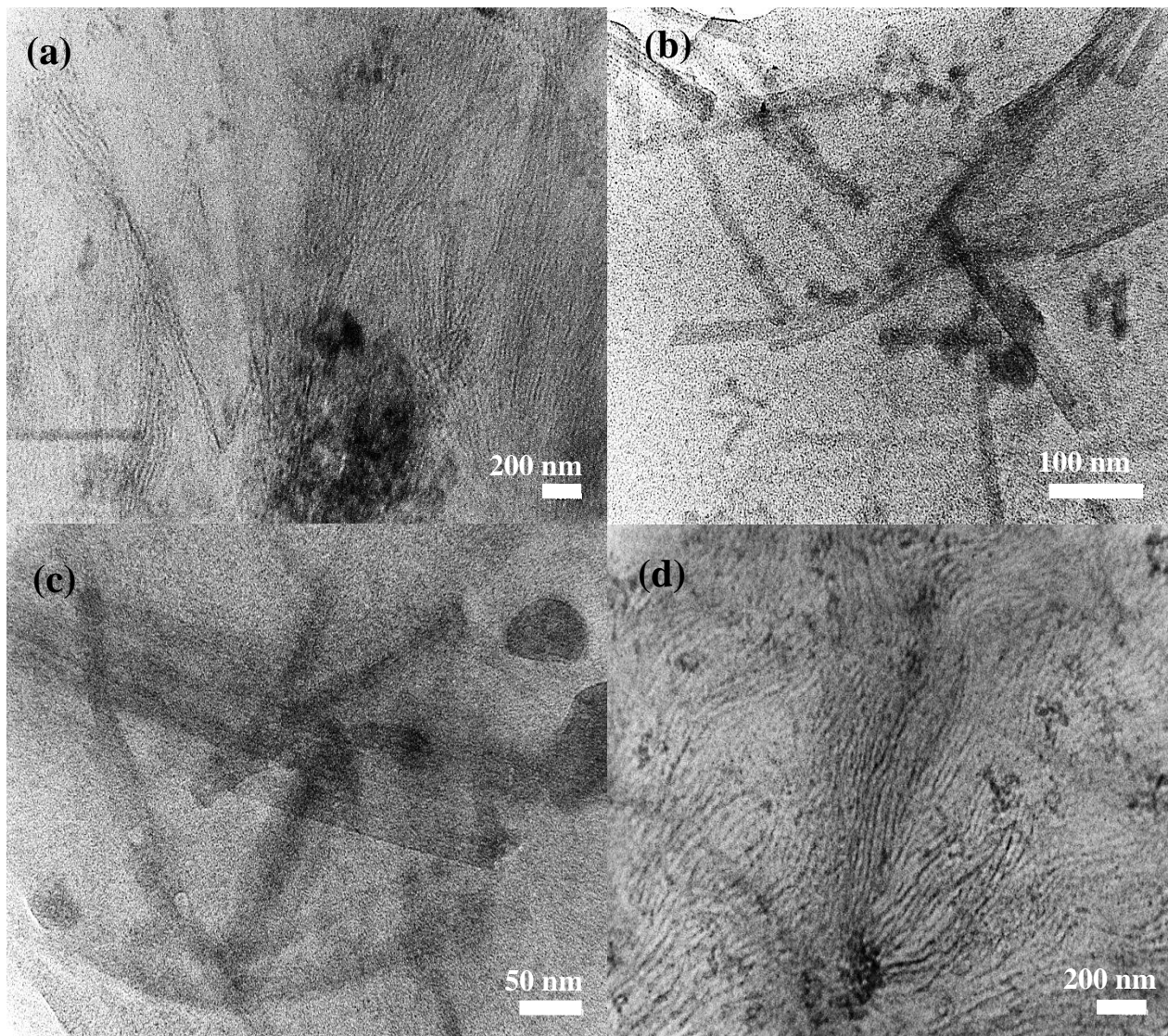


Figure 2.5. TEM images of PEO/7 wt% CNFs (a-c) and PEO/10 wt% CNFs (d).

2.4.3. FT-IR

FT-IR was used to evaluate the hydrogen bonding interaction between CNCs (or CNFs) and the PEO matrix. **Figure 2.6** shows the FT-IR absorption spectra in the hydroxyl stretching region ($3500 - 3000 \text{ cm}^{-1}$). Pure PEO exhibits a broad stretching peak centered at 3435.5 cm^{-1} . The stretching peaks for pure CNCs and CNFs are much sharper and stronger, indicating higher densities of the hydroxyl groups on the surfaces of CNCs and CNFs. Four

individual minor peaks are identified from CNCs' spectrum, i.e., 3486.0, 3439.4, 3331.1 and 3287.1 cm^{-1} . The former two peaks are ascribed to intramolecular hydrogen bonding and the latter two to intermolecular hydrogen bonding.^{38,39} These minor peaks are not as obvious on the spectrum of CNFs. Instead, a bump at 3427.8 cm^{-1} and two weak peaks at 3283.7 and 3323.3 cm^{-1} can be seen in **Figure 2.6** For both PEO/CNC and PEO/CNF composites, the stretching peaks shift to higher frequencies with increasing CNC or CNF contents, indicating the effects of the cellulose nanofibers on the PEO matrix through hydrogen bonding. For example, the 3331.1 cm^{-1} peak of pure CNCs shift to 3336.3 and 3338.3 cm^{-1} for the 7 and 10 wt% PEO/CNC composites, respectively. Similarly, the 3283.7 cm^{-1} peak of pure CNFs shifts to 3340.1 and 3343.1 cm^{-1} for the PEO/CNF composites. The larger shift on the PEO/CNF composites may indicate stronger hydrogen bonding between PEO and CNFs than between PEO and CNCs. Many hydroxyl groups on CNCs were replaced with SO_3^- during sulfuric acid hydrolysis and thus the potential for hydrogen bonding is reduced. The significant decrease of the intensity on the 3287.1 cm^{-1} (for CNCs) and 3323.3 cm^{-1} (for CNFs) peaks also shows their strong interactions with the PEO matrix.

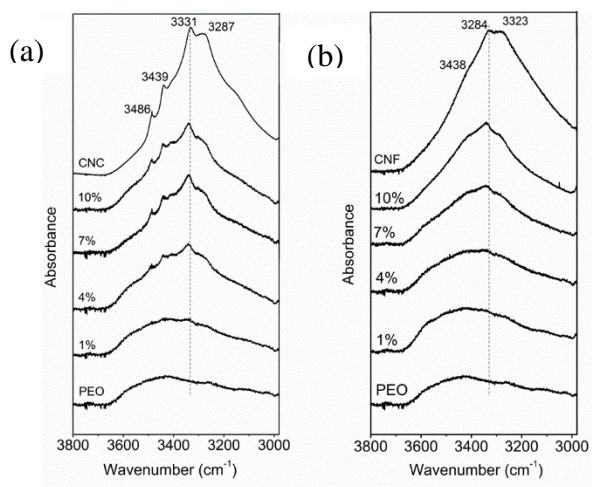


Figure 2.6. FT-IR spectra in the region of hydroxyl stretching for PEO/CNC (a) and PEO/CNF (b) composites with various nanofiber contents.

The peak at 957 cm^{-1} on the spectrum of pure PEO is attributed to CH_2 rocking and influenced by C-O-C stretching (**Figure 2.7**).⁴⁰ Neither CNCs nor CNFs show similar peaks at this region. However, the presence of CNCs or CNFs in the PEO/CNC or PEO/CNF nanocomposites upshifts the peak by approximate 5 cm^{-1} . Changes in the intensity ratio of 1143 cm^{-1} to 1096 cm^{-1} are also observed. The two peaks belong to the characteristic triplet of PEO (i.e., 1143 , 1096 and 1059 cm^{-1}), which is assigned to C-O-C stretching.⁴¹ The intensities and frequencies of the triplet are influenced by the crystallinity of PEO and the intermolecular interactions (e.g., hydrogen bonding) between C-O-C and other materials.^{42,43} C-O-C is a proton acceptor and can form hydrogen bonding with proton donors such as OH groups on CNCs and CNFs. Therefore, the change in the intensity ratio indicates that hydrogen bonding is established between PEO and CNCs (or CNFs). The perturbed C-O-C stretching subsequently causes the upshift of the CH_2 rocking peak.

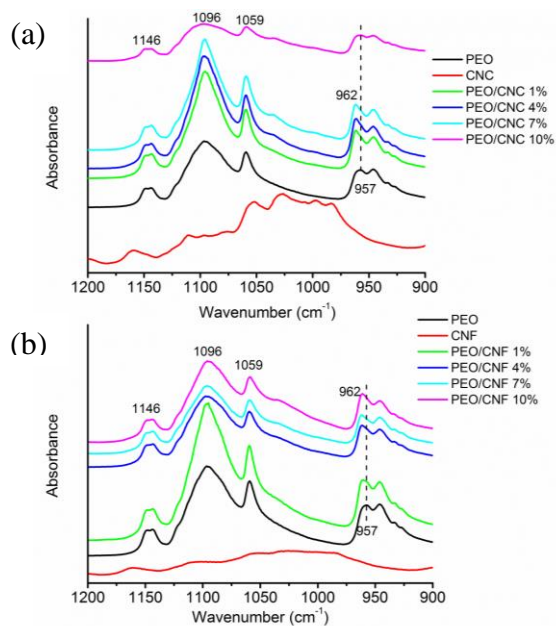


Figure 2.7. FT-IR spectra for PEO/CNC (a) and PEO/CNF (b) composites with various nanofiber contents..

2.4.4. DSC

Melting points (T_m), heat of fusion (ΔH_m), and crystallinity of all the samples are listed in **Table 2.2**. Neat PEO shows the highest values in all the three properties. The decreases in the polymer melting point and crystallinity after the addition of CNCs have been observed in poly(3-hydroxybutyrate-co-3-hydroxyvalerate)/CNC composites.⁴⁴ Similar results have also been reported for PEO/bacterial cellulose composites.⁴⁵ The reason is ascribed to the confinement effects of the nanoparticles, which hinders chain diffusion and folding at the crystal growth front and results in thin spherulite lamellar thickness.^{44,45} The strong interactions between PEO and CNCs also thermodynamically contribute to the melting point depression of PEO.⁴⁵

Table 2.2. Melting characteristics of neat PEO, PEO/CNCs and PEO/CNFs.

Filler	Content (wt%)	T_m (°C)	ΔH_m (J/g)*	Crystallinity (%)
CNCs	0	71.2	154.5	82
	1	66.9	144.8	77
	4	66.8	145.9	78
	7	67.4	137.6	73
	10	69.2	134.3	71
CNFs	1	70.7	139.3	74
	4	66.8	149.3	79
	7	66.8	145.7	77
	10	69.9	130.3	69

* ΔH_m is based on PEO weight. Heat of fusion of 100% crystallinity PEO is 188 J/g.^{46,47}

2.4.5. DMA

Loss tangents ($\tan \delta$) of PEO/CNCs and PEO/CNFs as a function of temperature are shown in **Figure 2.8 and 9**, respectively. Pure PEO shows a peak at approximately -48 °C (intensity 0.09), which is attributed to its glass transition (**Figure 2.8**). The peak shifts to higher temperature and the peak intensity is reduced in all PEO/CNC nanocomposites. For instance, $\tan \delta$ of PEO/CNCs at 4 wt% CNC loading peaks at approximately -42 °C with an intensity of 0.07,

which is 6 °C higher in temperature and 0.02 lower in $\tan \delta$ compared to the pure PEO. A similar trend is also observed in PEO/CNF nanocomposites as shown in **Figure 2.9**. The PEO/CNFs comprising 4 wt% CNFs shows a $\tan \delta$ peak of 0.06 at $\sim -40^\circ\text{C}$, 0.03 lower in $\tan \delta$ and 8°C higher in temperature than the pure PEO.

$\tan \delta$ is a measurement of viscoelastic damping of materials. The lower $\tan \delta$ after the addition of CNCs or CNFs indicates that the composites become more elastic and less energy is dissipated during mechanical vibrations. This is due to the presence of CNCs or CNFs in the PEO matrix which substantially restrains PEO chain segment movements through fiber-matrix interfacial actions and fiber-fiber interactions including physical fiber network structures at high fiber concentrations. The strong interfacial action (hydrogen bonding in this case as shown by FTIR results) is evident from the increases in PEO glass transition temperature. PEO chains are tethered to the surfaces of CNCs or CNFs through multiple hydrogen bonding sites and therefore more energy is required to achieve the same level of chain segment movement in the composites than in the pure PEO. A similar glass transition temperature (T_g) trend is also found in tunicin whiskers reinforced cross-linked polyether and lithium imide (LiTFSI) nanocomposites.⁴ The larger shift in glass transition temperature and $\tan \delta$ intensity demonstrated by PEO/CNFs indicates CNFs' bigger influence on the matrix than CNCs due to the former's stronger physical confinement effects²³ and more intensive hydrogen bonding interactions with the matrix. Glass transition temperature is also influenced by polymer crystallinity because the crystalline phase constrains mobility of the amorphous phase. However, the glass transition temperature increase in this study is not due to this reason because the crystallinity of PEO is reduced after the addition of the cellulose nanoparticles.

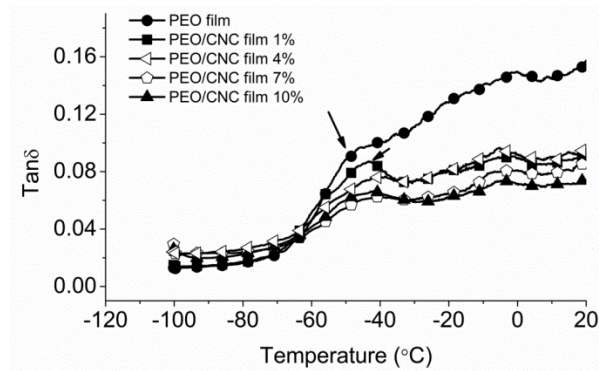


Figure 2.8. $Tan \delta$ of PEO/CNC nanocomposite films. The arrows point to the glass transition temperature (T_g) of pure PEO and the composites.

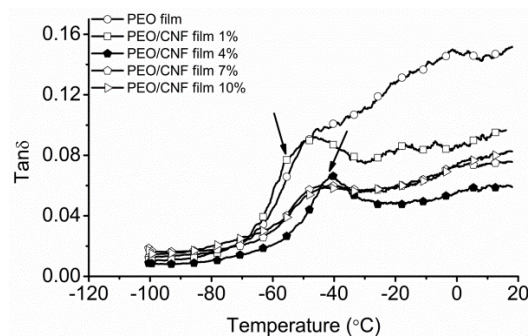


Figure 2.9. $Tan \delta$ of PEO/CNF nanocomposite films. The arrows point to the glass transition temperature (T_g) of pure PEO and the composites.

2.4.6. Mechanical reinforcing effects of CNCs and CNFs

The nanoscale dimensions and high mechanical properties of CNCs and CNFs make them ideal for polymer reinforcement. Representative stress-strain curves for PEO/CNC and PEO/CNF composite films are plotted in **Figures 2.10** and **2.11**, respectively. Pure PEO shows a ductile fracture with a strain-at-failure of ca. 90%. The horizontal section of the curves in **Figures 2.10** and **2.11** clearly demonstrates PEO's yielding behavior. After adding CNCs to the polymer, the strain range within which the yielding occurs is significantly expanded and an additional section of strain hardening (i.e. stress increased with strain) emerges (**Figure 2.10**). The addition of CNFs also leads to increases in strain-at-failure (smaller compared to CNCs) and the occurrence of strain hardening of the composites with various fiber concentrations (**Figure**

2.11). Most importantly, even at 1 wt% of CNCs or CNFs content, the yielding and strain hardening are increased by approximately five fold for both the PEO/CNC and PEO/CNF composites (**Figures 2.10** and **2.11**).

Young's modulus, yield strength, stress-at-failure, strain-at-failure and fracture toughness of the samples were obtained from the curves and are summarized in **Table 2.3**. These mechanical properties exhibit a general trend: The properties increase and then decrease as nanocellulose content increases. The optimal content appears at 7% for both CNCs and CNFs. In **Table 2.3**, the nanocomposite comprising 7 wt% CNCs shows a Young's modulus of ca. 937 MPa, yield strength of 17.6 MPa, stress-at-failure of 18.4 MPa and strain-at-failure of 526%, which are 23%, 124%, 44%, and 512% higher than those of pure PEO film respectively. The composite comprising 7 wt% CNFs shows even higher mechanical reinforcement (an increase of 127%, 192% and 110% in modulus, yield strength, and stress-at-failure, respectively) but lower strain-at-failure increase (295%). Even at 1% substitution, the increases in these mechanical properties are significant. The increases in tensile strength and modulus are attributed to CNFs and CNCs' high mechanical properties and their strong interactions with the PEO matrix as demonstrated in FTIR and DMA results. PEO crystallinity is excluded as the possible reason for the enhancement because the crystallinity was reduced after the addition of the nanocellulose. The decreases in properties at high nanocellulose concentration (10%) are presumed to be caused by nanocellulose agglomerations that could be clearly seen in the TEM micrograph (**Figure 2.5d**).

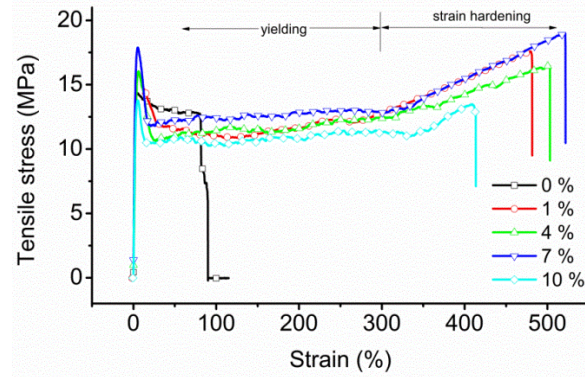


Figure 2.10. Tensile stress-strain curves for pure PEO and PEO/CNC films with 1%, 4%, 7%, and 10% CNCs.

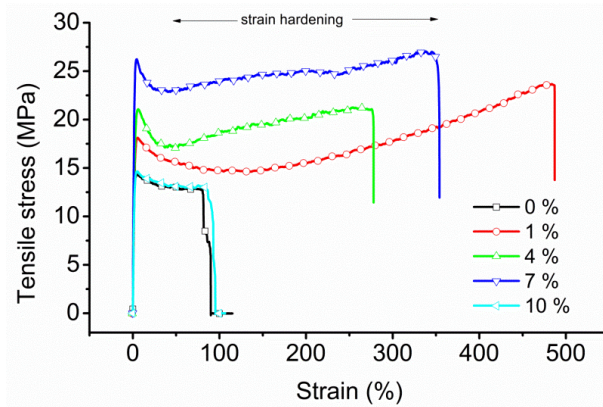


Figure 2.11. Tensile stress-strain curves for pure PEO and PEO/CNF films with 1%, 4%, 7%, and 10% CNFs.

Table 2.3. Mechanical properties of PEO/CNC and PEO/CNF nanocomposite films.

Filler	Content (wt%)	Young's modulus (MPa)	Yield strength (MPa)	Stress-at-failure (MPa)	Strain-at-failure (%)	Toughness (kJ/m ³)
CNCs	0	760±109	14.2±0.9	12.8±0.4	86±14	1161±20
	1	820±195	15.9±0.1	16.9±2.1	495±43	6157±573
	4	895±141	16.0±0.8	16.2±1.3	504±34	6371±618
	7	937±150	17.6±0.7	18.4±2.0	526±40	7083±686
	10	758±326	15.3±0.2	13.8±1.7	416±43	4750±705
CNFs	1	896±99	17.7±0.9	23.0±1.0	491±21	8267±277
	4	994±222	20.8±0.7	20.9±1.7	281±56	5898±539
	7	1727±102	27.3±0.9	26.9±1.7	340±62	9662±112
	10	1235±99	14.4±0.5	16.4±6.7	89±55	1648±300

It is also worth noting that in **Figure 2.10** the strain hardening of all the PEO/CNC samples starts at ca. 300% strain, while in **Figure 2.11** the hardening starts at much lower strains for PEO/CNF samples, with higher CNF concentration appearing to cause lower starts. Strain hardening occurred because CNCs or CNFs were expected to be increasingly aligned along the tensile direction during sample elongation and thus they were able to carry larger share of the load exerted on the samples. The stresses of the samples are therefore increased. Pure PEO does not show this behavior due to its lack of the reinforcing cellulose fibers. In addition, the large aspect ratio of CNFs and their entanglements, which assists in fiber-matrix and fiber-fiber load transfers,⁴⁵ also facilitates the early occurrence of the strain hardening of PEO/CNF samples.

The increases in strain-at-failure after the various substitution ratios of CNCs or CNFs are significant. In fiber reinforced polymer composites, the general trend is that strength and modulus of the composites are increased and strain-at-failure is decreased with fiber substitution. Reinforcement fibers are more rigid than their polymer matrixes and fracture at a lower strain compared to the matrixes. Their fractures not only create cracks throughout the composites but also shift the load that is originally carried by the fibers to the matrixes, which leads to swift matrix failure. Nanoparticles such as clay and calcium carbonate have been found to increase tensile strain of brittle polymer polylactic acid (PLA).^{48,49} The main mechanism behind this toughening effect is attributed to interfacial debonding induced plastic deformation of the matrix polymer. Interfacial debonding releases strain constraints on the matrix polymer and lowers its plastic resistance, which allows plastic deformation to occur under suitable stress levels. In a study by Jiang et al, pure PLA showed a smooth fracture surface with little sign of plastic deformation whereas the nanoparticle filled PLA showed abundant PLA fibrils being pulled out

from the fracture surface as a result of plastic deformation.⁴⁹ A similar contrast was observed between pure PEO and CNC or CNF filled PEO in this study as discussed in detail below.

2.4.7. Study of fracture surfaces

Tensile samples of pure PEO, PEO/CNCs, and PEO/CNFs changed from transparent to white materials with increasing strain during the tests. The white color is a result of light diffraction from the numerous crazes throughout the materials that are induced by the tensile stress. It is possible that CNCs and CNFs in the composites nucleate crazes at their surfaces through interfacial debonding. An example of the crazes on the side surface of pure PEO is shown in **Figure 2.12a**. The fracture surface of pure PEO shows signs of plastic deformation (e.g. rough and irregular surfaces, voids and dimples, and pull-out fibrils) (**Figure 2.12b**), which are in agreement with its ductile fracture as demonstrated by its stress-strain curve. The fracture surfaces of PEO/CNCs and PEO/CNFs exhibits intensive fibrillation as shown in **Figures 2.13a and 14a**, respectively. Nanofibrils of less than 50 nm diameter are evident in **Figures 2.13b and 14b**. These fibrils bridge the crazes throughout the samples, which contributes to the increased tensile strength and strain-at-failure. The composition of these nanofibrils remains unclear at this stage. They may be pure CNC (or CNF) bundles, pure PEO nanofibrils, or most likely CNC (or CNF) fibers (or bundles) with PEO sheaths. It appeared through FE-SEM observation that PEO/CNF samples showed a larger population of the bridging nanofibrils than did PEO/CNCs, which were possibly ascribed to CNFs' inter-fiber entanglements and much larger aspect ratio. **Figure 2.15** illustrates the failure mechanisms of PEO when it is reinforced by CNCs and CNFs, respectively. Due to CNFs' larger lengths and higher flexibility, one CNF fibril could bridge a craze at multiple locations. The long lengths, network structures, and entanglements with

connecting fibrils facilitates the formation of a large population of visible pullout nanofibrils and fibril interlocking (**Figure 2.14c**) on the fracture surfaces of PEO/CNFs.

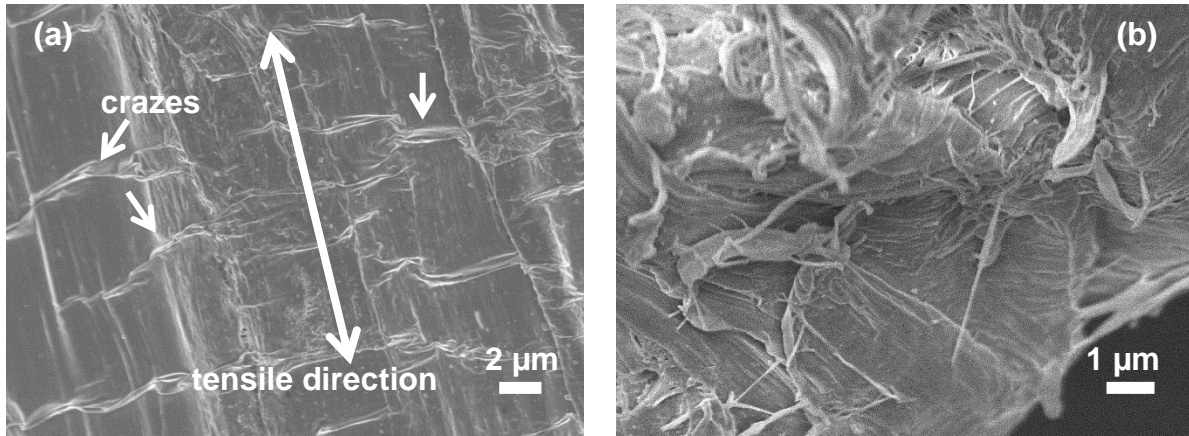


Figure 2.12. Side (a) and fracture (b) surfaces of pure PEO film.

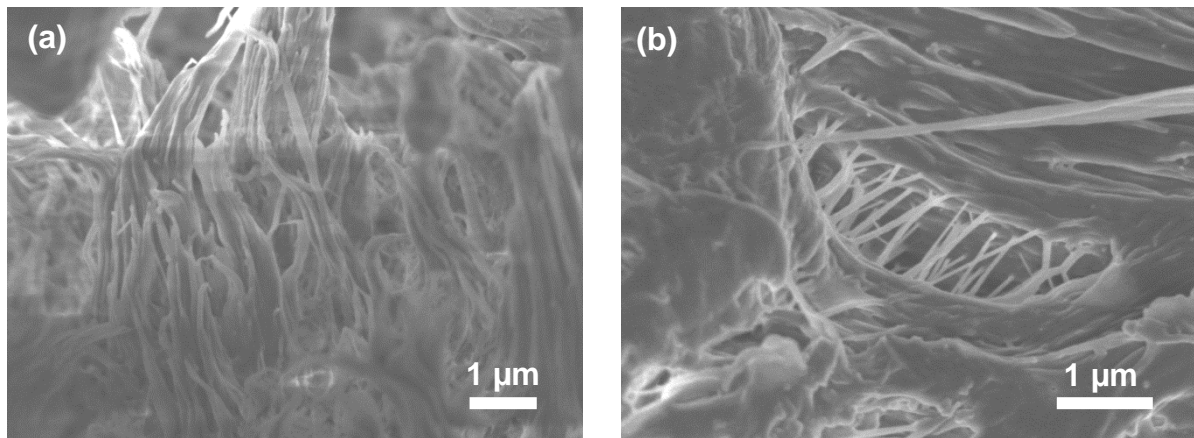


Figure 2.13. Fracture surfaces of PEO/CNC nanocomposite film with 7 wt% CNCs. The long arrow indicates the tensile load direction; the short arrows point to the crazes generated on the film surfaces after tensile tests.

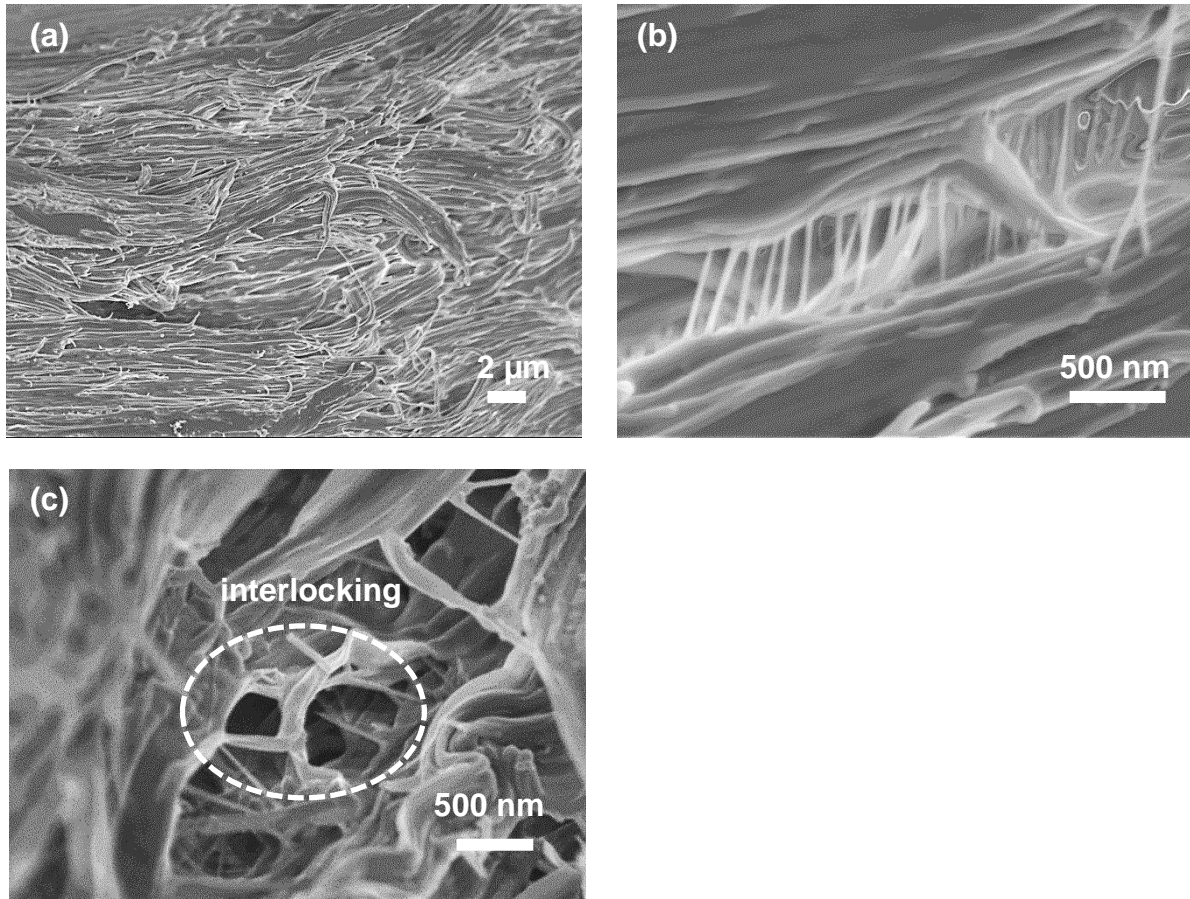


Figure 2.14. Fracture surfaces of PEO/CNF nanocomposite film with 7 wt% CNFs. Details circled by the ellipse indicate the interlocking between fibrils at the fracture surface.

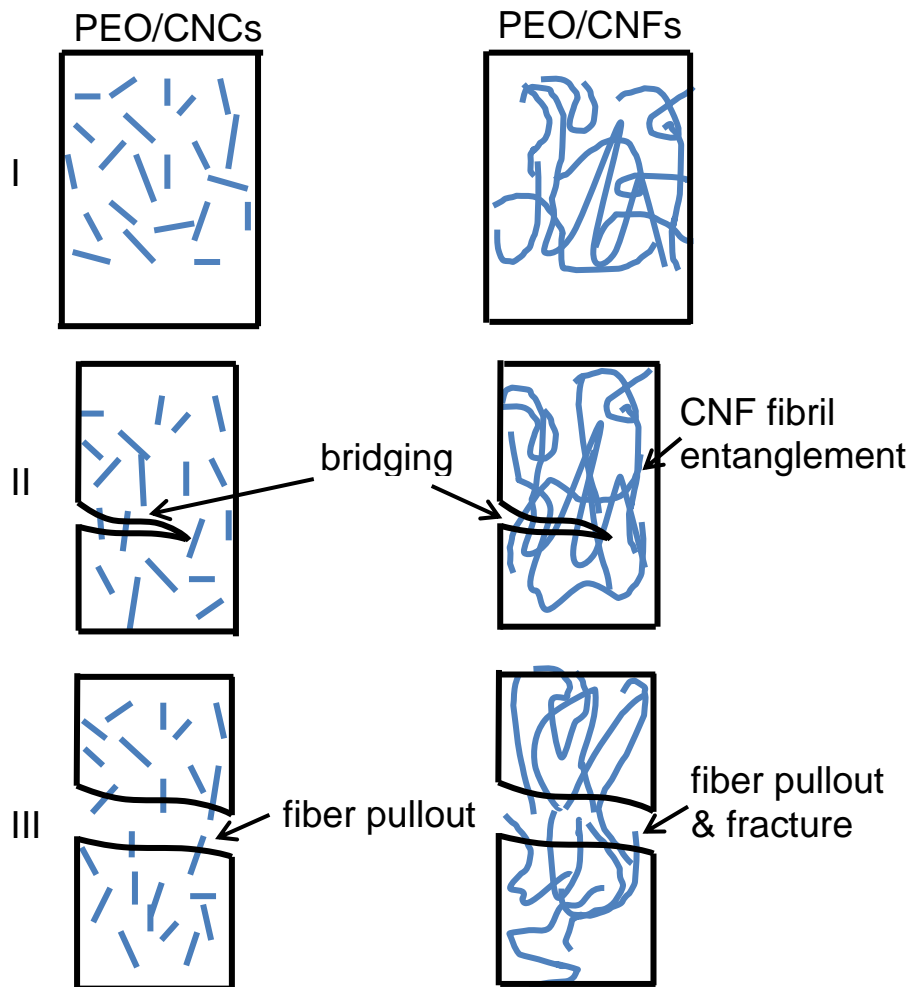


Figure 2.15. Illustrations of fracture mechanisms of PEO/CNC and PEO/CNF nanocomposites.

Siqueira et al. found increased modulus in PCL/CNC and PCL/CNF composites. The composites also showed decreases in strength and strain-at-failure after the addition of the nanofibers.²³ The authors ascribed the decreases to poor fiber-polymer interfacial adhesion and material defects due to fiber agglomerations. The increases in strength and strain-at-failure in this study resulted from the strong hydrogen bonding between PEO and the nanofibers and the relatively homogeneous dispersion of the fibers due to the strong interaction. Because of their increased strength and strain-at-failure, fracture toughness (the area below the stress-strain curves) of the PEO/CNC and PEO/CNF nanocomposites comprising 7 wt% cellulose nanofibers were 610% and 832% larger, respectively, than that of pure PEO.

2.4.8. Mechanical property modeling

The Halpin-Kardos model and the Ouali model were used to simulate the moduli of the composites and their results were compared with the experimental values. The Halpin-Kardos model is a semi-empirical model for oriented short fiber composites:⁵⁰

$$E_{\parallel} = E_m \frac{1 + \eta_{\parallel} \zeta \varphi_f}{1 - \eta_{\parallel} \varphi_f} \quad (2.3.)$$

$$E_{\perp} = E_m \frac{1 + 2\eta_{\perp} \varphi_f}{1 - \eta_{\perp} \varphi_f} \quad (2.4.)$$

where,

$$\eta_{\parallel} = \frac{\frac{E_f}{E_m} - 1}{\frac{E_f}{E_m} + \zeta} \quad (2.5.)$$

$$\eta_{\perp} = \frac{\frac{E_f}{E_m} - 1}{\frac{E_f}{E_m} + 2} \quad (2.6.)$$

where E_{\parallel} and E_{\perp} are the longitudinal and transverse Young's modulus of the unidirectional composite, φ_f is the fiber volume fraction, E_m is the Young's modulus of the matrix, and E_f is the modulus of the fiber. ζ is a shape factor dependent on fiber geometry and orientation. Different equations have been proposed to calculate ζ . Equation $\zeta = 2L/w$ is used for relatively short fibers such as CNCs.^{51,52} Equation $\zeta = (0.5L/w)^{1.8}$ is proposed by Van Es for high aspect ratio fibers.⁵³ The modulus of a 3D randomly oriented composite (E_C) can be calculated based on the laminate theory:⁵³

$$E_C = 0.184E_{\parallel} + 0.816E_{\perp} \quad (2.7.)$$

The Ouali model is based on the percolation theory and is an extension of the phenomenological series-parallel model proposed by Takayanagi.^{54,55,56} The Ouali model

simulates polymer composites using three phases: matrix, percolating filler network, and non-percolating filler phase. The model is given by the following equation:

$$E_c = \frac{(1 - 2\psi + \psi\varphi_f)E_m E_f + (1 - \varphi_f)\psi E_f^2}{(1 - \varphi_f)E_f + (\varphi_f - \psi)E_m} \quad (2.8.)$$

where the subscripts f and m refer to the filler and matrix phases, φ_f is the volume fraction of the filler, and E is the modulus. ψ denotes the volume fraction of the percolating filler network and is obtained from:

$$\psi = 0 \quad (2.9.)$$

$$\varphi_f \leq \varphi_c \quad (2.10.)$$

$$\psi = \varphi_f \left(\frac{\varphi_f - \varphi_c}{1 - \varphi_c} \right)^b \quad (2.11.)$$

$$\varphi_f > \varphi_c \quad (2.12.)$$

where b is the critical percolation exponent and a value of 0.4 is used for a three-dimensional network.^{54,55} φ_c is the critical percolation threshold (volume fraction):⁵⁷

$$\varphi_c = 0.7/(L/w) \quad (2.13.)$$

where L and w are the length and diameter of the filler, respectively. φ_c for CNCs and CNFs were calculated to be 8.75 and 1.35 vol% (12.7 and 1.8 wt%), respectively, when using PEO density of 1.2 g/cm³ and CNC (or CNF) density of 1.59 g/cm³. The modulus of PEO (E_m) was taken as 760 MPa based on the tensile results. The modulus of CNCs varies considerably (50–200 GPa) depending on the methods used to measure the property, types of cellulose (i.e. cellulose I or II), and the ratio between the two cellulose.^{58–60} The modulus of CNFs is scarce in literature. A value of 78 ± 17 GPa was obtained for a single bacterial cellulose nanofibril using an atomic force microscopy tip bending method.⁶¹ Based on the modulus of wood-derived CNF films (30 GPa),⁶² values of 90 and 80 GPa can be obtained for a single nanofibril using the

efficiency factors proposed by Cox⁶³ and Krenchel,⁶⁴ respectively. Most recently, using Raman spectroscopy the effective moduli of single fibrils of bacterial cellulose and CNFs were estimated to be ~84 and ~33 GPa, respectively.⁶⁵ In this study, a value of 145 GPa for CNCs⁶⁰ and 78 GPa for CNFs were used for theoretical modeling.

The experimental moduli of PEO/CNCs and PEO/CNFs and the simulation results based on the Halpin-Kardos and Ouali models are compared in **Figure 2.16**. Within the range of experimental nanofiber contents, the Halpin-Kardos model gives a close prediction of the moduli of the PEO/CNC composites. The Ouali model on the other hand underpredicts the moduli. For the PEO/CNF composites, both models predict the moduli with reasonable accuracy. The percolation model appeared to be able to capture the modulus jump after the CNF content exceeded φ_c .⁵² However, the theoretical φ_c which depends on L and w of CNFs deviated from its experimental value (**Figure 2.16**). This are probably attributed to two main errors. First, the values of L and w are estimated based on the CNFs dispersed in water. The CNFs in the PEO matrix could have more severe aggregations than in water due to the PEO solution's higher viscosity and weaker hydrogen bonding with the fiber. Second, the mechanical dispersion steps used to mix PEO and CNFs could also change the sizes of CNFs. Both errors could result in a reduced CNF aspect ratio and thus increase φ_c as demonstrated by the experimental moduli. Admittedly, a larger fiber content range is required to better compare the accuracy of the two models, especially for the results of the PEO/CNF composites. Nevertheless, the range is limited within 10 wt% in this study because fiber agglomerations occur when the fiber content exceeds 7 wt%.

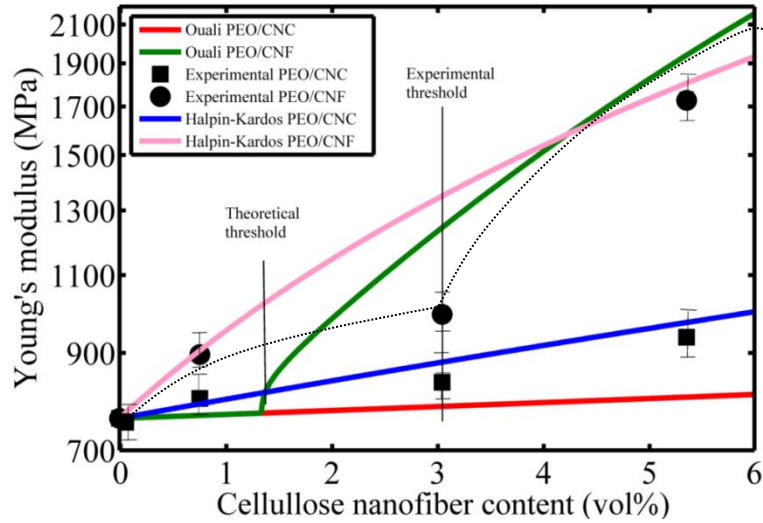


Figure 2.16. Young's modulus as a function of cellulose nanofiber content: experimental values vs. model predictions. $\zeta = 2L/w$ and $\zeta = (0.5L/w)^{1.8}$ are used for PEO/CNCs and PEO/CNFs, respectively, in the Halpin-Kardos model.

The Halpin-Kardos model is based on self-consistent theory by considering a single fiber encased in a cylindrical shell of matrix.⁴⁹ Interactions between fibers are not considered in this model. Takayanagi developed a phenomenological model to calculate the modulus of a multi-phase polymer system by symbolizing the system with serial/parallel phases. Ouali extended the Takayanagi model by adding a percolating filler network phase (in parallel) to a series part comprising a matrix phase and a nonpercolating filler phase.⁵⁴ When the volume ratio of filler exceeds its percolation threshold, filler-filler interactions are taken into account through the percolating filler phase in Ouali's model. Both Halpin-Kardos and Ouali models assume perfect filler-matrix bonding. Our results show that the Halpin-Kardos model is accurate for short fiber composites (i.e., PEO/CNCs) whose filler-filler interactions are negligible (i.e., filler concentration below percolation threshold). It fails to capture the modulus jump in long fiber composites (i.e., PEO/CNFs) above the filler percolation threshold because filler-filler interactions are not considered in this model. In contrast, the Ouali model predicts the trend of the modulus of PEO/CNFs. One may expect that the Ouali model provides higher prediction

accuracy than does the Halpin-Kardos model when the fiber concentration exceeds the tested range. The difference in the prediction results highlights the importance of filler-filler interactions to the properties of the composites containing high concentrations of fillers.

In **Figure 2.16** both model predictions and experimental values show that CNFs lead to higher composite moduli than do CNCs at the same fiber contents. This is mainly due to CNFs' larger aspect ratio as evidenced by the model equations. The extensive CNF fiber entanglements and percolation networks which are cemented together through hydrogen bonds and mechanical interlocking in the PEO matrix also contributes to the high moduli. These results have important implications in developing new polymer composites. The high strength and modulus of short fibers are often underused because their aspect ratios are too small to enable a full scale stress transfer from the matrixes to the fibers.⁶⁶ As a result, long fibers with relatively low strength and modulus can outperform short high-strength fibers in reinforcing composites. Moreover, long fibers reach percolation at low fiber contents. The fiber-fiber interactions caused by the percolation contribute to further improvement in the mechanic properties of composites. Therefore in searching for the right fibers for reinforcement, fiber aspect ratio should outweigh fiber strength as a more important consideration factor. This priority also has its economic benefits because low strength fibers are generally less costly.

2.5. Conclusions

A systematic comparison between CNCs and CNFs was made in this study with focus on their microstructures, interfacial bonding with the PEO matrix, and the resulting effects on the dynamic and mechanical properties of the PEO/CNC and PEO/CNF nanocomposites. The nanocomposites containing up to 10 wt% nanocellulose were prepared by simple solution casting. The maximum strength, modulus and fracture toughness of the composites were found

to occur at 7 wt% fiber content for both CNCs and CNFs. The increases were attributed to strong fiber-matrix interfacial bonding and large aspect ratios of the fibers. CNFs led to higher strength and modulus than did CNCs at the same fiber concentration due to CNFs' much larger aspect ratio and their percolation networks. The entanglements and percolation of CNFs also resulted in their higher probability of fiber agglomeration compared to CNCs, which caused lower strain-at-failure for PEO/CNF composites. The moduli of the composites were simulated using two models and their accuracies were compared. The Ouali model was found to be more accurate for PEO/CNF composites, whereas the Halpin-Kardos model was more suitable for PEO/CNC composites. The results from this comparative study are important for proper selection of nanocellulose materials as reinforcing agents in polymer composites.

2.6. References

1. Siqueira, G., Bras, J. & Dufresne, A. Cellulosic Bionanocomposites: A Review of Preparation, Properties and Applications. *Polymers* **2**, 728–765 (2010).
2. Habibi, Y., Lucia, L. A. & Rojas, O. J. Cellulose nanocrystals: chemistry, self-assembly, and applications. *Chemical Reviews* **110**, 3479–3500 (2010).
3. Wang, Q. Q. *et al.* Approaching zero cellulose loss in cellulose nanocrystal (CNC) production: recovery and characterization of cellulosic solid residues (CSR) and CNC. *Cellulose* **19**, 2033–2047 (2012).
4. Samir, M. A. S. A.; Alloin, F.; Paillet, M.; Dufresne, A. Tangling Effect in Fibrillated Cellulose Reinforced Nanocomposites. *Macromolecules* **37**, 4313–4316 (2004).
5. Samir, A., Alloin, F., Sanchez, J., Kissi, N. E. & Dufresne, A. Preparation of Cellulose Whiskers Reinforced Nanocomposites from an Organic Medium Suspension My Ahmed Sai. *Macromolecules* **37**, 1386–1393 (2004).
6. Park, W. I.; Kang, M., Kim, H. S. & Jin, H. J. Electrospinning of Poly(ethylene oxide) with Bacterial Cellulose Whiskers. *Macromol. Symp.* **249-250**, 289–294 (2007).
7. Cao, X.; Chen, Y.; Chang, P. R.; Muir, A. D.; Falk, G. Starch-based nanocomposites reinforced with flax cellulose nanocrystals. *Express Polym. Lett.* **2**, 502–510 (2008).

8. Qi, H., Cai, J., Zhang, L. & Kuga, S. Properties of films composed of cellulose nanowhiskers and a cellulose matrix regenerated from alkali/urea solution. *Biomacromolecules* **10**, 1597–1602 (2009).
9. Peresin, M. S., Habibi, Y., Zoppe, J. O., Pawlak, J. J. & Rojas, O. J. Nanofiber composites of polyvinyl alcohol and cellulose nanocrystals: manufacture and characterization. *Biomacromolecules* **11**, 674–681 (2010).
10. Cao, X., Dong, H. & Li, C. M. New nanocomposite materials reinforced with flax cellulose nanocrystals in waterborne polyurethane. *Biomacromolecules* **8**, 899–904 (2007).
11. Siqueira, G., Abdillahi, H., Bras, J. & Dufresne, A. High reinforcing capability cellulose nanocrystals extracted from *Syngonanthus nitens* (Capim Dourado). *Cellulose* **17**, 289–298 (2009).
12. Guhadós, G., Wan, W. & Hutter, J. L. Measurement of the elastic modulus of single bacterial cellulose fibers using atomic force microscopy. *Langmuir* **21**, 6642–6646 (2005).
13. Henriksson, M., Berglund, L. A., Isaksson, P., Lindström, T. & Nishino, T. Cellulose nanopaper structures of high toughness. *Biomacromolecules* **9**, 1579–1585 (2008).
14. Iwamoto, S., Nakagaito, A. N. & Yano, H. Nano-fibrillation of pulp fibers for the processing of transparent nanocomposites. *Appl. Phys. A* **89**, 461–466 (2007).
15. Wang, Q. Q. *et al.* Morphological development of cellulose fibrils of a bleached eucalyptus pulp by mechanical fibrillation. *Cellulose* **19**, 1631–1643 (2012).
16. Chinga-Carrasco, G. Cellulose fibres, nanofibrils and microfibrils: The morphological sequence of MFC components from a plant physiology and fibre technology point of view. *Nanoscale Res. Lett.* **6**, 417 (2011).
17. Nakagaito, A. N. & Yano, H. The effect of fiber content on the mechanical and thermal expansion properties of biocomposites based on microfibrillated cellulose. *Cellulose* **15**, 555–559 (2008).
18. Seydibeyoğlu, M. O.; Oksman, K. Novel nanocomposites based on polyurethane and micro fibrillated cellulose. *Compos. Sci. Technol.* **68**, 908–914 (2008).
19. Iwatake, a, Nogi, M. & Yano, H. Cellulose nanofiber-reinforced polylactic acid. *Compos. Sci. Technol.* **68**, 2103–2106 (2008).
20. Wu, Q., Henriksson, M., Liu, X. & Berglund, L. a A high strength nanocomposite based on microcrystalline cellulose and polyurethane. *Biomacromolecules* **8**, 3687–3692 (2007).

21. Cheng, Q., Wang, S. & Rials, T. G. Composites : Part A Poly (vinyl alcohol) nanocomposites reinforced with cellulose fibrils isolated by high intensity ultrasonication. *Compos. Part A* **40**, 218–224 (2009).
22. Choi, Y.; Simonsen, J. Cellulose Nanocrystals-filled carboxymethyl cellulose nanocomposites. *J. Nanosci. Nanotechnol.* **6**, 633–639 (2006).
23. Siqueira, G., Bras, J. & Dufresne, A. Cellulose whiskers versus microfibrils: influence of the nature of the nanoparticle and its surface functionalization on the thermal and mechanical properties of nanocomposites. *Biomacromolecules* **10**, 425–432 (2009).
24. Johnson, R. K., Zink-Sharp, A., Renneckar, S. H. & Glasser, W. G. A new bio-based nanocomposite: fibrillated TEMPO-oxidized celluloses in hydroxypropylcellulose matrix. *Cellulose* **16**, 227–238 (2008).
25. Lee, K. Y.; Tammelin, T., Schulfte, K., Kiiskinen, H., Samela, J. & Bismarck, A. High performance cellulose nanocomposites: comparing the reinforcing ability of bacterial cellulose and nanofibrillated cellulose. *ACS Appl. Mater. Interfaces* **4**, 4078–4086 (2012).
26. Liu, D., Chen, X., Yue, Y., Chen, M. & Wu, Q. Structure and rheology of nanocrystalline cellulose. *Carbohydr. Polym.* **84**, 316–322 (2011).
27. Asghar, A., Samad, Y. A. & Hashaikeh, R. Cellulose / PEO Blends with Enhanced Water Absorption and Retention Functionality. *J. Appl. Polym. Sci.* **125**, (2012).
28. Pielichowska, K. & Pielichowski, K. Biodegradable PEO/cellulose-based solid-solid phase change materials. *Polym. Adv. Technol.* **22**, 1633–1641 (2011).
29. Wang, Q. Q.; Zhu, J. Y.; Reiner, R. S.; Verrill, S. P.; Baxa, U.; McNeil, S. E. Cellulose Approaching Zero Cellulose Loss in Cellulose Nanocrystal (CNC) Production : Recovery and Characterization of Cellulosic Solid Residues (CSR) and CNC. *Cellulose* **19**, 2033–2047 (2012).
30. Scherrer, P. Bestimmung der Grösse und der inneren Struktur von Kolloidteilchen mittels Röntgenstrahlen. *Göttinger Nachrichten Gesell* **26**, 98–100 (1918).
31. Park, S., Baker, J. O., Himmel, M. E., Parilla, P. A. & Johnson, D. K. Cellulose crystallinity index: measurement techniques and their impact on interpreting cellulase performance. *Biotechnol. Biofuels* 3–10 (2010).doi:10.1186/1754-6834-3-10
32. Segal, L., Creely, J. J., Martin, A. E. & Conrad, C. M. An Empirical Method for Estimating the Degree of Crystallinity of Native Cellulose Using the X-Ray Diffractometer. *Tex. Res. J.* **29**, 786–794 (1959).
33. Li, R. *et al.* Cellulose whiskers extracted from mulberry: A novel biomass production. *Carbohydr. Polym.* **76**, 94–99 (2009).

34. Oudiani, A. E., Chaabouni, Y., Msahli, S. & Sakli, F. Crystal transition from cellulose I to cellulose II in NaOH treated *Agave americana* L. fibre. *Carbohydr. Polym.* **86**, 1221–1229 (2011).
35. Brown, R. D.; Jurasek, L. *Hydrolysis of Cellulose: Mechanisms of Enzymatic and Acid Catalysis*. (The Maple Press Co.: York, PA., 1979).
36. Moon, R. J., Martini, A., Nairn, J., Simonsen, J. & Youngblood, J. Cellulose nanomaterials review: structure, properties and nanocomposites. *Chem. Soci. Rev.* **40**, 3941–3994 (2011).
37. Elazzouzi-Hafraoui, S. *et al.* The shape and size distribution of crystalline nanoparticles prepared by acid hydrolysis of native cellulose. *Biomacromolecules* **9**, 57–65 (2008).
38. Kadla, J. F. & Kubo, S. Miscibility and Hydrogen Bonding in Blends of Poly(ethylene oxide) and Kraft Lignin. *Macromolecules* **36**, 7803–7811 (2003).
39. Kondo, T., Sawatari, C. & Gray, D. G. Characterization of Hydrogen Bonding in Cellulose-Synthetic Polymer Blend Systems with Regioselectively Substituted. *Macromolecules* **27**, 210–215 (1994).
40. Su, Y. L., Wang, J. & Liu, H. Z. Melt, hydration, and micellization of the PEO-PPO-PEO block copolymer studied by FTIR spectroscopy. *J. Colloid Interface Sci.* **251**, 417–423 (2002).
41. Kakade, M. V *et al.* Electric field induced orientation of polymer chains in macroscopically aligned electrospun polymer nanofibers. *J. Am. Chem. Soc.* **129**, 2777–2782 (2007).
42. Xu, X., Jiang, L., Zhou, Z., Wu, X. & Wang, Y. Preparation and properties of electrospun soy protein isolate/polyethylene oxide nanofiber membranes. *ACS Appl. Mater. Interfaces* **4**, 4331–4337 (2012).
43. Pereira, R. P., Rocco, A. M. & Bielschowsky, C. E. Poly(ethylene oxide): Electronic Structure, Energetics, and Vibrational Spectrum. *Macromol. Symp.* **108**, 12677–12684 (2004).
44. Brown, E. E. & Laborie, M.-P. G. Bioengineering bacterial cellulose/poly(ethylene oxide) nanocomposites. *Biomacromolecules* **8**, 3074–3081 (2007).
45. Ten, E., Jiang, L. & Wolcott, M. P. Crystallization kinetics of poly(3-hydroxybutyrate-co-3-hydroxyvalerate)/cellulose nanowiskers composites. *Carbohydr. Polym.* **90**, 541–550 (2012).

46. Cimmino, S. & Pace, E. Di Evaluation of the equilibrium melting temperature and structure analysis of poly (ethylene oxide)/ poly (methyl methacrylate) blends. *Die Makromolekulare Chemie* **191**, 2447–2454 (2003).
47. Rocco, a. M., Pereira, R. P. & Felisberti, M. I. Miscibility, crystallinity and morphological behavior of binary blends of poly(ethylene oxide) and poly(methyl vinyl ether–maleic acid). *Polymer* **42**, 5199–5205 (2001).
48. Ozkoc, G. & Kemaloglu, S. Morphology , Biodegradability , Mechanical , and Thermal Properties of Nanocomposite Films Based on PLA and Plasticized PLA. *J. Appl. Polym. Sci.* **114**, 2481–2487 (2009).
49. Jiang, L., Zhang, J. & Wolcott, M. P. Comparison of polylactide/nano-sized calcium carbonate and polylactide/montmorillonite composites: Reinforcing effects and toughening mechanisms. *Polymer* **48**, 7632–7644 (2007).
50. Halpin, J.C.; Kardos, J. L. Moduli of Crystalline Polymers Employing Composite Theory. *J. Appl. Phys.* **43**, 2235–2241 (1972).
51. Dalmas, F., Cavaille, J.-Y., Gauthier, C., Chazeau, L. & Dendievel, R. Viscoelastic behavior and electrical properties of flexible nanofiber filled polymer nanocomposites. Influence of processing conditions. *Compos. Sci. Technol.* **67**, 829–839 (2007).
52. Capadona, J. R., Shanmuganathan, K., Tyler, D. J., Rowan, S. J. & Weder, C. Stimuli-responsive polymer nanocomposites inspired by the sea cucumber dermis. *Science* **319**, 1370–1374 (2008).
53. Van Es, M. A.; Xiqiao, F.; van Turnhout, J.; van der Giessen, E. Van Es, M. A.; Xiqiao, F.; van Turnhout, J.; van der Giessen, E. *Specialty polymer additives: principles and applications* 391–414 (2001).
54. Ouali, N.; Cavaille, J. Y.; Perez, J. Elastic, viscoelastic, and plastic behavior of multiphase polymer blends. *Plast. Rubber Compos. Pro. Apps.* **16**, 55–60 (1991).
55. Takayanagi, M.; Uemura, S.; Minami, S. Takayanagi.pdf. *J. Polym. Sci., Part C: Polym. Symp.* **5**, 113 (1964).
56. Favier, V., Chanzy, H. & Cavaille, J. Y. Polymer nanocomposites reinforced by cellulose whiskers. *Macromolecules* **28**, 6365–6367 (1996).
57. Fourier, J.; Canova, G. R.; Shrivastava, S. C.; Cavaille, J. Y. Mechanical Percolation in Cellulose Whisker. *Polym. Eng. Sci.* **37**, 1732–1739 (1997).
58. Rusli, R. & Eichhorn, S. J. Determination of the stiffness of cellulose nanowhiskers and the fiber-matrix interface in a nanocomposite using Raman spectroscopy. *Appl. Phys. Lett.* **93**, 033111 (2008).

59. Lahiji, R. R. *et al.* Atomic force microscopy characterization of cellulose nanocrystals. *Langmuir* **26**, 4480–8 (2010).
60. Sturcová, A., Davies, G. R. & Eichhorn, S. J. Elastic modulus and stress-transfer properties of tunicate cellulose whiskers. *Biomacromolecules* **6**, 1055–1061 (2005).
61. Guhados, G., Wan, W. & Hutter, J. L. Measurement of the elastic modulus of single bacterial cellulose fibers using atomic force microscopy. *Langmuir* **21**, 6642–6646 (2005).
62. Hult, E. L., Iotti, M. & Lenes, M. Efficient approach to high barrier packaging using microfibrillar cellulose and shellac. *Cellulose* **17**, 575–586 (2010).
63. Cox, H. L. . The elasticity and strength of paper and other fibrous materials. *Br. J. Appl. Phys.* **3**, 72–79 (1952).
64. Krenchel, H. *Fibre Reinforcement: Theoretical and Practical Investigations of the Elasticity and Strength of Fibre-Reinforced Materials*. 11–20 (Akademisk Forlag: Copenhagen, 1964).
65. Tanpichai, S. *et al.* Effective Young's Modulus of Bacterial and Microfibrillated Cellulose Fibrils in Fibrous Networks. *Biomacromolecules* **13**, 1340–1349 (2012).
66. Agarwal, B. D.; Broutman, L. J.; Chandrashekhara, K. *Analysis and Performance of Fiber Composites*. 8–9 (Wiley: New York, 2006).

CHAPTER 3. COMPARISON BETWEEN CELLULOSE NANOCRYSTAL AND CELLULOSE NANOFIBRIL REINFORCED POLYETHYLENE OXIDE NANOFIBERS AND THEIR NOVEL SHISH-KEBAB-LIKE CRYSTALLINE STRUCTURES*

3.1. Abstract

Polyethylene oxide (PEO) nanofiber mats were produced by electrospinning. Biobased cellulose nanocrystals (CNCs) and cellulose nanofibrils (CNFs) as reinforcement nanofillers were also added to the polymer to produce composite nanofiber mats. The effects of the two cellulose nanofillers on the rheological properties of the PEO solutions and the microstructure, crystallization, and mechanical properties of the mats were systematically compared. The microstructural disparity between the CNCs and CNFs led to significant differences in the solution viscosity, nanofiber morphology and microstructure of the composite nanofiber mats. A unique shish-kebab-like crystalline structure was discovered in both pure and filled PEO nanofibers. Both CNCs and CNFs showed strong reinforcing effects on the nanofiber mats.

3.2. Introduction

The research on nano-sized cellulose fibers has experienced an explosive growth in recent years because of the unique combination of their properties including outstanding mechanical

* The content in this chapter was co-authored by Xuezhu Xu, Haoran Wang, Long Jiang, Xinnan Wang, Scott. A Payne, Junyong Zhu and Ruipeng Li. The content in this chapter was published in *Macromolecules* 05/2014; 47:3409-3416. Xuezhu Xu prepared samples and designed the experiments. Xinnan Wang designed and made the tensile test machine. Xuezhu Xu, Haoran Wang conducted the tensile tests. Long Jiang supervised this project, Xuezhu Xu, Long Jiang and Scott. A Payne analyzed the results. Xuezhu Xu drafted and revised the manuscript.

properties, rich surface chemistry, nontoxicity, biocompatibility, and abundant renewable sources.¹⁻⁶ Cellulose nanocrystals (CNCs) and cellulose nanofibrils (CNFs) are the two types of cellulose nanofibers with very similar chemical compositions yet differing on morphologies due to their different manufacturing methods.^{7,8} The CNCs are short, rod-like pure cellulose crystals whereas the CNFs are long, flexible and entangled fibrils that readily gel in water and exhibit stronger reinforcing effect in polymer nanocomposites than the CNCs do.⁹

In polymer crystallization, highly oriented shish-kebab morphology, rather than conventional isotropic spherulitic morphology, is induced by flow.^{10,11} The shishes consist of highly extended chains while the kebabs are lamellar crystals that grow epitaxially onto the shishes. Fibrillar fillers in polymer melts or solutions can also induce shish-kebab-like morphology during polymer crystallization without flow. In this case, the fillers, including inorganic whiskers, carbon nanotubes (CNTs), electrospun nanofibers, glass fibers and natural fibers, serve as the shishes and the crystalline polymers as the kebabs to form a hybrid structure.¹²⁻¹⁵ Depending on the density of the nuclei on the filler surfaces and the geometry of the growing polymer crystals, different interfacial crystallization morphologies including hybrid shish-kebab, hybrid shish-calabash and transcrystallization can be resulted.¹⁶ The shish-kebab structures in pure polymers have been shown to lead to higher mechanical properties, decreased permeability, and improved thermal stability.¹¹ The interfacial crystallization in polymer/fiber composites has been found to be a highly effective way to enhance polymer/fiber interactions and hence to increase mechanical properties of the composites.¹⁶

Although the CNCs or CNFs have been utilized to reinforce electrospun polymer nanofibers in several studies,¹⁷⁻²² the side-by-side comparisons in terms of their effects on rheological properties and spinnability of the electrospinning solutions, nanofiber diameter and

diameter distribution, crystallization and mechanical properties of the nanofiber mats have not been attempted. In this study, electrospun PEO nanofiber mats with CNC or CNF reinforcement were prepared and their properties were systematically compared. An in-depth study on the crystalline structure of the nanofibers revealed a rarely seen shish-kebab-like structure.

3.3. Experimental section

PEO powder ($M_v = 1,000,000$ g/mol) was purchased from Sigma-Aldrich. CNCs and CNFs (aqueous dispersions) were provided by the USDA Forest Service, Forest Products Laboratory (Madison, Wisconsin). The CNCs were produced by sulfuric acid hydrolysis, while the CNFs were produced through a multi-pass high-pressure grinding process using a Masuko MKZA6-2 Sangyo SuperMassColloider.^{7,8} To prepare PEO/CNC and PEO/CNF dispersions, pre-determined amounts of the PEO powder, distilled water and the CNC or CNF aqueous dispersions were mixed to result in loadings of 0, 1, 4, 7, and 10 wt% of CNCs or CNFs (with respect to PEO weight). The PEO concentration was kept constant at 4 wt% for all the dispersions. Before electrospinning the dispersions were homogenized using an IKA T25 digital Ultra-Turrax homogenizer for 5 minutes (6000 rpm, room temperature) followed by magnetic stirring at ~100 rpm at 60 °C for 12 hours. The electrospinning was performed through a 25-gauge blunt needle under a flow rate of 0.1 ml/h. A 12 kV voltage was applied between the needle and the fiber collector (a spinning disc covered with aluminum foil) using a DC ES30 high voltage power supply (Gamma High Voltage Research). The collected nanofiber mats were kept in a desiccator before characterization.

A JEOL 7600 field-emission scanning electron microscopy (FE-SEM) operating at 2 kV was used to study nanofiber morphology. Small pieces of the nanofiber mat samples were cut from the aluminum foils and attached to the FE-SEM sample mounts using conductive carbon

tapes. Prior to imaging, all samples were coated with a thin layer of carbon using a Cressington 208C carbon coater. The diameters of the nanofibers were determined based on the FE-SEM images using ImageJ software (National Institutes of Health, MD). One hundred total nanofibers for each sample were measured to obtain an average diameter. Transmission electron microscopy (TEM) imaging was performed using a JEOL JEM-2100 equipped with a LaB6 emitter. For CNC and CNF morphology, one droplet of CNC or CNF dispersion (diluted 100 times based on the as-received samples) was placed on a 300-mesh Formvar[®] coated carbon film copper grid, air dried and stained with 1% phosphotungstic acid. For the nanofibers, pure PEO, PEO/CNCs or PEO/CNFs were electrospun onto the copper grids, stained by the phosphotungstic acid and imaged to study the dispersion of CNCs and CNFs. Some fibers were etched with water before staining.

Rheological properties of the electrospinning solutions were studied using a TA AR G2 rheometer equipped with ϕ 25 mm parallel plates. Steady shear tests were performed within the shear rate range of 0.01~100 s⁻¹ using a gap size of 1 mm. Wide angle X-ray diffraction (WAXD) measurements were conducted using a Philips X'Pert MPD X-Ray powder diffractometer with a Cu K α X-ray source operating at 45 kV and 40 mA. Samples were scanned from 2.5 to 60 ° at 0.05 °/s. Crystallite sizes were calculated using software MDI Jade 5.0 (Materials Data, Inc.).

Differential scanning calorimetry (DSC) tests were performed on a TA Q1000 equipment. For each sample, 2 ~ 6 mg of the material was tested in a hermetic aluminum pan under 50 ml/min nitrogen flow. The sample was heated to 100 °C at 10 °C/min, equilibrated at 100 °C for 2 min and cooled down to 20 °C at 10 °C/min. Tensile properties of the electrospun nanofiber mats were measured using a micro-tensile tester developed in our facility. The tester

was equipped with a 5 lb LSM250 load cell (Futek Advanced Sensor Technology Inc) and LabVIEW software (National Instruments) for test control and data acquisition. A tensile specimen ($12.7 \times 6.35 \text{ mm}^2$) was cut from a nanofiber mat and glued onto a card-paper frame. The frame was loaded onto the tester and the sides of the frame were clipped before the tension was applied. The specimens were stretched at a deformation rate of 7.62 mm/min. Nine repetitions were tested for each sample.

3.4. Results and discussion

3.4.1. Rheology of the PEO/CNC and PEO/CNF dispersions

Nanoparticles show strong effects on the rheological properties of polymer solutions and melts because of their large surface areas. The effects of CNCs and CNFs on the rheology of PEO are expected to be different due to their different aspect ratios and microstructures as shown in **Figures 3.1a and 1a'**. The entangled network structure of CNFs should cause higher viscosity of the PEO solutions. Steady shear viscosities of the pure PEO solution, as-received CNC and CNF dispersions, and PEO/CNC and PEO/CNF dispersions are compared in **Figures 3.1b and 1c**. The pure PEO solution exhibits a low-shear Newtonian region and a high-shear shear-thinning region, a typical rheological behavior of high molecular weight polymer solutions. The as-received CNC dispersion (5.7 wt%) shows the lowest zero shear viscosity (13 Pa.s) among all the tested samples because of the lack of inter-particle interactions (i.e. no network structure) at such low CNC concentration. The dispersion also exhibits strong shear thinning behavior over the whole shear rate range due to progressive CNC alignment in the flow direction. Viscosities of the PEO/CNC dispersions are only slightly higher than that of the pure PEO solution, indicating the lack of inter-particle interaction and that the increase in viscosity is largely due to a hydrodynamic effect (**Figure 3.1b**). By contrast, the as-received CNF dispersion (2.3 wt%)

shows the highest zero shear viscosity (4450 Pa.s) and the strongest shear thinning behavior among all the tested samples (**Figure 3.1c**), which is ascribed to the network structure of CNFs and its progressive disruption under shearing.²³ Viscosities of the PEO/CNF dispersions are also much higher than those of the comparable PEO/CNC dispersions because of the entanglements between individual CNFs. **Figure 3.1d** compares the zero shear viscosities of the two dispersions over 0 – 10 wt% loading range. While the viscosities of PEO/CNCs remain nearly constant, the viscosities of PEO/CNFs show a rapid increase above 7 wt% CNFs (corresponding to 0.28 wt% CNFs with respect to water), which appears to indicate the formation of a percolated CNF network structure in the PEO/CNF dispersions. For comparison, the zero shear viscosities of pure CNF aqueous dispersions containing different concentrations of CNFs were also measured and the results are shown in **Figure 3.1d** inset. The results indicate a CNF percolation concentration of 0.5 wt%. This higher percolation threshold suggests that PEO chains in the PEO/CNF dispersions facilitate CNF percolation, possibly by bridging CNFs through the strong interactions between the two components.⁹ The percolation of the CNFs tends to clog the needle during electrospinning and hence to interrupt the process, as will be discussed later.

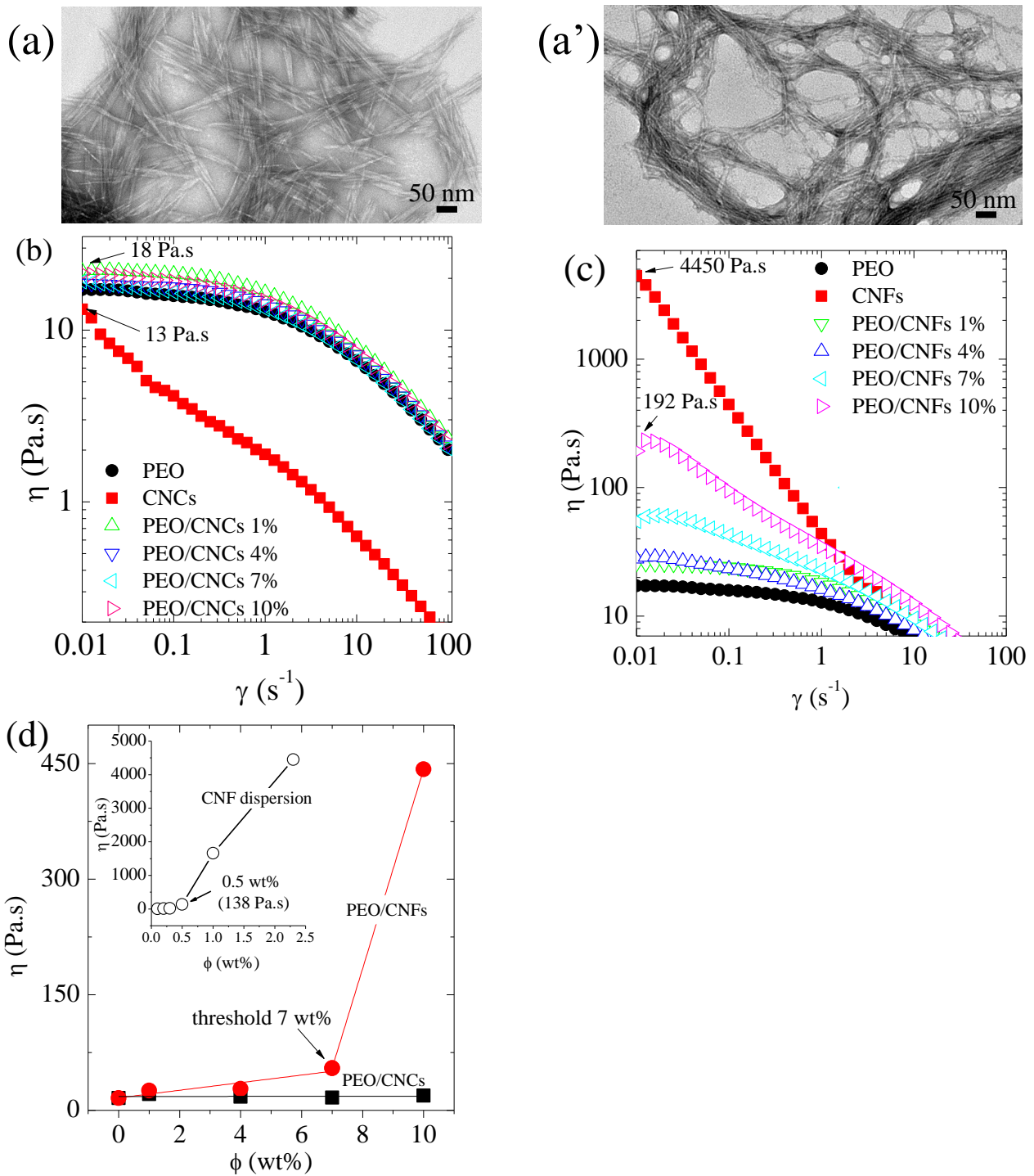


Figure 3.1. TEM images of needle-like CNCs (a) and network of CNFs (a'); (b) viscosity vs. shear rate of the PEO/CNC dispersions; (c) viscosity vs. shear rate of the PEO/CNF dispersions. (d) comparison of zero-shear viscosity between PEO/CNC and PEO/CNF dispersions. Inset: zero-shear viscosity of pure aqueous CNF dispersions.

3.4.2. Morphology of electrospun nanofibers

Figures 3.2a-d show the surface morphologies of the PEO/CNC and PEO/CNF nanofibers. Both nanofibers exhibit smooth surfaces without any sign of surface coarsening due to the addition of the nanosized cellulose fibers, suggesting homogeneous dispersion of the cellulose fibers in the PEO matrix, which is facilitated by the hydrogen bonding between them.⁹ It is worth noting that above 10 wt% CNF concentration, the electrospinning process of the PEO/CNF dispersion was frequently interrupted by the ejection of large droplets from the needle due to the high viscosity of the dispersion and/or CNF flocculation induced phase separation in the dispersion.¹⁹ The PEO/CNC dispersions, on the other hand, could be successfully electrospun into homogenous nanofibers up to 20 wt% CNC concentration because of the lack of CNC flocculation.

The diameter histogram of the PEO/CNC nanofibers and the average diameter (ϕ) for each fiber are shown in **Figure 3.2e**. All the fibers exhibit a unimodal size distribution and the average diameter decreases with increasing CNC concentration. The decrease can be ascribed to the increased conductivity of the dispersions that results in larger electrostatic pulling force on the jets.²⁴⁻²⁷ In contrast, all the PEO/CNF nanofibers exhibit a bimodal size distribution as shown in **Figure 3.2f**. Basically, during the electrospinning, a primary jet splits into multiple secondary jets once the electrical charge-induced radial repulsive force exceeds the cohesive force of the jet.²⁸ The bimodal diameter distribution may be due to the uneven distribution of the charges induced by the highly entangled network structure of CNFs, which leads to uneven splitting of the jet when subjected to the electric field.²⁹ This phenomenon has also been frequently reported in other highly viscous liquids with the electrical instability by other investigators.^{30,31}

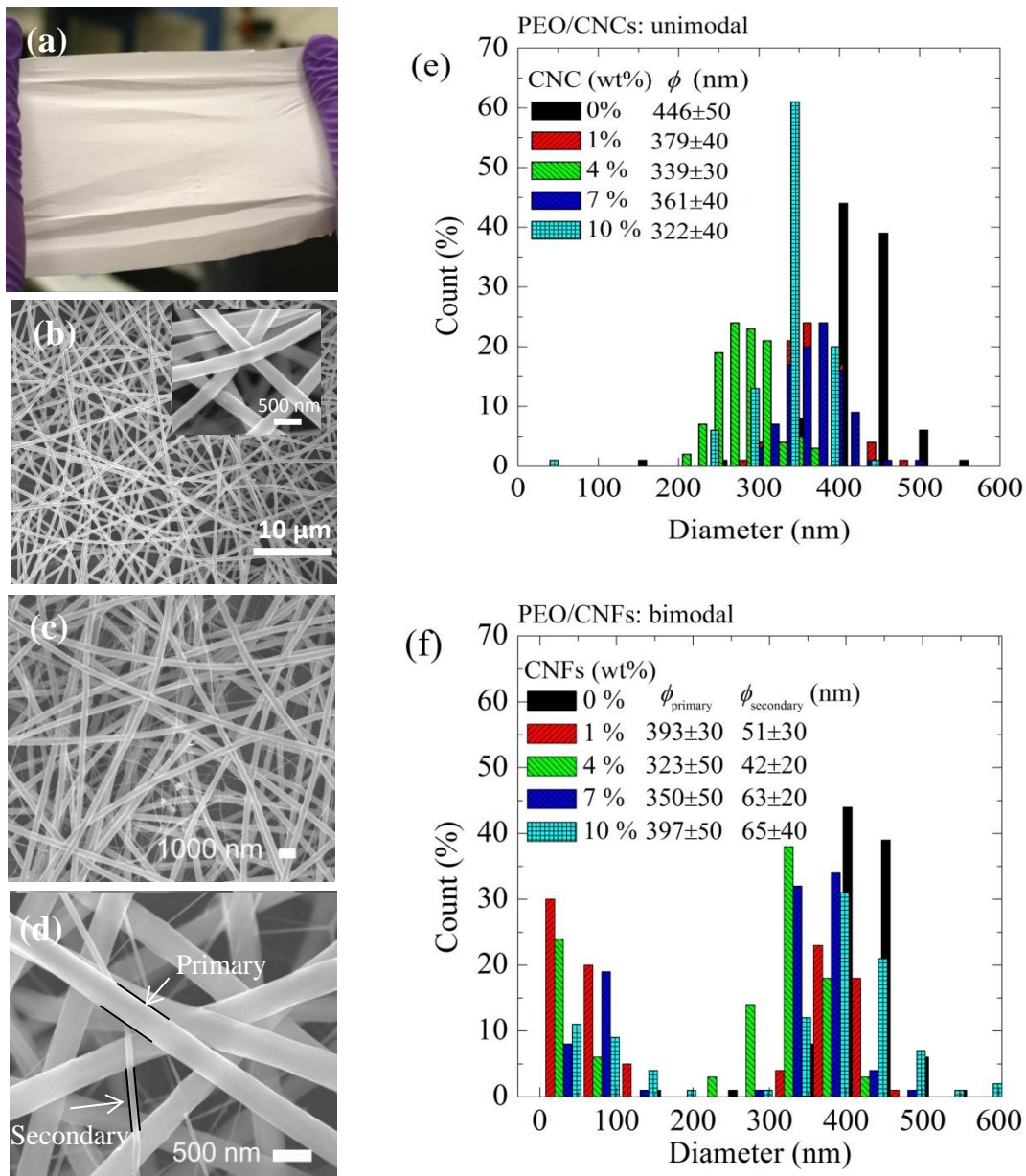


Figure 3.2. Photo (a) and FE-SEM micrograph (b) of PEO/CNC 1% nanofiber mat; (c – d) FE-SEM images of PEO/CNF 1% nanofiber mat; (e) diameter distribution of the PEO/CNC nanofibers; (f) diameter distribution of PEO/CNF nanofibers.

3.4.3. PEO crystallization in the electrospun nanofibers

Figure 3.3a shows a TEM micrograph of the pure PEO nanofiber. A shish-kebab-like crystal structure can be clearly seen. The “kebabs” are perpendicular to the fiber axis and are periodically located along the fiber. Such configuration of crystal structure is rarely seen in

electrospun nanofibers. Wang et al. have reported PEO nano hybrid shish-kebab (NHSK) structure, where PEO kebabs grow on electrospun PEO nanofibers in a controlled solution crystallization process.³² The TEM micrograph of this NHSK structure appears similar to **Figure 3.3a**. However, the origins of the kebabs in the two studies are totally different: the “kebabs” in this study are formed inside the electrospun nanofiber whereas in Wang’s study the kebabs crystallize onto the nanofiber surfaces in a secondary crystallization process. The “kebabs” in this study exhibit an average thickness of 11 nm and a period of 9~25 nm. The period is much smaller than that of the NHSK kebabs¹³ and classic polymer shish-kebabs formed under flow.¹²

The shish-kebab-like crystal structures also exist in PEO/CNC and PEO/CNF nanofibers as shown in **Figure 3.3b**. A brief water etching process on the nanofiber led to a shish-kebab-like PEO crystal structure (**Figure 3.3c**) similar to that of electrospun polyethylene (PE) nanofibers, where extended PE shishes and perpendicular kebabs were clearly identified.³³ The selected area electron diffraction (SAED) pattern (**Figure 3.3d**) taken from **Figure 3.3b** exhibits characteristic (120) diffraction that suggests unidirectional orientation of the PEO chains in the fiber direction.^{32,34} Long time water etching dissolved all PEO and only the cellulose nanofillers remained. The nanofillers appear to be largely aligned in the axial direction of the fiber due to the jet stretching during electrospinning¹⁹ (**Figure 3.3e-f**). Regarding the formation mechanism of the shish-kebab-like structures in the pure PEO nanofibers, some PEO chains were firstly oriented in the axial direction by the stretching force and possibly formed extended chain crystals.³² The remaining crystallizable PEO chains crystallized epitaxially or soft-epitaxially on the extended chains to form the “kebabs”. For the PEO/CNC or PEO/CNF nanofibers, the cellulose nanofillers could also serve as the “shishes” to facilitate the growth of PEO “kebabs”.³⁵ A schematic illustration of such shish-kebab-like structure is shown in **Figure 3.3g**.

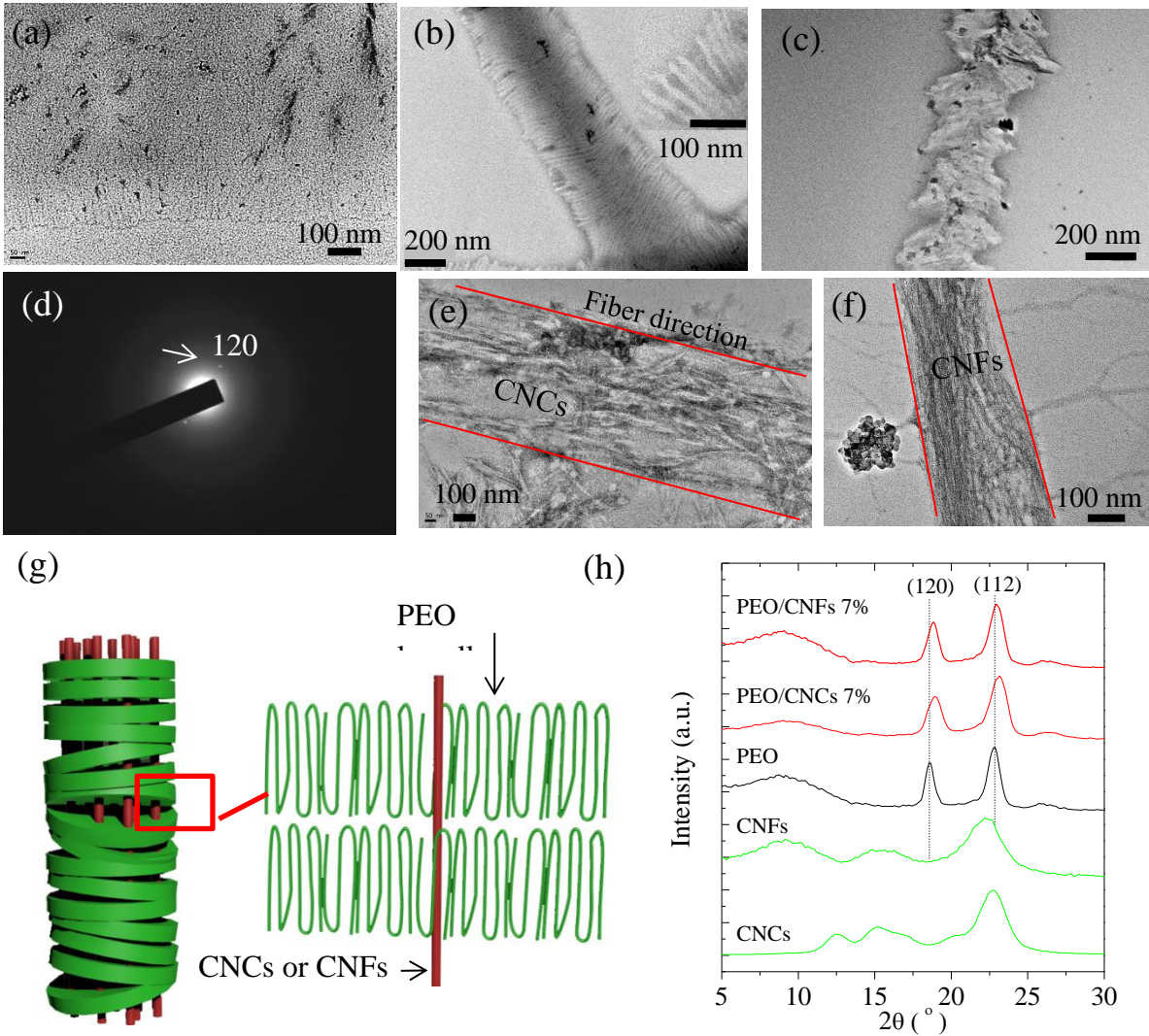


Figure 3.3. (a) TEM images of pure PEO nanofibers; (b) PEO/CNF 4% nanofibers; (c) PEO/CNF 4% nanofiber after mild water etching; (d) SAED pattern taken from Figure b; (e) PEO/CNC 4% and (f) PEO/CNF 4% nanofibers after PEO removal; (g) illustration of the shish-kebab-like structure; (h) WAXD patterns of PEO/CNC and PEO/CNF 7% nanofibers.

WAXD was used to determine PEO crystal structures in the nanofibers. The diffraction patterns and the derived crystal characteristics including 2θ , d-spacing and average crystallite size (L) are given in **Figure 3.3h** and **Table 3.1**, respectively. The crystallite size was calculated based on the Scherrer's equation:

$$L = K\lambda/B \cos \theta \quad (3.1.)$$

where K is the Scherrer constant (0.89), λ is the wavelength of the Cu K α X-ray (1.54 Å), and B is the full width at half maximum (FWHM) of diffraction peaks. The pure PEO nanofibers exhibit two strong peaks at 19 ° and 23 °, which are attributed to the diffraction of the (120) and (112) crystal planes.²⁶ The CNCs and CNFs feature typical diffraction peaks of cellulose I and II.⁹ The (120) and (112) diffraction peaks are broadened and shifted to higher angles when CNCs or CNFs are incorporated into the nanofibers, suggesting reduced d-spacing and crystallite size. As shown in **Table 3.1**, the d-spacings for both PEO/CNCs and PEO/CNFs show slight decreases whereas the crystallite sizes exhibit substantial decreases. For example, pure PEO exhibits crystal sizes of 157 and 106 Å at (120) and (112) planes respectively, whereas PEO/CNF 7 wt% possesses comparable sizes of 110 and 94 Å. The sizes are reduced by 4.7 and 1.2 nm in the two directions.

Table 3.1. XRD results of the pure PEO, PEO/CNC (7 wt%), and PEO/CNF (7 wt%) nanofibers.

Sample	(120)				(112)			
	2 θ (°)	d-spacing (Å)	FWHM	L (Å)	2 θ (°)	d-spacing (Å)	FWHM	L (Å)
PEO	18.6	4.8	0.614	157	22.8	3.9	0.769	106
PEO/CNCs	18.9	4.7	0.805	96	23.1	3.8	0.997	88
PEO/CNFs	18.8	4.7	0.676	110	22.9	3.9	0.789	94

3.4.4. Thermal properties of PEO/CNC and PEO/CNF nanofibers

The effects of the CNCs and CNFs on the melting and crystallization of PEO nanofibers were studied using DSC. Pure PEO powder and pure electrospun PEO nanofiber were also tested for comparisons. In **Figures 3.4**, the pure PEO powder exhibits one single melting peak at 68.4 °C whereas the pure nanofiber exhibits a broad melting region which can be separated into a low (66.3 °C) and a high (71.9 °C) melting peak. Double-melting peak has been reported on electrospun nanofibers^{36,37} and polymers having high degree of shear-induced chain orientation.³⁸ It can indicate the co-existence of two different crystalline types: lamellar crystals

(low melting point) and extended chain crystals (high melting point) in the pure PEO nanofibers. The melting point of the lamellae in the electrospun nanofiber is even lower than that of the regular lamellae in the PEO powder because of rapid solidification of the fiber during electrospinning. The electrospun nanofibers containing CNCs or CNFs also exhibit broadened double melting peaks, indicating similar co-existence of non-oriented and oriented crystals. However, at 10% CNCs or CNFs, the double melting is substantially suppressed because high concentration of nanoparticles hinders the growth of PEO lamellae.³⁹

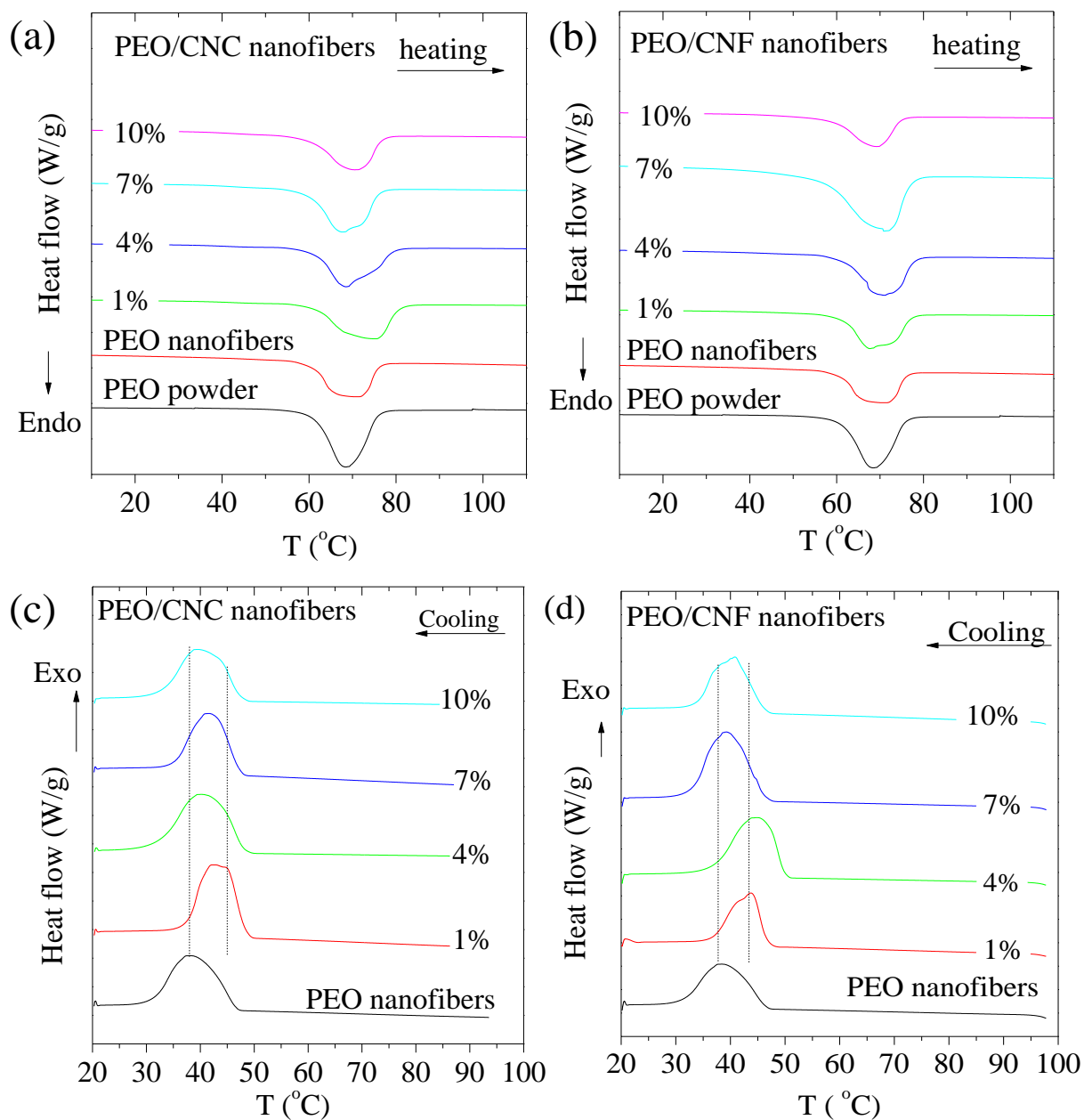


Figure 3.4. DSC thermograms for the melting and non-isothermal crystallization of PEO/CNC and PEO/CNF nanofibers. (a) PEO/CNC melting; (b) PEO/CNF melting; (c) PEO/CNC crystallization; (d) PEO/CNF crystallization.

The melting point (T_m), heat of fusion (ΔH) and crystallinity (X_c) of the samples were derived from the DSC thermograms and their results are summarized in **Table 3.2**. The crystallinity of the PEO nanofibers is substantially lower than that of the PEO powder (73 % vs.

90 %) due to the rapid solidification of nanofibers, which restricts crystal growth. The nucleation effects of CNCs and CNFs increase the crystallinity of PEO/CNC and PEO/CNF nanofibers at low filler concentrations. However, at high concentrations, the diffusion of PEO chains and hence the growth of the lamellae are hindered and as a result, the crystallinity starts to decrease. The nucleation effects of CNCs and CNFs are also demonstrated by the cooling thermograms in **Figures 3.4c-d**. The crystallization peaks of PEO are shifted to higher temperatures when CNCs or CNFs are added, and then the peak temperature (T_c) in general decreases with increasing nanofiller concentrations due to suppressed crystal growth. The largest increases in the T_c and T_o (onset temperature) are 6.3 °C and 3.5 °C, respectively, which both occur on the 4% PEO/CNF nanofibers.

Table 3.2. DSC results for the electrospun nanofibers.

	Sample	0%	1%	4%	7%	10%
T_m (°C)	PEO/CNCs	66.3, 71.9	68.7, 75.6	68.2, 75.6	68.0, 72.1	70.2
	PEO/CNFs		67.2, 73.3	67.6, 73.3	70.2	68.7
ΔH (J/g)	PEO/CNCs	157	183.8	181.3	179.2	177.3
	PEO/CNFs		167.1	161.1	164.6	154.8
* X_c (%)	PEO/CNCs	73	87	88	81	79
	PEO/CNFs		79	80	83	80
T_o (°C)	PEO/CNCs	46.4	48.3	48.1	47.3	47.3
	PEO/CNFs		46.4	49.9	46.4	46.3
T_c (°C)	PEO/CNCs	38.6	43.0	40.3	41.8	39.7
	PEO/CNFs		44.0	44.9	39.3	40.8

* $X_c = \Delta H / [\Delta H_{100\%} \times (1 - W)]$, where $\Delta H_{100\%}$ is the heat of fusion for 100% crystallized PEO (213.7 J/g).³⁴ W is the weight fraction of CNCs or CNFs. The T_m , ΔH and X_c for PEO powder was 68.4 °C, 192.1 J/g, and 90 %, respectively.

It is also worth noting from **Table 3.2** that melting temperatures of PEO/CNCs are generally higher than those of PEO/CNFs. We postulate that this is due to higher perfection of the shish-kebab-like structure in the former. CNCs can be aligned during electrospinning more

readily than CNFs because of the following two reasons: CNCs are rigid rods without entanglements and PEO/CNC solutions exhibit lower viscosities than PEO/CNF solutions. Both reasons lead to lower resistance to CNC rotation and therefore higher degree of CNC alignment, which facilitates the formation of PEO “shish kebab”. In addition, the lower viscosity of the PEO/CNC solutions allows PEO chains to diffuse at a higher rate to the growing fronts of the “kebabs”, promoting growth of the structure.

Comparing the melting points of the nanofiber mats to those of the cast films in our previous study,⁹ it is obvious that the melting points of the former are generally increased by the cellulose nanofibers (especially at low CNC or CNF concentrations), whereas the melting points are decreased by the nanofibers in the latter due to the nanofiber confinement effect which hinders chain diffusion and folding. This comparison shows that the formation of the shish-kebab-like structures, which is facilitated by the extensional flow generated by electrospinning and CNC (or CNF) assisted PEO chain alignment and crystallization, dominates the crystallization process of the nanofiber mats.

3.4.5. Mechanical properties of nanofiber mats

Representative tensile stress-strain curves of the PEO/CNC and PEO/CNF nanofiber mats and their FE-SEM micrographs after tensile fracture are shown in **Figure 3.5**. The Young’s modulus, tensile strength, strain-at-failure and toughness of the samples are summarized in **Table 3.3**. For the CNC reinforced nanofiber mats, all the measured properties peak at 1 wt% filler concentration and then continuously decrease with the increasing concentration. The tensile strength and Young’s modulus for the 1 wt% mat are 2.2 and 3.5 times as large as those of the pure PEO membrane. Strain-at-failure and fracture toughness at the same time increase to 1.3 and 3 times the control values. For the CNF reinforced mats, the maximum values of all the

properties occur at 4 wt% CNF concentration. At this concentration, the strength, modulus, strain and toughness are 2.5, 1.4, 1.3, and 2.2 times the control values, respectively. For both types of mats, at the 10 wt% highest concentration, the strength and modulus of the mats are still comparable to the control values, if not higher. However, the strain and toughness are significantly lower (less than half), indicating increased brittleness of the mats after incorporating high concentrations of the cellulose nanofillers. No direct correlations can be found between fiber diameter and the mechanical properties for both PEO/CNC and PEO/CNF nanofiber mats. More discussion on this is given below.

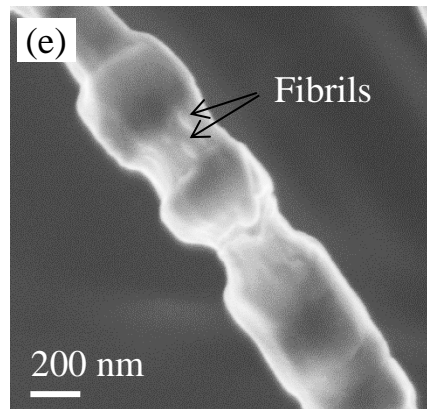
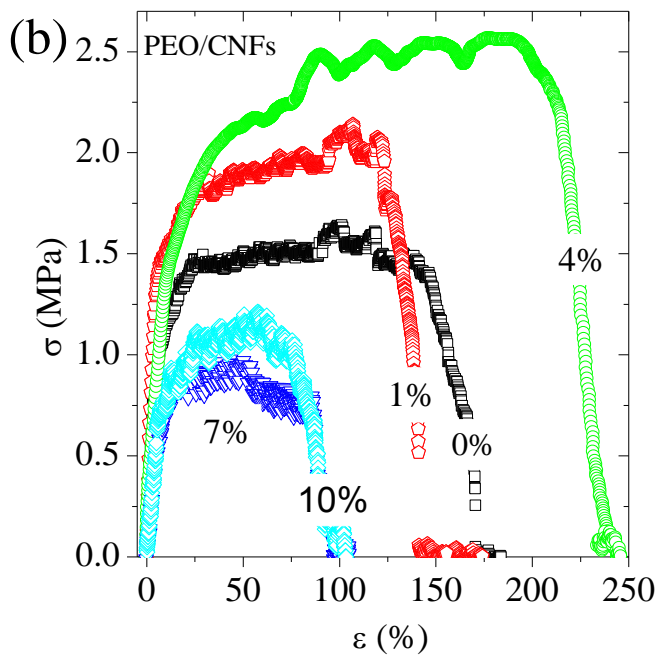
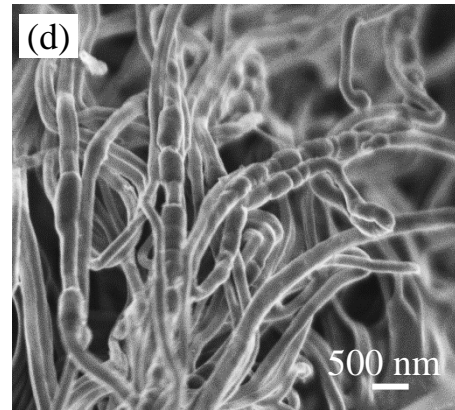
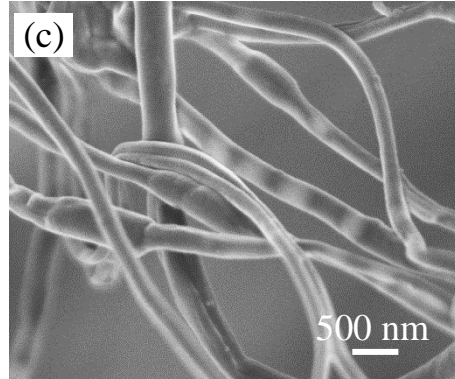
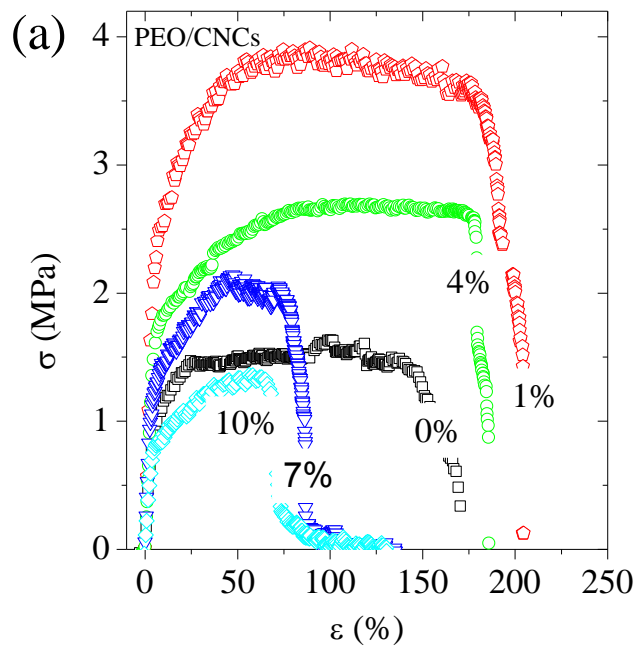


Figure 3.5. Stress-strain curves of PEO/CNC (a) and PEO/CNF (b) nanofiber mats with various filler contents; (c) FE-SEM images of pure PEO nanofiber membrane after testing; (d) 1 wt% PEO/CNC nanofiber membrane after testing; (e) fibrillation in the neck region of the PEO/CNF 4% fiber.

Table 3.3. Mechanical properties of PEO/CNC and PEO/CNF nanofiber mats

Filler	Filler Content (wt%)	Young's modulus (MPa)	Tensile strength (MPa)	Strain-at-failure (%)	Fracture toughness (kJ/m ³)
PEO	0	20±1	1.6±0.2	152±31	232±20
	1	72±20	3.5±0.6	204±30	702±45
CNCs	4	56±20	2.9±0.4	185±11	448±16
	7	50±10	1.9±0.2	87±12	153±11
	10	22±3	1.3±0.2	71±7	84±3
CNFs	1	44±9	2.1±0.1	119±25	400±40
	4	51±10	2.2±0.3	197±10	513±16
	7	24±10	0.8±0.2	86±18	72±22
	10	20±3	1.2±0.3	75±12	86±9

Failure mechanisms of the PEO/CNC and PEO/CNF nanofiber mats were studied based on the SEM micrographs of the fractured mats. Multi-necking can be clearly seen from the pure PEO nanofibers (**Figure 3.5c**). This phenomenon has also been reported on electrospun carbon nanotube (CNT) reinforced polymer nanofibers.^{40–42} In polymer deformation, necking refers to localized large scale plastic deformation initiated by material defects (voids, cracks, etc.) and inclusions (nanofibers, particles, etc.) which cause stress concentration. During the necking process, the material in the neck is cold-drawn and the cross-sectional area is reduced. The polymer chains in the neck are aligned in the stretching direction and the material is strain hardened. The degree of necking is characterized by the draw ratio that can be defined as the diameter of the fiber out of the neck region divided by that in the neck region. A large draw ratio and high-frequency multi-necking lead to large strain-at-failure and fracture toughness of the material. The pure PEO nanofibers (**Figure 3.5c**) exhibit a relatively small average draw ratio of 1.27, whereas the ratios for the PEO/CNC (1 wt%) and PEO/CNF (4 wt%) nanofibers increase to 2.49 and 1.64, respectively, matching the increasing trend of the strain-at-failure and fracture toughness. Moreover, the frequency of necking also appears to increase in the CNC or CNF

filled nanofibers (**Figure 3.5d**) because of the additional stress concentration sites caused by the nanofillers.⁴²

The fibrils formed after crazing can be clearly seen in the neck region of the nanofibers (**Figure 3.5e**). Ye et al. reported the similar phenomenon in stretched electrospun CNT-polyacrylonitrile nanofibers and proposed a two-stage deformation mechanism including crazing and fiber pull-out in the neck region.⁴¹ In our study, CNCs and CNFs at their low concentrations promote and stabilize multi-necking and hence increase the failure strain and toughness. The nanofillers in the neck region, being largely aligned in the longitudinal direction by the stretching and by the prior electrospinning process, share the load from the PEO matrix and hinder rapid craze propagation in the matrix, thus causing the increase in the strength of the nanofibers.^{41,42} The crazing fibrils shown in **Figure 3.5e** contains CNCs or CNFs and their encapsulating PEO sheath. Due to the strong hydrogen bonding between the nanofillers and PEO, we postulate that no CNC or CNF fiber pull-out occurs in this system. Rather, the PEO molecules around the nanofillers slip and align by shearing along the nanofillers, leading to the fibrillar structure shown in **Figure 3.5e**.⁴²

The continuous decreases of all the mechanical properties at high CNC (> 1 wt%) or CNF (> 4 wt%) concentrations are believed to be mainly caused by nanofiller agglomeration, which is likely to occur during fiber solidification after it is ejected out of the needle. Instead of facilitating crazing, large nanofiller agglomerates lead to cracks that propagate readily in the nanofibers and result in premature fiber fractures. The reason for the higher transition concentration of CNFs is unclear. It may be related to the bimodal distribution of the PEO/CNF nanofibers, which leads to microstructural disparities between the PEO/CNF and PEO/CNC nanofiber mats. It should be pointed out that in this study nonwoven fiber mats rather than single

fiber or unidirectional fiber mats was used for the tensile tests. As a result, the mechanical properties obtained from the tests (**Table 3.3**) do not directly represent those of single nanofibers. Pai et al. developed a quantitative microstructure-based model that relates the moduli of electrospun nanofiber mats to those of the individual nanofibers.⁴³ The model indicates that the moduli of the mats is a function of the moduli of the individual nanofibers, porosities of the mats, fiber diameters, junction lengths, and radii of curvature of the nanofibers. The last two parameters are further shown to be proportional to the fiber diameter. A larger diameter causes higher junction length and radius of curvature, which in turn leads to an increase in the modulus of the nanofiber mats. However, the increase can be offset by the decrease in intrinsic nanofiber modulus, which is attributed to reduced chain orientation. As a result, the moduli and strengths of poly(trimethyl hexamethylene terephthalamide) model mats remain largely constant with increasing nanofiber diameter (113 - 3643 nm).

The above-mentioned study sheds light on the mechanical properties of the nanofiber mats in this research. All the PEO/CNF nanofiber mats exhibit similar fiber diameter and diameter distribution regardless of their CNF contents. Their porosities have also been found similar (0.79 ± 0.04) based on the densities of the mats and the densities of PEO/CNF cast films (Pai has also shown nearly constant mat porosity (0.88 - 0.90) for a fiber diameter range of 113 - 3643 nm).⁴³ Due to the consistency in fiber diameter and in mat porosity across the PEO/CNF mats, the substantial variations in their mechanical properties (**Table 3.3**) can only be caused by the changes in the intrinsic properties of the individual nanofibers, which vary according to the concentration of CNFs. As for the PEO/CNC nanofiber mats, their porosity also remains relatively constant (0.85 ± 0.03). Although the fiber diameter decreases moderately with increasing CNC concentration, the diameter change alone should not cause large variations in the

strength and modulus of the mats base on the results of Pai.⁴³ Therefore, the variations that do occur on PEO/CNC nanofiber mats (**Table 3.3**) is due to the mechanical property changes of individual PEO/CNC nanofibers. In conclusion, the increases in mechanical properties of the nanofiber mats are primarily caused by the reinforcing effects of CNCs or CNFs on the individual nanofibers, with the microstructural effects of the fiber mats being relatively small.

In addition to the reinforcing effects of CNCs and CNFs, the effects of PEO crystallinity and crystal size on the mechanical properties of the nanofibers should not be ignored. Our DSC results show that PEO crystallinity is higher in the samples containing CNCs or CNFs while the WAXD results indicate that the size of PEO crystals is smaller. This means that CNCs and CNFs lead to higher density but smaller PEO crystals in the nanofibers. Mechanical properties of a semi-crystalline polymer such as PEO can be simulated using composite mechanics - a rigid crystalline phase dispersed in a relatively soft amorphous matrix as reinforcement.⁴⁴ Based on the composite theory, modulus of the semi-crystalline polymer increases with the fraction of the rigid crystalline phase.⁴⁵ Strength of the composite can also be increased if there is a strong interfacial bonding between the two phases, which is often the case for semi-crystalline polymers because of the existence of tie chains that connect the crystalline and amorphous phases. Smaller crystals means larger interfacial area between the two phases (assuming equal crystallinity) and less stress concentration, both of which positively contribute to the strength of the semi-crystalline polymer. Therefore, the increased crystallinity and reduced crystal size of the PEO/CNC and PEO/CNF nanofibers as well as the reinforcement of CNCs (or CNFs) contribute synergistically to the increases in mechanical properties of the nanofiber mats at low CNC (or CNF) concentrations. At high concentrations, CNC (or CNF) agglomeration dominates the above factors and causes decreases in mechanical properties of the nanofiber mats.

3.5. Conclusions

CNCs and CNFs were used as reinforcement materials in electrospun PEO nanofiber mats and their effects on the viscosity of the spinning solutions, nanofiber diameter and diameter distribution, crystalline structures of the nanofibers, and the mechanical properties of the nanofiber mats were systematically studied. The CNFs caused high viscosity of the PEO solutions, relatively poor spinnability and bimodal fiber diameter distribution due to their entangled network structure. Rare shish-kebab-like PEO crystalline structures were discovered in the electrospun nanofibers. Mechanical properties of the nanofiber mats, including strength, modulus and fracture toughness, were significantly improved by the addition of low concentrations of CNCs and CNFs. The properties deteriorated at high concentrations of the nanofillers due to filler agglomeration.

3.6. References

1. Habibi, Y.; Lucia, L. A. & Rojas, O. J. Cellulose Nanocrystals: Chemistry, Self-Assembly, and Applications. *Chem. Rev.* **110**, 3479–500 (2010).
2. Peng, B. L.; Dhar, N.; Liu, H. L. & Tam, K. C. Chemistry and Applications of Nanocrystalline Cellulose and Its Derivatives: A Nanotechnology Perspective. *Can. J. Chem. Eng.* **89**, 1191–1206 (2011).
3. Siró, I.; Plackett, D. Microfibrillated Cellulose and New Nanocomposite Materials: A Review. *Cellulose* **17**, 459–494 (2010).
4. Dufresne, A. Polysaccharide Nanocrystal Reinforced Nanocomposites. *Can. J. Chem.* **86**, 484–494 (2008).
5. Eichhorn, S. J.; Dufresne, A.; Aranguren, M.; Marcovich, N. E.; Capadona, J. R. et al. Review: Current International Research into Cellulose Nanofibres and Nanocomposites. *J. Mater. Sci.* **45**, 1–33 (2010).
6. Durán, N.; Lemes, A. P. & Seabra, A. B. Review of Cellulose Nanocrystals Patents: Preparation, Composites and General Applications. *Recent pat. Nanotechnol.* **6**, 16–28 (2012).

7. Wang, Q. Q.; Zhu, J. Y.; Gleisner, R.; Kuster, T. A.; Baxa, U. & McNeil, S. E. Morphological Development of Cellulose Fibrils of A Bleached Eucalyptus Pulp by Mechanical Fibrillation. *Cellulose* **19**, 1631–1643 (2012).
8. Wang, Q. Q.; Zhu, J. Y.; Reiner, R. S.; Verrill, S. P.; Baxa, U. & McNeil, S. E. Approaching Zero Cellulose Loss in Cellulose Nanocrystal (CNC) Production: Recovery and Characterization of Cellulosic Solid Residues (CSR) and CNC. *Cellulose* **19**, 2033–2047 (2012).
9. Xu, X.; Liu, F.; Jiang, L. & Zhu, J. Cellulose Nanocrystals vs. Cellulose Nanofibrils: A Comparative Study on Their Microstructures and Effects as Polymer Reinforcing Agents. *ACS Appl. Mater. Interfaces* **5**, 2999–3009 (2013).
10. Somani, R. H.; Yang, L.; Zhu, L. & Hsiao, B. S. Flow-Induced Shish-Kebab Precursor Structures in Entangled Polymer Melts. *Polymer* **46**, 8587–8623 (2005).
11. Wang, K.; Chen, F.; Zhang, Q. & Fu, Q. Shish–Kebab of Polyolefin by “Melt Manipulation” Strategy in Injection-Molding: A Convenience Pathway From Fundament to Application. *Polymer* **49**, 4745–4755 (2008).
12. Yang, J.; Wang, C.; Wang, K.; Zhang, Q.; Chen, F.; Du, R. & Fu, Q. Direct Formation of Nanohybrid Shish-Kebab in the Injection Molded Bar of Polyethylene/Multiwalled Carbon Nanotubes Composite. *Macromolecules* **42**, 7016–7023 (2009).
13. Ning, N.; Luo, F.; Pan, B.; Zhang, Q.; Wang, K. & Fu, Q. Observation of Shear-Induced Hybrid Shish Kebab in the Injection Molded Bars of Linear Polyethylene Containing Inorganic Whiskers. *Macromolecules* **40**, 8533–8536 (2007).
14. Dufresne, A.; Kellerhals, M. B. & Witholt, B. Transcrystallization in Mcl- PHAs/Cellulose Whiskers Composites. *Macromolecules* **32**, 7396–7401 (1999).
15. Zhong, G. J.; Li, Z. M.; Li, L. & Shen, K. Crystallization of Oriented Isotactic Polypropylene (IPP) in the Presence of In Situ Poly(Ethylene Terephthalate) (PET) Microfibrils. *Polymer* **49**, 4271–4278 (2008).
16. Ning, N.; Fu, S.; Zhang, W.; Chen, F.; Wang, K.; Deng, H.; Zhang, Q. & Fu, Q. Realizing The Enhancement of Interfacial Interaction in Semicrystalline Polymer/Filler Composites via Interfacial Crystallization. *Prog. Polym. Sci.* **37**, 1425–1455 (2012).
17. Li, Y.; Ko, F. K. & Hamad, W. Y. Effects of Emulsion Droplet Size on the Structure of Electrospun Ultrafine Biocomposite Fibers with Cellulose Nanocrystals. *Biomacromolecules* **14**, 3801–3807 (2013).
18. Fortunato, G.; Zimmermann, T.; Lübben, J.; Bordeanu, N. & Hufenus, R. Reinforcement of Polymeric Submicrometer-Sized Fibers by Microfibrillated Cellulose. *Macromol. Mater. Eng.* **297**, 576–584 (2012).

19. Olsson, R. T.; Kraemer, R.; López-Rubio, A.; Torres-Giner, S.; Ocio, M. J. & Lagarón, J. M. Extraction of Microfibrils from Bacterial Cellulose Networks for Electrospinning of Anisotropic Biohybrid Fiber Yarns. *Macromolecules* **43**, 4201–4209 (2010).
20. Medeiros, E. S.; Mattoso, L. H. C.; Ito, E. N.; Gregorski, K. S.; Robertson, G. H.; Offeman, R. D.; Wood, D. F.; Orts, W. J. & Imam, S. H. Electrospun Nanofibers of Poly(Vinyl Alcohol) Reinforced with Cellulose Nanofibrils. *J. Biobased Mater. Bio.* **2**, 231–242 (2008).
21. Park, W.; Kang, M.; Kim, H. S. & Jin, H. J. *Macromol. Symp.* **249–250** (1), 289.
22. Changarn, S.; Mendez, J. D.; Shanmuganathan, K.; Foster, E. J.; Weder, C. & Supaphol, P. *Macromol. Rapid Commun.* **32**(17), 1367 (2011).
23. Liu, D.; Chen, X.; Yue, Y.; Chen, M. & Wu, Q. Structure and Rheology of Nanocrystalline Cellulose. *Carbohyd. Polym.* **84**, 316–322 (2011).
24. Yarin, A. L.; Koombhongse, S. & Reneker, D. H. Bending Instability in Electrospinning of Nanofibers. *J. Appl. Phys.* **89**, 3018 (2001).
25. Reneker, D. H.; Yarin, A. L.; Fong, H. & Koombhongse, S. Bending Instability of Electrically Charged Liquid Jets of Polymer Solutions in Electrospinning. *J. Appl. Phys.* **87**, 4531 (2000).
26. Zhou, C.; Chu, R.; Wu, R. & Wu, Q. Electrospun Polyethylene Oxide/Cellulose Nanocrystal Composite Nanofibrous Mats with Homogeneous and Heterogeneous Microstructures. *Biomacromolecules* **12**, 2617–25 (2011).
27. Demir, M. M.; Yilgor, I.; Yilgor, E. & Erman, B. Electrospinning of Polyurethane Fibers. *Polymer* **43**, 3303–3309 (2002).
28. Reneker, D. H. & Chun, I. Nanometre Diameter Fibres of Polymer, Produced by Electrospinning. *Nanotechnol.* **7**, 216–223 (1996).
29. Hsu C. M.; Shivkumar, S. *N,N*-Dimethylformamide Additions to the Solution for the Electrospinning of Poly(ϵ -Caprolactone) Nanofibers. *Macromol. Mater. Eng.* **289**, 334–340 (2004).
30. Hsu, C. M.; Shivkumar, S. Nano-Sized Beads and Porous Fiber Constructs of Poly(ϵ -Caprolactone) Produced by Electrospinning. *J. Materi. Sci.* **39**, 3003–3013 (2004).
31. Ku, B. K.; Kim, S. S. Electro Spray Characteristics of Highly Viscous Liquids. *J. Aerosol Sci.* **33**, 1361–1378 (2002).
32. Wang, B.; Li, B.; Xiong, J. & Li, C. Y. Hierarchically Ordered Polymer Nanofibers via Electrospinning and Controlled Polymer Crystallization. *Macromolecules* **41**, 9516–9521 (2008).

33. Yoshioka, T.; Dersch, R.; Tsuji, M. & Schaper, A. K. Orientation Analysis of Individual Electrospun PE Nanofibers by Transmission Electron Microscopy. *Polymer* **51**, 2383–2389 (2010).
34. Chen, X.; Dong, B.; Wang, B.; Shah, R. & Li, C. Y. Crystalline Block Copolymer Decorated, Hierarchically Ordered Polymer Nanofibers. *Macromolecules* **43**, 9918–9927 (2010).
35. Xu, H.; Xie, L.; Chen, Y.; Huang, H.; Xu, J. & Zhong, G. Strong Shear Flow-Driven Simultaneous Formation of Classic Shish- Kebab, Hybrid Shish-Kebab, and Transcrystallinity in Poly(lactic acid)/Natural Fiber Biocomposites. *ACS Sustainable Chem. Eng.* **1**(12), 1619-1629 (2013).
36. Xu, X.; Jiang, L.; Zhou, Z.; Wu, X. & Wang, Y. Preparation and Properties of Electrospun Soy Protein Isolate/Polyethylene Oxide Nanofiber Membranes. *ACS Appl. Mater. Interfaces* **4**, 4331–4337 (2012).
37. Bai, H.; Deng, H.; Zhang, Q.; Wang, K.; Fu, Q.; Zhang, Z. & Men, Y. Effect of Annealing on the Microstructure and Mechanical Properties of Polypropylene with Oriented Shish-Kebab Structure. *Polym. Int.* **61**, 252–258 (2012).
38. Somani, R. H.; Yang, L.; Sics., I.; Hsiao, B. S.; Pogodina, N.; Winter, H. H.; Agarwal, P.; Fruitwala, H. & Tsou, A. Orientation Induced Crystallization in Isotactic Polypropylene Melt by Shear Deformation. *Macromol. Symp.* **185**, 105–117 (2002).
39. Ten, E.; Jiang, L. & Wolcott, M. P. Crystallization Kinetics of Poly(3-Hydroxybutyrate-co-3-Hydroxyvalerate)/Cellulose Nanowhiskers Composites. *Carbohydr. Polym.* **90**, 541–550 (2012).
40. Liu, L. Q.; Tasis, D.; Prato, M. & Wagner, H. D. Tensile Mechanics of Electrospun Multiwalled Nanotube/Poly(methyl methacrylate) Nanofibers. *Adv. Mater.* **19**, 1228–1233 (2007).
41. Ye, H.; Lam, H.; Titchenal, N.; Gogotsi, Y. & Ko, F. Reinforcement and Rupture Behavior of Carbon Nanotubes–Polymer Nanofibers. *Appl. Phys. Lett.* **85**, 1775 (2004).
42. Sui, X.; Wagner, H. D. Tough Nanocomposites: The Role of Carbon Nanotube Type. *Nano Lett.* **9**, 1423–1426 (2009).
43. Pai, C. L.; Boyce, M. C. & Rutledge, G. C. On the Importance of Fiber Curvature to the Elastic Moduli of Electrospun Nonwoven Fiber Meshes. *Polymer* **52**, 6126–6133 (2011).
44. Young, R. J. & Lovell, P. A. *Introduction to Polymers*: CRC Press: Boca Raton (2010).
45. Agarwal, B. D.; Broutman, L. J. & Chandrashekhara, K. *Analysis and performance of fiber composites*: John Wiley & Sons, Inc.: Hoboken (2010).

CHAPTER 4. POROUS CORE-SHELL CARBON FIBERS DERIVED FROM LIGNIN AND CELLULOSE NANOFIBRILS*

4.1. Abstract

This letter reports a method to produce lignin and cellulose nanofibrils (CNFs) based porous core-shell carbon fibers via co-electrospinning followed by controlled carbonization. Lignin formed the shell of the fiber while CNF network formed the porous core. Polyacrylonitrile (PAN) was added to the lignin solution to increase its electrospinnability. CNFs were surface acetylated and dispersed in silicon oil to obtain a homogenous dispersion for electrospinning the porous core. Hollow lignin fibers were also electrospun using glycerin as the core material. FT-IR measurements confirmed the CNF acetylation. SEM micrographs showed the core-shell and hollow fiber nanostructures before and after carbonization. The novel carbon fibers synthesized in this study exhibited increased surface area and porosity that are promising for many advanced applications.

4.2. Introduction

Carbon nanofibers have received tremendous research interest because of their great potential in energy, chemical sensing and adsorption, and catalysis applications. Synthesis of carbon nanofibers based on renewable materials represents a relatively new but high-impact

* The content in this chapter was co-authored by Xuezhu Xu, Jian Zhou, Long Jiang, Gilles Lubineau, Ye Chen, Xiang-fa Wu, Robert Piere. The content in this chapter was published in *Materials Letters* 07/2013; 109: 175-178. Xuezhu Xu and Long Jiang generated the idea. Xuezhu Xu prepared samples and designed the experiments. Jian Zhou helped with electrospinning experiment. Xiangfa-Wu and Robert Piere provided useful discussions and suggestions. Gilles Lubineau and Long Jiang supervised the project, provided useful discussions and suggestions. Xuezhu Xu drafted the manuscript.

research direction with obvious environmental benefits. Lignin and cellulose are two most abundant natural polymers and have been shown to be effective carbon precursors. Submicron diameter carbon fibers has been produced by carbonizing electrospun lignin fibers.¹ Natural cellulose fibers have been converted into carbon fibers through controlled pyrolysis and the effects of the pyrolysis conditions on the conversion and the properties of the obtained carbon fibers have been studied.^{2,3,4} CNFs are one type of cellulose nanofibers that have very large aspect ratio and form percolated network structures in water or polymer matrices. They have been under intensive investigation for use as potential biobased nanoreinforcements in polymer nanocomposites.⁵

The performance of carbon nanofibers in many applications depends on their surface areas. Hollow fibers,⁶ porous fibers⁷ and fibers with carbon nanotubes grown on the fiber surface⁸ have been developed to increase the surface area. In this letter, we reported the preparation of core-shell carbon fibers via electrospinning biobased precursors followed by controlled carbonization. Lignin was used as the spinning material for the shell part of the fiber while a portion of PAN was added to increase its spinnability. CNFs were used to form the porous core structure of the fiber. The obtained core-shell carbon fibers exhibited increased surface area which is expected to improve their performance in many advanced applications.

4.3. Materials, preparations and characterizations

4.3.1. Materials

Alkali kraft lignin and PAN with an average Mw of 150,000 were purchased from Sigma-Aldrich. Cellulose nanofibril gel (2.3 wt%) produced by repeated mechanical grinding⁹ was kindly provided by USDA Forest Products Laboratory (Madison, WI). N,N-Dimethylformamide (DMF) ($\geq 99.8\%$), chloroform ($\geq 99.8\%$), glacial acetic acid ($\geq 99.7\%$),

sulfuric acid (95.0-98.0%), acetic anhydride ($\geq 97\%$), and poly(dimethylsiloxane) (96%) were purchased from Fisher Scientific. Ethyl alcohol (EtOH, 100%) was purchased from VWR. All chemicals are used as received without further purification.

4.3.2. Preparation of acetylated CNFs/silicone oil suspension

CNFs were dispersed in DMF through solvent exchange before acetylation reaction. 100 mL DMF was gradually added into 43.48 g CNF gel (1 g dry CNFs) under continuous stirring at 100 °C. 50 g white gel-like CNF/DMF suspension (2 wt%) was obtained after ~3 hour stirring. Acetylation was conducted in a three-neck round flask under N₂ protection. 40 mL acetic acid and 2 mL sulfuric acid were added into the 50 g CNF/DMF suspension at room temperature to activate the CNF surfaces (5 hours). Then 40 mL acetic anhydride was added to trigger the acetylation. The reaction lasted 7 hours at 90 °C under continuous stirring. The reaction product was transferred to a 2,000 mL narrow-neck flask and then 1,000 mL EtOH was added afterward. The mixture was stirred at room temperature for over 30 hours. The precipitate (i.e., acetylated CNFs) of the mixture was collected and unreacted chemicals were removed by repeated centrifugation (Eppendorf centrifuge 5810, 4,000 rpm for 2 min). The acetylated CNFs were dispersed in 60 mL silicone oil (90 °C) using a high speed homogenizer (IKA T18 basic) at ~500 rpm until the mixture became transparent (about 1 hour). 10 mL chloroform was added into the suspension to further increase the dispersion of the acetylated CNFs. Finally, a homogenous acetylated CNFs/silicone oil/chloroform mixture was obtained which remained stable over 24 hours.

4.3.3. Electrospinning and fiber carbonization

Lignin and PAN were dissolved in DMF by stirring overnight at 60 °C. The ratio between lignin and PAN was 1:1 and the total solid content of the solution was 17 wt%. The

obtained solution was used to spin the shell part of the core-shell fibers while the acetylated CNF/silicone oil/chloroform mixture was used for the core part. Electrospinning was conducted on an EC-DIG electrospinning apparatus (IME Technologies, Netherlands) equipped with a co-axial spinneret with the inner and outer gauges being 19 and 15, respectively. A voltage of 17 kV was applied between the needle and the fiber collector (grounded). The feeding rates of the core and shell materials were adjusted to both 0.03 mL/h. The distance between the needle tip and the collector was kept at ~20 cm. Pure glycerin was used for the core material when hollow lignin/PAN fiber was produced. All spinning processes were performed under a relative humidity of 63% at 21 °C.

The obtained fibers were carbonized in a home-made horizontal tubular furnace. The temperature of the furnace was first increased from 21 to 550 °C at 10 °C/min and maintained for 2 h in a mixture atmosphere of 500 ml/min hydrogen (H₂) and 1 ml/min argon (Ar). Then the temperature was increased to 1000 °C at 10 °C/min and maintained for 1 h in 500 ml/min Ar to fulfill the carbonization process.

4.3.4. Characterizations

Scanning electron microscope (SEM) imaging was performed on a Quanta 3D FEG (FEI) operating at 10 kV. Cross-sections of the electrospun nanofibers were obtained by first dipping the fibers in liquid nitrogen followed by a clean cut using a razor blade. Carbonized nanofibers were directly cut without the cryo-treatment. Before imaging, the samples were coated with a thin layer of Au using an Emitech K575X sputter coater. FT-IR spectra were obtained on a Nicolet iS10 from Thermo Fisher Scientific Inc. The fiber samples were ground with KBr (ratio 1:100) and molded into discs. The spectrum between 4,000 and 500 cm⁻¹ was collected for each sample based on 32 scans with a resolution of 4 cm⁻¹. The spectra were processed and analyzed

using OMNIC 8.1 (Thermo Scientific). Background reference was obtained by scanning a pure KBr disc under the same condition.

4.4. Results and discussion

CNFs were acetylated because they could not be homogeneously dispersed in non-polar silicon oil due to their high surface polarity. This high polarity can be greatly decreased by acetylation. The reaction scheme of CNF surface acetylation is shown in **Figure 4.1a**. The active hydroxyl groups (-OH) on the surfaces of CNFs react with acetic acid or acetic anhydride to produce acetyl groups (-COCH₃).¹⁰ The acetylation of CNFs lowers their hydrophilicity and thus improves their dispersion in non-polar solvents such as silicon oil. The stability of the acetylated CNF dispersion can be further improved by adding chloroform into silicon oil due to the similarity between the polarity of the acetylated CNFs and chloroform.¹⁰ The suspension remained stable over 72 h. In **Figure 4.1(b)**, the acetylated CNFs is dispersed in a silicon oil/chloroform mixture (1:6), producing a stable translucent suspension. This suspension was used to spin the core part of the core-shell fibers in electrospinning.

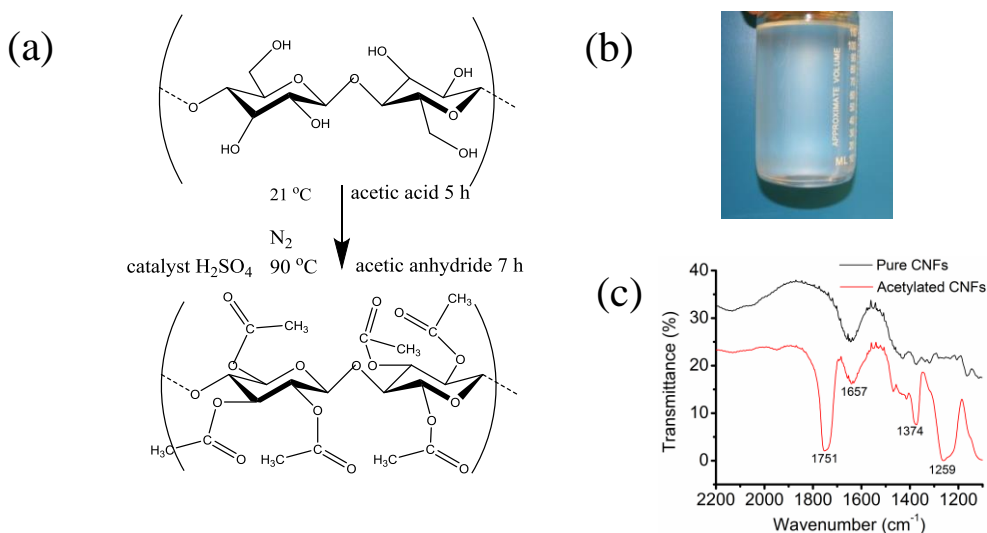


Figure 4.1. (a) Reaction scheme of CNF acetylation; (b) Acetylated CNFs dispersed in a silicone oil/chloroform mixture (~0.5 wt%) and (c) FT-IR spectra of pure CNFs and surface modified CNFs.

Figure 4.1c compares the FT-IR spectra for pure and surface-modified CNFs. The peak at 1657 cm^{-1} , which does not change after acetylation, can be assigned to the bending motion of absorbed water and the carboxylate groups yielded during CNF production.¹¹ Three new peaks appear on the spectrum of the acetylated CNFs at wavenumbers of 1751 , 1374 and 1259 cm^{-1} , which are attributed to carbonyl stretching ($\nu_{\text{C=O}}$), methyl in-plane bending ($\delta_{\text{C-H}}$) and C-O stretching ($\nu_{\text{C-O}}$), respectively.¹⁰ These new vibrational peaks confirm the successful acetylation of CNFs.

Microstructures of the electrospun lignin/PAN hollow nanofibers are shown in **Figure 4.2a**. The hollow fibers show an average outer diameter (OD) of 476 nm and inner diameter (ID) of 330 nm , resulting in an average wall thickness of $\sim 72\text{ nm}$. The structures suggest that glycerin is an effective liquid for forming and maintaining the tubular structure of the nanofibers.

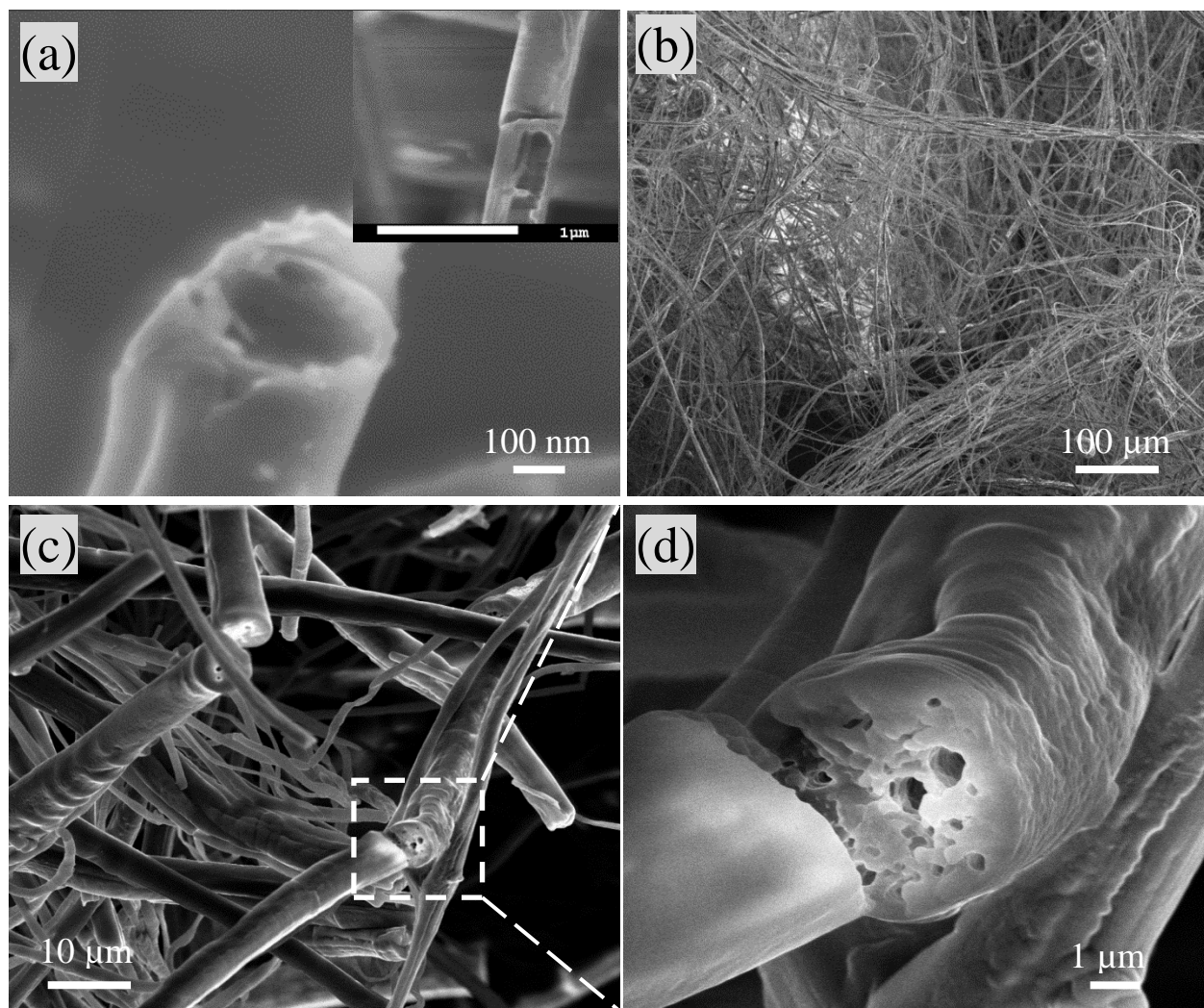


Figure 4.2. SEM images of electrospun lignin/PAN hollow fibers (a) and CNFs-lignin/PAN core-shell fibers (b, c, d).

Core-shell CNF-lignin/PAN fibers are shown in **Figures 4.2b, c, and d**. The fibers exhibit relatively smooth, bead-free surfaces with an average fiber diameter of 3.5 μm . The relatively large diameter is commonly observed in electrospinning core-shell fibers^{6,12} due to utilization of the outer capillary with a large diameter (1.5 mm). The average draw ratio (DR) of the fibers is estimated to be 430 based on the diameters of the capillary and the fiber. **Figure 4.2d** shows the cross sectional surface of a cryo-cut core-shell fiber. The porous core of the fiber

is mainly consisted of CNF network. At this stage migration of polymers (i.e., lignin and PAN) from the shell portion to the core portion cannot be completely excluded.

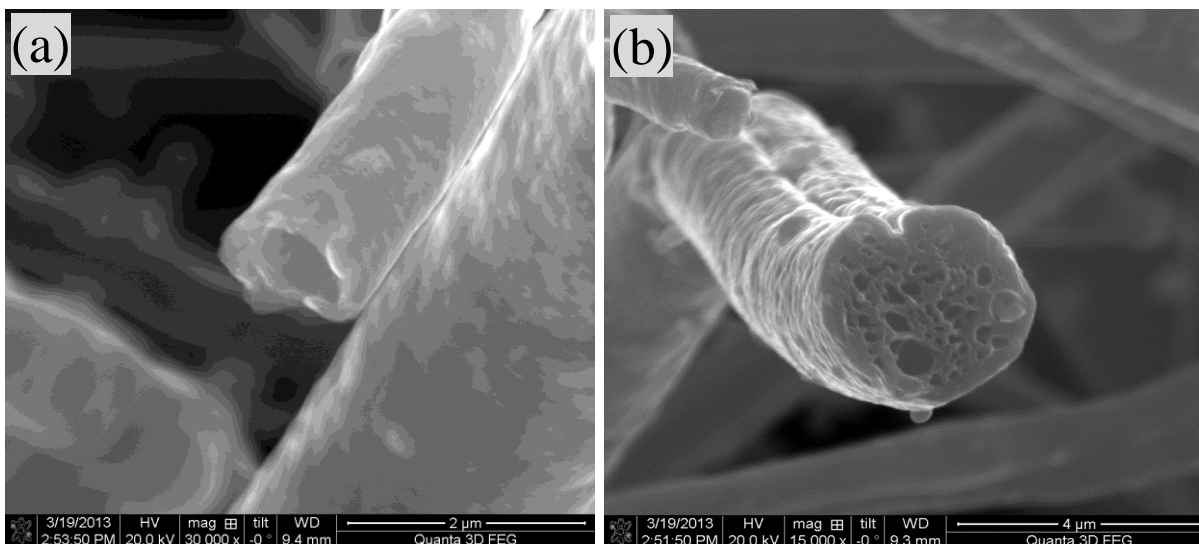


Figure 4.3. SEM images of carbonized lignin/PAN hollow fiber (a) and CNFs-lignin/PAN core-shell fiber (b).

Figure 4.3 shows the cross section of carbonized hollow and core-shell fibers. The fibers virtually maintained their initial structures after the carbonization process. Further material characterizations such as surface area and conductivity measurement are under way. The hollow and porous core-shell fibers provide much larger surface area and porosity than do the solid fibers with the same diameter. The increased surface area and porosity provide an improved platform for various interactions between the fibers and their surrounding environments and therefore potentially enhance the performance of the fibers in some advanced applications including energy storage, gas sensing and adsorption, catalysis, and environmental remediation (e.g., chemical or biological substance detection and removal). To increase the production rate of the core-shell carbon fibers, a mass production method of nanofibers such as bubble electrospinning¹³ will be considered.

4.5. Conclusions

In this study we have produced novel hollow and porous core-shell carbon fibers using mostly biobased materials. Lignin was readily electrospun into hollow fibers or fiber shell after adding PAN as a co-spinning polymer. CNFs were difficult to disperse in non-polar solvents and surface acetylation had to be performed. Acetylated CNF dispersion in silicon oil/chloroform mixture was stable and suitable for electrospinning to form fiber core. The obtained hollow and core-shell fibers were successfully carbonized without causing obvious changes on the fiber structure. The two types of new fibers, especially the porous core-shell one, exhibit increased surface area and porosity over the conventional solid fibers and are expected to have a great potential in many advanced applications.

4.6. References

1. Ruiz-Rosas, R. *et al.* The production of submicron diameter carbon fibers by the electrospinning of lignin. *Carbon* **48**, 696–705 (2010).
2. Nogi, M.; Kurosaki, F.; Yano, H.; Takano, M. Preparation of nanofibrillar carbon from chitin nanofibers. *Carbohydr. Polym.* **81**, 919–924 (2010).
3. Yutaka, K.; Miu, O.; Yhuki, Y.; Emi, S.; Akira, Y. Norio, I.; Noriko, Y.; Masaya, K. No Title. *Carbon 2012* **50**, 4750–4764 (2012).
4. Jazaeri, E.; Zhang, L.; Wang, X.; Tsuzuki, T. No Title. *Cellulose* **18**, 1481–1485 (2011).
5. Xu, X., Liu, F., Jiang, L. & Zhu, J. Cellulose Nanocrystals vs. Cellulose Nanofibrils: A Comparative Study on Their Microstructures and Effects as Polymer Reinforcing Agents. *ACS Applied Materials & Interfaces* **5**, 2999–3009 (2013).
6. Lallave, M. *et al.* Filled and Hollow Carbon Nanofibers by Coaxial Electrospinning of Alcell Lignin without Binder Polymers. *Advanced Materials* **19**, 4292–4296 (2007).
7. Ji, L.; Lin, Z.; Medford, A. J. Zhang, X. Porous carbon nanofibers from electrospun polyacrylonitrile/SiO₂ composites as an energy storage material. *Carbon* **47**, 3346–3354 (2009).
8. Hou, H. & Reneker, D. H. Carbon Nanotubes on Carbon Nanofibers: A Novel Structure Based on Electrospun Polymer Nanofibers. *Advanced Materials* **16**, 69–73 (2004).

9. Wang, Q. Q. *et al.* Morphological development of cellulose fibrils of a bleached eucalyptus pulp by mechanical fibrillation. *Cellulose* **19**, 1631–1643 (2012).
10. Tingaut, P., Zimmermann, T. & Lopez-Suevos, F. Synthesis and characterization of bionanocomposites with tunable properties from poly(lactic acid) and acetylated microfibrillated cellulose. *Biomacromolecules* **11**, 454–64 (2010).
11. Zussman, E., Yarin, A. L., Bazilevsky, A. V., Avrahami, R. & Feldman, M. Electrospun Polyaniline/Poly(methyl methacrylate)-Derived Turbostratic Carbon Micro-/Nanotubes. *Advanced Materials* **18**, 348–353 (2006).

CHAPTER 5. FLEXIBLE, HIGHLY GRAPHITIZED CARBON AEROGEL BASED ON BACTERIAL CELLULOSE/LIGNIN: CATALYST-FREE SYNTHESIS AND ITS APPLICATION IN ENERGY STORAGE DEVICES*

5.1. Abstract

Currently most carbon aerogels are made of carbon nanotubes or graphene through a catalyst-assisted chemical vapor deposition method. Biomass based organic aerogels and carbon aerogels, featuring low cost, high scalability and small environmental footprint, represent an important new research direction in (carbon) aerogel development. Cellulose and lignin are the two most abundant natural polymers in the world and the aerogels based on them are very promising. Classic silicon aerogels and available organic resorcinol-formaldehyde (RF) or lignin-resorcinol-formaldehyde (LRF) aerogels are brittle and fragile; toughening of the aerogels is highly desired to expand their applications. This study reports the first attempt to toughen the intrinsically brittle LRF aerogel and carbon aerogel using bacterial cellulose. The facile process is catalyst-free and cost-effective. The toughened carbon aerogels, consisting of blackberry-like, core-shell structured, and highly graphitized carbon nanofibers, are able to undergo at least 20%

* The content in this chapter was co-authored by Xuezhu Xu, Jian Zhou, D. H. Nagaraju, Long Jiang, Val R. Marinov, Gilles Lubineau, Husam N. Alshareef and Myungkeun Oh. The content in this chapter was published in *Advanced Functional Materials* 04/2015; 25(21): 3193-3202. Xuezhu Xu and Long Jiang generated the idea. Xuezhu Xu prepared samples and designed the experiments. Jian Zhou helped with SEM and electrical conductivity experiment. D. H. Nagaraju contributed on the electrochemical experiments. Long Jiang supervised the project; Gilles Lubineau provided useful discussions and suggestions. Xuezhu Xu drafted the manuscript.

reversible compressive deformation. Due to their unique nanostructure and large mesopore population, the carbon materials exhibit an areal capacitance higher than most of the reported values in the literature. This property makes them suitable candidates for flexible solid-state energy storage devices. Beside energy storage, the conductive interconnected nanoporous structure can also find applications in oil/water separation, catalyst supports, sensors, etc.

5.2. Introduction

Aerogels, a family of three-dimensional (3D) nanostructured porous materials characterized by low density, large porosity, high specific surface area and low thermal conductivity, have been used in a broad range of important applications. While silica aerogels prepared by CO₂ supercritical drying are the most classic aerogels, carbon aerogels have attracted increasing research attention in recent years due to their great potential in applications such as supercapacitors,¹ gas sensors,² absorbents,³ and catalyst supports.⁴ Current carbon aerogel research is mainly focused on novel precursors, drying methods, nanostructures, and mechanical property improvements (especially toughness) of the aerogels.⁵

Regarding the novel precursors, biomass such as coconut shells,⁶ cellulose⁷⁻¹⁰ and lignin¹¹ have drawn great interest because of their renewability, low cost and non-toxicity. Lignin as an abundant carbon-rich biopolymer comprises three different phenolic alcohol monomers linked together by C-C or C-O-C linkages to form a 3D polymer network. Lignin shows chemical reactivity similar to resorcinol and has been used to substitute resorcinol in producing lignin-resorcinol-formaldehyde (LRF) aerogels through freeze-drying¹² and freeze-thaw-drying¹³. The aerogels exhibit a network structure of interconnected zero-dimensional nano-aggregates, which form numerous 15-30 nm mesopores inside the aerogels. Lignin-phenol-

formaldehyde,¹⁴ lignin-tannin,¹⁵ and lignin-cellulose^{16,17} aerogels have also been synthesized using similar techniques.

Cellulose, synthesized by plants, algae and bacteria, is the most abundant natural polymer on the earth. Bacterial cellulose (BC) gels are produced by bacteria *gluconacetobacter xylinus* in culture and they comprise high-crystallinity (up to 90%), ultrafine (5~50 nm) cellulose nanofibers. BC nanofibers share many properties of plant-based cellulose nanofibers, including outstanding mechanical properties, rich surface chemistry, nontoxicity, biocompatibility and high transparency (in films). However, BC in general is considered superior to the plant-based cellulose nanofibers because they are of higher crystallinity and free of lignin/semicellulose and their production requires no harsh chemical/mechanical treatments. BC gels have been converted into aerogels through freeze-drying, which are then used as templates to grow other nanomaterials such as anatase nanowires¹⁸ and magnetic nanoparticles.¹⁹ BC-based aerogels have further been converted into carbon aerogels through pyrolysis, which exhibit high mechanical flexibility, outstanding fire resistance and strong adsorption capability²⁰.

The fragility of the lignin-based aerogels, which originates from the interconnected nano-aggregates inside the gels, is the main drawback of these innovative products and therefore has limited their applications.²¹ The main goal of this study is to develop flexible lignin-based aerogels and carbon aerogels. For the first time, both gels are toughened using BC as a scaffold. BC is impregnate with LRF solution and BC-LRF hydrogels are obtained through polycondensation of LRF. BC-LRF aerogels and carbon aerogels are subsequently produced using CO₂ supercritical drying and catalyst-free carbonization. The obtained carbon aerogels exhibit a unique blackberry-like nanostructure and their mechanical behavior is similar to that of carbon nanotube- or graphene-based carbon sponges, which are generally synthesized by

catalyst-assisted growing processes.^{3,22,22,23} Catalyst-free synthesis is a more cost-effective and environment-friendly process and the obtained carbons need no further treatments for catalyst removal. The blackberry-like structure, with the BC-converted carbon nanofibers as the backbone and the LRF-converted carbon nano-aggregates as the blackberry-like coating, shows modest surface areas but surprisingly high areal capacitance. This high value is due to the highly conductive BC carbon fiber network and the porous “blackberry” surface suitable for ion storage.

5.3. Experimental section

5.4.1. Materials and BC-LRF hydrogel preparation

Alkali lignin ($M_w = 10,000$), resorcinol (> 99 %) and formaldehyde (37 % aqueous solution) were purchased from Sigma-Aldrich. Nitric acid (70 %) was purchased from EMD and sodium hydroxide from ACROS. All the chemicals were used as received. Bacterial cellulose (BC) gel cubes were produced by Thai Agri Foods Public Company. The cubes were cleaned by soaking in distilled water for 15 days and the water was changed every 24 h. The cleaned gel had a BC concentration of 0.5 %. To prepare LRF hydrogels, lignin, resorcinol, formaldehyde and sodium carbonate were added in 0.25 M sodium hydroxide to obtain a solution. The total concentration of the lignin, resorcinol and formaldehyde in the solution was maintained at 10 wt% and the concentration of the sodium carbonate was fixed at 0.05 wt%. LRF hydrogels were obtained after the solutions were kept at 80 °C for 48 h. To produce BC-LRF hydrogels, the cleaned BC gel cubes (~ 8.25 g) were impregnated with the LRF gel precursors by immersing the cubes in the solutions. Sonication was applied to accelerate the impregnation process. The same condition was used to gel the LRF precursor inside the BC cubes.

5.4.2. Preparation of BC-LRF carbon aerogel

The BC-LRF hydrogels were converted to aerogels by CO₂ supercritical drying. The hydrogels first underwent solvent exchange to replace their contained water with ethanol, and then were put in a custom-built supercritical dryer. The dryer was immediately filled with 600 mL ethanol, which was gradually exchanged with liquid CO₂ (bone dry, Airgas) according to the following steps. 600 mL liquid CO₂ was added to the dryer and the pressure was increased to 5.5 MPa while maintaining the temperature at 15 °C. The dryer was drained after 4 hours and a fresh amount of liquid CO₂ was added. This rinse process was repeated ~15 times to make sure all ethanol was removed. After that, the temperature and pressure were raised to 65 °C and 8.3 MPa, above the critical point for CO₂ (31.1 °C and 7.39 MPa), and the conditions were maintained for 30 min. Finally, the chamber was slowly depressurized at a controlled rate (~ 100 KPa/min) and the BC-LRF aerogels were obtained.

Carbonization of the aerogels was conducted using an Atomate 110 horizontal tube furnace. The process included a sequence of steps: 30 °C - 500 °C temperature ramp at 10 °C/min, 100 min isothermal holding, 500 °C to 1000 °C ramp at 20 °C/min, and finally 60 min isothermal holding. 200 sccm argon flow was supplied during the whole process. To increase the wettability of the obtained carbon aerogels, the materials were treated using 70 % nitric acid at 60 °C for 90 min and then washed with 0.2 M sodium hydroxide and distilled water thoroughly.

5.4.3. Characterizations

A JEOL 7600 field-emission scanning electron microscopy (FE-SEM) operating at 2 kV was used to study the morphology of the obtained organic and carbon aerogels. Transmission electron microscopy (TEM) imaging was performed using a JEOL TEM-2100 equipped with a LaB6 emitter. To prepare the TEM samples, the carbon aerogel was dispersed in ethanol by

mechanical stirring and a drop of the dispersion was placed on a 300-mesh Formvar-coated carbon film copper grid. Surface chemical bonding of the BC-LRF carbon aerogels was characterized by Fourier transform infrared spectroscopy (FTIR) using a Nicolet 6700 spectrometer from Thermo Scientific. An average spectrum (4000 to 650 cm^{-1}) for each sample was obtained based on 32 repetitive scans. X-ray photoelectron spectroscopy (XPS) spectra were obtained using a Kratos *Axis Ultra* XPS System. An ASAP2420 surface area and porosity system from Micromeritics was used to determine the surface areas and pore sizes of the organic and carbon aerogels.

To study the electrochemical properties of the BC-LRF carbon aerogels, the aerogels (85 wt%), polytetrafluoroethylene (PTFE) (10 wt%) and acetylene black (5 wt%) were mixed in ethanol by sonication for 30 min to obtain stable dispersions. Electrodes were prepared by coating Ni foam with the dispersions and allowing them to dry at 60 °C for 12 h. The mass loading of the materials is about 2-3 mg/cm. Electrochemical tests were performed using a Biologic VMP3 workstation and a three-electrode configuration with the carbon aerogel as the working electrode, Ag/AgCl as the reference electrode and a platinum wire as the counter electrode. 6 M aqueous potassium hydroxide (KOH) solution was used as the electrolyte. Cyclic voltammetry tests were conducted at different potential scan rates (2 - 25 mV/s) between -1 and 0 V. Galvanostatic charge/discharge experiments were performed using current densities between 0.5 and 5 A/g. The specific gravimetric capacitances were calculated from the discharge curves using the equation $C = (I\Delta t)/(m\Delta V)$, where I is the constant discharge current (A), Δt is the discharge time (s), ΔV is the discharge voltage excluding the IR drop (V), and m is the mass of the active materials. Bare Ni foam was also tested using the identical conditions to estimate its

contribution to the capacitance. Electrochemical impedance spectroscopy (EIS) was conducted within the frequency range between 100 kHz and 0.01 Hz.

5.5. Results and discussion

5.5.1. Formation of lignin-resorcinol-formaldehyde (LRF) hydrogels

Lignin molecules contain reactive sites similar to those of phenol/resorcinol (i.e., ortho, meta and para carbons on the benzene rings) and hence they have been used to partially replace phenol/resorcinol to produce organic hydrogels and aerogels using formaldehyde as the crosslinker.^{14,24} During gelation, formaldehyde first reacts with phenol/resorcinol and lignin to form hydroxymethyl ($-\text{CH}_2\text{OH}$) derivatives of the three chemicals, which subsequently form methylene ($-\text{CH}_2-$) and methylene ether ($-\text{CH}_2\text{OCH}_2-$) bridged gel networks through condensation (**Figure 5.1A**).^{25,26} **Figure 5.1B** shows the Fourier transform infrared spectroscopy (FTIR) spectra of dried LRF gel powder, where the additional peaks at 1473.3 cm^{-1} and 1087.7 cm^{-1} are associated with $-\text{CH}_2$ and C-O bending vibrations of benzyl ether linkages,¹⁴ confirming the successful formation of the gel network. The effect of the L:R:F ratio on the gel property is shown in the ternary plot in **Figure 5.1C**. Rigid gels (LRF9 and LRF10) are formed at low lignin concentrations; weak gels (LRF1, 11, 12, and 13) are formed when the resorcinol concentration is low; strong elastic gels are obtained for samples LRF15, 16, 17, 18, 19 and 20, which are all located in the central region of the triangle. The rest of the samples show no sign of gelation. All the hydrogels exhibit similar densities ($\sim 0.8\text{ g/cm}^3$) and water contents ($\sim 80\%$), suggesting that the different strength/modulus of the gels are mainly due to their varying crosslinking densities. Lignin has less reactive sites and higher steric hindrance compared to phenol/resorcinol because its aromatic rings are highly substituted.¹⁴ Therefore a low resorcinol concentration means reduced reactive carbons available for the reactions with formaldehyde, causing low crosslinking

density and low gel strength/modulus. At low lignin concentrations, there are plenty of resorcinol and formaldehyde to react to form highly crosslinked hard gels.

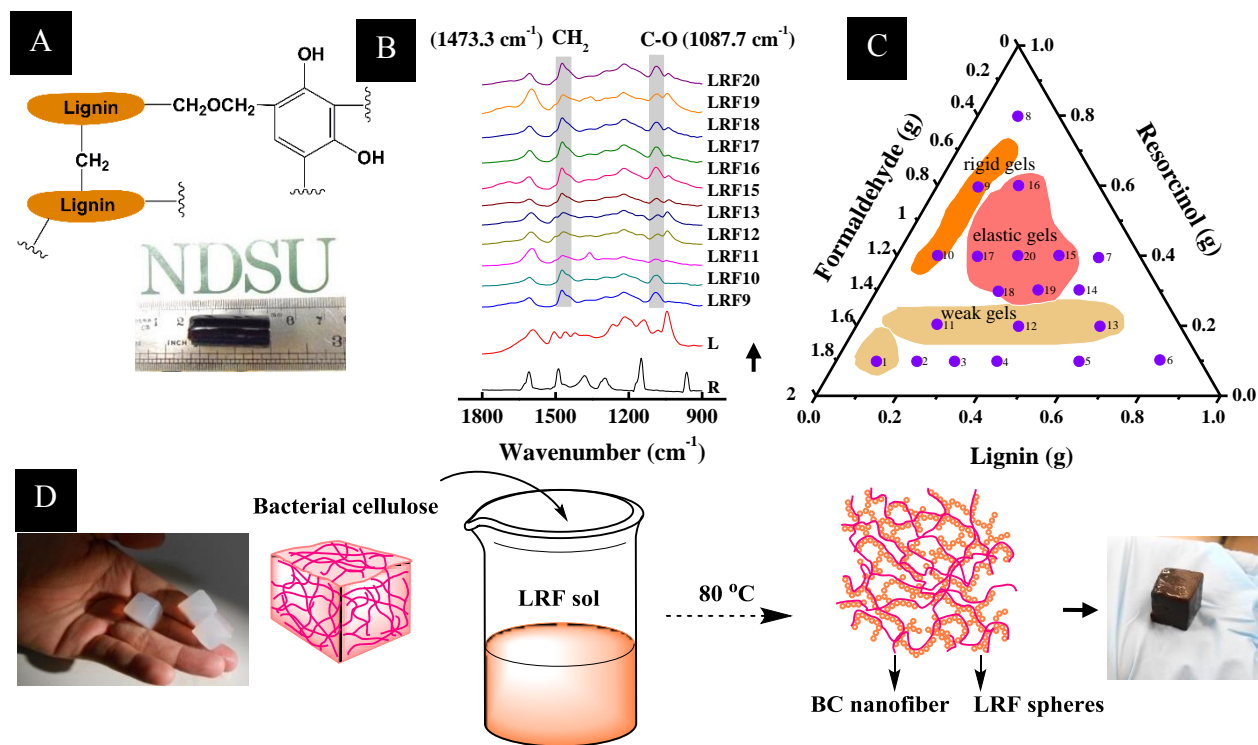


Figure 5.1. (A) Schematic macromolecular structure of a LRF hydrogel and a LRF16 hydrogel sample; (B) FTIR spectra of dried LRF gel powder; (C) Ternary plot of the gel property of various LRF hydrogels (refer to Table 5.S1 for the formulation of each sample); (D) Process to produce BC-LRF hydrogel.

5.5.2. Formation and microstructure of BC-LRF carbon aerogels

After the formulation-gelation behavior relationship was determined, the L:R:F ratios that yielded elastic hydrogels were chosen to synthesize BC-LRF carbon aerogels. BC-LRF hydrogels were first obtained by crosslinking the LRF, which was impregnated into BC (**Figure 5.1D**) and the products were subsequently dried using supercritical CO_2 to produce BC-LRF aerogels. For comparison pure BC and LRF hydrogels were also converted into aerogels using the same drying conditions. SEM micrographs of the BC, LRF and BC-LRF aerogels are compared in **Figure 5.2**. BC nanofibers (**Figure 5.2A**) and LRF nano-aggregates (**Figure 5.2B**)

can be clearly seen in their respective aerogels. In the BC-LRF aerogel, the LRF nano-aggregates were decorated on the surface of the BC nanofibers to form the blackberry-like hierarchical structure (**Figure 5.2C**). The diameter of the BC nanofibers is almost doubled due to the decoration (**Table 5.1**). The carbon aerogels converted from the above aerogels are shown in **Figure 5.2D - I**. The carbonization process preserves the structure of the aerogels, though significantly reduces the size of the nanofibers and nano-aggregates (**Table 5.1**). The BC-LRF carbon aerogel has an average diameter of 41.1 nm and the fibers are continuous. The evolution of the blackberry-like structure from the hydrogel to the carbon aerogel is illustrated in **Figure 5.2J**.

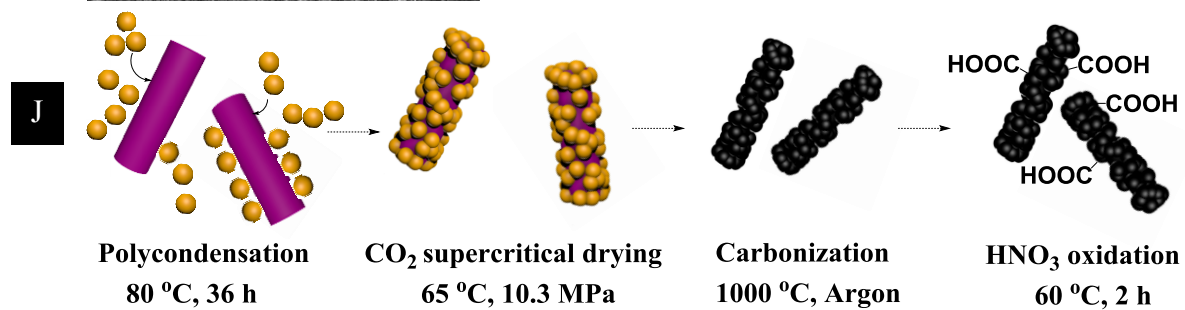
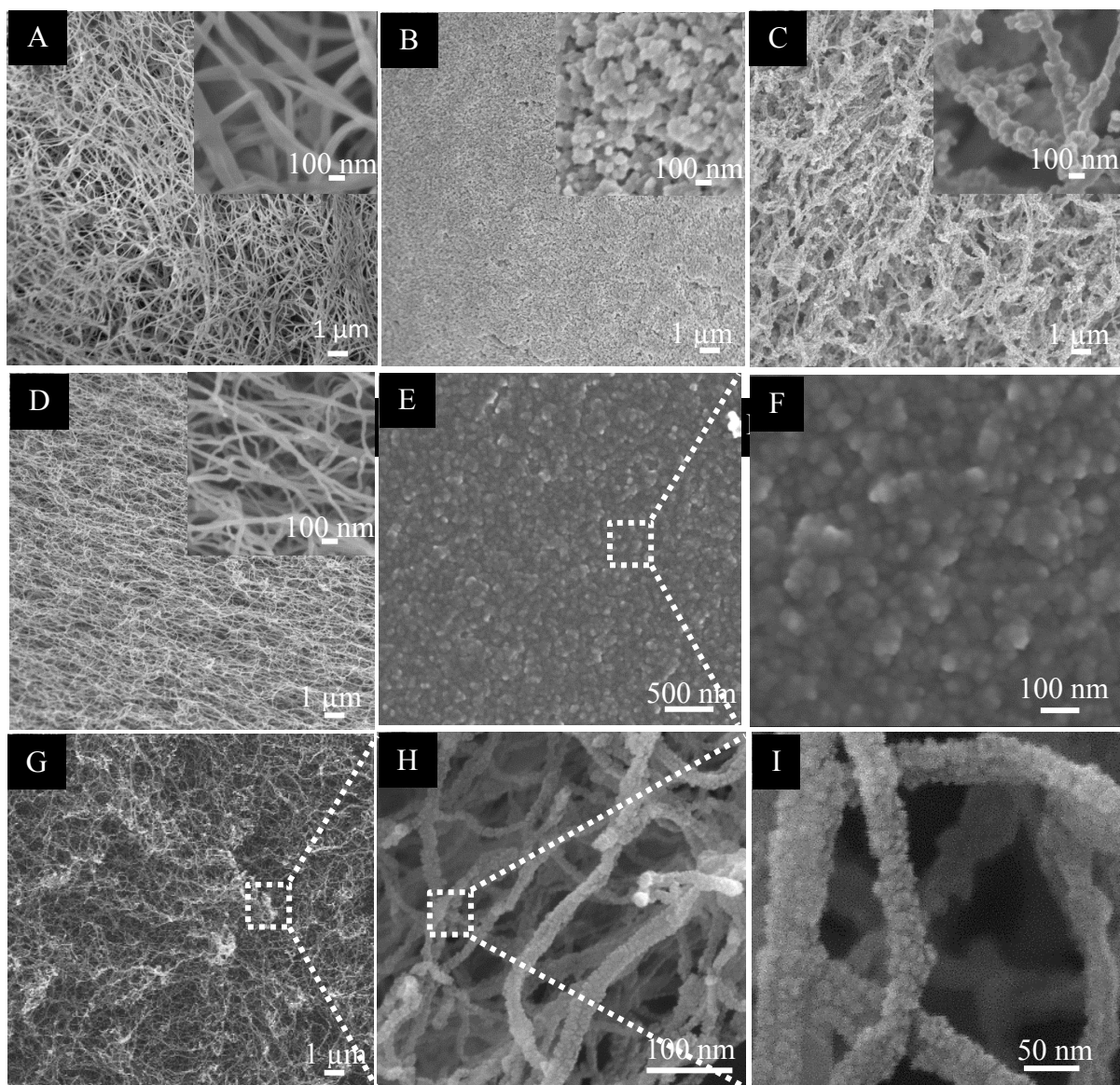


Figure 5.2. SEM images of (A) BC aerogel; (B) LRF16 aerogel; (C) BC-LRF16 aerogel; (D) BC carbon aerogel; (E - F) LRF16 carbon aerogel; (G - I) BC-LRF16 carbon aerogel; (J) Microstructure evolution of the BC-LRF carbon aerogel.

Table 5.1. Sizes of the nanofibers or nano-aggregates in BC, LRF, and BC-LRF aerogels and carbon aerogels.

Material	Mean diameter (nm)	Standard deviation (nm)	Shape
<i>BC aerogel</i>	69.0	24.5	Continuous fiber
<i>LRF aerogel</i>	59.0	8.2	aggregate
<i>BC-LRF aerogel</i>	128.3	47.1	Continuous fiber
<i>BC carbon aerogel</i>	25.6	4.7	Continuous fiber
<i>LRF carbon aerogel</i>	57.9	16.2	aggregate
<i>BC-LRF carbon aerogel</i>	41.1	6.6	Continuous fiber

TEM micrographs of the BC and BC-LRF carbon aerogels are compared in **Figure 5.3**. The BC-converted carbon nanofibers are smooth and continuous (**Figure 5.3A**) while the LRF decoration renders the BC-LRF carbon nanofibers wavy and rough (**Figure 5.3B**). High magnification TEM (**Figure 5.3C**) shows highly ordered graphitic carbon and the selected area electron diffraction (SAED) of the two carbon aerogels display the patterns resembling those of single crystals of AB Bernal-stacked graphite (**Figure 5.3D and 5.3E**).²⁷ Diffraction spot streaking and additional diffraction spots on the patterns can be caused by different reasons, including crystalline lattice distortion,²⁸ rotational stacking faults,²⁹ and overlapping domains.³⁰ The interlayer spacing in **Figure 5.3C** is measured to be 3.12 Å (**Figure 5.3F**), which is close to that of graphite.

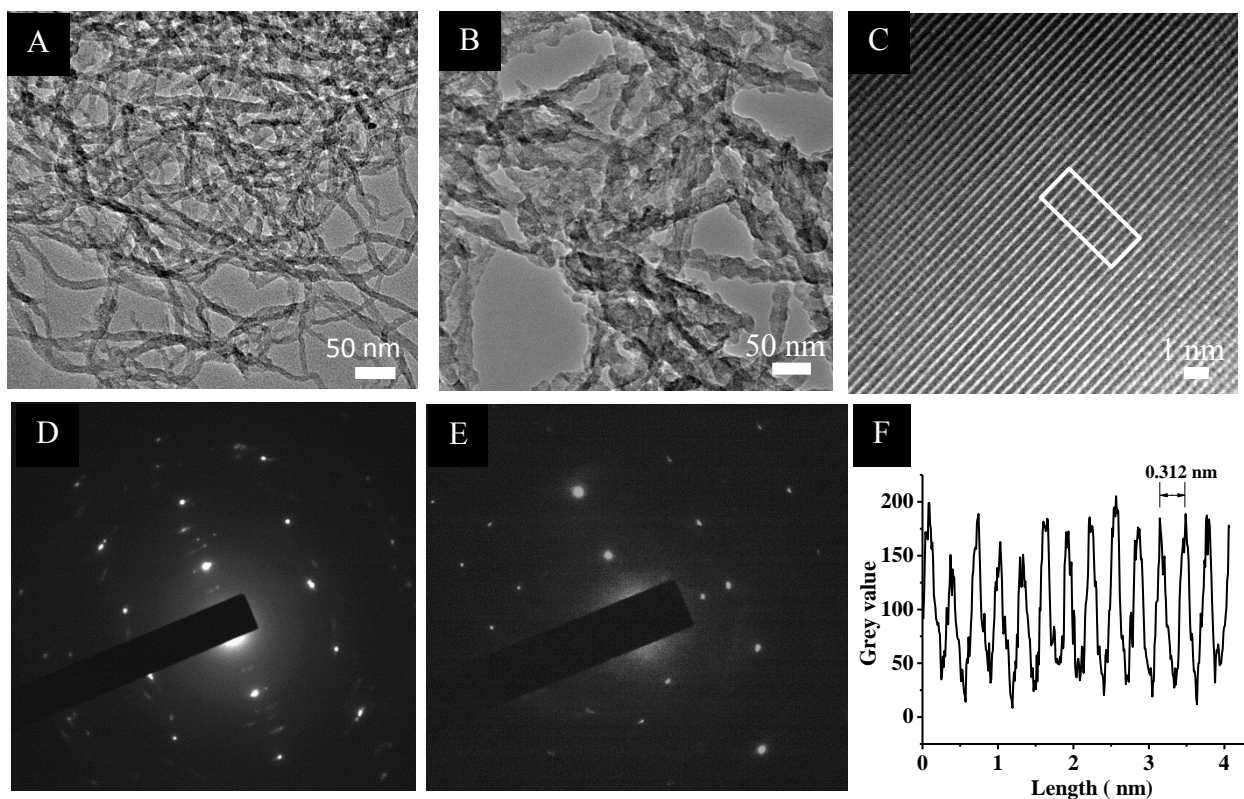


Figure 5.3. (A) TEM image of BC carbon aerogel; (B) TEM image of BC-LRF16 carbon aerogel; (C) high magnification of TEM image of BC carbon aerogel; (D-E) SAED of BC carbon aerogel and BC-LRF16 carbon aerogel; (F) intensity profile taken by the box in C.

5.5.3. Mechanical properties of hydrogels and carbon aerogels

Properties of the pristine BC hydrogel were first evaluated. The hydrogel contains large fraction of water (up to 99.5 wt%) and the water can be squeezed out of the gel without damaging the BC network. **Figure 5.4A and 5.4B** show that the gel cube can be compressed from thickness 13.5 mm to 0.6 mm (a 96% compression ratio) and subsequently recovers to its original size after being immersed in water for over two hours. This result indicates the outstanding strength/elasticity of the BC network and its strong capability to reversibly absorb/desorb liquids under mechanical stresses. Such property is not obtainable by many traditional polymer hydrogels (e.g. polyvinyl alcohol hydrogel), where the absorbed liquids cannot be pressed out without rupturing the gels due to weak gel network and/or overly strong

water-polymer bonding. This unique property of the BC gel allows convenient liquid impregnation for different application purposes.

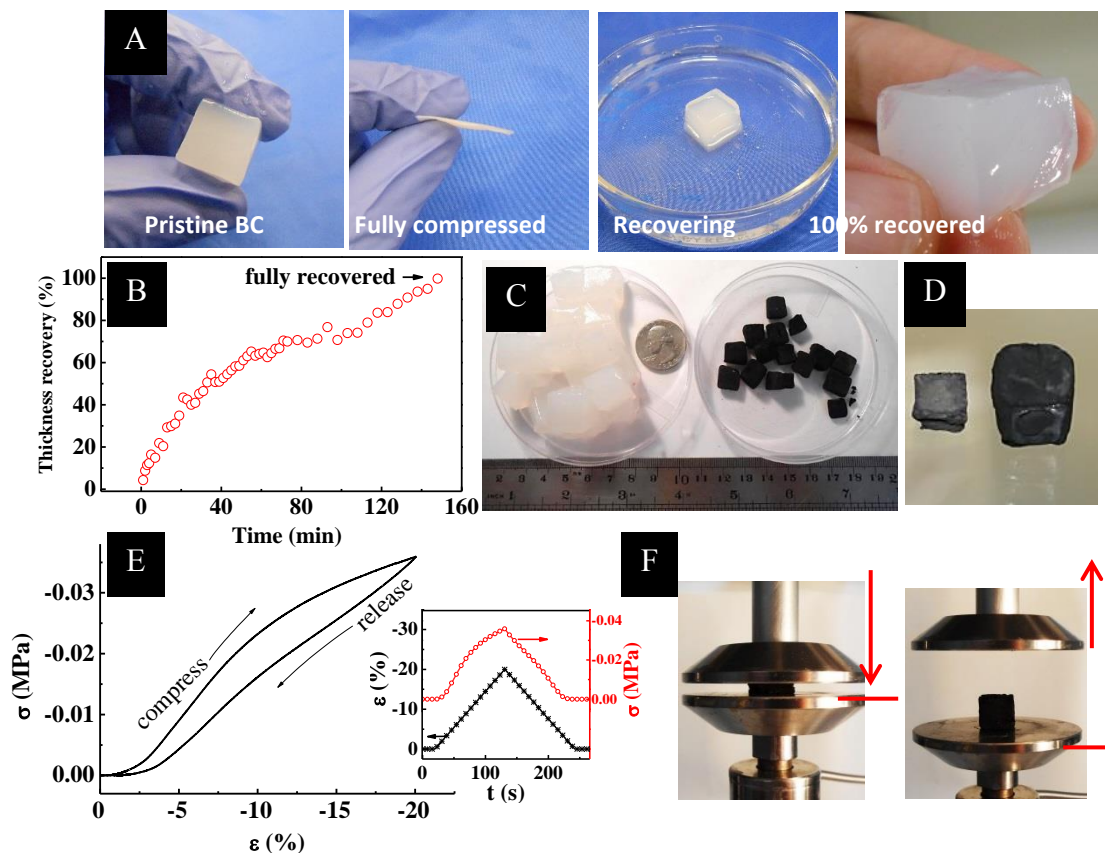


Figure 5.4. (A) Shape recovery of pristine BC hydrogels; (B) Thickness recovery versus time for the hydrogel after being immersed in water; (C) Comparison of BC hydrogels and BC-LRF carbon aerogels; (D) Comparison between BC carbon aerogel and BC-LRF carbon aerogel; (E) Representative compression test curve of BC-LRF16 carbon aerogels; the inset shows the stain and stress profiles; (F) Reversible deformation of the BC-LRF carbon aerogel under 20% strain.

Carbonization of the aerogels reduces their volumes. The volumes of pure BC and BC-LRF carbon aerogels are 20 % and 67 % of their corresponding aerogels (**Figure 5.4C and 4D**). The lower shrinkage rate for BC-LRF is due to the filling of the LRF nano-aggregates that are coated on the BC nanofiber's surfaces. As a result, the density of the BC-LRF16 carbon aerogel increases to $\sim 0.026 \text{ g/cm}^3$ from $\sim 0.013 \text{ g/cm}^3$ of the pure BC carbon aerogel. These densities compare favorably to that of the carbon aerogel made from watermelon (0.058 g/cm^3).³¹ **Figure**

5.4E shows the stress-strain curve for the BC-LRF16 carbon aerogel under cyclic compression at a maximum strain of 20 %. A maximum stress of 0.03 MPa and a Young's modulus of ~ 0.328 MPa were achieved, which are comparable to previously reported values.³¹ The moduli of carbon aerogels are often low and vary significantly depending on their densities.^{32,33} Nardecchia et al. have shown a modulus range between 0.05 and 29 MPa for different carbon aerogels.³⁴ The stress-strain curve in **Figure 5.4E** and the picture in **Figure 5.4F** show that the carbon aerogel can undergo at least 20% reversible deformation. The weak hysteresis loop suggests that part of the mechanical energy is dissipated during the deformation. Traditional RF and LRF carbon aerogels are brittle and fragile.³⁵ The discovery made here to significantly toughen these aerogels using BC nanofiber network removes a serious drawback of the materials and expands their applications.

5.5.4. Surface area and porosity of BC-LRF carbon aerogels

Representative N₂ adsorption-desorption isotherms of the carbon aerogels are shown in **Figure 5.5A**. The initial volume jump at near zero P/P₀, the plateau for 0 < P/P₀ < 0.8 and the hysteresis, and the rapid increase at high P/P₀ indicate the presence of micropores (< 2 nm), mesopores (2 – 50 nm), and macropores (> 50 nm) in the aerogels, respectively.^{36,37} Based on the isotherms, the total specific surface area (SSA_{total}), specific surface areas of micropores (SSA_{micro}) and mesopores (SSA_{meso}), and average pore width of the carbon aerogels were calculated using Barrett-Joyner-Halenda (BJH) and the density functional theory (DFT). The results are summarized in **Table 5.2**. SSA_{total} of the BC-LRF carbon aerogels ranges between 82 and 250 m²/g. Their average pore width varies between 8.5 nm and 19.8 nm, indicating that the majority of the pores are mesopores. Indeed, mesopores account for 71% - 93% of the total surface area as indicated by the SSA_{meso}/SSA_{total} values in **Table 5.2**. This pore size distribution

can also be recognized from **Figure 5.5B**, where the peaks for mesopores largely dominate the chart. Within the micropore size range, **Figure 5.5C** does show that most of the micropores have a width of ~ 0.75 nm or ~ 1.25 nm. The dominant mesopores in the carbon aerogels are most likely inherited from their precursor aerogels, which are produced by CO_2 supercritical drying. Organic aerogels produced using this method have been shown to comprise mainly mesopores: 10.5 \sim 28.9 nm in lignocellulose aerogels,¹³ 20 \sim 40 nm in soy-tannin aerogels³⁸ and 15 \sim 30 nm in LRF aerogels.¹² The high population of mesopores is attributed to the low surface tension at the supercritical CO_2 /hydrogel interface, which hinders the agglomeration of the hydrogel networks when the CO_2 is extracted. The SSA of the aerogels in this study is relatively small compared to many other studies, which can be attributed to their high percentage of mesopores (rather than micropores) and the marked presence of macropores. The lack of micropores in these carbon aerogels is understandable because they do not undergo the acid or alkali assisted high temperature activation process, which is most commonly used to produce carbon materials with extremely high SSA.^{36,39} In the following sections, the electrochemical properties of the carbon aerogels are studied and BC-LRF16 is chosen as a representative sample for discussion.

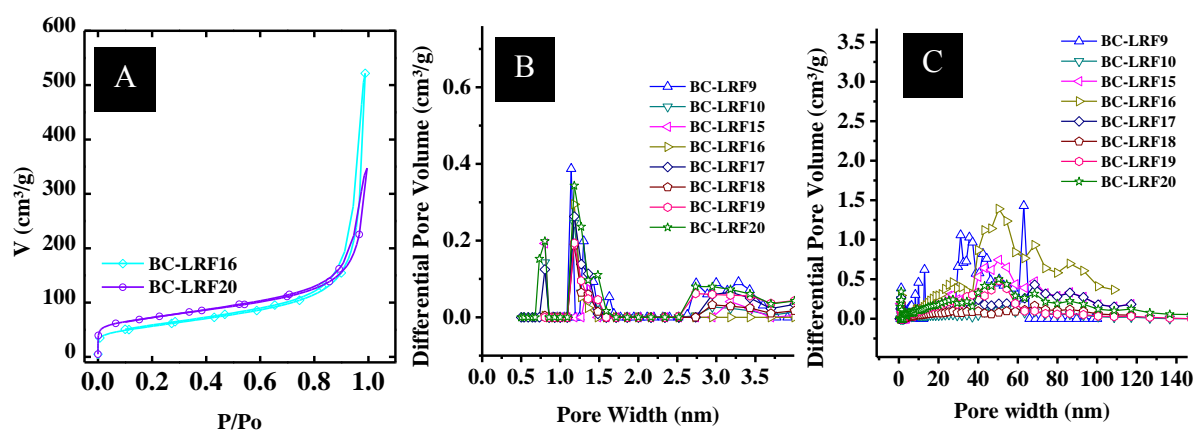


Figure 5.5. (A) Representative N_2 adsorption-desorption isotherms; (B) pore size distributions of the BC-LRF carbon aerogels; (C) the same pore size distributions within a smaller size range.

Table 5.2. Surface area and pore size for BC-LRF carbon aerogels.

Sample	SSA _{total} (m ² /g)	SSA _{micro} (m ² /g)	SSA _{meso} (m ² /g)	SSA _{micro} /SSA _{total} (%)	SSA _{meso} /SSA _{total} (%)	Mean pore width (nm)
<i>BC-LRF9</i>	88.5	8.0	62.8	9	71	18.9
<i>BC-LRF10</i>	111.1	16.5	92.2	15	83	8.5
<i>BC-LRF15</i>	191.8	10.0	163.0	5	85	13.5
<i>BC-LRF16</i>	199.4	11.7	157.5	6	79	17.8
<i>BC-LRF17</i>	215.3	17.4	187.3	8	87	10.0
<i>BC-LRF18</i>	109.5	9.1	99.6	8	91	9.4
<i>BC-LRF19</i>	117.6	7.1	109.4	6	93	11.1
<i>BC-LRF20</i>	250.5	24.4	200.4	10	80	10.2

5.5.5. Functionalization and dispersion of BC-LRF carbon aerogels

Functionalization by nitric acid (HNO₃) oxidation followed by sodium hydroxide (NaOH) neutralization has been used to increase the wettability of carbon materials and electrodes,^{40,41} which can improve the dispersion of the carbon in electrode fabrication and increase the contact between the electrolytes and electrodes in use. FTIR spectra for the pristine and HNO₃-NaOH treated carbon aerogels are compared in **Figure 5.6A**, where the pristine carbon aerogel shows a C=C stretch at 1571 cm⁻¹ of the graphite⁴² and the treated one exhibits an additional peak at 1709 cm⁻¹ due to the C = O stretch of the added -COOH after HNO₃ oxidation^{30,40}. The X-ray photoelectron spectroscopy (XPS) spectra of the two samples are compared in **Figure 5.6B**. Three peaks located at 975.3, 532.3, and 284.5 eV for oxygen (KLL and 1s) and carbon (1s) can be identified on both spectra.³¹ The peak intensity ratios of *O1s:C1s* are 0.20 and 0.44 for the untreated and treated samples, respectively, which suggests more oxygen element on the treated sample surface. The existence of the weak oxygen peaks on the pristine carbon aerogel indicates remaining non-carbon sites on the carbon aerogels. A higher carbonization temperature and/or longer carbonization time may eliminate most of them.

To confirm that the treated aerogel shows better dispersion in electrode fabrication, the ground BC-LRF16 carbon aerogel, acetylene black and polytetrafluoroethylene (85:10:5) were dispersed in ethanol. The dispersion containing the treated BC-LRF16 remained stable without aggregation and precipitation after 48 h (**Figure 5.6B inset**) whereas the dispersion containing the pristine carbon aerogel could not even be evenly dispersed (not shown). The stable dispersion could form highly transparent film on a glass slide via spin coating, indicating again the effect of the treatment.

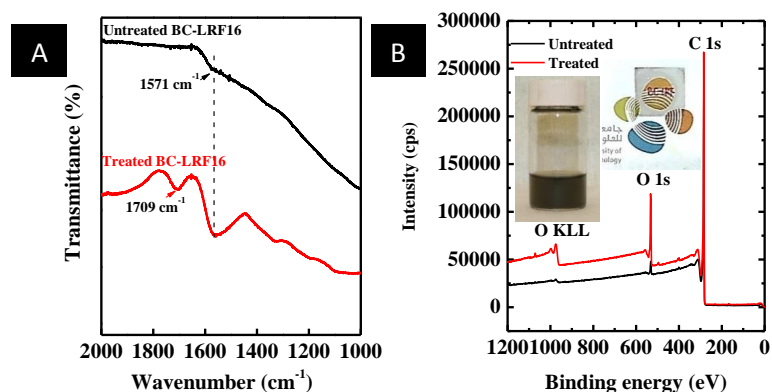


Figure 5.6. (A) FTIR spectra of the pristine and HNO₃-NaOH treated BC-LRF16 carbon aerogels; (B) XPS spectra of the two carbon aerogels. The insets show a stable dispersion of the treated BC-LRF16/acetylene black/PTFE (85:10:5) in ethanol (left) and the spin-coated film of the dispersion on a glass slide (right).

5.5.6. Electrochemical properties of BC-LRF carbon aerogels

The electrochemical performances of the BC-LRF16 carbon aerogel based electrodes were measured in 6 M KOH using a three-electrode configuration. In **Figure 5.7A**, the near-rectangular shape of the cyclic voltammograms is well maintained at a scan rate up to 25 mV/s. The galvanostatic charge/discharge (GCD) plots exhibit a triangular shape with a small internal resistance (**Figure 5.7B**). The curvature shown on the lines may suggest a certain degree of pseudocapacitive behavior of the electrode due to the existence of the oxygen-containing groups as revealed in the FTIR and XPS results.^{36,43} The specific capacitances were calculated based on

the GCD plots and the results are present in **Figure 5.7C**. The electrode shows specific capacitances of 124 and 107 F/g at scan rates of 0.5 and 1 A/g, respectively. The contributions to these capacitances from the Ni foam current collector were found to be very small. The electrode also exhibits outstanding cycle stability - 98 % capacity retention after 10000 charge-discharge cycles (**Figure 5.7C inset**). The intersection of a Nyquist plot with the real axis indicates the equivalent series resistance (ESR) of an electrode. The ESR for BC-LRF16 is only ~ 0.3 ohms (**Figure 5.7D inset**), suggesting good conductivity and high quality of the electrode.^{36,43} The negligible semi-circle on the plot indicates good electrode contact and high charge transfer rate at the electrode/electrolyte interface,^{36,44} which can be partially attributed to the high wettability of the HNO₃ treated carbon aerogel.

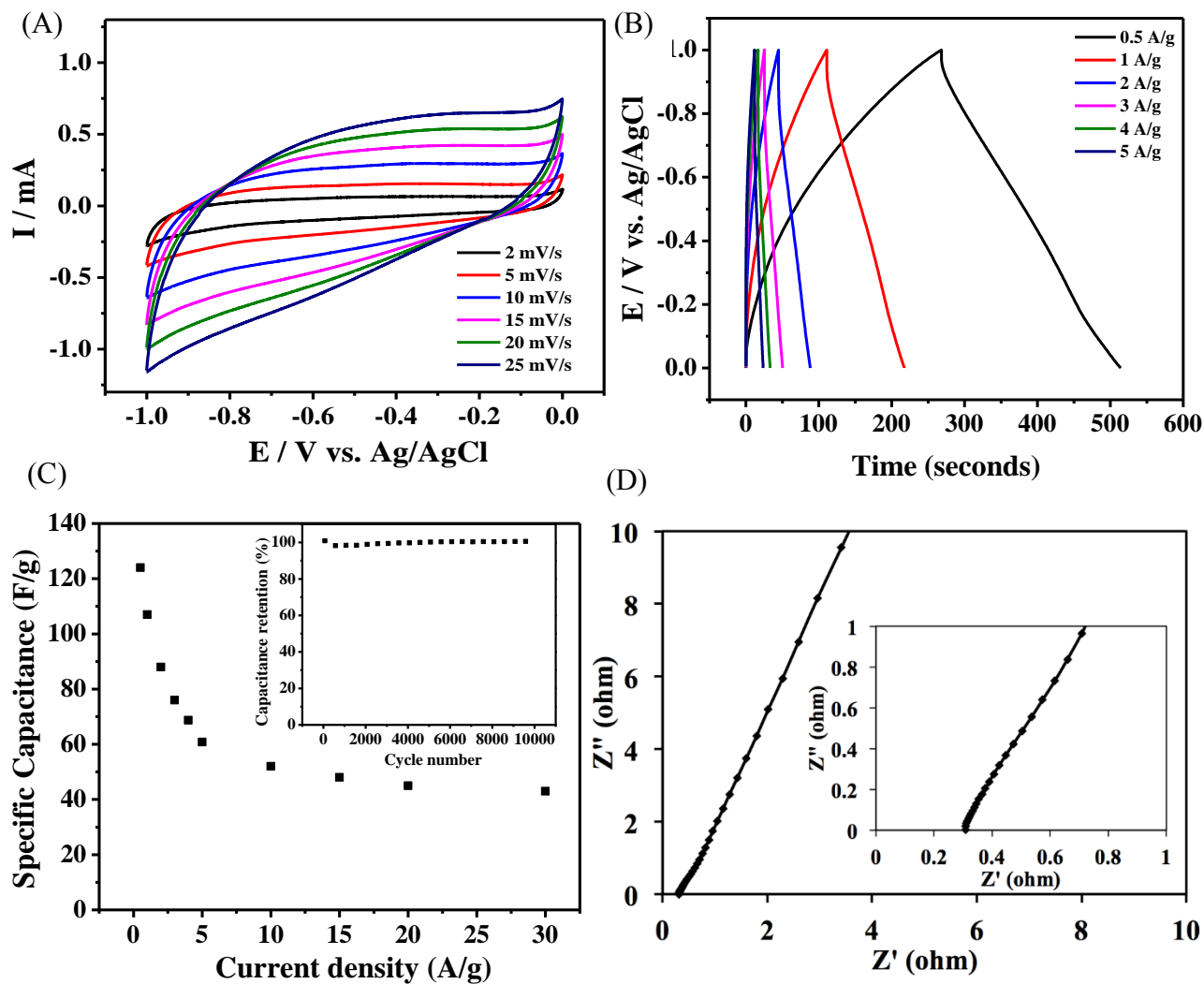


Figure 5.7. Electrochemical characteristics of BC-LRF16 carbon aerogel based electrodes. (A) Cyclic voltammograms between 2 and 50 mV/s. (B) Galvanostatic charge-discharge curves at various current densities. (C) Specific capacitance as a function of current density. The inset shows capacitance retention under repeated charge-discharge. (D) Nyquist plots (inset is the expanded view at high frequencies).

5.5.7. High areal capacitance of BC-LRF carbon aerogels

The surface area available for electrolyte ion adsorption (i.e. effective surface area) and the charge separation distance are the two main factors determining the capacitance of electrical double-layer capacitors (EDLCs). Increasing the effective surface area through creating hierarchical nanostructured electrodes represents a major method to improve capacitor

performance. Both experimental results and theoretical modeling have shown that, while the increase in the average diameter of mesopores moderately improves the specific capacitance of an electrode, significant capacitance increases can be produced by the micropores less than 1 nm (about the size of electrolyte ions).^{45–47} To obtain extremely high specific capacitance, there has to be abundant micropores for efficient ion trapping and adequate amount of mesopores serving as ion transportation pathways. The mesopores, while also trapping the ions and contributing to the capacitance, are important to the rate capability of the electrode by providing fast ion transportation. As shown by the N₂ adsorption-desorption results, mesopores are the primary pores in the BC-LRF carbon aerogels, which explains the electrode's moderate specific capacitance and the fast charge transfer shown by the Nyquist plot. The dominant role of the mesopores also exhibits in the specific capacitance-SSA_{meso} relationship (**Figure 5.8**), which shows that the capacitance increases almost proportionally with the SSA_{meso}.

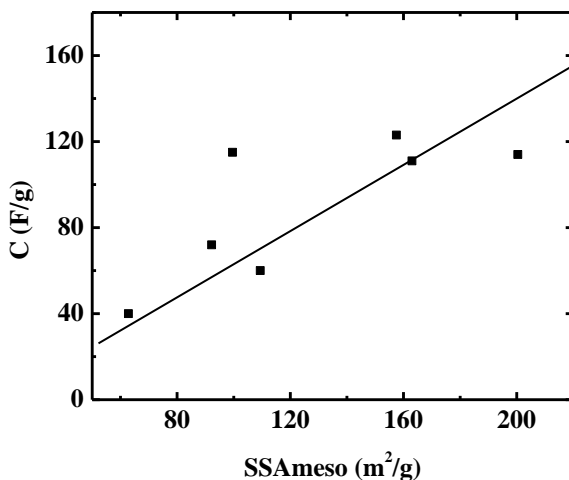


Figure 5.8. Specific capacitance as a function of mesopore surface area for the BC-LRF carbon aerogels.

The areal capacitance, defined as capacitance/surface area, is an important parameter to evaluate the effectiveness of the surface area of an electrode for charge storage⁴⁸. The areal capacitances calculated using the total surface area (C_{total}) and the mesopore surface area (C_{meso})

are listed in **Table 5.3** for the BC-LRF carbon aerogels. BC-LRF16 exhibits a C_{total} and a C_{meso} of 62.2 and 78.7 $\mu\text{F}/\text{cm}^2$ respectively, much higher than the C_{total} of titanium carbide-derived carbon ($13 \mu\text{F}/\text{cm}^2$)⁴⁵ and graphene ($19 \mu\text{F}/\text{cm}^2$)⁴⁹, which possess large total surface areas (1000 and 1310 m^2/g , respectively). Two recent articles show that KOH activated graphene with a specific surface area between 3100 and 3290 m^2/g only exhibits a specific capacitance of 160 - 170 F/g ($\sim 5.2 \mu\text{F}/\text{cm}^2$).^{39,50} Microbead-based activated carbon shows a specific capacitance of 100 F/g ($4.7 \mu\text{F}/\text{cm}^2$) at 2130 m^2/g specific surface area.⁵¹ The much higher areal capacitance achieved in this study indicates that the BC-LRF carbon aerogels have adequate mesopore/micropore ratios and good inter-pore connections that allow higher utilization of the surface areas. The aforementioned “high surface area, low capacitance” carbon materials possess abundant micropores that may not be sufficiently supplied with electrolyte ions through well connected mesopores during charge-discharge processes.

Table 5.3. Areal capacitance of the BC-LRF aerogels

Sample	$C_{gravimetric}$ (F/g)	C_{total} ($\mu F/cm^2$)	C_{meso} ($\mu F/cm^2$)	SSA_{total} (m^2/g)
<i>BC-LRF9</i>	40	45.2	63.7	88.5
<i>BC-LRF10</i>	72	64.8	78.1	111.1
<i>BC-LRF15</i>	114	59.4	69.9	191.8
<i>BC-LRF16</i>	124	62.2	78.7	199.4
<i>BC-LRF17</i>	111	51.6	59.3	215.3
<i>BC-LRF18</i>	60	54.8	60.2	109.5
<i>BC-LRF19</i>	60	51.0	54.8	117.6
<i>BC-LRF20</i>	115	45.9	57.4	250.5
<i>Activated carbon</i> ⁵¹	100	4.7	-	2130
<i>Graphene</i> ^{39,50}	160	5.2	-	3100
<i>Graphene</i> ⁵⁷	170	5.2	-	3290
<i>Carbide-derived carbon</i> ⁵²	140	13	-	80
<i>Graphene</i> ⁵	128	18.2	-	-
<i>Graphene</i> ⁶	247	19	-	-

Carbon aerogels have important applications in environmental remedies such as oil and dye removal due to their large surface area and superhydrophobicity.^{34,53} Toughness is important for the carbon materials in these applications because mechanical forces are used when the materials are deployed, pressed to release adsorbates and prepared for reuse. Lignin based carbon aerogels are fragile and hence restrained in these (and broader) applications. Toughening them using BC opens an innovative avenue to improve their handling and therefore can expand their applications.

Energy storage is another key application area of carbon materials. A wide array of carbon, including sphere-like activated carbon particulates (based on different carbon sources), electrospun nanofiber-converted carbon nanofibers,⁵⁴ 3D-architected carbon aerogels based on CNTs and graphene,³⁴ watermelon-based carbon aerogel,³¹ and others,⁵⁵ have been used as electrode materials in supercapacitors. The BC-LRF carbon aerogels developed in this study

represent a new category of biomass-based carbon materials suitable for supercapacitor electrode use. The process used is facile, catalyst-free, and cost-effective. The products are high-purity CNT-like carbon fibers and fiber networks (aerogels) containing high percentage of mesopores. Their high areal capacitance makes them promising electrode materials for supercapacitors. The specific capacitance of the carbon aerogels can be further improved through commonly used carbon activation methods (acid, alkaline, or steam) to increase the micropore volume.

5.6. Conclusion

In this work, we report a facile methodology to synthesize catalyst-free, flexible, mesoporous, and highly graphitized carbon aerogels based on bacterial cellulose toughened LRF gels. The carbon aerogels consist of core-shell structured carbon nanofibers, where the core and shell are graphitized BC nanofibers and LRF nanoaggregates, respectively. We show for the first time that large reversible deformations in BC-LRF carbon aerogels are attainable by utilizing the toughening effect of the BC nanofiber network. The unique blackberry-like structure and large mesopore concentration of these materials facilitate ion transportation and adsorption and lead to their high areal capacitance. Some of the potential applications of the carbon aerogels include oil/water separation, supercapacitors, batteries, catalyst supports, and sensors.

5.7. References

1. Dong, X. *et al.* 3D Graphene-Cobalt Oxide Electrode for High-Performance Supercapacitor and Enzymeless Glucose Detection. *ACS nano* 3206–3213 (2012).
2. Yavari, F. *et al.* High sensitivity gas detection using a macroscopic three-dimensional graphene foam network. *Scientific reports* **1**, 166 (2011).
3. Gui, X. *et al.* Carbon nanotube sponges. *Advanced materials (Deerfield Beach, Fla.)* **22**, 617–21 (2010).
4. Wu, Z., Yang, S., Sun, Y., Parvez, K. & Feng, X. 3D Nitrogen-Doped Graphene Aerogel-Supported Fe₃O₄ Nanoparticles as Efficient Electrocatalysts for the Oxygen Reduction Reaction. *J. Am. Chem. Soc.* **134**, 9082–9085 (2012).

5. Zhao, N. *et al.* Bioinspired Materials : from Low to High Dimensional Structure. *Advanced Materials* DOI: 10.1002/adma.201401718 (2014).doi:10.1002/adma.201401718
6. Sun, L. *et al.* From coconut shell to porous graphene-like nanosheets for high-power supercapacitors. *Journal of Materials Chemistry A* **1**, 6462 (2013).
7. Phan, N. H. *et al.* Production of fibrous activated carbons from natural cellulose (jute, coconut) fibers for water treatment applications. *Carbon* **44**, 2569–2577 (2006).
8. Monoliths-characterization, W. Wood monoliths-characterization. *Carbon* **35**, 267–273 (1997).
9. Wang, H. *et al.* Interconnected Carbon Nanosheets Derived from Hemp for Ultrafast Supercapacitors with High Energy. *ACS Nano* DOI: **10.10**, (2013).
10. Wang, B., Karthikeyan, R., Lu, X.-Y., Xuan, J. & Leung, M. K. H. Hollow Carbon Fibers Derived from Natural Cotton as Effective Sorbents for Oil Spill Cleanup. *Industrial & Engineering Chemistry Research* **52**, 18251–18261 (2013).
11. Xu, X. *et al.* Porous core-shell carbon fibers derived from lignin and cellulose nanofibrils. *Materials Letters* **109**, 175–178 (2013).
12. synthesis and structural characteristics of orgainc aerogels with different content of lignin.pdf.
13. Lu, Y. *et al.* Fabrication of mesoporous lignocellulose aerogels from wood via cyclic liquid nitrogen freezing–thawing in ionic liquid solution. *Journal of Materials Chemistry* **22**, 13548 (2012).
14. Grishechko, L. I. *et al.* Lignin–phenol–formaldehyde aerogels and cryogels. *Microporous and Mesoporous Materials* **168**, 19–29 (2013).
15. Grishechko, L. I. *et al.* New tannin–lignin aerogels. *Industrial Crops and Products* **41**, 347–355 (2013).
16. Sescousse, R., Smacchia, A. & Budtova, T. Influence of lignin on cellulose-NaOH-water mixtures properties and on Aerocellulose morphology. *Cellulose* **17**, 1137–1146 (2010).
17. Aaltonen, O. & Jauhiainen, O. The preparation of lignocellulosic aerogels from ionic liquid solutions. *Carbohydrate Polymers* **75**, 125–129 (2009).
18. Zhang, D. & Qi, L. Synthesis of mesoporous titania networks consisting of anatase nanowires by templating of bacterial cellulose membranes. *Chemical communications* 2735–7 (2005).doi:10.1039/b501933h
19. Olsson, R. T. *et al.* Making flexible magnetic aerogels and stiff magnetic nanopaper using cellulose nanofibrils as templates. *Nature nanotechnology* **5**, 584–8 (2010).
20. Wu, Z.-Y., Li, C., Liang, H.-W., Chen, J.-F. & Yu, S.-H. Ultralight, flexible, and fire-resistant carbon nanofiber aerogels from bacterial cellulose. *Angewandte Chemie (International ed. in English)* **52**, 2925–9 (2013).

21. Cai, J. *et al.* Cellulose-Silica Nanocomposite Aerogels by In Situ Formation of Silica in Cellulose Gel. *Angewandte Chemie* **124**, 2118–2121 (2012).
22. Zou, J. *et al.* Ultralight multiwalled carbon nanotube aerogel. *ACS nano* **4**, 7293–302 (2010).
23. Zou, J. *et al.* Ultralight multiwalled carbon nanotube aerogel. *ACS nano* **4**, 7293–302 (2010).
24. Xu, Z.; Zhang, Y.; Li, P. Gao, C. Strong , Conductive , Lightweight , Neat Graphene Aerogel Fibers with Aligned Pores. *ACS Nano* **6**, 7103–7113 (2012).
25. Yamamoto, H., Amaike, M., Saitoh, H. & Sano, Y. Gel formation of lignin and biodegradation of the lignin gels by microorganisms. *Materials Science and Engineering: C* **7**, 143–147 (2000).
26. Gutiérrez, M. C., Rubio, F. & Del Monte, F. Resorcinol-Formaldehyde Polycondensation in Deep Eutectic Solvents for the Preparation of Carbons and Carbon–Carbon Nanotube Composites. *Chemistry of Materials* **22**, 2711–2719 (2010).
27. Al-Muhtaseb, S. a. & Ritter, J. a. Preparation and Properties of Resorcinol-Formaldehyde Organic and Carbon Gels. *Advanced Materials* **15**, 101–114 (2003).
28. Geng, D. *et al.* Uniform hexagonal graphene flakes and films grown on liquid copper surface. *Proceedings of the National Academy of Sciences of the United States of America* **109**, 7992–6 (2012).
29. Pan, C.-T. *et al.* In-situ observation and atomic resolution imaging of the ion irradiation induced amorphisation of graphene. *Scientific reports* **4**, 6334 (2014).
30. Warner, J. H., Ru, M. H., Gemming, T., Bu, B. & Briggs, G. A. D. Direct Imaging of Rotational Stacking Faults in Few Layer Graphene 2009. *Nano letters* **9**, 102–106 (2009).
31. Zhang, X., Sreekumar, T. V, Liu, T. & Kumar, S. Properties and Structure of Nitric Acid Oxidized Single Wall Carbon Nanotube Films. *J. Phys. Chem. B* **108**, 16435–16440 (2004).
32. Wu, X. *et al.* Biomass-derived sponge-like carbonaceous hydrogels and aerogels for supercapacitors. *ACS Nano* (2013).
33. Zhou, J. & Lubineau, G. Improving Electrical Conductivity in Polycarbonate Nanocomposites Using Highly Conductive PEDOT/PSS Coated MWCNTs. *ACS applied materials & interfaces* **5**, 6189–200 (2013).
34. Zhou, J., Gao, Q., Fukawa, T., Shirai, H. & Kimura, M. Macroporous conductive polymer films fabricated by electrospun nanofiber templates and their electromechanical properties. *Nanotechnology* **22**, 275501 (2011).
35. Nardecchia, S., Carriazo, D., Ferrer, M. L., Gutiérrez, M. C. & Del Monte, F. Three dimensional macroporous architectures and aerogels built of carbon nanotubes and/or graphene: synthesis and applications. *Chemical Society reviews* **42**, 794–830 (2013).

36. Anderson, M. L.; Stroud, R. M.; Rolison, D. R. Enhancing the Activity of Fuel-cell Reactions 3D Nanostructured Architectures- Carbon–Silica Aerogels.pdf. *Nano lett.* **2**, 235–240 (2002).
37. Zhang, L. L. *et al.* Highly conductive and porous activated reduced graphene oxide films for high-power supercapacitors. *Nano Letters* **12**, 1806–12 (2012).
38. Kruk, M. & Jaroniec, M. Gas Adsorption Characterization of Ordered Organic - Inorganic Nanocomposite Materials. 3169–3183 (2001).
39. Amaral-Labat, G. *et al.* Highly mesoporous organic aerogels derived from soy and tannin. *Green Chemistry* **14**, 3099 (2012).
40. Tae Young Kim, Gyujin Jung Seonmi Yoo, Kwang S. Suh, R. S. R. Activated Graphene-Based Carbons as Supercapacitor Electrodes with Macro- and Mesopores. *ACS Nano* 6899–6905 (2013).
41. Worsley, K. a, Kalinina, I., Bekyarova, E. & Haddon, R. C. Functionalization and dissolution of nitric acid treated single-walled carbon nanotubes. *Journal of the American Chemical Society* **131**, 18153–8 (2009).
42. Pandolfo, A. G. & Hollenkamp, A. F. Carbon properties and their role in supercapacitors. *Journal of Power Sources* **157**, 11–27 (2006).
43. Hamon, M. A., Hui, H., Bhowmik, P., Itkis, H. M. E. & Haddon, R. C. Ester-functionalized soluble single-walled carbon nanotubes. *Applied Physics A Materials Science & Processing* **338**, 333–338 (2002).
44. Worsley, K. a, Kalinina, I., Bekyarova, E. & Haddon, R. C. Functionalization and dissolution of nitric acid treated single-walled carbon nanotubes. *Journal of the American Chemical Society* **131**, 18153–8 (2009).
45. Zhang, X., Sreekumar, T. V, Liu, T. & Kumar, S. Properties and Structure of Nitric Acid Oxidized Single Wall Carbon Nanotube Films. *J. Phys. Chem. B* **108**, 16435–16440 (2004).
46. Zhi, M. *et al.* Effects of Pore Structure on Performance of An Activated-Carbon Supercapacitor Electrode Recycled from Scrap Waste Tires. *ACS Sustainable Chemistry & Engineering* **2**, 1592–1598 (2014).
47. Portet, C., Lillo-Ródenas, M. A., Linares-Solano, A. & Gogotsi, Y. Capacitance of KOH activated carbide-derived carbons. *Physical chemistry chemical physics : PCCP* **11**, 4943–5 (2009).
48. Chmiola, J. *et al.* Anomalous increase in carbon capacitance at pore sizes less than 1 nanometer. *Science* **313**, 1760–3 (2006).
49. Huang, J., Sumpter, B. G. & Meunier, V. A universal model for nanoporous carbon supercapacitors applicable to diverse pore regimes, carbon materials, and electrolytes. *Chemistry (Weinheim an der Bergstrasse, Germany)* **14**, 6614–26 (2008).
50. Huang, J., Sumpter, B. G. & Meunier, V. Theoretical model for nanoporous carbon supercapacitors. *Angewandte Chemie (International ed. in English)* **47**, 520–4 (2008).

51. Raymundo-Piñero, E., Kierzek, K., Machnikowski, J. & Béguin, F. Relationship between the nanoporous texture of activated carbons and their capacitance properties in different electrolytes. *Carbon* **44**, 2498–2507 (2006).
52. Yoo, J. J. *et al.* Ultrathin planar graphene supercapacitors. *Nano Letters* **11**, 1423–7 (2011).
53. Zhu, Y. *et al.* Carbon-based supercapacitors produced by activation of graphene. *Science* **332**, 1537–41 (2011).
54. Qu, D. & Shi, H. Studies of activated carbons used in double-layer capacitors. *Journal of Power Sources* **74**, 99–107 (1998).
55. Largeot, C. *et al.* Relation between the Ion Size and Pore Size for an Electric Double-Layer Capacitor. *Journal of American Chemical Society* 2730–2731 (2008).doi:10.1016/j.carbon.2007.10.023.(15)
56. Sun, H., Xu, Z. & Gao, C. Multifunctional, ultra-flyweight, synergistically assembled carbon aerogels. *Advanced materials* **25**, 2554–60 (2013).
57. Inagaki, M., Yang, Y. & Kang, F. Carbon nanofibers prepared via electrospinning. *Advanced materials (Deerfield Beach, Fla.)* **24**, 2547–66 (2012).
58. Simon, P. & Gogotsi, Y. Materials for electrochemical capacitors. *Nature materials* **7**, 845–54 (2008).

CHAPTER 6. TRANSPARENT, LOW-HAZE, FLEXIBLE HYBRID CELLULOSE NANOPAPER AS ELECTRODES FOR APPLICATION IN LIGHT EMITTING DIODE DEVICES*

6.1. Abstract

Developing flexible, transparent electrodes using cellulose nanopaper (CNP) as the substrate is considered very promising. These electrodes are essential for the function of flexible/wearable displays and are required to possess high mechanical flexibility/robustness and high transparency and electrical conductivity. Current CNP is made from one single type of cellulose nanofibers and often exhibits low direct transmittance and high haze. In this research, we developed a facile method to produce hybrid CNP consisting of cellulose nanofibrils (CNFs) and cellulose nanocrystals (CNCs). The obtained CNP shows highly tailorable optical and mechanical properties by varying the CNF:CNC ratio; the CNP made of optimized ratios exhibits higher direct transmittance and much lower haze compared to those of the current CNP. Further, flexible, transparent electrodes were produced by depositing a layer of silver nanowires (AgNWs) on the hybrid CNP substrate. The electrodes maintain their high transmittance and show high electrical conductivity, which remains constant during cyclic bending deformation.

* The content in this chapter was co-authored by Xuezhu Xu, Jian Zhou, Long Jiang, Gilles Lubineau, Tienkhee Ng, Boon S. Ooi, Hsien-Yu Liao, Chao Shen and Long Chen. Xuezhu Xu, Gilles Lubineau and Long Jiang generated the idea. Xuezhu Xu prepared samples and designed the experiments. Jian Zhou helped with SEM and electrical conductivity experiment. Tienkhee Ng, Boon S. Ooi, Hsien-Yu Liao and Chao Shen contributed on the light emitting device experiments. Gilles Lubineau and Long Jiang supervised the project, provided useful discussions and suggestions. Xuezhu Xu drafted the manuscript.

The electrodes also show a linear relationship between their electric resistance and applied tensile strain, a property that can be used to make CNP-based strain sensor. A light emitting diode (LED) device was made using the CNP-based electrodes as a proof-of-concept application to demonstrate their high potential in flexible displays.

6.2. Introduction

Mechanically flexible/robust, highly transparent/conductive electrodes are required in next generation large-area displays, touch screens¹, light-emitting diode (LED) light sources² and solar energy devices³. Indium tin oxide (ITO) has long been used to make glass based transparent electrodes. The drawbacks with these traditional electrodes are obvious: brittleness, high cost, limited/unrenewable raw materials, and environmentally damaging manufacturing processes. To overcome these challenges, PEDOT/polystyrene sulfonate (PSS),^{4,5} carbon nanotubes (CNTs), graphene and silver nanowires (AgNWs)⁶⁻⁹ have been coated on flexible polymer substrates with the aim of replacing ITO/glass electrodes. These new flexible electrodes show performance comparable to the traditional ones; they also provide additional advantages including light-weight, rollability, stretchability, high electrical conductivity,¹⁰ and high processibility during device assembling (rollable, heatable and printable).

Very recently, cellulose nanofiber reinforced polymers and all-cellulose nanopapers have been attempted as the substrates for transparent, flexible electrodes.¹¹⁻²⁰ CNFs were initially used as nanoreinforcements in polymers to make transparent composite substrate.^{21,22,23} All-CNF nanopapers were subsequently developed using a filtration and pressing process,^{12,14,24,25} and the products show high toughness/strength/modulus and high transparency. However, even with high transparency, the nanopapers show high haze because of its high percentage of diffusive transmittance caused by strong light scattering by large fiber bundles and/or pores in the

nanopaper.^{26,27,10,28} The transparency T of a medium is defined as the ratio of transmitted radiant power to incident radiant power, where the transmitted radiant power is the sum of direct transmittance T_{direct} and diffuse transmittance $T_{diffuse}$, i.e., $T = T_{direct} + T_{diffuse}$. Therefore nanopaper can have high transparency and high haze at the same time if its $T_{diffuse}$ is larger than its T_{direct} . While high haze of the nanopapers is a useful feature for applications such as skylight, indoor lighting and solar cells,²⁶ which often prefers diffuse light, such nanopapers are not suitable for applications that requires high optical transparency, e.g., flexible displays and touch screens.

An extensive literature review reveals that current transparent nanopapers developed by different research groups are mostly based on wood-based CNFs or a mixture of CNFs and micro-sized cellulose fibers.²⁶ These nanopapers have fixed mechanical and optical properties and their $T_{diffuse}$ is high. In this study, a facile fabrication method is developed to produce highly transparent CNC/CNF hybrid nanopaper with low haze. The optical and mechanical properties of the nanopaper can be tailored by adjusting the ratio between the CNCs and CNFs. By coating a layer of AgNWs, the nanopaper is transformed into a transparent electrode that shows high conductivity and stability of conductivity under large bending deformation.

6.3. Materials and methods

6.3.1. Materials

Cellulose nanofibrils (CNFs) and cellulose nanocrystals (CNCs) derived from bleached eucalyptus pulp were used for cellulose nanopaper (CNP) fabrication. They were kindly provided by the USDA Forest Service Laboratory and were used as-received. The sizes of the two cellulose nanofibers are as follows: 20 ± 14 nm (diameter) and 1030 ± 334 nm (length) for the CNFs; 19 ± 5 nm (diameter) and 151 ± 39 nm (length) for the CNCs.^{29,30} Both of them were

provided in the form of aqueous suspension. Polyvinylpyrrolidone (PVP, $M_w = 30,000$), ethylene glycol (EG), sodium chloride (NaCl), silver nitrate (AgNO_3), ammonium hydroxide (NH_4OH) were used to synthesize silver nanowires (AgNWs). All the reagents and chemicals were purchased from Sigma-Aldrich.

6.3.2. Fabrication of cellulose nanopaper (CNP)

CNFs and CNCs with predetermined weight ratios were mixed by an ultrasonic processor (Cole-Parmer) for 5 mins (250 W, room temperature). The dry mass content of the CNF/CNC mixtures was kept constant at 0.2 wt.% for all the formulations. The mixtures were then filtered using a polyethylene filter (30 μm pore size) to remove any remaining large aggregates. The mixtures were vacuum-filtered again using Anopore membranes (0.02 μm pore size, Whatman International Ltd) in a Wheaton funnel. The obtained wet nanopaper was sandwiched between two membranes under pressure and dried in a vacuum oven at 120 $^\circ\text{C}$ for 30 min.

6.3.3. Synthesis of silver nanowires

0.339 g PVP powder was dissolved in 25 mL EG by mild stirring at 170 $^\circ\text{C}$ for ~ 1 h till complete dissolution. A NaCl solution in EG (50 μL , 0.43 M) and a AgNO_3 solution in EG (50 μL , 0.43 M) were simultaneously injected into the PVP solution and the mixture was stirred for 15 min. Another AgNO_3 solution in EG (10 mL, 0.12 M) was added dropwise for 12 min while stirring. The mixture was stirred for an additional 4 min afterwards. The reaction mixture was then cooled to room temperature and ~ 100 mL water was added to stop the reaction. To clear the impurities, 2 mL aqueous NH_4OH was added to the mixture to dissolve the residual AgCl generated during the reaction.

6.3.4. Fabrication of nanopaper electrode

A predetermined amount of the AgNWs solution from Section 2.3 was diluted in 20 g water. Wet nanopaper was prepared using the method detailed in Section 2.2. Before removing the wet nanopaper from the funnel, the new AgNWs solution was added into the funnel and vacuum-filtered through the nanopaper. The obtained AgNWs/nanopaper bilayer structure was dried using the same method in Section 2.2 to eventually produce transparent nanopaper electrodes.

6.3.5. Preparing LED device on nanopaper electrode

A patterned AgNWs layer was deposited on the surface of the nanopaper by putting a patterned polyvinylidene fluoride (PVDF) mask on the wet nanopaper before filtering the AgNWs solution. Commercially available aluminum gallium indium phosphide (AlGaInP)-based red LED was embedded between two patterned nanopaper electrodes to prepare nanopaper based LED devices. The electronic characteristics of the devices were measured using a customized L-I-V (light-current-voltage) testing system comprising a Keithley 2400 source meter, a Newport 2936C optical power meter and an Ocean optics 65000+ spectrometer.

6.3.6. Characterizations

Nanostructures of the prepared CNP, AgNWs and AgNWs/CNP electrodes were studied using a scanning electron microscope (SEM, Quanta 600F from FEI Company) operating at 5 or 10 kV and a transmission electron microscope (TEM, Titan G2 80-300 CT from FEI Company) operating at 300 kV. Mechanical properties of the CNP were measured through tensile testing on an Instron 5882 equipped with a 500 N load cell. At least ten rectangular specimens (4 mm × 16 mm) were measured for each type of nanopaper. The specimens were stretched at 2 mm/min under 20.5 °C and 59 % relative humidity. Optical properties of the CNP and AgNWs/CNP

electrodes were measured using a UV-VIS-NIR (UV-3600) spectrophotometer equipped with an ISR-3100 integrating sphere from Shimadzu Company. The sample transmittance was measured between 200-1200 nm wavelength.

Resistivity of the AgNWs/CNP electrodes was measured *in-situ* during tensile tests on a 4 mm × 1 cm area of a nanopaper electrode. Two 15 cm long and 0.004” diameter-copper wires (alloy: C510, United wire technologies, Inc) were soldered horizontally 0.5 cm far from sample center by using conductive epoxy (Circuitworks CW2400 from ITW Chemtronics). Resistivity was measured by an Agilent U1252B true RMS multimeter, and the data was recorded by a computer. An Instron 5944 with a 5 N load cell (Instron 2711-006) was used for the tensile tests.

Atomic force microscopy (AFM, Asylum MFP-3D) was employed to acquire amplitude and phase images of nanopaper surface. Probes (FESP from Bruker) with a spring constant of 2.8 N/m were used under tapping mode. Roughness of the surface was calculated by Gwyddion software. Porosity and bulk density of the samples was measured using a Micromeritics AutoPore IV mercury porosimeter. The measurements were performed between 0.1 and 45,000 Pa after outgassing the sample for 2 hours at ambient temperature. Software AutoPore IV 9500 (version 1.09) was used to analyze the data.

6.4. Results and discussion

6.4.1. Preparation of CNP and AgNWs/CNP electrodes

At the same concentration the dispersions of CNCs and CNFs in water appear differently due to their different sizes and interactions with neighboring cellulosic nanofibers. **Figure 6.1A** compares the visual appearance of the aqueous suspensions of CNFs, CNCs and their mixtures. Micro-sized wood pulp fiber (commercial filter paper from Whatman company) dispersed in water is also included for comparison. The pulp fiber has large diameter and precipitates in water

(#1 in **Figure 6.1A**). CNFs and CNCs both form stable dispersions in water, with the former being translucent (#2) and the latter transparent (#8). This difference can be attributed to the presence of relatively large CNF bundles and networks³⁰ that scatter light more strongly than individual CNCs. The CNF bundles are formed through hydrogen bonding between the –OH groups on the fiber surface and the networks are due to physical entanglement between the fibers; CNCs mostly remain as individual fibers in the dispersion due to their surface sulfate groups produced by sulfuric acid hydrolysis. The transparency of the CNC/CNF mixture dispersions increases with the rising CNC content (#3 through #7). The addition of CNCs to the dispersions makes a twofold contribution: it reduces the total number of CNFs in the dispersions and also acts as “spacers” to prevent CNFs from forming bundles and networks, at least to a certain extent. **Figure 6.1B** illustrates the forming process of the AgNWs/CNP electrodes. Wet CNP is produced in the first step using a typical nanopaper-making technique, i.e., vacuum assisted filtration.³¹ A layer of AgNWs is coated on top of the wet nanopaper in the second step. The product is dried in a vacuum oven under pressure to obtain the AgNWs/CNP electrodes. The second step is not necessary if only CNP is produced.

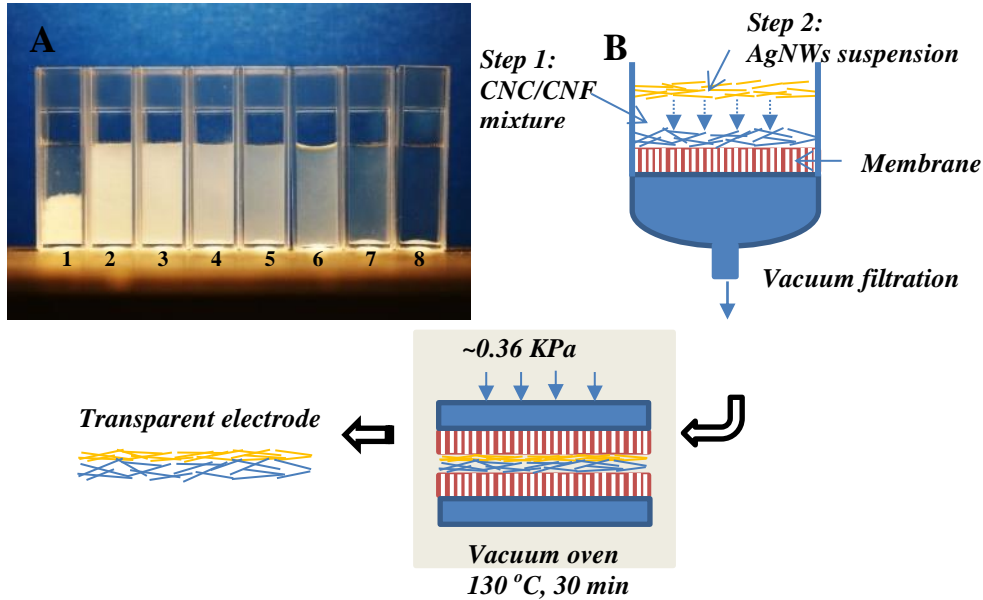


Figure 6.1. (A) From left to right, aqueous CNFs/CNCs aqueous suspension with increasing CNC content from 0 % to 100 % based on CNFs+CNCs total weight, all suspensions have the same fiber content of 4 wt.%; the first suspension shows a micron-sized pulp fiber suspension as a comparison; (B) Schematic of the process to prepare CNP and AgNWs/CNP electrodes.

6.4.2. Optical properties of CNP

The visual appearance of a piece of CNC/CNF hybrid CNP is shown in **Figure 6.2A**, which demonstrate high optical transparency. Hu’s group reports the production of CNP with high transparency (T up to 90% at 600 nm wavelength) using CNFs,^{32,33} the CNP also shows high haze because of its low T_{direct} (as low as ~20 %) cause by strong light scattering.^{33,32,34} Nogi et al have shown that the light scattering (and consequently the haze) can be largely decreased by polishing or coating the surface of the nanopaper to increase its T_{direct} to 71.6 %.³⁵ In this study, over the entire wavelength range T_{direct} of the hybrid CNP is significantly larger than that of pure CNF-based CNP and that of “traditional” paper (**Figure 6.2B**), which is made from micro-sized wood pulp fibers using the same filtration/drying process as used to make CNP. By increasing the content of CNCs in the hybrid CNP, T_{direct} (at 600 nm wavelength) increases from 31.1 % for the pure CNF-based CNP to 75.1% for the CNP comprising 62.5 %

(6:10) CNCs. T_{direct} shows no significant change when the CNC content rises further (**Figure 6.2C**). This high T_{direct} exceeds most reported values for CNF-based CNP; it also approaches that of poly (ethylene terephthalate) (PET, > 85 %),³⁶ ITO glass (85 %)³⁷ and pure silicon oxide glass (92 %). This high T_{direct} is attributed to the reduced surface roughness, porosity and internal pore size of the CNP after the addition of CNCs, as discussed below.

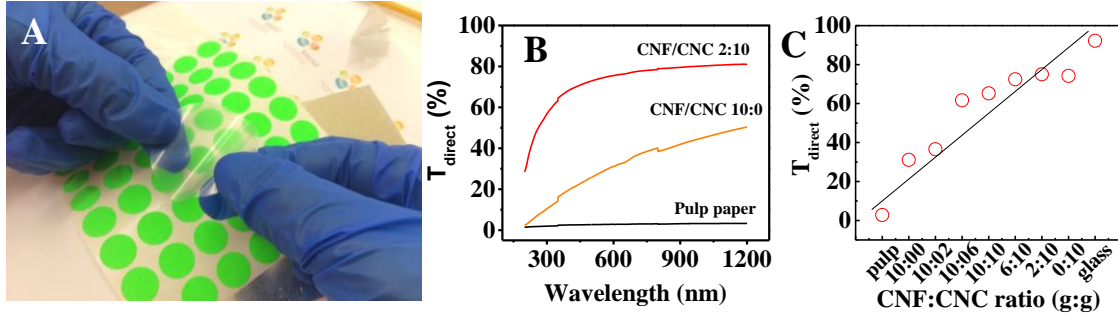


Figure 6.2. (A) Demonstration of a piece of plastic-like nanpaper (CNF:CNCs 6:10); (B) Direct transmittance of nanpaper; (C) Direct transmittance of various nanpaper with different CNFs:CNCs weight ratio.

The (transmission) haze (H_T)⁴⁰ and diffuse reflection (R)⁴¹ of the CNP are studied below.

H_T is defined as:⁴⁰

$$H_T = \frac{T_{diffuse}}{T_{total}} \times 100\% \quad (6.1.)$$

Where $T_{diffuse}$ is the amount of forward scattering of light (light scattered more than 2.5° from the incident light)). A higher H_T suggests that a larger portion of light is scattered (diffused), resulting in a lower portion of in-line transmission (illustrated in (**Figure 6.3A** inset), which makes sample translucent and milky. All-CNF nanpaper has a H_T of 62.0 %, which is similar to the values from other studies. It lends the sample a milky appearance, especially when the sample is held from a distance from the background (**Figure 6.3C**). H_T decreases down to 10.0 % at 83 % CNC content (**Figure 6.3A**) and the sample becomes more transparent (**Figure 6.3C**) This value falls in the same range of that of transparent plastic films, glass and ITO glass

(3 to 18.1 % (Figure 6.3A and Table 6. S3⁴²⁻⁵¹) suggesting the hybrid nanopaper's great potential to replace the traditional materials. As a comparison, H_T of the regular micro-sized paper is 91.4 %.

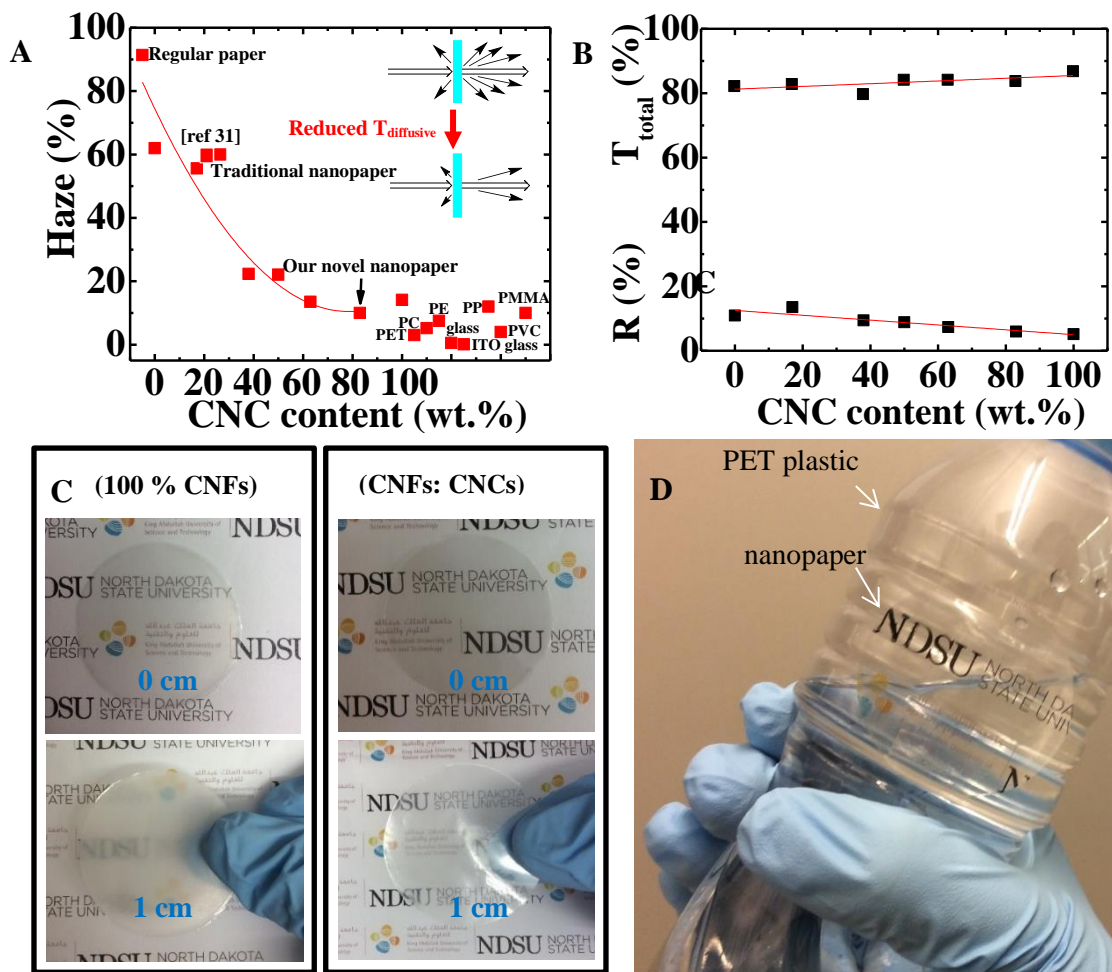


Figure 6.3. (A) Haze values of the hybrid nanopapers compared to commercial transparent substrates;⁴²⁻⁵¹ (B) Total transmittance and diffuse reflection as a function of CNC content; (C) Comparison of visual appearance of all-CNF nanopaper and hybrid nanopaper (CNC content: 83 wt.%), samples were located 0 and 1 cm from the background; (D) A piece of nanopaper pasted on a PET bottle. “NDSU” is printed on the nanopaper by a commercial ink-printer.

Diffuse reflection (R) is caused by surface roughness and inhomogeneity of a material. A material with low R exhibits high gloss. Figure 6.3B shows that R decreases with increasing CNC content while T increases. The low R , low H_T and high T values for the nanopaper with

high CNC contents result in its transparent, shiny, plastic-like appearance as shown in **Figure 6.3C and D**, where a piece of nanopaper is printed with “NDSU” by a commercial ink-jet printer and pasted on the surface of a PET bottle.

6.4.3. Mechanism for high optical transparency

The transparency and haze of CNP have been related to its surface roughness and porosity.^{38,39} A qualitative comparison can be made in **Figure 6.4**, which demonstrates that the pure CNFs-based CNP has a much rougher surface than the hybrid CNP. In **Figure 6.4**, SEM images of micron-sized paper, traditional nanopaper made of 100 % CNFs and our microstructured nanopaper made of CNFs:CNCs = 2:10 were demonstrated. The regular paper exhibits visible micron-sized cellulose fibers with an average diameter of $15.7 \pm 2.7 \mu\text{m}$ and a length exceeding hundreds of μm . However, the nanopaper made of 100 % CNFs have smooth surface without exhibiting fibers; However, slightly roughness was observed while comparing to our novel nanopaper based on CNFs:CNCs = 2:10. The change of surface topographies was believed to be associated with the addition of the CNCs.

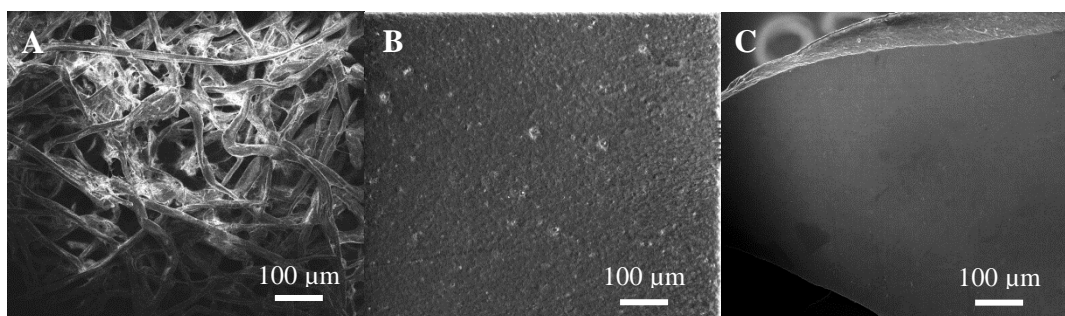


Figure 6.4. SEM images of (A) regular paper made of micron-sized pulp paper; (B) traditional CNP; (C) our novel CNP (CNFs:CNCs=2:10).

The surface roughness and porosity were further measured for the CNP to establish quantitative relationships. R_{RMS} calculated on a $1 \mu\text{m}$ line is 1.21 nm with a maximum valley depth (R_v) of 4.71 nm for CNP made of CNFs:CNCs = 2:10 (**Figure 6.4A-C**). These values are

comparable to the values from Huang et al's work on transparent nanopaper derived from TEMPO-preoxidized and microfluidized cellulose nanofibrils.¹¹ R_{RMS} (within a $1 \times 1 \mu\text{m}^2$ area) of the CNP with different CNC contents is plotted in **Figure 6.4D**, which shows that the CNP with 100% CNFs has the highest R_{RMS} of 22.11 nm and the value decreases with increasing CNC content almost linearly to 5.749 nm for the CNP with 100% CNCs. The porosity (pores accessible by mercury) of the CNP displays a completely opposite trend: the value decreases linearly from 13.3 % to 7.5% as the CNC content increases from 0% to 100% (**Figure 6.5D**). Both trends indicate that the surface of CNP is smoothed and the voids are filled due to the addition of CNCs. The bulk density of CNP measured by mercury porosimetry increases from 1.3 to 1.5 g/cm^3 between 0 % and 100 % CNC contents (**Figure 6.5D**), confirming the decreasing porosity of the nanopaper. As a comparison, the paper made from micron-sized pulp fiber using the same process, shows a bulk density of 0.3 g/cm^3 and a porosity of 80.6 %.

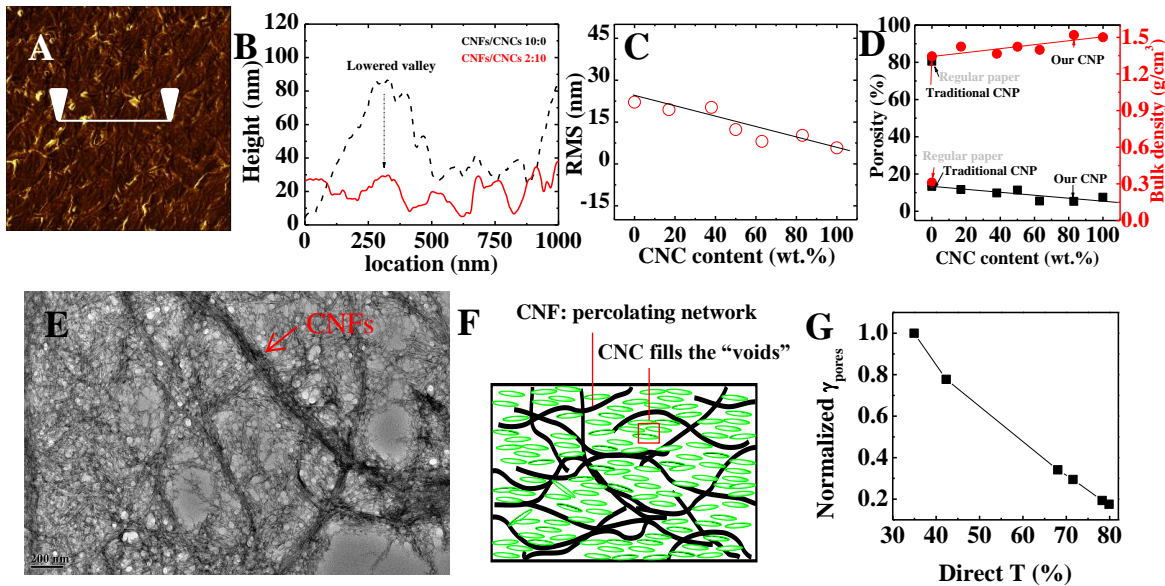


Figure 6.5. (D) SEM image of traditional nanopaper (CNFs: 100 %) and (E) SEM image of our novel nanopaper (CNFs/CNCs 83 %). (A) AFM phase image (dimension $2 \times 2 \mu\text{m}^2$) of a hybrid CNP (CNC content: 83 wt.%); (B) R_{RMS} vs. CNC content; (C) Porosity and bulk (apparent) density vs. CNC content; (D) TEM image of CNF/CNC network in CNP; (E) Illustration of CNF/CNC network: CNFs form a percolating network while CNCs fill the “voids” within the network. (F) Relationship of calculated scattering factor γ_{pores} and the direct transmittance.

Increasing nanopaper transparency by reducing surface roughness and porosity of the paper has been reported by Nogi³⁵ and Zhu et al.³³ These two factors lead to high diffusive light scattering and result in low direct transmittance and high haze. Filling the “voids” between large fiber bundles by chemicals including oil, PVA, epoxy and etc have been reported as well. some formulations such as lamination with plastics or decreasing the nanofiber size has been proven successful for decreasing the “voids”.^{21355213–15,28} In this study, to our knowledge, for the first time, we found out the important role of CNCs as a “filling” agent for CNF nanopaper network (**Figure 6.5E-F**). Hence, we examined the relationship of pores and transmission loss of various nanopaper with respect to addition of CNCs. Theoretically, causes of transmission loss are scattering by pores or second phase, scattering by grain boundaries, absorption, birefringence, and surface roughness. It has been shown that scattering by residual porosity is the main cause of scattering of light on its passage through a medium. The surface scattering can be neglected after a careful polishing treatment, as Nogi did for the traditional CNP.³⁵ For any transparent thin film sample with t thickness, the direct transmittance T_{direct} is described as:⁵³

$$T = (1 - R) \cdot \exp(-\gamma_{pore} t) \quad (6.2.)$$

Where R is the reflectivity, γ_{pore} is the scattering of the pores, t is the film thickness. The direct T , R , and t (measured from *UV-vis* spectra at wavelength of 600 nm, **Table 6.S2**) are known experimental parameters; hence the values of γ_{pore} for samples were calculated. We normalized the γ_{pore} for CNFs/CNCs with CNC contents to the control sample: CNFs/CNCs 0 %, and the normalized values were plotted with respect to the direct T (**Figure 6.6E**). The curve shows a linear dependency of direct T on the scattering factors. The higher direct T , the higher normalized γ_{pore} . Meanwhile, the γ_{pore} is strongly related to the pore volume V_{pore} . Through

experimental determination, pore volume V_{pore} (porosity) was gradually decreased by addition of CNCs in CNFs. In above equation, the scattering coefficient γ_{pore} is described as:⁵⁴

$$\gamma_{pore} = NC_{sca} = NQ_{sca}\pi a^2 = \frac{3V_{pore}}{4a} Q_{sca} \quad (6.3.)$$

Where N is the number of pores, C_{sca} is the scattering centers, V_{pore} is the specific pore volume, scattering coefficient Q_{sca} can be calculated by Mie theory. a is radius of spherical pores. This equation is suggesting that, the scattering coefficient γ_{pore} has a dependancy on the pore size, volume of pores. The theory agrees well with our porosity and density measurements (**Fig. 6.5G**). Hence, we conclude that, the short CNCs densely pack within the CNF network, which lowers the surface roughness, pore volume, and the scattering factors. This action contributes to the high direct transmittance of light passing through our nanopaper.

6.4.4. Mechanical properties of the hybrid CNP

Combining CNCs and CNFs at different ratios also provides an effective method to tailor the mechanical properties of CNP. Young's modulus (E), tensile strength (σ) and strain at break (ϵ) of the CNP containing different contents of CNCs are shown in **Figure 6.6A to C**. In general, E increases while σ and ϵ decrease with rising CNC content. From 0 to 100% CNC content, E increases from 2.9 GPa to 10.2 GPa and σ decreases from 89.6 MPa to 10.0 MPa, forming a large property envelope; ϵ in the meantime decreases from 6.78 % to 1.65 %. As shown in **Figure 6.5E-F**, the CNFs in CNP forms a network structure that allows a certain degree of deformation under stress. The addition of CNCs fills the voids between the CNFs and the mobility of the network is hindered by the rigid CNC fillers, which results in increased modulus. The CNP containing 100% CNCs shows the highest modulus but the lowest strain at break because of the high rigidity of CNCs and the lack of deformable network structures in the

nanopaper. Its strength is also the lowest one due to the weak hydrogen bonding between the CNC fibers and the lack of fiber entanglement. The addition of CNCs into CNFs can increase the distance between neighboring CNFs, reduce their entanglement density and hinder the formation of a tight CNF network. Therefore, the strength of CNP decreases with increasing CNC concentration. As a comparison, the paper made from micro-sized pulp fiber exhibits a much lower E (60 MPa) and σ (0.45 MPa) as well as a similar ε (6.05 %) compared to the CNP containing pure CNFs.

Figure 6.6D compares mechanical properties of the CNP (CNFs:CNCs = 2:10 ratio) and several commonly used engineering polymers. For example, the Polyethylene terephthalate (PET) with an E of 1.4 GPa,³⁶ polycarbonate (PC) with an E of 1.74 GPa,⁵⁵ are much lower than our high performance nanopaper with a E value (obtained from films with a ratio of 2:10) of 5.5 GPa. The ultimate tensile strength (stress at break) of various plastics was in the range of 0-100 MPa. From the comparison, our nanopaper with an average E value of 5.5 GPa and σ of 32.73 MPa is performing much higher than most of the plastics.

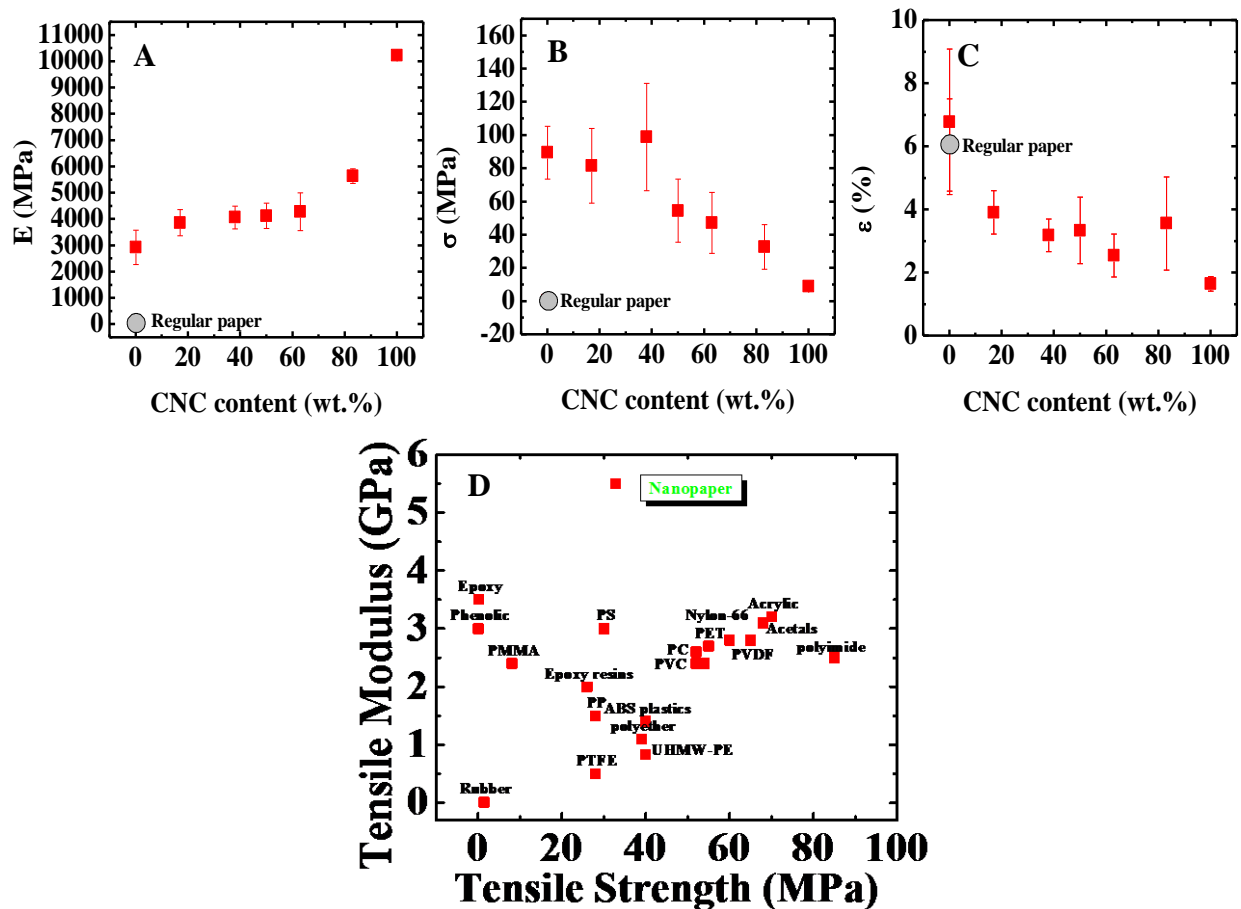


Figure 6.6. Mechanical properties of various CNP films, (A) Young's modulus E vs. CNC content; (B) stress at break σ vs. CNC content; (C) strain at break ϵ and (C); (D) tensile modulus E vs. ultimate tensile strength σ of our nanopaper compared to various plastics.⁵⁶⁻⁵⁹

6.4.5. Sheet resistance and transmittance of AgNWs/CNP electrodes

The conductive network of AgNWs deposited on the CNP substrate is shown in **Figure 6.7A and B** with a nanowire areal density (defined as loaded AgNWs weight per unit substrate area) ranging from 87.0 to 1044.5 mg/m². It is evident that the nanowire network becomes denser with the increasing areal density. The AgNWs have an average diameter of 74 nm and a mean length of 37.5 μ m, yielding an aspect ratio of 506. A high aspect ratio results in a percolated AgNW network at a low areal density.⁶⁰ In **Figure 6.7C** the sheet resistances R_s of the electrodes is shown to decrease rapidly within the low AgNW density range and tends to stabilize within the high range, suggesting a percolation threshold of 121 mg/m² (**Table 6.1**). The R_s values (1.2

– 23.5 Ω/sq) reported here for the AgNWs/CNP electrodes are comparable to the values (16 Ω/sq) for Ag nanowire mesh on glass electrodes with a Transmittance of 86 % in the literature.⁶¹

Total transmittance (T_{total}) of the AgNWs/CNP electrode is compared with that of AgNWs and CNP as separate layers and the paper made from micro-sized pulp fiber over the 200-1200 nm wavelength range (**Figure 6.7D**). The AgNWs layer exhibits the highest T_{total} followed by the CNP layer. Stacking the highly transparent AgNWs layer on top of the CNP layer, T_{total} of the obtained AgNWs/CNP electrode only slightly decreases from that of the CNP. As a comparison, the paper based on micro-sized fiber shows the lowest transmittance. As expected, the transmittance decreases with increasing AgNW areal density for both the electrode and the AgNW layer (**Figure 6.7E**). The fact that the two lines in the figure are parallel to each other suggests that the decrease are primarily due to the increasing areal density of the AgNWs. **Figure 6.7F** demonstrates the conductivity of the AgNWs/CNP electrode (CNC content 83 wt.%) by using it to connect a circuit, where current travels through the transparent electrode and lights up a LED.

Table 6.1. Electrical and optical properties of AgNWs/CNP electrodes.

AgNW areal density (mg/m^2)	R_s of AgNWs/CNP (Ω/\square)	T_{total} of AgNWs (%)	T_{total} of AgNWs/CNP (%)
1044	1.2 (0.1)	63.0	46.4
696	2.3 (0.5)	76.6	60.0
348	5.2 (0.8)	82.9	66.3
243	5.8 (0.5)	86.1	70.0
174	23.5 (2.6)	92.1	75.5
121	75.5 (40.1)	95.4	78.8
87	104.3 (49.5)	95.8	79.2
69	6328.0 (1334.0)	99.1	80.0
17	10230600 (959887.9)	99.8	82.5

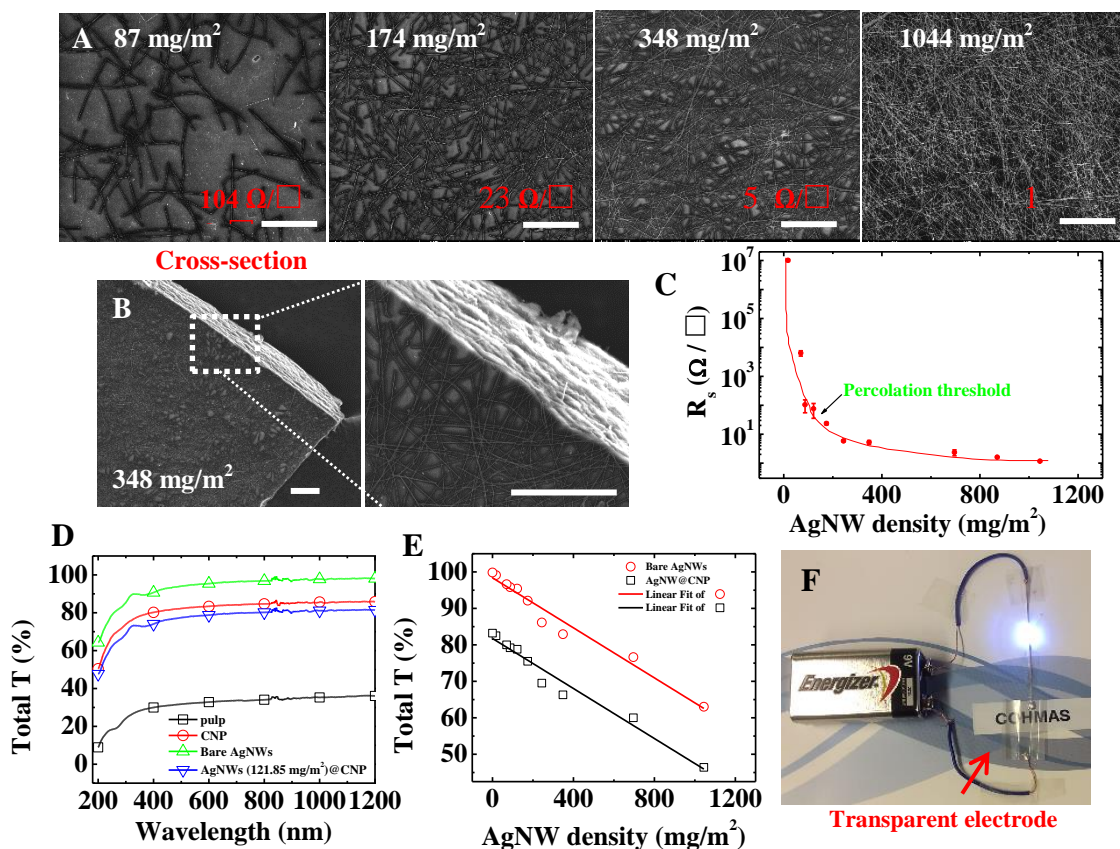


Figure 6.7. (A) SEM images of nanopaper electrodes and their sheet resistance dependent on AgNW density; (B) Representative SEM image of nanopaper electrode cross-section area; Scale bars in pictures are 20 μm ; (C) Sheet resistance as a function of AgNW areal density. (D) Total transmittance of various samples vs. wavelength; (E) total transmittance as a function of AgNW areal density; (F) Demonstration presents a series circuit composed of a battery, a $2 \times 3 \text{ cm}^2$ transparent AgNWs/CNP paper (CNC: 83 wt.%) and a LED lamp.

6.4.6. Damage-tolerant electrical conductivity of AgNWs/CNP electrodes

Electrical resistance (R) of the electrode was constantly monitored while it was under cyclic bending/folding between two grips (**Figure 6.8A**). The bending was realized by changing the distance between the grips and the degree of bending was quantified by a strain defined as the ratio of the travel distance of one of the grips to the initial gap distance between the two grips. **Figures 6.8B and C** show the resistance of the electrodes with different AgNW areal densities under the varying strain. It is clear that R decreases with the increasing areal density and for each sample R remains nearly constant after 1000 cycles of bending. This result

demonstrates high robustness of the electrodes under mechanical loading, which can be attributed to strong adhesion between the AgNWs and the CNP substrate and between intersecting AgNWs. R of a representative electrode was also measured when the sample was under increasing cyclic tensile strain (until the sample fracture at $\sim 4\%$ strain after 9 cycles). Comparing the R and strain curves in **Figure 6.8D** one should notice that the R curve traces the strain curve, suggesting a linear relationship between the strain and the resistance. A tensile strain exerted on the electrode can elongate the nanowires and/or break some connections between the nanowires, both of which increase the resistance. However, the reversibility of the resistance demonstrated under the cyclic strain indicates that the deformation/breakage is transient. The observed R vs. strain relationship shows the electrode's potential as a novel strain sensor.

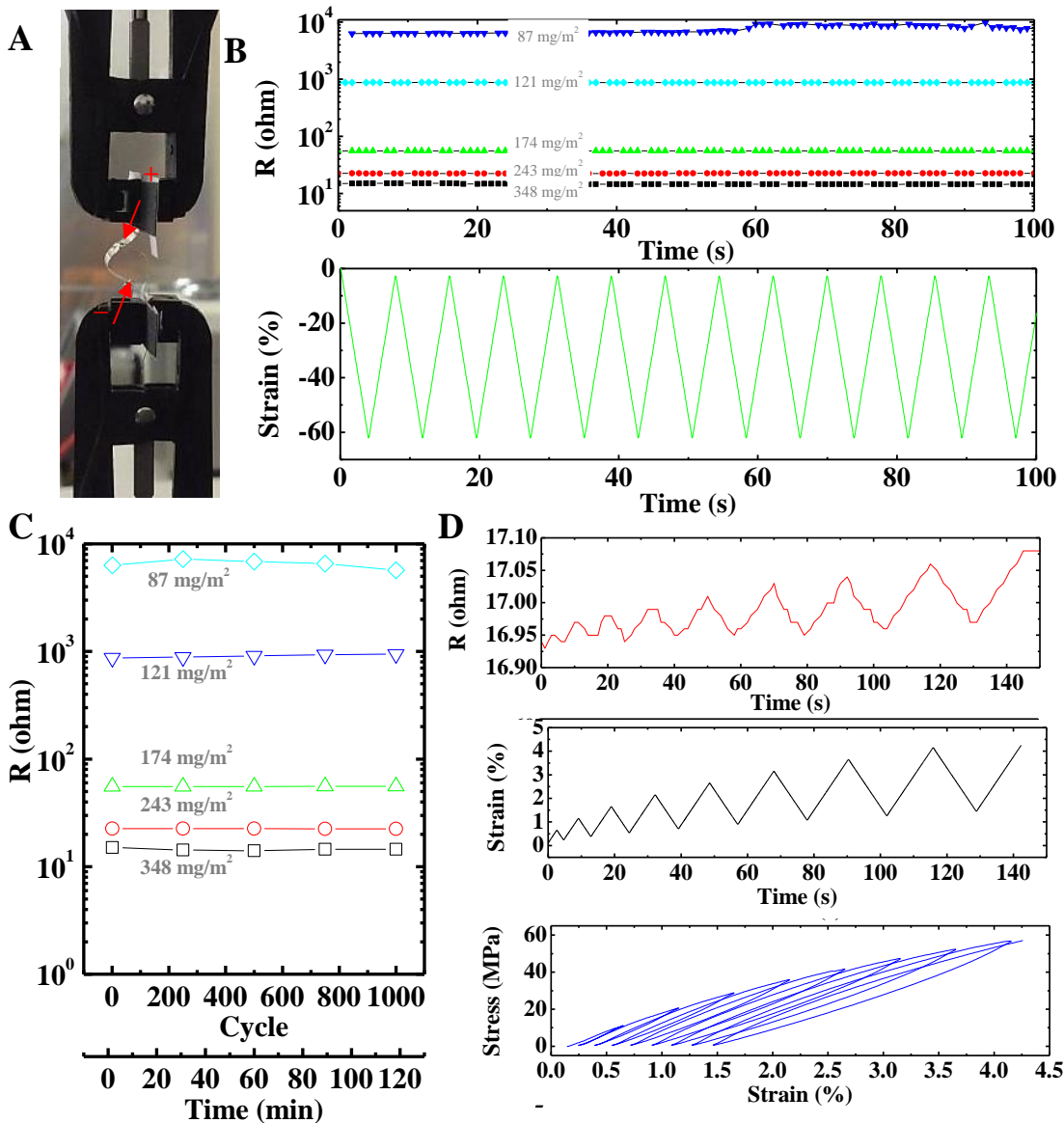


Figure 6.8. (A) in-situ electrical resistance measurement setup, conductive paper electrode: CNP (CNC content: 83 %) with 174 mg/m² AgNWs under bending, the resistance is measured for a middle area of the sample (Length: 0.8 cm; Width: 0.2 cm); (B) initial 12 cycles for electrical resistivity measurement and in-situ cyclic bending of various paper electrodes; (C) 1000 cycles electrical resistivity measurements under cyclic compression for various samples; (D) In-situ electrical resistivity of a representative electrode (348 mg/m² AgNW density) under tensile mode.

6.4.7. AgNWs/CNP electrodes in LED devices

As a primitive demonstration, the electrodes were used to build AlGaInP-based red LED display devices. **Figure 6.9A** shows a transparent electrode with a micro-sized lead formed by

the patterned AgNW layer. The schematic structure of the LED device using the AgNWs/CNP as the electrode and counter electrode is shown in **Figure 6.9B inset** (top view of one electrode) and **Figure 6.9C inset** (side view of LED devices between laminated paper electrodes). The device successfully lights up when a certain level of voltage is applied (**Figure 6.9C**). The current density vs. voltage (I - V) characteristic of the device were measured and the result is compared with that of the device using standard Ti/Au metallic leads (**Figure 6.9D**). The I - V curve shows that the turn-on voltage of the LED with the CNP-based electrodes is similar to that of the standard one. A localized annealing may be able to improve the contact of the former and decrease its resistance. The output power and external quantum efficiency (EQE) between the standard LED and the new LED are also compared (**Figure 6.9E**). Due to its higher resistance, the output power and EQE of the new LED are moderately lower compared to the standard device. Nevertheless, we demonstrate for the first time the feasibility of using the hybrid nanopaper in LED devices. This demonstration paves the way for further development of flexible, robust displays using the nanopaper.

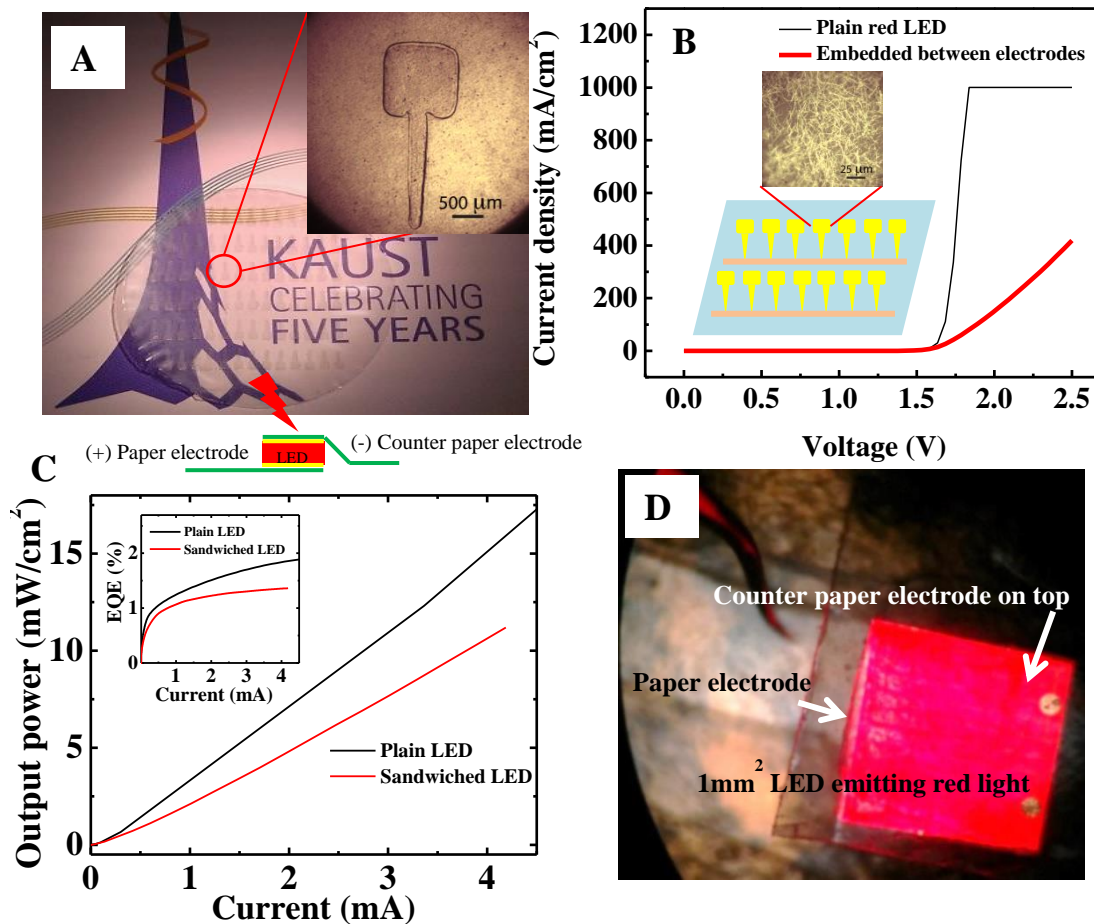


Figure 6.9. (A) Photo of nanopaper electrode with AgNWs grids for sandwiching LED devices; inset is an optical microscopy image of surface morphology of the AgNWs grids (two micron-sized probes were inset into nanopaper electrode to measure the conductivity); (B-C) current density vs. voltage (I-V) characteristic and light output power vs. current (L-I) characteristics, and (inset) external quantum efficiency vs. current (EQE-I) characteristics of freestanding LED device and embedded red LED device; (D) Sandwiched paper electrode/LED device/paper electrode emitting red light.

6.5. Conclusion

In this study, we developed a facile methodology to synthesize highly transparent, mechanically robust, hybrid CNP consisting of CNFs and CNCs. Mechanical and optical properties of the nanopaper can be tailored by varying the ratio between CNFs and CNCs. The concentration of CNCs affects the surface roughness, porosity and CNF entanglement of the nanopaper, and therefore results in its different transmittance and mechanical properties. The

hybrid CNP in this research shows equivalent or higher total transmittance and much smaller haze compared to the nanopaper reported in the literature. This is due to the hybrid CNP's low surface roughness and porosity caused by the "filling" effect of CNCs.

Depositing AgNWs on the hybrid CNP substrate produces transparent, flexible electrodes, whose conductivity is highly dependent on the areal density of AgNWs. In-situ measurement of the conductivity during cyclic loadings shows that the electrical property of the electrode is damage tolerant under bending deformation. Under tensile deformation, the electrical resistance of the electrode exhibits a linear relationship with the tensile strain, suggesting its potential to be used as a strain sensor. A proof-of-concept LED device has been produced to demonstrate the electrode's potential in flexible electronic devices. Further development will be carried out to decrease the contact resistance of the electrode and use it in large area flexible displays.

6.6. References

1. Madaria, A. R., Kumar, A. & Zhou, C. Large scale, highly conductive and patterned transparent films of silver nanowires on arbitrary substrates and their application in touch screens. *Nanotechnology* **22**, 245201 (2011).
2. Reineke, S. *et al.* White organic light-emitting diodes with fluorescent tube efficiency. *Nature* **459**, 234–8 (2009).
3. Leem, D.-S. *et al.* Efficient organic solar cells with solution-processed silver nanowire electrodes. *Advanced materials (Deerfield Beach, Fla.)* **23**, 4371–5 (2011).
4. Zhou, J. & Lubineau, G. Improving electrical conductivity in polycarbonate nanocomposites using highly conductive PEDOT/PSS coated MWCNTs. *ACS Applied Materials & Interfaces* **5**, 6189–200 (2013).
5. Zhou, J., Fukawa, T., Shirai, H. & Kimura, M. Anisotropic Motion of Electroactive Papers Coated with PEDOT/PSS. *Macromolecular Materials and Engineering* **295**, 671–675 (2010).
6. Hu, L., Kim, H. S., Lee, J., Peumans, P. & Cui, Y. Scalable Coating and Properties of Transparent, Flexible, Silver Nanowire Electrodes. *ACS Nano* **4**, 2955–2963 (2010).

7. De, S. *et al.* Silver nanowire networks as flexible, transparent, conductive films: extremely high DC to optical conductivity ratios. *ACS Nano* **3**, 1767–1774 (2009).
8. Zeng, X.-Y., Zhang, Q.-K., Yu, R.-M. & Lu, C.-Z. A new transparent conductor: silver nanowire film buried at the surface of a transparent polymer. *Advanced materials (Deerfield Beach, Fla.)* **22**, 4484–8 (2010).
9. Liang, J. *et al.* Silver nanowire percolation network soldered with graphene oxide at room temperature and its application for fully stretchable polymer light-emitting diodes. *ACS nano* **8**, 1590–600 (2014).
10. Hu, L. *et al.* Transparent and conductive paper from nanocellulose fibers. *Energy & Environmental Science* **6**, 513 (2013).
11. Huang, J. *et al.* Highly transparent and flexible nanopaper transistors. *ACS nano* **7**, 2106–13 (2013).
12. Sehaqui, H., Liu, A., Zhou, Q. & Berglund, L. a Fast preparation procedure for large, flat cellulose and cellulose/inorganic nanopaper structures. *Biomacromolecules* **11**, 2195–8 (2010).
13. Huang, J. *et al.* Highly transparent and flexible nanopaper transistors. *ACS nano* **7**, 2106–13 (2013).
14. Zhu, H. *et al.* Transparent nanopaper with tailored optical properties. *Nanoscale* **5**, 3787–92 (2013).
15. Fang, Z. *et al.* Novel nanostructured paper with ultrahigh transparency and ultrahigh haze for solar cells. *Nano letters* **14**, 765–73 (2014).
16. Sehaqui, H. *et al.* Cellulose Nanofiber Orientation in Nanopaper and Nanocomposites by Cold Drawing. *ACS Applied Materials & Interfaces* **4**, 1043–1049 (2012).
17. Walther, A., Timonen, J. V. I., Díez, I., Laukkanen, A. & Ikkala, O. Multifunctional high-performance biofibers based on wet-extrusion of renewable native cellulose nanofibrils. *Advanced materials* **23**, 2924–8 (2011).
18. Eichhorn, S. J. *et al.* Review: current international research into cellulose nanofibres and nanocomposites. *Journal of Materials Science* **45**, 1–33 (2009).
19. Fang, Z. *et al.* Highly transparent and writable wood all-cellulose hybrid nanostructured paper. *Journal of Materials Chemistry C* **1**, 6191 (2013).
20. Tang, H., Butchosa, N. & Zhou, Q. A Transparent, Hazy, and Strong Macroscopic Ribbon of Oriented Cellulose Nanofibrils Bearing Poly(ethylene glycol). *Advanced materials* **27**, 2070–6 (2015).

21. Yano, H. *et al.* Optically Transparent Composites Reinforced with Networks of Bacterial Nanofibers. *Advanced Materials* **17**, 153–155 (2005).
22. Fernandes, S. C. M. *et al.* Novel transparent nanocomposite films based on chitosan and bacterial cellulose. *Green Chemistry* **11**, 2023 (2009).
23. Iwamoto, S., Nakagaito, a. N., Yano, H. & Nogi, M. Optically transparent composites reinforced with plant fiber-based nanofibers. *Applied Physics A* **81**, 1109–1112 (2005).
24. Henriksson, M., Berglund, L. A., Isaksson, P., Lindström, T. & Nishino, T. Cellulose nanopaper structures of high toughness. *Biomacromolecules* **9**, 1579–1585 (2008).
25. Sun, X., Wu, Q., Ren, S. & Lei, T. Comparison of highly transparent all-cellulose nanopaper prepared using sulfuric acid and TEMPO-mediated oxidation methods. *Cellulose* **22**, 1123–1133 (2015).
26. Fang, Z. *et al.* Novel nanostructured paper with ultrahigh transparency and ultrahigh haze for solar cells. *Nano letters* **14**, 765–73 (2014).
27. Hsieh, M.-C., Kim, C., Nogi, M. & Suganuma, K. Electrically conductive lines on cellulose nanopaper for flexible electrical devices. *Nanoscale* **5**, 9289–95 (2013).
28. Fang, Z. *et al.* Highly transparent paper with tunable haze for green electronics. *Energy Environ. Sci.* **7**, 3313–3319 (2014).
29. Xu, X., Liu, F., Jiang, L. & Zhu, J. Cellulose Nanocrystals vs. Cellulose Nanofibrils: A Comparative Study on Their Microstructures and Effects as Polymer Reinforcing Agents. *ACS Applied Materials & Interfaces* **5**, 2999–3009 (2013).
30. Xu, X. *et al.* Comparison between Cellulose Nanocrystal and Cellulose Nanofibril Reinforced Poly(ethylene oxide) Nanofibers and Their Novel Shish-Kebab-Like Crystalline Structures. *Macromolecules* **47**, 3409–3416 (2014).
31. Liu, A., Walther, A., Ikkala, O., Belova, L. & Berglund, L. a Clay nanopaper with tough cellulose nanofiber matrix for fire retardancy and gas barrier functions. *Biomacromolecules* **12**, 633–41 (2011).
32. Zhu, H. *et al.* Biodegradable transparent substrates for flexible organic-light-emitting diodes. *Energy & Environmental Science* **6**, 2105 (2013).
33. Zhu, H., Fang, Z., Preston, C., Li, Y. & Hu, L. Transparent paper: fabrications, properties, and device applications. *Energy & Environmental Science* **7**, 269–287 (2014).
34. Hu, L. *et al.* Transparent and conductive paper from nanocellulose fibers. *Energy & Environmental Science* **6**, 513 (2013).

35. Nogi, M., Iwamoto, S., Nakagaito, A. N. & Yano, H. Optically Transparent Nanofiber Paper. *Advanced Materials* **21**, 1595–1598 (2009).
36. Kunugi, T., Ichinose, C. & Suzuki, A. Preparation of High-Modulus and High-Strength Poly (ethylene Terephthalate) Film by Zone-Annealing Method. *Journal of Applied Polymer Science* **31**, 429–439 (1986).
37. Choi, D. Y., Kang, H. W., Sung, H. J. & Kim, S. S. Annealing-free, flexible silver nanowire-polymer composite electrodes via a continuous two-step spray-coating method. *Nanoscale* **5**, 977–83 (2013).
38. HunterLab Haze Application Note. *www.barnett-technical.com* **9**, <http://barnett-technical.com/HunterLab%20Haze%20Ap> (2008).
39. Corning, D. Optical Properties, Definitions and Measurements. *www.Dowcorning.com* <https://www.dowcorning.com/content/publishedlit/11> (2015).
40. Wan, C., Qiao, X., Zhang, Y. & Zhang, Y. Effect of different clay treatment on morphology and mechanical properties of PVC-clay nanocomposites. *Polymer Testing* **22**, 453–461 (2003).
41. Mechanical and Optical Properties of Polyethylene Filled with Nano-SiO₂.pdf.
42. Krč, J., Zeman, M., Smole, F. & Topič, M. Optical modeling of a-Si:H solar cells deposited on textured glass/SnO₂ substrates. *Journal of Applied Physics* **92**, 749 (2002).
43. Resch, K. Optical Properties of Highly Transparent Polypropylene Cast Films : Influence of Material Structure , Additives , and Processing Conditions. (2006).doi:10.1002/pen
44. Zhou, R. & Burkhart, T. Optical Properties of Particle-Filled Polycarbonate , Polystyrene , and Poly (methyl methacrylate) Composites. (2009).doi:10.1002/app
45. Wydeven, T. Plasma polymerized coating for polycarbonate : single layer , abrasion resistant , and antireflection. **16**, 717–721 (1977).
46. Gu, Q. G. & Zhou, Q. L. PREPARATION OF HIGH STRENGTH AND OPTICALLY TRANSPARENT SILICONE RUBBER. **34**, (1998).
47. Galdi, B. M. R., Nicolais, V., Maio, L. Di & Incarnato, L. Production of Active PET Films : Evaluation of Scavenging Activity and Science. 257–268 (2008).doi:10.1002/pts
48. Jagadish, R. S. & Raj, B. Properties and sorption studies of polyethylene oxide–starch blended films. *Food Hydrocolloids* **25**, 1572–1580 (2011).

49. Zhang, J., Tu, W. & Dai, Z. Synthesis and characterization of transparent and high impact resistance polyurethane coatings based on polyester polyols and isocyanate trimers. *Progress in Organic Coatings* **75**, 579–583 (2012).
50. Hongsingthong, A., Krajangsang, T., Yunaz, I. A., Miyajima, S. & Konagai, M. ZnO Films with Very High Haze Value for Use as Front Transparent Conductive Oxide Films in Thin-Film Silicon Solar Cells. *Applied Physics Express* **3**, 051102 (2010).
51. Chem, J. P., Stehling, F. C., Speed, C. S. & Westerman, L. Causes of Haze of Low-Density Polyethylene Blown Films. *Macromolecules* **14**, 698–708 (1981).
52. Liang, H.-W. *et al.* Highly conductive and stretchable conductors fabricated from bacterial cellulose. *NPG Asia Materials* **4**, e19 (2012).
53. Apetz, R. & Bruggen, M. P. B. Van Transparent Alumina : A Light-Scattering Model. *Journal of American Ceramic Society* **86**, 480–486 (2003).
54. Boulesteix, R., Maître, A., Chrétien, L., Rabinovitch, Y. & Sallé, C. Microstructural Evolution During Vacuum Sintering of Yttrium Aluminum Garnet Transparent Ceramics: Toward the Origin of Residual Porosity Affecting the Transparency. *Journal of the American Ceramic Society* **96**, 1724–1731 (2013).
55. Zhou, J., Ventura, I. A. & Lubineau, G. Probing the Role of Poly(3,4-ethylenedioxythiophene)/ Poly(styrenesulfonate)-Coated Multiwalled Carbon Nanotubes in the Thermal and Mechanical Properties of Polycarbonate Nanocomposites. *Industrial & Engineering Chemistry Research* **53**, 3539–3549 (2014).
56. International, P. Material Properties-Electrical/Physical Properties. *Plastic International* http://www.plasticsintl.com/sortable_material_s.ph (2015).
57. EngineeringToolBox.com Engineering Materials-Comparing some typical properties of common engineering materials like steel, plastics, ceramics and composites. *www.EngineeringToolBox.com* <http://www.engineeringtoolbox.com/engineering-mate> (2015).
58. Toolbox.com, T. E. Tensile Modulus - Modulus of Elasticity or Young's Modulus - for some common Materials. *The Engineering Toolbox.com* http://www.engineeringtoolbox.com/young-modulus-d_ (2015).
59. PELLA, T. Properties of Plastics. *TED PELLA, INC.* https://www.tedpella.com/company_html/plastics-pro (2015).
60. Ye, S., Rathmell, A. R., Chen, Z., Stewart, I. E. & Wiley, B. J. Metal Nanowire Networks: The Next Generation of Transparent Conductors. *Advanced Materials* **26**, 6670–6687 (2014).

61. Lee, J., Connor, S. T., Cui, Y. & Peumans, P. Solution-Processed Metal Nanowire Mesh Transparent Electrodes. *Nano letters* **8**, 689–692 (2008).

CHAPTER 7. CONCLUSIONS AND FUTURE WORK

7.1. Conclusions

Compared to other nanofibers such as CNTs, cellulose nanofibers represent a new frontier in nanomaterial research. Their unique combination of properties, i.e. high strength and modulus, high functionality, nontoxic and biocompatibility, and renewability, has attracted intense research interest. Initial applications of the cellulose nanofibers in polymer nanocomposites, hydrogels, nanopaper, etc. have been developed. Based on the previous studies, this Ph.D. project is targeted to push the boundaries of cellulose nanofiber research. It is mainly focused on nanocomposites and novel energy and flexible device applications. New knowledge has been generated and proof-of-concept applications have been demonstrated through this study.

More specifically, fundamental understanding and implementation of processes for the following five areas have been advanced: **1).** CNF and CNC reinforced polymer nanocomposites – similarities, differences, failure mechanisms and modeling; **2).** Effects of CNFs and CNCs on the electrospinning process and on the properties (size, crystallization, mechanical performance and failure behavior) of the electrospun nanofibers; **3).** CNFs and lignin based carbon tubes and core-shell carbon fibers via electrospinning and subsequent carbonization; **4).** Flexible carbon aerogels derived from BC and lignin hydrogels and their application in energy storage devices; **5).** Transparent, flexible, CNC/CNF-based hybrid nanopaper and electrodes and their application in LED devices.

First, a systematic comparison between CNCs and CNFs was made with focus on their microstructures, interfacial bonding with the PEO matrix, and the resulting effects on the dynamic and mechanical properties of the PEO/CNC and PEO/CNF nanocomposites. The

maximum strength, modulus and fracture toughness of the composites were found to occur at 7 wt % fiber content for both CNCs and CNFs. The increases were attributed to strong fiber-matrix interfacial bonding and large aspect ratios of the fibers. CNFs led to higher strength and modulus than did CNCs at the same fiber concentration due to CNFs' much larger aspect ratio and their percolation networks. The entanglements and percolation of CNFs also resulted in their higher probability of fiber agglomeration compared to CNCs, which caused lower strain-at-failure for PEO/CNF composites. The moduli of the composites were simulated using two models and their accuracies were compared. The Ouali model was found to be more accurate for PEO/CNF composites, whereas the Halpin-Kardos model was more suitable for PEO/CNC composites. The results from this comparative study are important for proper selection of cellulose nanofibers as nanoreinforcements in polymer composites.

In the second study, CNCs and CNFs were used to reinforce electrospun PEO nanofiber mats and their effects on the viscosity of the spinning solutions, nanofiber diameter and diameter distribution, crystalline structures of the nanofibers, and the mechanical properties of the nanofiber mats were systematically studied. The CNFs caused high viscosity of the PEO solutions, relatively poor spinnability and bimodal fiber diameter distribution due to their entangled network structure. Rare shish-kebab-like PEO crystalline structures were discovered in the electrospun nanofibers. Mechanical properties of the nanofiber mats, including strength, modulus and fracture toughness, were significantly improved by the addition of low concentrations of CNCs and CNFs. The properties deteriorated at high concentrations of the nanofibers due to fiber agglomeration.

Third, novel hollow and porous core-shell carbon fibers using mostly biobased materials. Lignin was readily electrospun into hollow fibers or fiber shell after adding PAN as a co-

spinning polymer. CNFs were difficult to disperse in non-polar solvents and surface acetylation had to be performed. Acetylated CNF dispersion in silicon oil/chloroform mixture was stable and suitable for electrospinning to form fiber core. The obtained hollow and core-shell fibers were successfully carbonized without causing obvious changes on the fiber structure. The two types of new fibers, especially the porous core-shell one, exhibit increased surface area and porosity over the conventional solid fibers and are expected to have a great potential in many advanced applications.

In the fourth part, a facile methodology to synthesize catalyst-free, flexible, mesoporous, and highly graphitized carbon aerogels based on BC-toughened LRF gels is developed. The carbon aerogels consist of core-shell structured carbon nanofibers, where the core and shell are graphitized BC nanofibers and LRF nanoaggregates, respectively. For the first time large reversible deformations in BC-LRF carbon aerogels are attained by utilizing the toughening effect of the BC nanofiber network. The unique blackberry-like structure and large mesopore concentration of these materials facilitate ion transportation and adsorption and lead to their high areal capacitance. Some of the potential applications of the carbon aerogels include oil/water separation, supercapacitors, batteries, catalyst supports, and sensors.

Finally, a facile technique is developed to synthesize highly transparent, mechanically robust, hybrid CNP consisting of CNFs and CNCs. Mechanical and optical properties of the CNP can be tailored by varying the ratio between CNFs and CNCs. This CNP shows equivalent or higher total transmittance and much smaller haze compared to the nanpaper reported in the literature due to the hybrid CNP's low surface roughness and porosity caused by the "filling" effect of CNCs. Depositing AgNWs on the hybrid CNP substrate produces transparent, flexible electrodes, whose conductivity is highly dependent on the areal density of AgNWs. The

conductivity is stable during repeated bending deformation and decreases with increasing tensile strain. A proof-of-concept LED device is produced to demonstrate the electrode's potential in flexible electronic devices.

7.2. Future work

This Ph.D. study has generated new knowledge about cellulose nanofibers and has developed novel products using these renewable nanomaterials. The following further investigations are suggested to continue to deepen the understanding and expand the applications of the materials.

In the comparative studies of CNCs and CNFs as nanoreinforcements in polymer matrices (Chapters 2 & 3), PEO, a water soluble polymer, was used as a model polymer. Other commodity polymers such as polyethylene and polypropylene can be used in the future to confirm the findings from this study or to make new discoveries. These polymers are not water soluble and therefore are difficult to be used as the matrices for the cellulose nanofibers. However, the research is important because the wide spread applications of the commodity polymers. To continue the research in this direction, surface functionalization of the cellulose nanofibers and melt blending of the nanofibers and the polymers should be developed.

In Chapter 5, lignin is used to replace resorcinol to make flexible carbon aerogels. The low reactivity of the commercial lignin limits its loading in the hydrogel synthesis. To increase the biocontents of the aerogels, more research efforts are needed to increase the use of lignin, including depolymerization and functionalization of lignin.

In Chapter 6, we develop highly transparent CNCs/CNFs hybrid nanopaper with tunable optical and mechanical properties. This nanopaper has shown great potential in flexible electronic devices. In the future, BC, with its uniform diameter and long length, is also a great

candidate for transparent nanopaper and should be investigated as another raw material for the nanopaper.

APPENDIX. LIST OF PUBLICATIONS

A.1. Publications in Thesis (5)

This thesis is based on five papers, which consist of the studies on various cellulose nanofiber systems. The papers are appended at the end of the thesis.

- I. Cellulose Nanocrystals vs. Cellulose Nanofibrils: A Comparative Study on Their Microstructures and Effects as Polymer Reinforcing Agents.
Xuezhu Xu, Fei Liu, Long Jiang, Junyong Zhu, Darrin Haagenson, Dennis P. Wiesenborn: ACS Applied Materials & Interfaces 03/2013; 5(8): 2999-3009.
- II. Comparison between Cellulose Nanocrystal and Cellulose Nanofibril Reinforced Poly(ethylene oxide) Nanofibers and Their Novel Shish-Kebab-Like Crystalline Structures.
Xuezhu Xu, Haoran Wang, Long Jiang, Xinnan Wang, Scott A. Payne, J. Y. Zhu, Ruipeng Li: Macromolecules 05/2014; 47:3409-3416.
- III. Porous Core-Shell Carbon Fibers Derived from Lignin and Cellulose Nanofibrils.
Xuezhu Xu, Jian Zhou, Long Jiang, Gilles Lubineau, Ye Chen, Xiang-Fa Wu, Robert Piere: Materials Letters 07/2013; 109: 175-178.
- IV. Flexible, Highly Graphitized Carbon Aerogels Based on Bacterial Cellulose/Lignin: Catalyst-Free Synthesis and its Application in Energy Storage Devices.
Xuezhu Xu, Jian Zhou, D. H. Nagaraju, Long Jiang, Val R. Marinov, Gilles Lubineau, Husam N. Alshareef, Myungkeun Oh: Advanced Functional Materials 04/2015; 25(21): 3193-3202.
- V. Transparent, flexible electrodes based on hybrid cellulose nanofibers and their application in Light Emitting Diode Devices.
Xuezhu Xu, Jian Zhou, Long Jiang, Gilles Lubineau, Tienkhee Ng, Boon S. Ooi, Hsien-Yu Liao, Chao Shen, Long Chen. At final stage of preparation, 2015.

A.2. Other related publications (15)

A.2.1. Book Chapters (1)

- I. Crystallization Behavior of Cellulose Nanofibril and Cellulose Nanocrystal Based Nanocomposites. Handbook of Cellulose Nanocomposites.
Editors: K Hanieh, D Alain, T Sabu, A Ishak, et al. Chapter author: Long Jiang, Xuezhu Xu: Wiley-VCH. About to submit, 2015.

A.2.2. Journal Publications (4)

- I. Semi-metallic, Strong and Stretchable Wet-spun Conjugated Polymer Microfibers.
Jian Zhou, Er Qiang Li, Ruipeng Li, Xuezhu Xu, Isaac Aguilar Ventura, Ali Moussawi,

Dalaver H. Anjum, Mohamed Nejib Hedhili, Detlef-M. Smilgies, Gilles Lubineau, Sigurdur T. Thoroddsen: Journal of Materials Chemistry C 01/2015; 3: 2528-2538.

- II. Temperature-dependent microstructure of PEDOT/PSS films: insights from morphological, mechanical and electrical analyses.
Jian Zhou, Dalaver H. Anjum, Long Chen, Xuezhu Xu, Isaac Aguilar Ventura, Long Jiang, Gilles Lubineau: Journal of Materials Chemistry C 08/2014; 2: 9903-9910.
- III. Preparation and Properties of Electrospun Soy Protein Isolate/Polyethylene Oxide Nanofiber Membranes.
Xuezhu Xu, Long Jiang, Zhengping Zhou, Xiangfa Wu, Yechun Wang: ACS Applied Materials & Interfaces 07/2012; 4(8):4331-4337.
- IV. Lignin-based Carbon Fibers: Carbon Nanotube Decoration and Superior Thermal Stability
Xuezhu Xu, Jian Zhou, Long Jiang, Gilles Lubineau, Scott A Payne, David Gutschmidt:: Carbon 08/2014; 80:91-102.

A.2.3. Conference Posters/Proceedings (10)

- I. Plastic-like Transparent and Robust Nanopaper.
Xuezhu Xu, Jian Zhou, Long Jiang, Gilles Lubineau: Invited Speaker at KAUST Research Conference: Recent Trends in Predicting and Monitoring the Integrity of Composites (COMINT), 06/01 – 06/02/2015. Jeddah, the Kingdom of Saudi Arabia.
- II. Flexible, Highly Graphitized Carbon Aerogel and Its Application in Energy Storage Devices.
Xuezhu Xu, Long Jiang: ND EPSCoR 2015 State Conference, 04/22/2015. Fargo, U.S.
- III. Cellulose Nanocrystals and Cellulose Nanofibrils: Use in Composites and other Applications.
Long Jiang, JY Zhu, Xuezhu Xu: 2014 TAPPI International Conference on Nanotechnology, 06/23 - 26/2014. Vancouver, Canada.
- IV. Biobased Nano-structured Carbon Materials. 13th International symposium on Bioplastics,
Long Jiang, Xuezhu Xu, Gilles Lubineau, Jian Zhou: Biocomposites & Biorefining. 05/19 - 24/2014. Guelph, Ontario, Canada.
- V. Porous Core-Shell Carbon Fibers Derived from Lignin and Cellulose Nanofibrils.
Xuezhu Xu, Long Jiang, Gilles Lubineau: ND EPSCoR-IDeA State Conference, 04/29/2014. Grand Forks, ND, U.S.
- VI. Biomass Based Cellulose Nanofibers for Advanced Applications.
Long Jiang, Xuezhu Xu, Gilles Lubineau, J Zhu: 2013 AIChE Annual Meeting, 11/03-08/2013. San Francisco, CA.

- VII. Polymer Nanocomposites Comprising Cellulose Nanowhiskers (CNW) and Cellulose Nanofibrils (CNF) as Reinforcing Agents.
Long Jiang, Xuezhu Xu, Ellen Ten, MP Wolcott, JY Zhu: 20th Anniversary of the Bio-Environmental Polymer Society Annual Meeting, 09/18 - 21/2012. Denton, TX, U.S.
- VIII. Preparation and Properties of Electrospun Soy Protein Isolate/Polyethylene Oxide Nanofiber Membranes.
Xuezhu Xu, Long Jiang, Zhengping Zhou, Xiang-fa Wu, Yechun Wang. 2nd Annual Engineering Research Summit, A Conference for Engineering Faculty from NDSU, SDSU and UND, 05/23, 2012. Grand Forks, ND, U.S.
- IX. Use of Cellulose Nanowhiskers as an Effective Reinforcement in Composites.
Long Jiang, M Wolcott, Ellen Ten, Xuezhu Xu. 244th ACS National Meeting, 08/19 - 23/2012. Philadelphia, PA, U.S.
- X. Cellulose Nanocrystals and Cellulose Nanofibrils: A Comparison Study on Their Effects in Composite Rheology and Reinforcement.
Xuezhu Xu, Long Jiang: 2012 Renewable Materials Summit: Markets for Building the Biorefinery, Hosted by LifeScience Alley & The BioBusiness Alliance of Minnesota, 05/15, 2012. Fargo, ND, U.S.